Functional Renormalization-Group Approaches to Multiband Models and Antiferromagnetically Ordered Phases

Von der Fakultät für
Mathematik, Informatik und Naturwissenschaften
der RWTH Aachen University
zur Erlangung des akademischen Grades
eines Doktors der Naturwissenschaften
genehmigte Dissertation

vorgelegt von
Diplom-Physiker Stefan Maier
aus Günzburg a. d. Donau

Berichter: Univ.-Prof. Dr. Carsten Honerkamp
Univ.-Prof. Dr. Manfred Salmhofer

Tag der mündlichen Prüfung: 14.03.2014

Diese Dissertation ist auf den Internetseiten der Hochschulbibliothek online verfügbar.

Abstract

This thesis is devoted to purely fermionic functional renormalization-group (fRG) studies of multiband effects and of antiferromagnetically ordered phases.

The formal framework of the one-particle irreducible fRG scheme is recapitulated and extended for charge-conserving theories with a collinear spin symmetry. For multiband models, point-group symmetries and their interplay with the phases of Bloch basis states are discussed. Further, an improved truncation of the fRG flow equations is proposed that keeps track of three-particle interactions generated by virtual excitations of bands away from the Fermi surface.

The feedback of this three-particle term on the two-particle interaction is first investigated in a g-ology approach to a simple two-band model for cuprate superconductors at weak coupling. The results suggest a potentially strong impact of the three-particle term. Subsequently, the three-band Emery model is analyzed within a channel-decomposition, again at weak coupling. In contrast to earlier work, the approach pursued here does not rely on a form-factor expansion, which allows for the observation of a deformed d-wave pairing gap for increasingly incommensurate ordering tendencies in the magnetic channel. In this more refined study, the three-particle feedback plays a minor role. Despite considerable qualitative agreement with results for the one-band Hubbard model with effective parameters, multi-orbital effects are found to play an important role on a quantitative level.

Phases of antiferromagnetic ordering are first studied for a reduced mean-field model. In order to go beyond the mean-field picture, a hierarchy of approximations is devised, which starts from the corresponding channel-decomposed one-loop flow equations. Interaction terms breaking discrete symmetries are thereby successively neglected. In the course of these approximations, also an exchange parametrization is employed. For the spin-density wave phase of a two-pocket model initially proposed by Chubukov *et al.* in Phys. Rev. B **78** 134512, the flow equations are then integrated numerically at the most approximate level of the hierarchy. This yields a gap that is significantly reduced compared to mean-field theory. The resulting violation of the SU(2) Ward identity appears acceptable on a qualitative level, suggesting that the approximations causing this violation are physically meaningful.

Deutsche Zusammenfassung

Die folgende Arbeit ist dem Studium von Mehr-Band-Effekten und antiferromagnetisch geordneten Phasen mit Hilfe der funktionalen Renormierungsgruppe (fRG) für Fermionen gewidmet.

Die formalen Grundlagen des Ein-Teilchen-irreduziblen fRG-Schemas werden dargestellt und für ladungserhaltende Theorien mit kollinearer Spin-Ordnung erweitert. Die Punktgruppensymmetrien von Mehr-Band-Modellen und ihr Zusammenspiel mit den Phasen der Bloch-Basiszustände werden diskutiert. Es wird ferner eine verbesserte Trunkierung der Flussgleichungen der fRG zur Einbeziehung von Drei-Teilchen-Wechselwirkungen vorgeschlagen, die durch virtuelle Anregungen in von der Fermi-Fläche entfernten Bändern erzeugt werden.

Die Rückwirkung dieses Drei-Teilchen-Terms auf die Zwei-Teilchen-Wechselwirkung wird zunächst im Rahmen einer so genannten g-ology für ein einfaches Zwei-Band-Modell für Kuprate bei schwacher Kopplung untersucht. Die dabei erhaltenen Ergebnisse sprechen für eine wichtige Rolle des Drei-Teilchen-Terms. Eine Kanal-zerlegte Instabilitätsanaylse des Emery-Modells mit drei Bändern (wieder bei schwacher Kopplung) schließt sich an. Im Gegensatz zu früheren Arbeiten fußt dieser neuartige Zugang nicht auf einer Formfaktor-Entwicklung, sodass eine Verformung der d-Wellen Energielücke mit wachsender Inkommensurabilität antiferromagnetischer Tendenzen beobachtet werden kann. Im Rahmen dieser Betrachtungen erweist sich der Drei-Teilchen-Term als unbedeutend. Trotz qualitativer Übereinstimmung mit den Ergebnissen für das Einband-Hubbard-Modell mit effektiven Parametern spielen Mehr-Orbital-Effekte auf quantitativer Ebene eine wichtige Rolle.

Phasen mit antiferromagnetischer Ordnung werden zunächst im Rahmen eines reduzierten Molekularfeld-Modells untersucht. Für weitergehende Betrachtungen wird eine Hierarchie von Näherungstufen entwickelt. Sie beginnt bei den betreffenden Kanal-zerlegten Flussgleichungen in der Ein-Schleifen-Trunkierung. Wechselwirkungsterme, die diskrete Symmetrien brechen, werden dann sukzessive vernachlässigt. Ferner wird eine Austausch-Parametrisierung vorgenommen. Für die Spin-Dichte-Wellen-Phase eines ursprünglich von Chubukov *et al.* in Phys. Rev. B **78** 134512, vorgeschlagenen vereinfachten Modells für Eisen-basierte Supraleiter erfolgt eine Integration der fRG Flussgleichungen auf der stärksten Näherungsstufe. Dabei ergibt sich eine signifikante Erniedrigung

der Energielücke gegenüber der Molekularfeld-Theorie. Die dabei auftretende Verletzung der SU(2) Ward-Identität bleibt auf qualitativem Niveau annehmbar und somit erscheinen die Näherungen, die sie verursachen, physikalisch sinnvoll.

Contents

Introduction

In the past years, the term 'emergent phenomena' has become ubiquitous. In complex systems, phenomena of interest often occur at low energy scales, while (more) fundamental theories apply at higher scales (for a general overview, see Ref. [1]). Superconducting and magnetically ordered low-temperature phases of solids are well-known examples thereof. Often, effective low-energy theories are available for such systems, while the results of *ab initio* calculations describe the physics at higher energy scales. For example, a solid with a high-energy band structure that can be calculated from density-functional theory (DFT), may be well described by a Ginzburg-Landau functional for the Copper-pair wavefunction or by a Heisenberg Hamiltonian for localized spins at low temperatures. While such effective theories may give a consistent description of low-temperature phases, they generically make no statement on how low-temperature phenomena follow from more fundamental properties of the system.

For unconventional superconductors, this is a very intriguing question. These materials have rich phase diagrams and the properties of their various low-energy phases are still a matter of current research. (For a recent piece of work on the pseudogap in the cuprates, for example, see [2].) Although finding suitable effective descriptions for such phases can still be a challenging task, the following theoretical questions also seem worth asking.

- Can the phase diagram of such materials then be predicted theoretically? Or, in other words, can one infer the nature of low-temperature phases from microscopic model Hamiltonians?

- Can one further make predictions for quantities in the low-temperature phases, e.g. the size of a pairing gap?

For correlated materials, these questions have been addressed by resorting to various many-particle techniques. From the knowledge of the chemical composition of the respective material and for a given set of external parameters one may first write down a model Hamiltonian with parameters that can be obtained from *ab initio* methods. In the absence of a sign problem, the system then can be directly assessed by Monte Carlo techniques. For small systems sizes, the model Hamiltonian may also be diagonalized exactly. For cases where the fermionic degrees of freedom interact strongly, dynamical mean-field theory [3–10] (DMFT), dynamical cluster quantum Monte Carlo (DCQMC)

techniques [11, 12] and the so-called variational cluster approach [13–16] (VCA) have been used in the literature. Also these methods are still being extended and developed further in order to hopefully promote a deeper understanding of the cuprate superconductors.

As renormalization group (RG) methods relate theories at different scales, they can be used to interpolate between microscopic models at higher energies and effective low-energy theories. In the traditional Wilsonian approach, [17] the degrees of freedom above some infrared cutoff are integrated out perturbatively and this cutoff is successively lowered with a differential stepsize. This way, flow equations for (typically a few) running couplings are obtained. In a functional renormalization group (fRG) framework, [18, 19] in contrast, the flow of a functional of the fields is governed by an exact flow equation. There are different fRG schemes corresponding to different functionals, [19, 20] which are related to the bare action of the system by a functional integral. Due to its exactness, the corresponding fRG flow equation can be regarded as a way to rephrase the original problem of calculating this functional integral.

Although such differential equations for functionals are generically not exactly solvable, they allow for a great flexibility in devising physically meaningful approximations. Typical approximation schemes are gradient and vertex expansions. In the former case, interactions between fermions are usually expressed as mediated by bosonic fields and the fRG flow is run for a functional of both kinds of fields. [18] This approach has been proven to be useful for the investigation of universal features such as critical phenomena. In a purely fermionic language, one typically expands the generating functional in monomials of the fields. [19] Form this latter approach, estimates for phase diagrams of the two-dimensional (single-band) Hubbard model [21–27], of interacting fermions on one- and multilayer honeycomb lattices, [28–33] of the pnictide superconductors [34–40] and of other two-dimensional systems [41–44] have been obtained within so-called instability analyses. Also phases of broken symmetries have been entered within a purely fermionic language — a charge-density wave phase in Refs. [45, 46] and singlet superfluid phases in Refs. [47–51]. (For fRG out of equilibrium and applications to one- and zero-dimensional systems, the reader shall be referred to Ref. [19] and the references therein.)

In this thesis, I will follow a purely fermionic one-particle irreducible (1PI) approach. Obtaining reliable phase diagrams and calculating quantities in phases of broken symmetries also would involve keeping track of non-universal, material-dependent features. Therefore, together with other authors' work, this thesis is geared at pushing the fRG for fermions into a more quantitative direction. I will focus on two aspects, namely on a convenient treatment of multiband models and on fRG flows into antiferromagnetic phases. Before giving an outline of this thesis, I will first briefly point out on why these two aspects are of particular interest.

If one desires to use the fRG as a tool to capture less universal features, material char-

acteristics should already be partly included in the model Hamiltonian. In other words, more degrees of freedom will be included in more quantitative studies. For the iron pnictides, for example, it appears then worthwhile to consider multiband models with bands away from the Fermi surface instead of only resorting to the fermionic degrees of freedom around the hole and electron pockets of these materials. For the cuprate superconductors, one may consider multiband extensions of the single-band Hubbard model in order to take excitations outside the conduction band into account.

This however comes at a price. The band index represents an additional quantum number of the fields. In a brute-force implementation of the fRG flow equations, this would significantly increase the requirements for computational resources, which makes an efficient parametrization of the band-index dependence desirable. Moreover, it may not be necessary to treat the low-energy sector and bands further away from the Fermi surface on equal footing. Instead, it may suffice to take fermionic degrees of freedom with higher energies only into account perturbatively.

But the impact of these high-energy degrees of freedom should not be expected to dominate the multiband features. Even for degrees of freedom close to the Fermi surface, the interactions of extended Hubbard models acquire a non-trivial momentum dependence in the band language. This effect has been dubbed *orbital makeup* by some authors [52] and *matrix element effect* by others. [43] As a testbed for multiband fRG, one may consider extended Hubbard models for the cuprates (see, for example, Refs. [53–55]) at (probably unrealistically) weak coupling. Such a study has already been undertaken within a Fermi-surface-patching implementation of the fRG flow equations, where the interaction is projected to the Fermi surface. [41] This approach, however, comes with discretization artefacts. Therefore, a systematic study of multiband effects within an improved implementation appears desirable. In contrast to Ref. [41], an approach based on a channel decomposition [24, 56] is used in this thesis.

Let us now turn our attention to fRG flows into phases of broken symmetry. Typically, model Hamiltonians for correlated fermions exhibit a U(1) symmetry, which corresponds to charge conservation, and a SU(2) spin symmetry. In the high-T_c cuprates and in iron-based superconductors, there are low-energy phases which break these symmetries. Namely, the U(1) symmetry is broken in the superconducting phase, while the alignment of spins in an antiferromagnetic or stripe spin-ordering phase goes along with the breaking of the SU(2) symmetry. The fRG flow equations preserve these symmetries and the onset of symmetry breaking manifests itself in a diverging interaction at some nonzero energy scale. In an instability analysis, the flow is run in the symmetric phase and the leading instability at such a divergence reflects the nature of the corresponding low-temperature phase, while the respective RG scale can be regarded as an estimate for the critical energy scale. However, this approach clearly lacks direct access to measurable quantities.

From previous purely fermionic fRG studies of symmetry-broken phases, [45–51, 57] the following generic picture emerges. Continuing a purely fermionic fRG flow into a symmetry-broken phase requires adding a small symmetry-breaking term to the bare action. This allows for the opening of a gap, which renders the interaction finite at the critical scale. In the absence of potential other instabilities *inside* the symmetry-broken phase, the cutoff can then be completely removed within the fRG flow. This way, a certain value for the energy gap is obtained. Compared to an instability analysis, symmetry-broken fRG flows provide a more quantitative picture in this sense, since the energy gap represents a measurable quantity.

In the literature, such studies have first been undertaken for reduced mean-field models for charge-density wave ordering [45, 46] and pairing. [48, 57] Clearly, these models can be solved by simpler means than fRG, but, in order to go beyond the mean-field picture, reproducing mean-field results correctly seems to represent an essential step. Within a purely fermionic framework, beyond-mean field studies have so far only been undertaken for singlet-superfluids. [47, 49–51] Although antiferromagnetically ordered phases play an essential role in the phase diagram of unconventional superconductors, these phases have not been studied yet within an fRG framework. The simultaneous breaking of the (discrete) translational symmetry and the (continuous) SU(2) symmetry may lead to additional complications compared to recent studies of singlet superfluids. Nevertheless, also for antiferromagnetic phases, it seems to be sensible to consider a reduced mean-field model first, before other models are taken into account. Due to the simultaneous breaking of a discrete and a continuous symmetry, the numerical integration of the flow equations may be very demanding in antiferromagnetic cases. Consequently, physically meaningful approximations that may reduce the computational effort seem desirable.

If a reliable purely fermionic fRG approach to antiferromagnetic phases can be established, its outcome could complement very recent work on the superconducting phase of the repulsive two-dimensional Hubbard model in Ref. [50]. This goal however is beyond the scope of this thesis, where a first step in this direction will be undertaken. In the long run, one may hope that studying multiband effects and the spin-density and superconducting phases of unconventional superconductors will promote a deeper understanding of those materials.

This thesis is organized as follows: In the first chapter, the basic fRG formalism is provided. The general framework is recapitulated in Chapter 1.1, which closely follows Refs. [19,58]. In Chapter 1.2, SU(2) symmetric fRG flows are considered, starting with a review of the corresponding flow equations and their channel decomposition. As an own result, I will discuss the truncated form-factor expansion underlying the implementation of such a channel decomposition in Refs. [24–26] from a group-theoretic viewpoint. In Chapter 1.3, the remaining symmetries in the presence of collinear spin ordering are exploited and, in the last section of the first chapter, a channel decomposition of the resulting flow equations is given.

The second chapter is devoted to formal problems specific to multiband Hubbard models. In a first section, the second-quantization procedure underlying these models is reviewed with an emphasis on the freedom in the choice of different basis sets of wavefunctions. In Chapter 2.2, the (nontrivial) point-group behavior of the coupling functions is discussed and conditions for particularly well-behaved basis sets of Bloch functions are given. A prescription for the calculation of an effective low-energy action for multiband models follows in Chapter 2.3. This effective action contains a non-vanishing three-particle interaction, which can be taken into account in fRG flows as described in Chapter 2.4.

Instability analyses of multiband models for cuprate materials are the subject of the third chapter. The interaction in these models will be chosen unrealistically weak in order to allow for fRG methods to apply. The results obtained should therefore not be taken as predictions for real materials, but should provide a valid picture of generic multiband effects. First, the feedback of the above mentioned three-particle term on the flow of the two-particle interaction is considered for a simple two-band model in a so-called two-patch approximation. For the (three-band) Emery model, multiband effects are classified in the second section, before their importance in the numerical fRG results is discussed in Chapter 3.3. These results are obtained form a channel-decomposed approach that avoids the biases of a truncated form factor expansion.

In the fourth chapter, the focus switches from multiband models to fRG flows into antiferromagnetically ordered phases. A reduced mean-field model with a perfectly nested dispersion is studied in a first section. In Chapter 4.2, symmetries are discussed and exploited in the channel decomposition of the flow equations for models with a more general interaction. But even then a direct integration of these differential equations would be a challenging numerical task and, in addition to the one-loop truncation of the fRG flow, other approximations seem in order. As a first step in this direction, time-reversal invariance is enforced in the interaction in Chapter 4.2.3, while it is still broken at the one-particle level. I then resort to an exchange parametrization in Chapter 4.3. Contributions to the interaction that are not of s-wave type are then neglected in Chapter 4.4. From the resulting flow equations, the mean-field gap equation can be exactly reproduced at the RPA level. This still holds if momentum non-conserving interaction terms are neglected (Nambu-normal approximation).

In the last chapter, the flow equations at this last, minimal level of approximation are solved numerically for a simple two-pocket model at perfect nesting. In the first section, peculiar features of this model are discussed, including an approximate weak-coupling solution of the gap equation for its spin-density wave phase. Subsequently, the implementation of the fRG flow equations is described and the momentum dependence of the exchange propagators is parametrized by a Lorentzian. This implementation has been devised in a way that avoids parallelization issues, so as to allow for an inclusion of neglected interaction terms in future work. The numerical results obtained in Nambu-normal approximation are discussed in Chapter 5.3 with a particular focus on

the violation of the global SU(2) Ward identity.

Chapter 1.

Functional Renormalization-Group Formalism for Fermions

This chapter contains the formalism on which the remainder of this thesis will be based. For charge-conserving theories, the functional renormalization group (fRG) framework is reviewed. For the case of an additional SU(2) *spin symmetry, also the channel decomposition of the fRG flow equations is recapitulated and the form-factor expansion used in earlier work by other authors is reviewed from a group-theoretic viewpoint. For phases of collinear spin ordering, an efficient parametrization exploiting the remaining spin symmetry is given along with the corresponding flow equations. For the case of commensurate antiferromagnetism, a channel decomposition of these flow equations is performed and a physical interpretation of the different renormalization channels is presented.*

Parts of this chapter have previously been published in Refs. [59] and [60].

Renormalization group (RG) methods can serve as a tool for relating theories of a particular system at different energy scales. In the context of correlated electronic systems, *ab initio* methods are generically applicable at high temperatures. At low temperatures, however, collective phenomena may play a role and the Landau Fermi liquid description may break down. In an RG approach, the emergence of such phenomena can be studied by successively lowering an infrared cutoff. Renormalizations of the interaction may give rise to the breakdown of Fermi liquid theory.

In contrast to Wilsonian RG, which has a perturbative starting point, function renormalization group (fRG) methods are based on an exact flow equation for a functional of

the fields. As methods for the direct solution of such a functional differential equation are unknown, one then has to resort to approximation schemes. Among various fRG schemes [19, 20] with different generating functionals, the one-particle irreducible (1PI) scheme seems to be preferable in many cases in the theory of correlated electric systems. But, as well other (formally equivalent) schemes can be of practical use.

For purely fermionic fRG flows, these functionals are often expanded in monomials of the fields, giving rise to an infinite hierarchy of flow equations for the resulting vertex functions. [19, 20] In contrast, gradient expansions are widespread for purely bosonic or mixed flows. [18] Both approaches have been applied to models for correlated fermions on two-dimensional lattices. Focusing on universal features such as the role of Goldstone fluctuations, it seems advantageous to Hubbard-Stratonovich decouple fermionic two-particle interactions and rebosonize such interaction terms that are generated in the flow. This has been done in a series of publications on the Hubbard model in two dimensions. [61–64] In these studies, however, the momentum dependence outside the low-energy sector of the theory is only crudely approximated. Therefore, in an attempt to proceed toward more quantitative results, purely fermionic RG flows appear desirable. fRG flows for the single-band [21–26, 65–67] Hubbard model and a number of multiband Hubbard models [28–39, 41–44, 68, 69] have been studied in the symmetric phase. The onset of spontaneous symmetry breaking then manifests itself in a flow to strong coupling and the nature of this divergency can be related to possible low-temperature phases. Moreover, phases of broken symmetries can be entered by adding a small symmetry-breaking term to the bare action. In the literature, this has been done for the (continuous) U(1) symmetry [47–51, 57] and the (discrete) translational symmetry [45, 46].

Fermionic fRG flows are the main subject of the present thesis. Multiband Hubbard models will be studied within an instability analysis, while phases of antiferromagnetic (AF) order will be accessed in a purely fermionic approach for the first time. Accordingly, this first chapter is organized as follows. The 1PI fRG scheme in a vertex expansion is briefly reviewed starting from the exact flow equation for the generating functional of 1PI vertices. Then the flow equations for U(1) invariant (charge conserving) theories are given. In the second section of this chapter, the flow equations for the symmetric phase, which shows a spin SU(2) invariance in addition, are recapitulated including a channel decomposition, [24–26, 33, 43, 44, 48–51, 56, 67] which facilitates their numerical solution. The form-factor expansion underlying the exchange parametrization put forward in Ref. [24], is then reviewed from a group theoretical viewpoint. While results from the literature are reviewed up to Section 1.2.2, I present my own contributions in the remainder of this chapter, starting with a group-theoretical discussion of form-factor expansions.

In the third section, I first give a parametrization of the two-particle interaction for collinear spin order, i.e. broken SU(2) symmetry, and derive the corresponding flow equations. In the fourth section, a channel decomposition is then proposed in a Nambu

language suited for the study of AF phases. Also the splitting of the pairing triplet in the absence of an SU(2) spin symmetry will be discussed.

1.1. General framework

1.1.1. Exact flow-equation for the 1PI functional

In a functional integral approach [70], the fermionic field operators in a given normally ordered Hamiltonian are replaced by Grassmann fields $\bar{\psi}(\xi)$ and $\psi(\xi)$ which depend on $\xi = (\tau, \boldsymbol{x})$, i.e. imaginary time τ and a collection $\boldsymbol{x}$ of other quantum numbers, such as position or momentum, spin and some kind of flavor indices. These Grassmann fields are antiperiodic in Euclidean time with period $\beta = 1/(k_{\mathrm{B}}T)$, where T denotes the temperature. In the following, the imaginary-time dependence of fields will be expressed in Fourier space, i.e. as a dependence on Matsubara frequencies.

A scalar product between to Grassmann fields can be defined as

$$(\bar{\psi}, \chi) = \int d\xi \, \bar{\psi}(\xi) \, \chi(\xi) \, .$$

For a given model for correlated fermions, the partition function

$$Z = \int \mathcal{D}(\bar{\psi}, \psi) \, e^{-\mathcal{A}[\bar{\psi}, \psi]}$$

and the generating functional

$$\mathcal{G}[\bar{\eta}, \eta] = \int \mathcal{D}(\bar{\psi}, \psi) \, e^{-\mathcal{A}[\bar{\psi}, \psi]} \, e^{(\bar{\eta}, \psi) + (\bar{\psi}, \eta)} \tag{1.1}$$

of the n-particle Green's functions with fermionic source fields $\bar{\eta}$ and η can be expressed in terms of a functional integral. For simplicity, normalization constants have been absorbed into the measure $\mathcal{D}(\bar{\psi}, \psi)$. For a given normally ordered Hamiltonian $H[\Psi^\dagger, \Psi]$ with fields Ψ, the action reads as

$$\mathcal{A}[\bar{\psi}, \psi] = \left(\bar{\psi}, \partial_\tau \psi\right) - H\left[\bar{\psi}, \psi\right] = \left(\bar{\psi}, C^0 \psi\right) + \sum_{n \geq 2} \mathcal{A}^{(2n)}[\bar{\psi}, \psi] \, .$$

Its quadratic part is given by the inverse C^0 of the bare one-particle propagator and n-particle interaction terms $\mathcal{A}^{(2n)}$ are of $2n$th order in the fields. In this context, I should point out that, throughout this thesis, the functional integrals are *not* normalized by the partition function

$$Z_0 = \int \mathcal{D}(\bar{\psi}, \psi) \, e^{-\left(\bar{\psi}, C^0 \psi\right)}$$

for free fermions unlike in Ref. [58].

If these interaction terms were absent, a formal solution of the functional integral in the partition function $Z = Z_0 = \det C^0$ can be written down. In their presence, one may try to resort to perturbation theory. But this may fail, especially if the low-energy physics of the system is governed by collective (bosonic) modes. In such a case, one should expect an expansion around *unrenormalized* fermionic quasiparticles to be ill-converged. Indeed, for models with an ordered low-temperature phase, such as the BCS model [], Feynman diagrams are plagued by infrared divergencies reflecting the onset of spontaneous symmetry breaking.

In order to make progress, one may therefore regularize these divergencies with some infrared cutoff λ and study the behavior under a lowering of this cutoff. In an fRG framework, a plethora of regularization schemes can be used, which all introduce a scale-dependence in the inverse of the bare one-particle propagator. More precisely spoken, C^0 in the action is replaced by some C^0_λ with the following properties:

i) The one-particle propagator can be arbitrarily suppressed, i.e. $\lim_{\lambda\to\infty}(C^0_\lambda)^{-1} = 0$. Therefore, perturbation theory applies in the ultraviolet.

ii) In the infrared, the original problem is recovered, i.e. $C^0_{\lambda=0} = C^0$.

In practice, such a regulator will suppress modes close to the Fermi surface and/or at low Matsubara frequencies which may cause infrared divergencies.

When such a cutoff is introduced, also the functional $\mathcal{G}$ acquires a scale-dependence, which is governed by an exact first-order differential equation. For the considerations that follow, correlation functions can be more conveniently encoded in other generating functionals. So I will only discuss the so-called one-particle irreducible (1PI) fRG scheme and refer to Refs. [19, 20] for other fRG schemes. Let me therefore recall that $\mathcal{W}[\bar\eta, \eta] = -\ln \mathcal{G}[\bar\eta, \eta]$ plays the role of a generating functional for the connected Green's functions and that its Legendre transform (also called *effective potential* in the literature [70])

$$\Gamma[\bar\chi, \chi] = W[\bar\eta, \eta] - (\bar\eta, \chi) - (\bar\chi, \eta)$$

with the reciprocity relations

$$\frac{\partial\Gamma}{\partial\chi} = -\bar\eta\,, \qquad \frac{\partial\Gamma}{\partial\bar\chi} = \eta$$

plays the role of the generating functional of the 1PI vertices. From these vertices, the connected Green's functions can be recovered by fairly simple rules. [70] The scale-dependent functional Γ_λ serves as a generating functional of scale-dependent 1PI vertices for modes above and as an effective average action for modes below the cutoff. Its flow

is governed by the equation

$$\dot{\Gamma}_\lambda[\bar{\chi},\chi] = -(\bar{\chi},\dot{C}^0_\lambda\chi) - \frac{1}{2}\mathrm{tr}\left\{\dot{\mathbf{C}}^0_\lambda\left(\mathbf{\Gamma}^{(2)}_\lambda[\bar{\chi},\chi]\right)^{-1}\right\}, \tag{1.2}$$

where the dot denotes a derivative with respect to λ and where the matrix of second functional derivatives is given by

$$\mathbf{\Gamma}^{(2)}_\lambda[\bar{\chi},\chi] = \begin{pmatrix} \frac{\partial^2\Gamma_\lambda[\bar{\chi},\chi]}{\partial\bar{\chi}(\xi)\,\partial\chi(\xi')} & \frac{\partial^2\Gamma_\lambda[\bar{\chi},\chi]}{\partial\bar{\chi}(\xi)\,\partial\bar{\chi}(\xi')} \\ \\ \frac{\partial^2\Gamma_\lambda[\bar{\chi},\chi]}{\partial\chi(\xi)\,\partial\chi(\xi')} & \frac{\partial^2\Gamma_\lambda[\bar{\chi},\chi]}{\partial\chi(\xi)\,\partial\bar{\chi}(\xi')} \end{pmatrix}.$$

In Eq. (1.2), the inverse of this matrix appears in a trace with

$$\mathbf{C}^0_\lambda = \begin{pmatrix} C^0_\lambda & 0 \\ 0 & -(C^0_\lambda)^{\mathrm{T}} \end{pmatrix},$$

where $(C^0_\lambda)^{\mathrm{T}}(\xi,\xi') = C^0_\lambda(\xi',\xi)$. Note that this trace includes not only a summation over the matrix entries, but also over the quantum numbers of the fields, i.e.

$$\mathrm{tr}\,\{\mathbf{AB}\} = \sum_{i,j}\int d\xi\, d\xi'\; A_{i,j}(\xi,\xi')\,B_{j,i}(\xi',\xi)\,.$$

In the derivation of Eq. (1.2), no approximations have been made. Therefore this exact flow equation interpolates between the bare action $\Gamma_\infty = \mathcal{A}$ and the full 1PI functional $\Gamma = \Gamma_0$, from which all correlation functions can be extracted. In other words, we have reformulated the functional integral in Eq. (1.1) by a first-order differential equation Eq. (1.2) for a functional of Grassmann fields.

In order to obtain an approximate solution of such an exact flow equation for a functional of the fields, one may proceed in different ways. For interacting bosons and theories with both bosons and fermions, one often resorts to a gradient expansion (for a review see Ref. [18]). For purely fermionic fRG flows, vertex expansions are more widespread. [19, 58] If Γ_λ is expanded in monomials of the fields, the exact flow equation (1.2) then translates to an infinite hierarchy of flow equations for the vertices. The first three of these flow equations are depicted in Fig. 1.1. In the following section, I will recapitulate the flow equations in the so-called level-two truncation underlying a considerable number, if not the majority of purely fermionic fRG studies in the literature.

1.1.2. Level-two truncation for charge-conserving theories

Since all flows in this thesis are in U(1)-symmetric phases, a parametrization, where only U(1) invariance (i.e., charge conservation) is assumed, seems appropriate as a starting

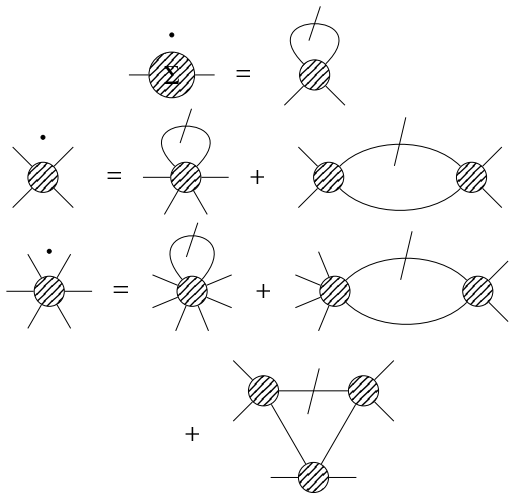

Figure 1.1.: Flow equations for the self-energy, the four-point and six-point vertices, all one-particle-irreducible. A dot represents a derivative with respect to the cutoff. Lines with a slash correspond to the single-scale propagator $S = \dot{G} - G\dot{\Sigma}G$. For more details, see e.g. Ref. [19].

point. More precisely, the effective action is parametrized as

$$\Gamma_\lambda[\bar{\chi},\chi] = (\bar{\chi}, C_\lambda \chi) + \frac{1}{4}\int d\xi_1 \ldots d\xi_4 \; f(\xi_1,\xi_2,\xi_3,\xi_4)\; \bar{\chi}(\xi_1)\,\bar{\chi}(\xi_2)\,\chi(\xi_3)\,\chi(\xi_4) + \ldots \,, \quad (1.3)$$

where the 1PI self-energy $\Sigma(\xi,\xi')$ enters in $C(\xi,\xi') = C^0(\xi,\xi') - \Sigma(\xi,\xi')$ and where $f(\xi_1,\xi_2,\xi_3,\xi_4)$ denotes the coupling function of the two-particle interaction. Note that both the self-energy and the two-particle interaction are scale-dependent and that their scale-dependence is just suppressed in the notation for convenience. The Pauli principle gives rise to the constraints

$$f(\xi_1,\xi_2,\xi_3,\xi_4) = -f(\xi_2,\xi_1,\xi_3,\xi_4) = -f(\xi_1,\xi_2,\xi_4,\xi_3)$$

for the two-particle coupling function. In a level-two truncation, the infinite hierarchy of flow equations is closed by neglecting three-particle and higher-order interaction terms. In Chapter 2.4, an extension of this truncation will be given that allows to keep track of a bare three-particle term induced by high-energy bands that have already been integrated out.

For U(1)-symmetric phases, the level-two flow equations can be found in paragraph 4.1 of Ref. [58] and read as follows. The self-energy flows according to

$$\dot{\Sigma}(\xi_1,\xi_2) = \int d\eta_1\, d\eta_2\, S(\eta_2,\eta_1)\, f(\xi_1,\eta_1,\eta_2,\xi_2)\,, \quad (1.4)$$

where S denotes the single-scale propagator

$$S(\xi_1,\xi_2) = \dot{G}(\xi_1,\xi_2) - \int d\eta_1\, d\eta_2\, G(\xi_1,\eta_1)\,\dot{\Sigma}(\eta_1,\eta_2)\,G(\eta_2,\xi_2)\,.$$

The flow of the two-particle interaction for a charge-conserving theory is given by

$$\dot{f}(\xi_1,\xi_2,\xi_3,\xi_4) = \mathcal{F}_{\mathrm{pp}}(\xi_1,\xi_2,\xi_3,\xi_4) + \mathcal{F}_{\mathrm{ph}}(\xi_1,\xi_2,\xi_3,\xi_4) - \mathcal{F}_{\mathrm{ph}}(\xi_1,\xi_2,\xi_4,\xi_3)\,, \tag{1.5}$$

where

$$\begin{aligned}\mathcal{F}_{\mathrm{pp}}(\xi_1,\xi_2,\xi_3,\xi_4) = \frac{1}{2}\int & d\eta_1\, d\eta_2\, d\eta_3\, d\eta_4\, f(\xi_1,\xi_2,\eta_2,\eta_3) \\ & \times f(\eta_4,\eta_1,\xi_3,\xi_4)\left[\partial_\lambda G(\eta_2,\eta_1)\, G(\eta_3,\eta_4)\right]\,,\end{aligned}$$

$$\begin{aligned}\mathcal{F}_{\mathrm{ph}}(\xi_1,\xi_2,\xi_3,\xi_4) = -\int & d\eta_1\, d\eta_2\, d\eta_3\, d\eta_4\, f(\eta_4,\xi_2,\xi_3,\eta_1) \\ & \times f(\xi_1,\eta_2,\eta_3,\xi_4)\left[\partial_\lambda G(\eta_1,\eta_2)\, G(\eta_3,\eta_4)\right]\,.\end{aligned}$$

In contrast to Ref. [58], a so-called Katanin substitution [71] of the loops has already been performed here, i.e. single-scale propagators in the loops above have been replaced by full scale-derivatives of the propagators. Note that this substitution does not affect the flow equation (1.4) for the self-energy. It is performed in order to account for non-overlapping three-particle contributions which are essential for reproducing the exact solution of reduced mean-field models such as the one discussed in Chapter 4.1. Moreover, in the presence of a gauge field, it leads to an RG flow in which local Ward identities violated in the standard level-two truncation [20] are preserved. As has recently been shown, *global* Ward identities are in contrast only preserved on the two-loop level. [51].

1.2. SU(2) symmetric RG flows

Generically, the tight-binding models discussed in this work are fully SU(2) symmetric in spin space. In further decreasing the computational cost of an integration of the RG flow equations, it is rewarding to exploit this symmetry as well. In a first subsection, I will therefore recapitulate the SU(2)-invariant parametrization of Paragraph 4.2 of Ref. [58] including the resulting flow equations. Then a channel decomposition [24–26, 33, 43, 44, 48–51, 56, 67] of these flow equations will be given. Finally, I will review the exchange parametrization as pursued in Refs. [24–26] from a group-theoretic viewpoint.

1.2.1. Parametrization and flow equation of the two-particle vertex

In the following, the variables ξ_i will be assumed to consist of a spin-projection component σ_i and a $1+D$ momentum $k_i = (k_i^0, \mathbf{k}_i)$ with Matsubara frequency k_i^0 and wavevector $\mathbf{k}_i$. Further quantum numbers will be suppressed in this chapter. This

means that, if such additional quantum numbers are present in a particular model, they can be regarded as tacitly included in k_i.

For a general SU(2) symmetric, momentum and energy conserving theory, the two-particle term of the 1PI functional Γ can be described by one spin-independent coupling function $V(k_1, k_2, k_3)$ according to [19, 58]

$$\begin{aligned} f(\xi_1, \xi_2, \xi_3, \xi_4) = [&V(k_1, k_2, k_3)\, \delta_{\sigma_1,\sigma_4}\delta_{\sigma_2,\sigma_3} - V(k_2, k_1, k_3)\, \delta_{\sigma_1,\sigma_3}\delta_{\sigma_2,\sigma_4}] \\ &\times \delta(k_1 + k_2 - k_3 - k_4)\,. \end{aligned} \tag{1.6}$$

In this formula, the δ-function ensures momentum and energy conservation. For fermions on a lattice, the sum in its argument is to be understood modulo reciprocal lattice vectors. The new coupling function obeys the relation

$$V(k_1, k_2, k_3) = V(k_2, k_1, k_1 + k_2 - k_3)$$

stemming from the Pauli principle.

The quadratic part of Γ is diagonal in spin-space, which implies

$$G(\xi_1, \xi_2) = \delta_{\sigma_1,\sigma_2}\delta(k_1 - k_2)\, G(k_1) \quad \text{and} \quad \Sigma(\xi_1, \xi_2) = \delta_{\sigma_1,\sigma_2}\delta(k_1 - k_2)\, \Sigma(k_1)$$

for the one-particle propagator G and the 1PI self-energy Σ, which flows according to

$$\dot{\Sigma}(k) = \int dp\; S(p)\; [V(p, k, p) - 2V(k, p, p)]\;.$$

The scale derivative of the coupling function V consists of three parts

$$\dot{V}(k_1, k_2, k_3) = \mathcal{T}_{\mathrm{pp}}(k_1, k_2, k_3) + \mathcal{T}_{\mathrm{ph}}^{\mathrm{cr}}(k_1, k_2, k_3) + \mathcal{T}_{\mathrm{ph}}^{\mathrm{d}}(k_1, k_2, k_3)\,.$$

The particle-particle contribution

$$\mathcal{T}_{\mathrm{pp}} = -\int dp\; [\partial_\lambda G(p)\, G(k_1 + k_2 - p)]\, V(k_1, k_2, p)\, V(k_1 + k_2 - p, p, k_3) \tag{1.7}$$

and the crossed particle-particle part

$$\mathcal{T}_{\mathrm{ph}}^{\mathrm{cr}} = -\int dp\; [\partial_\lambda G(p)\, G(p + k_3 - k_1)]\, V(k_1, p + k_3 - k_1, k_3)\, V(p, k_2, p + k_3 - k_1) \tag{1.8}$$

can each be represented by one diagram (see Fig. 1.2). Note that an RPA resummation in the Cooper or particle-hole channel is equivalent to an RG flow in which all terms except $\mathcal{T}_{\mathrm{pp}}$ or $\mathcal{T}_{\mathrm{ph}}^{\mathrm{cr}}$, respectively, are neglected. (The corresponding Bethe-Salpether equation is then equivalent to the flow equation for the two-particle vertex. [24]) Vertex correction and particle-hole screening, however, are accounted for by the direct particle-hole diagrams depicted in Fig. 1.2(c).

$$\begin{aligned} \mathcal{T}_{\mathrm{ph}}^{\mathrm{d}} = \int dp\; &[\partial_\lambda G(p)\, G(p + k_3 - k_1)]\, [2V(k_1, p + k_2 - k_3, p)\, V(p, k_2, k_3) \\ &- V(k_1, p + k_2 - k_3, k_1 + k_2 - k_3)\, V(p, k_2, k_3) \\ &- V(k_1, p + k_2 - k_3, p)\, V(p, k_2, p + k_2 - k_3)]\;. \end{aligned} \tag{1.9}$$

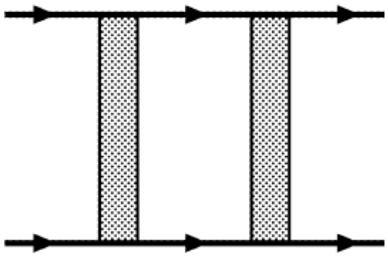

(a) Particle-particle diagram $\mathcal{T}_{\mathrm{pp}}$

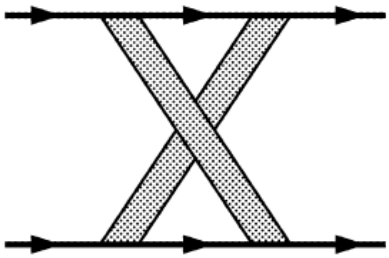

(b) Crossed particle-hole diagram $\mathcal{T}_{\mathrm{ph}}^{\mathrm{cr}}$

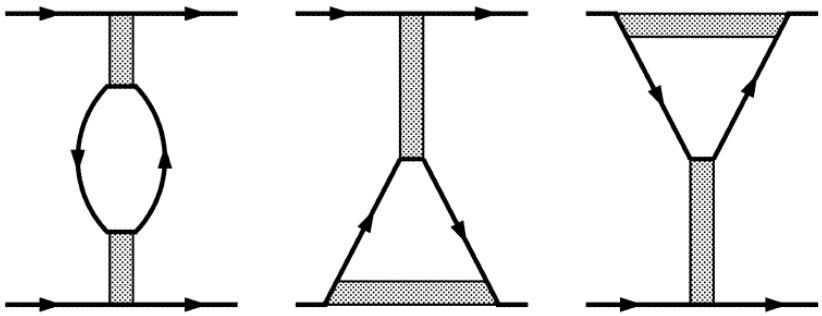

(c) Direct particle-hole diagrams $\mathcal{T}_{\mathrm{ph}}^{\mathrm{d}}$

Figure 1.2.: The five diagrams driving the flow of the two-particle interaction $V(k_1, k_2, k_3)$ of an U(1) and SU(2) invariant theory. For the closed loops in these diagrams, a scale derivative is implicit. (These figures have been taken from Ref. [58].)

1.2.2. Channel decomposition

If the flow equations derived in the preceeding section are solved numerically, redundant summations over spin indices are avoided in the calculation of the diagrams on their right-hand side. But still a direct discretization of all three momentum and frequency arguments of the coupling function $V(k_1, k_2, k_3)$ would be very costly and the resulting code would probably be hard to parallelize.

In many previous works, all frequencies have been projected to zero and the flow of the self-energy has been neglected. Since this considerable facilitates the loop integrations in the flow of the two-particle interaction and reduces the number of running couplings, I will also do so in Chapter 3. More recent studies [25–27] on one-band models taking into account parts of the self-energy and frequency-dependent vertices show that the flows to strong coupling are not changed in character if these two approximations are made *simultaneously*.

But even then, a direct discretization if all three momenta with an acceptable resolution may be too costly. In an older approach to handle this problem, the momentum dependence of V was projected to a finite number of patches on the Fermi surface (FS). [23] This FS patching was designed to reproduce the low-energy physics properly, but renormalizations away from the FS are only crudely approximated. In multiband problems, already the bare interactions, expressed in the band language, show a significant wavevector-dependence away from the FS. (This so-called *orbital makeup* will be discussed in Chapter 2.1.2.) Moreover, improving the resolution of e.g. a sharp peak at $k_1 + k_2 = 0$ corresponding to a pairing instability drastically increases the computational cost in this FS patching approach.

Progress can be made within a channel decomposition proposed by Karrasch *et al.* [56] for the frequency- and by Husemann and Salmhofer [24] for the momentum-dependence of the vertices. In such an approach, the coupling function $V(k_1, k_2, k_3)$ is decomposed into contributions resulting from three different channels. More precisely, we then have

$$\begin{aligned} V(k_1, k_2, k_3) = U(k_1, k_2, k_3) &- \Phi_{\mathrm{SC}}(k_1 + k_2, k_1, k_3) + \Phi_{\mathrm{M}}(k_3 - k_1, k_1, k_2) \\ &+ \frac{1}{2}\Phi_{\mathrm{M}}(k_2 - k_3, k_1, k_2) - \frac{1}{2}\Phi_{\mathrm{K}}(k_2 - k_3, k_1, k_2)\,, \end{aligned}$$

with the bare interaction U and coupling functions Φ_{SC}, Φ_{M} and Φ_{K} of the pairing, the magnetic and the forward scattering channel, respectively. These single-channel coupling functions are generated during the flow according to

$$\begin{aligned} \dot{\Phi}_{\mathrm{SC}}(k_1 + k_2, k_1, k_3) &= -\mathcal{T}_{\mathrm{pp}}(k_1, k_2, k_3) \\ \dot{\Phi}_{\mathrm{M}}(k_3 - k_1, k_1, k_3) &= \mathcal{T}^{\mathrm{cr}}_{\mathrm{ph}}(k_1, k_2, k_3) \\ \dot{\Phi}_{\mathrm{K}}(k_3 - k_1, k_1, k_3) &= -2\mathcal{T}^{\mathrm{d}}_{\mathrm{ph}}(k_1, k_2, k_3) + \mathcal{T}^{\mathrm{cr}}_{\mathrm{ph}}(k_1, k_2, k_1 + k_2 - k_3)\,. \end{aligned}$$

At weak coupling in a one-loop truncation, the diagrams on the right-hand sides of these flow equation depend strongly on the total or transfer momenta that appear in the loops, while their variation with other combinations of external momenta is weak. Since the single-channel coupling functions are renormalized by diagrams with the same loop momentum, they depend strongly on their first argument and weakly on the other two.[1]

This way, a channel decomposition can pave the road to refined discretization schemes as well as to further parametrization of the coupling functions. In an exchange parametrization [24–26, 33, 43, 44, 48–51], the weak momentum dependences are captured by an expansion in a set of form-factors. This expansion will be reviewed in the following section from a group-theoretic perspective. The remaining strong momentum dependence was then discretized in these works. In Chapter 5, I will also resort to an exchange parametrization and parametrize the strong momentum dependences in the spirit of a gradient expansion.

In practice, the form-factor expansion (FFE) underlying such an exchange parametrization has to be truncated behind a few terms, since the computational cost of the integration of the flow equations would otherwise be excessive. But even if all momenta are discretized, a channel decomposition may be helpful. Namely, the loop momenta (i.e. the first argument of the single-channel coupling functions) can be put on a much finer grid than the remaining momenta on which the coupling functions only depend weakly. Based on an idea of Jutta Ortloff [67], I have implemented such an approach for the calculations in Chapter 3.2.

1.2.3. Comments on form-factor expansions

In this subsection, I will look at the exchange parametrization pursued in Refs. [24–26] from a group-theoretic perspective. In particular, I will elaborate on the question to what extend a channel-decomposed, renormalized two-fermion interaction can be conveniently expressed as one resulting from a *small number* of bosonic channels. Regarding the classification of such order-parameter fields, I will proceed similarly to Vojta *et al.* in Ref. [72], where different types of commensurate ordering within the $d_{x^2-y^2}$-wave superconducting phase have been classified according to the irreducible representations (IRs) of the point group. The group-theoretical considerations underlying this subsection will be laid out in Appendix A. For the SMFRG approach, similar considerations have been undertaken. [73]

[1] In an exchange parametrization, the strong momentum dependence of so-called *box diagrams* (see Fig. 4.2) may be assigned either to internal fermionic or bosonic lines. [51] At weak coupling, however, the contribution from the exchange bosons can be expected to be of minor importance. For non-negligible two-loop corrections, however, the situation may be different and the loop momenta may have to be assigned to bosonic lines in the box diagrams.

	s-wave	p-wave	$d_{x^2-y^2}$-wave	d_{xy}-wave	g-wave
E	1	2	1	1	1
$2C_4$	1	0	-1	-1	1
C_2	1	-2	1	1	1
$2I$	1	0	1	-1	-1
$2I'$	1	0	-1	1	-1

Table 1.1.: Character table of C_{4v}. The classes I and I' correspond to reflections with respect to the $(0,1),(1,0)$ axes or the $(1,1),(1,-1)$ axes, respectively.

Let us now decompose the renormalized interaction V in the spirit of a Hubbard-Stratonovich transform using a set of orthonormal form factors f_i. In the Cooper channel, for example, one then has

$$\Phi_{\mathrm{SC}}(l,q,q') = \sum_{i,j} f_i(\mathbf{l}/2-\mathbf{q})\, f_j(\mathbf{l}/2-\mathbf{q}')\, D_{ij}(l)\,,$$

with bosonic propagators $D_{ij}(l)$. The form factors play the role of fermion-boson vertices, with indices i and j labeling different bosonic species (flavors). They are frequency-independent here, which allows for choosing real form factors. They obey the orthonormality relation $\int d\mathbf{q}\, f_i(\mathbf{q})\, f_j(\mathbf{q}) = \delta_{i,j}$. Here and throughout, integrals $\int d\mathbf{q}$ run over the whole Brillouin zone (BZ) and a normalization factor has been absorbed into the measure such that $\int d\mathbf{q}\, 1 = 1$. For given Φ_{SC}, the matrix elements $D_{ij}(l)$ are thus uniquely defined. The two-particle coupling functions are assumed to transform trivially under point-group operations. For fermions on a square lattice, for example, we thus have

$$\Phi_{\mathrm{SC}}(R_{\hat{O}}l, R_{\hat{O}}q, R_{\hat{O}}q') = \Phi_{\mathrm{SC}}(l,q,q') \quad \forall\, \hat{O} \in C_{4v}$$

and likewise for Φ_{M} and Φ_{K}, where $R_{\hat{O}}$ denotes the rotation matrix corresponding to the point-group operation $\hat{O}$. It then appears natural to choose basis functions of the IRs as form factors. For the present example of a C_{4v} symmetry, one may choose $f_s(\mathbf{q}) = 1$ for s-wave, $f_{p,\pm}(\mathbf{q}) = \sin(q_x) \pm \sin(q_y)$ for p-wave, and $f_d(\mathbf{q}) = \cos(q_x) - \cos(q_y)$ for $d_{x^2-y^2}$-wave. (Note that the IR corresponding to a p-wave is two-dimensional, while the other ones are one-dimensional.)

When one projects to zero frequency, the coupling function can be fully recovered by using a complete set of form factors. For a C_{4v} symmetry, one can easily construct such a complete basis set with elements that transform according to of the IRs (cf. Tab. 1.1) by (anti)symmetrizing the real Fourier basis functions on the first BZ with respect to the point-group operations. By equivalence transformations of the IR, these form factors can be rendered well-behaved in the sense of Appendix A. The form factors f_s, $f_{p,\pm}$ and f_d mentioned above are the most slowly varying basis functions of the respective IRs, which corresponds to the formation of exchange bosons from constituents residing on the same site or on neighboring unit cells.

Let us now further look at an exchange parameterization for C_{4v} symmetric system. For the bosonic ordering vectors $\mathbf{l} = (0,0)$ and (π,π), the little group $\mathcal{L}_\mathbf{l}$ equals the full point group. According to Corollary A.1.1, which is proven in Appendix A, matrix elements of $D(l)$ mixing bosons of inequivalent IRs vanish at these momenta. Different form factors transforming according to equivalent IRs may however mix. In the following, this effect will be referred to as the admixture of higher harmonics. In flavor space, the non-vanishing matrix elements of D_{ij} appear in $d \times d$ blocks corresponding to a d-dimensional IR. Note that Schur's first lemma [74] implies that all these remaining blocks are then a multiple of the unit matrix, if the form factors are well-behaved in the sense of Appendix A, where this statement is proven as Corollary A.1.3.

At $\mathbf{l} = (0,\pi)$ and $(\pi,0)$, the little group reduces to $\mathcal{L}_\mathbf{l} = C_{2v}$ and therefore, again by virtue of Corollary A.1.1, the five IRs of C_{4v} decay into three sets of form factors that do not mix with another. One contains s- and $d_{x^2-y^2}$-wave, one d_{xy}- and g-wave, while the third one purely consists of p-wave form factors. This p-wave set splits into two, each transforming with a one-dimensional IR of C_{2v}. Altogether, this corresponds to the four IRs of the little group. For example, the most slowly varying p-wave basis functions $\sin(q_x)$ and $\sin(q_y)$ then transform with two inequivalent one-dimensional IRs of C_{2v}, which may be referred to as p_x- and p_y-wave.

For bosonic momenta $\mathbf{l}$ on the boundary of the first BZ, i.e. for $\mathcal{L}_\mathbf{l} = C_s$, there are two such sets, one for $s, p_{x/y}, d_{x^2-y^2}$- and the other one for $p_{y/x}, d_{xy}$ and g-wave. Again, those two sets correspond to the IRs of the little group. For bosonic momenta that do not lie on any of the symmetry axes, the little group just contains the identity element and all form factors may get mixed.

Let us now assume that the form-factors are well-behaved in the sense of Appendix A. If the mixing between inequivalent IRs of the full point-group is neglected, the bosonic propagators of the four one-dimensional IRs then inherit the full C_{4v} symmetry of the coupling function according to Corollary A.1.2. In contrast, the p-wave block still transforms with two-dimensional IR matrices. Let us note in passing that a mixing of different IRs has already been observed in Ref. [75] for the RPA pairing susceptibility at incommensurate Copper pair momenta.

So far, only a FFE in the Cooper channel has been considered. Of course, such an expansion can as well be used in the other channels, which are then decomposed as

$$\Phi_\mathrm{M}(l,q,q') = \sum_{i,j} f_i(\mathbf{l}/2+\mathbf{q})\, f_j(-\mathbf{l}/2+\mathbf{q}')\, M_{ij}(l)\,,$$
$$\Phi_\mathrm{K}(l,q,q') = \sum_{i,j} f_i(\mathbf{l}/2+\mathbf{q})\, f_j(-\mathbf{l}/2+\mathbf{q}')\, K_{ij}(l)\,.$$

If one wishes to simplify the RG flow equations by performing a FFE, the expansion has to be truncated behind a few terms in order not to exceed available computational

resources. This may be conveniently done in the following way.

i.) Neglect the mixing between inequivalent IRs of C_{4v} (or the respective full point group for other lattice geometries).

ii.) Only consider the most slowly varying form factor among equivalent IRs, i.e. neglect the admixture of higher harmonics.

(In addition to these approximations, the p-, d_{xy}, and g-wave sectors have been neglected in Ref. [24].) If these approximations are adequate, the FFE of the RG flow equations should in principle capture the important momentum dependences well. If, in contrast, the admixture of higher harmonics plays a role, a large number of bosonic channels might be needed. At least for the one-band Hubbard model, the above approximations seem to be fine for a large region of the parameter space. [67] The question now is, whether important orbital makeup effects are still captured within a viable truncation of an FFE.

If the fermionic momenta are directly put on a grid, as in Chapter 3.3, one can easily keep track of mixing between inequivalent IRs. This mixing can be expected to play a minor role, if the ordering vectors of leading and subleading instabilities are $\mathbf{l} = 0$ or (π, π) or very close. By diagonalization of the coupling functions as matrices in q and q' with $\mathbf{l}$ fixed to the ordering vector, optimized form factors can then be attributed to these instabilities. In the case of the Emery model, these optimized form factors will turn out to be close to the most slowly varying ones for most parameters considered in Chapter 3.3, but in some cases also higher harmonics will play a role. A sensible truncation of the FFE then consists in only retaining the terms corresponding to the most relevant eigenvalues. Clearly, the optimized form factors are scale-dependent in an fRG flow. In principle, it should be possible to parametrize this scale dependence. [76] Let me note in passing that similar form-factor deformation effects have already been discussed within a Bethe-Salpether equation approach. [77]

For incommensurate AF, however, the potentially non-zero mixing between inequivalent IRs of the point-group symmetry of the lattice may prohibit the calculation of an optimized form factor that is defined on the whole BZ. In such a case, a faithful truncation of the FFE would already contain too many terms to be numerically tractable. I will come back to the question of the applicability of a truncated FFE when numerical results are discussed in Chapter 3.3.

1.3. Flows into phases of collinear spin ordering

So far, the four-point vertex was parametrized for theories that remain SU(2)-symmetric in spin space. If some model is in an ordered phase for a given set of parameters, the solution of the flow equations then yields a flow to strong coupling where at least one class of contributions to the four-point vertex diverge at a nonzero scale. If the FS is nested and if the initial short-range interaction is repulsive, the flow to strong coupling usually indicates an AF instability where the static spin susceptibility becomes infinitely large. The interpretation of this instability is that below this critical scale, AF order sets in. This regularizes the growth of the four-point vertex in a reasonable way that is discussed further below, and definitely breaks the SU(2)-spin rotational symmetry. Hence, in order to understand the low-scale regime, one needs to continue the flow into the broken-symmetry regime. In this section, the question of an efficient parametrization of the interaction in presence of collinear spin-ordering is addressed and the corresponding flow equations are derived. Let me note in passing that the more special case of the Kitaev-Heisenberg model has very recently been considered by other authors. [78]

1.3.1. Parametrization of the interaction

In order to keep the resulting numerical calculations tractable, I will restrict the analysis to spin-1/2-fermions exhibiting collinear AF, i.e. the spin-symmetry is broken only in one direction. More specifically, let us allow for $\langle S_z \rangle \neq 0$ while we still require $\langle S_x \rangle = \langle S_y \rangle = 0$, where S_i denotes the ith component of the spin operator. For such a case, a similar parametrization [79] has been given in real space. The two-point Green's function only has diagonal entries in spin space and can then be split into a spin-flip symmetric and a spin-antisymmetric part $G_{\sigma_1,\sigma_2} = G_1 \delta_{\sigma_1,\sigma_2} + G_z \tau^z_{\sigma_1,\sigma_2} = G_{\sigma_1}$, with the Pauli z-matrix τ^z and the spin indices σ_i being $\uparrow$ or $\downarrow$. The elements of the remaining spin symmetry group U_z are $U(\varphi) = e^{i\varphi\tau^z}$ with arbitrary real φ. Consider now the two-particle coupling function $f(\xi_1, \xi_2, \xi_3, \xi_4)$ introduced in Eq. (1.3) of a charge conserving theory. Under the remaining symmetry transformations $U(\varphi)$, it transforms according to

$$f(\xi_1, \xi_2, \xi_3, \xi_4) \to e^{i\varphi(-\sigma_1 - \sigma_2 + \sigma_3 + \sigma_4)} f(\xi_1, \xi_2, \xi_3, \xi_4)\,,$$

implying conservation of the projected spin z-components, $\sigma_1 + \sigma_2 = \sigma_3 + \sigma_4$. There are six spin configurations satisfying this constraint, namely

$$\uparrow\uparrow\uparrow\uparrow, \quad \downarrow\downarrow\downarrow\downarrow, \quad \uparrow\downarrow\uparrow\downarrow, \quad \uparrow\downarrow\downarrow\uparrow, \quad \downarrow\uparrow\uparrow\downarrow, \quad \downarrow\uparrow\downarrow\uparrow\ .$$

Since $f(\xi_1, \xi_2, \xi_3, \xi_4)$ is antisymmetric under $\xi_1 \leftrightarrow \xi_2$ and $\xi_3 \leftrightarrow \xi_4$, the spin-dependence of the interaction can be parametrized using three independent momentum- and frequency-

dependent coupling functions

$$\begin{aligned} f(\xi_1,\xi_2,\xi_3,\xi_4) = {} & V_\uparrow(k_1,k_2,k_3,k_4)\,\delta_{\boldsymbol{\sigma},\uparrow\uparrow\uparrow\uparrow} + V_\downarrow(k_1,k_2,k_3,k_4)\,\delta_{\boldsymbol{\sigma},\downarrow\downarrow\downarrow\downarrow} \\ & + V_{\uparrow\downarrow}(k_1,k_2,k_3,k_4)\,\delta_{\boldsymbol{\sigma},\uparrow\downarrow\uparrow\downarrow} - V_{\uparrow\downarrow}(k_1,k_2,k_4,k_3)\,\delta_{\boldsymbol{\sigma},\uparrow\downarrow\downarrow\uparrow} \\ & + V_{\uparrow\downarrow}(k_2,k_1,k_4,k_3)\,\delta_{\boldsymbol{\sigma},\downarrow\uparrow\downarrow\uparrow} - V_{\uparrow\downarrow}(k_2,k_1,k_3,k_4)\,\delta_{\boldsymbol{\sigma},\downarrow\uparrow\uparrow\downarrow}\,. \end{aligned} \tag{1.10}$$

Due to the antisymmetry property of $f(\xi_1,\xi_2,\xi_3,\xi_4)$, $V_\uparrow$ and $V_\downarrow$ are antisymmetric under $k_1 \leftrightarrow k_2$ and $k_3 \leftrightarrow k_4$, whereas $V_{\uparrow\downarrow}$ does not obey a Pauli principle constraint. Particle-hole symmetry implies

$$\begin{aligned} V_\uparrow(k_1,k_2,k_3,k_4) &= V_\uparrow(k_4,k_3,k_2,k_1)\,, \\ V_\downarrow(k_1,k_2,k_3,k_4) &= V_\downarrow(k_4,k_3,k_2,k_1)\,, \\ V_{\uparrow\downarrow}(k_1,k_2,k_3,k_4) &= V_{\uparrow\downarrow}(k_3,k_4,k_1,k_2)\,, \end{aligned}$$

while restoring the SU(2) symmetry would impose the constraint

$$V_\uparrow(k_1,k_2,k_3,k_4) = V_\downarrow(k_1,k_2,k_3,k_4) = V_{\uparrow\downarrow}(k_1,k_2,k_3,k_4) - V_{\uparrow\downarrow}(k_2,k_1,k_3,k_4) \tag{1.11}$$

on the coupling functions. A global SU(2) Ward identity can be derived as in the U(1) case in Ref. [57], Eq. (85). One obtains

$$\begin{aligned} C_z(k_1,k_2) - C_z^0(k_1,k_2) = -\int & dp_1\,dp_2\,dp_3\,dp_4\,C_z^0(p_1,p_2)\,G_\downarrow(p_2,p_3)\,G_\uparrow(p_4,p_1) \\ & \times V_{\uparrow\downarrow}(k_1,p_3,p_4,k_2)\,, \end{aligned} \tag{1.12}$$

where C_z and C_z^0 denote the spin-antisymmetric part of the inverse of the full and the bare propagator, respectively. Note that G_σ represents the full propagator and that $V_{\uparrow\downarrow}$ enters as a renormalized interaction.

1.3.2. Flow equations

This new parametrization allowing for collinear spin order in the z direction can now be inserted into the flow equations (1.4) for the general one-particle-irreducible self-energy $\Sigma(\xi_1,\xi_2)$ and (1.5) for the four-point vertices f. Parametrizing the effective interaction according to Eq. (1.10) simplifies the numerical solution of the RG flow. The flow equations then read as follows. The right-hand side of the flow equations for the interaction can be decomposed into particle-particle and particle-hole diagrams

$$\partial_\lambda V_\sigma(k_1,k_2,k_3,k_4) = T_\sigma^{\mathrm{pp}}(k_1,k_2,k_3,k_4) + T_\sigma^{\mathrm{ph}}(k_1,k_2,k_3,k_4)\,, \tag{1.13}$$

$$\partial_\lambda V_{\uparrow\downarrow}(k_1,k_2,k_3,k_4) = T_{\uparrow\downarrow}^{\mathrm{pp}}(k_1,k_2,k_3,k_4) + T_{\uparrow\downarrow}^{\mathrm{ph}}(k_1,k_2,k_3,k_4)\,. \tag{1.14}$$

With the short-hand notation $L_{\sigma_1,\sigma_2}(p,p';q,q') = \partial_\lambda \left[G_{\sigma_1}(p,p')\, G_{\sigma_2}(q,q')\right]$ for the loop diagrams, one obtains the following contributions:

$$T_\uparrow^{\rm pp}(k_1,k_2,k_3,k_4) = \frac{1}{2}\int dp\, dp'\, dq\, dq'\, V_\uparrow(k_1,k_2,p,q)\, V_\uparrow(q',p',k_3,k_4)\, L_{\uparrow,\uparrow}(p,p';q,q')\,, \tag{1.15}$$

$$\begin{aligned} T_\uparrow^{\rm ph}(k_1,k_2,k_3,k_4) = &-\int dp\, dp'\, dq\, dq'\ \left[V_\uparrow(q',k_2,k_3,p)\, V_\uparrow(k_1,p',q,k_4)\right. \\ &\left. -V_\uparrow(q',k_2,k_4,p)\, V_\uparrow(k_1,p',q,k_3)\right]\ L_{\uparrow,\uparrow}(p,p';q,q') \\ &-\int dp\, dp'\, dq\, dq'\ \left[V_{\uparrow\downarrow}(k_2,q',k_3,p)\, V_{\uparrow\downarrow}(k_1,p',k_4,q)\right. \\ &\left. -V_{\uparrow\downarrow}(k_2,q',k_4,p)\, V_{\uparrow\downarrow}(k_1,p',k_3,q)\right] L_{\downarrow,\downarrow}(p,p';q,q')\,. \end{aligned} \tag{1.16}$$

Likewise, one has

$$T_\downarrow^{\rm pp}(k_1,k_2,k_3,k_4) = \frac{1}{2}\int dp\, dp'\, dq\, dq'\, V_\downarrow(k_1,k_2,p,q)\, V_\downarrow(q',p',k_3,k_4)\, L_{\downarrow,\downarrow}(p,p';q,q')\,, \tag{1.17}$$

$$\begin{aligned} T_\downarrow^{\rm ph}(k_1,k_2,k_3,k_4) = &-\int dp\, dp'\, dq\, dq'\ \left[V_\downarrow(q',k_2,k_3,p)\, V_\downarrow(k_1,p',q,k_4)\right. \\ &\left. -V_\downarrow(q',k_2,k_4,p)\, V_\downarrow(k_1,p',q,k_3)\right]\ L_{\downarrow,\downarrow}(p,p';q,q') \\ &-\int dp\, dp'\, dq\, dq'\ \left[V_{\uparrow\downarrow}(q',k_2,p,k_3)\, V_{\uparrow\downarrow}(p',k_1,q,k_4)\right. \\ &\left. -V_{\uparrow\downarrow}(q',k_2,p,k_4)\, V_{\uparrow\downarrow}(p',k_1,q,k_3)\right] L_{\uparrow,\uparrow}(p,p';q,q') \end{aligned} \tag{1.18}$$

and

$$T_{\uparrow\downarrow}^{\rm pp}(k_1,k_2,k_3,k_4) = -\int dp\, dp'\, dq\, dq'\, V_{\uparrow\downarrow}(k_1,k_2,p,q)\, V_{\uparrow\downarrow}(p',q',k_3,k_4)\, L_{\uparrow,\downarrow}(p,p';q,q')\,, \tag{1.19}$$

$$\begin{aligned} T_{\uparrow\downarrow}^{\rm ph}(k_1,k_2,k_3,k_4) = &-\int dp\, dp'\, dq\, dq'\, V_{\uparrow\downarrow}(q',k_2,k_3,p)\, V_{\uparrow\downarrow}(k_1,p',q,k_4)\, L_{\downarrow,\uparrow}(p,p';q,q') \\ &-\int dp\, dp'\, dq\, dq'\, V_{\uparrow\downarrow}(q',k_2,p,k_4)\, V_\uparrow(k_1,p',q,k_3)\, L_{\uparrow,\uparrow}(p,p';q,q') \\ &-\int dp\, dp'\, dq\, dq'\, V_\downarrow(q',k_2,k_4,p)\, V_{\uparrow\downarrow}(k_1,p',k_3,q)\, L_{\downarrow,\downarrow}(p,p';q,q')\,. \end{aligned} \tag{1.20}$$

For the flow of the self-energy, one finds

$$\partial_\lambda \Sigma_\uparrow(k_1,k_2) = -\int dp\, dp'\, \left[S_\uparrow(p,p')\, V_\uparrow(k_1,p',p,k_2) - S_\downarrow(p,p')\, V_{\uparrow\downarrow}(k_1,p',k_2,p)\right] \tag{1.21}$$

$$\partial_\lambda \Sigma_\downarrow(k_1,k_2) = -\int dp\, dp'\, \left[S_\downarrow(p,p')\, V_\downarrow(k_1,p',p,k_2) - S_\uparrow(p,p')\, V_{\uparrow\downarrow}(p',k_1,p,k_2)\right]\,. \tag{1.22}$$

The first-order differential equations (1.13), (1.14), (1.21), and (1.22) have to be solved together.

1.4. Channel decomposition for commensurate antiferromagnets

A direct and unbiased discretization of the coupling functions in the flow equations (1.15)–(1.20) would either require further approximations, such as projection to the Fermi surface and to zero frequency, or result in even more prohibitive numerical effort than in the SU(2) symmetric case. Therefore a channel decomposition also seems in order in the case of broken spin symmetry. In this section, such a channel decomposition will be presented for AF phases, where not only the SU(2) symmetry, but also the translational symmetry is broken.

1.4.1. Consequences of symmetry breaking

In order to get some intuition for the particularities of the channel-decomposed flow equations in an antiferromagnetically ordered phase, let me first discuss processes mediated by some kind of exchange boson that comply with the remaining symmetries. In addition to the contributions that are already present in the symmetric phase, there will be processes that violate the translational or SU(2) symmetries or both.

Let me start with discussing the Nambu-index dependence of the interaction. In the case of commensurate AF, the renormalized interaction is only invariant under translations by an even number of sites. In momentum space, the ordering vector $\mathbf{Q}$ then corresponds to half a reciprocal lattice vector. Accordingly, the coupling functions can be decomposed into a momentum-conserving part V_X^{c} and a non-conserving part V_X^{nc}, which is generated during the flow. One then has

$$\begin{aligned} V_X(k_1,k_2,k_3,k_4) = V_X^{\mathrm{c}}(k_1,k_2,k_3)\,\delta\left(k_1+k_2-k_3-k_4\right) + V_X^{\mathrm{nc}}(k_1,k_2,k_3) \\ \times\,\delta\left(k_1+k_2-k_3-k_4+Q\right)\,, \end{aligned}$$

with $Q=(0,\mathbf{Q})$. In Nambu representation with pseudo-spinors

$$\mathbf{\Psi}_\sigma(k) = \begin{pmatrix} \psi_\sigma(k) \\ \psi_\sigma(k+Q) \end{pmatrix}\,,$$

the interaction can be parameterized in the same way as in the conventional representation with coupling functions $V_X(k_1,\ldots,k_4)$ using coupling functions $W_X(K_1,\ldots,K_4)$, where $K_i=(k_i,s)$ with Nambu indices s.

For an even number of equal Nambu indices $s=\pm 1$, the interaction W_X in Nambu representation then corresponds to V_X^{c} and to V_X^{nc} for an odd number of equal Nambu

indices. Thus, one has

$$W_X(K_1,K_2,K_3,K_4) = \tilde{\delta}_{\{k_i\}} \begin{cases} V_X^{\mathrm{c}}(\varkappa_1,\varkappa_2,\varkappa_3) & \sum_i \frac{s_i}{2} \text{ even} \\ V_X^{\mathrm{nc}}(\varkappa_1,\varkappa_2,\varkappa_3) & \sum_i \frac{s_i}{2} \text{ odd} \end{cases},$$

with physical momenta $\varkappa_i = k_i + (1-s)\,Q/2$. In this formula, the momenta k_i are restricted to half the BZ, and therefore $\tilde{\delta}_{\{k_i\}}$ ensures momentum conservation up to multiples of the ordering vector $\mathbf{Q}$.

In contrast to the discrete translational invariance, the SU(2) symmetry is a continuous one. Its breaking is therefore accompanied by the emergence of massless Goldstone modes. In a purely fermionic language, this will be reflected by the divergence of some contributions to the two-particle interaction in the limit of a vanishing seed field, as for a broken U(1) symmetry. [47–49, 57] The radial mode, however, will have a mass and therefore the corresponding contributions to the interaction remain regular for a vanishing seed field. Let me now define the fermionic spin-density wave (SDW) bilinear

$$S_i^{s_1 s_2}(l) = \sum_{\sigma\sigma'} \int d'k\, \bar{\Psi}_\sigma^{s_1}(k+l)\, \tau^i_{\sigma\sigma'} \Psi_{\sigma'}^{s_2}(k)\,,$$

where τ^i denotes the ith Pauli matrix and there the momentum integration only runs over the reduced BZ, which is indicated by the prime in the measure $d'k$. Note that the Nambu indices are treated as some kind of flavor quantum numbers here. If $s_1 \neq s_2$, the physical SDW ordering momentum amounts to $\mathbf{l}+\mathbf{Q}$.

In an boson-exchange picture, the Goldstone and radial vertices then correspond to $S_x^2 + S_y^2$ and S_z^2 terms, respectively. (For a pictorial representation of the S_z^2 term, see Fig. 1.3(a).) If the SU(2) symmetry is broken, those terms differ. Even though, they both are still invariant under a flip of the spin-projection quantum number. In the following, I will call such contributions to the interaction spin-normal. The remaining $\mathrm{U}_z(1)$ symmetry also allows for spin-anomalous terms of the form $S_x S_y$. So in a channel decomposition of the fRG flow equations, the magnetic channel of Refs. [24–26] should split into radial and Goldstone as well as spin-anomalous contributions. In addition, there will be charge-density wave (CDW) contributions of the form n^2 (see Fig. 1.3(b)), where

$$n^{s_1 s_2}(l) = \sum_{\sigma} \int d'k\, \bar{\Psi}_\sigma^{s_1}(k+l)\, \Psi_\sigma^{s_2}(k)$$

denotes the CDW bilinear. Also spin-anomalous $S_z n$ contributions as depicted in 1.3(c) are allowed.

So far, I have discussed different particle-hole exchange processes. One may now wonder whether the breaking of the SU(2) symmetry has also nontrivial consequences for contributions to the interaction induced by the exchange of virtual Cooper pairs. One

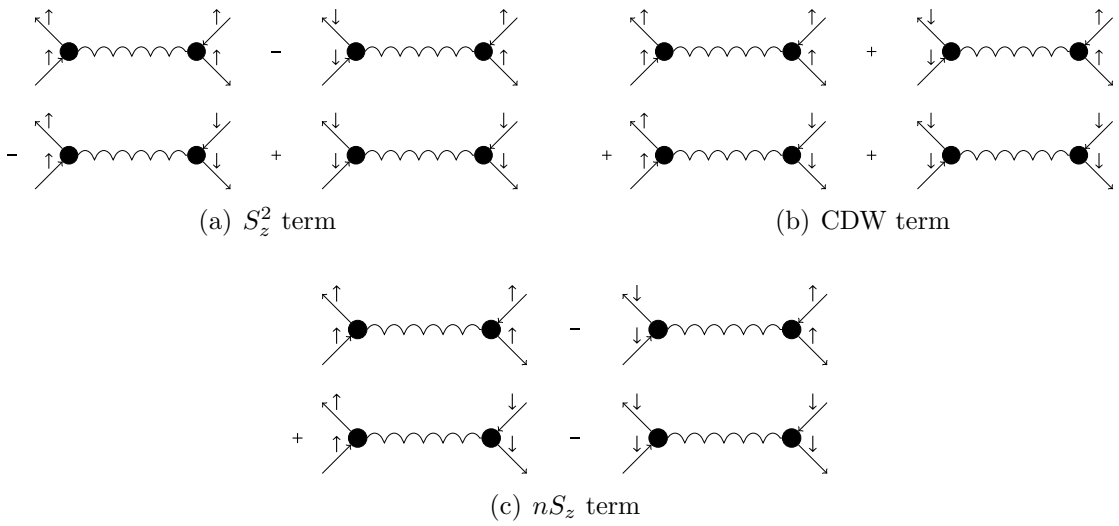

(a) S_z^2 term (b) CDW term

(c) nS_z term

Figure 1.3.: CDW, S_z^2 and spin-anomalous $S_z n$ terms in an boson-exchange picture.

may intuitively expect that there will be singlet and triplet-pairing terms, but this classification does not apply in a strict sense if the SU(2) symmetry is broken. This can be seen by considering the Cooper-pair bilinear

$$\phi_{\sigma_1\sigma_2}^{s_1 s_2}(l) = \int d'q \, \bar{\Psi}_{\sigma_1}^{s_1}\left(\frac{l}{2}+q\right) \bar{\Psi}_{\sigma_2}^{s_2}\left(\frac{l}{2}-q\right) ,$$

which equals $-\phi_{\sigma_2\sigma_1}^{s_2 s_1}(l)$ due to the Pauli principle. A general SU(2) transformation will map $(\phi_{\uparrow\downarrow} - \phi_{\downarrow\uparrow})/\sqrt{2}$ onto itself, while $\phi_{\uparrow\uparrow}$, $\phi_{\downarrow\downarrow}$ and $(\phi_{\uparrow\downarrow} + \phi_{\downarrow\uparrow})/\sqrt{2}$ get mixed. Consequently, ϕ can uniquely be decomposed into a singlet and a triplet component with values that remain unaltered under a SU(2) transformation. If this invariance is however broken and if one has only a $\mathrm{U}_z(1)$ invariance instead, $(\phi_{\uparrow\downarrow} - \phi_{\downarrow\uparrow})/\sqrt{2}$, $\phi_{\uparrow\uparrow}$, $\phi_{\downarrow\downarrow}$ and $(\phi_{\uparrow\downarrow} + \phi_{\downarrow\uparrow})/\sqrt{2}$ do not get mixed by such a transformation. So, the triplet is split or, in other words, ϕ can be decomposed into four $\mathrm{U}_z(1)$ invariant parts. This observation has independently been made by D. Scherer *et al.* in the context of the Kitaev-Heisenberg model. [78] In the following, the terms 'singlet' and 'triplet pairing' will only be used for SU(2) invariant contributions to the interaction. Conversely, SU(2)-breaking contributions in the pairing channels will be called 'anomalous pairing terms'. Having qualitatively discussed the consequences of the broken SU(2) and translational symmetries, we are now in a position, where a channel decomposition of the fRG flow equations can be performed.

1.4.2. Formal decomposition

The three coupling functions from Section 1.3.1 are now decomposed as follows. Renormalizations of equal-spin interactions $W_\uparrow$ and $W_\downarrow$ can be regarded as a sum $\Phi_{\mathrm{SC}\sigma}$ of triplet

and anomalous pairing terms and a spin-dependent particle-hole term $\Phi_{K\sigma}$, which enter according to

$$\begin{aligned} W_\sigma(K_1,K_2,K_3,K_4) = \tilde{\delta}_{\{k_i\}} \Big[& U_\sigma^{\{s\}}(k_1,k_2,k_3) + \Phi_{\mathrm{SC},\sigma}^{\{s\}}(k_1+k_2,k_1,k_3) \\ & - \Phi_{K,\sigma}^{\{s\}}(k_1-k_3,k_1,k_2) + \Phi_{K,\sigma}^{\{\tilde{s}\}}(k_3-k_2,k_1,k_2) \Big] \,. \end{aligned} \tag{1.23}$$

In this equation, U_σ stems from the bare interaction and $\{\tilde{s}\}$ denotes (s_1,s_2,s_4,s_3). The particle-hole part $\Phi_{K,\sigma}$ contains S_z^2 and n^2 (CDW) contributions as well as terms of $S_z n$ form, where n represents the charge density.

The coupling function $W_{\uparrow\downarrow}$ with bare values $U_{\uparrow\downarrow}$ is renormalized by a particle-particle part $\Phi_{\mathrm{SC},\uparrow\downarrow}$, which may contain triplet, singlet and anomalous pairing terms, and magnetic contributions Φ_{plane} corresponding to $S_x^2+S_y^2$ or S_xS_y and Φ_{axis}, which contains S_z^2, CDW and $S_z n$ terms

$$\begin{aligned} W_{\uparrow\downarrow}(K_1,K_2,K_3,K_4) = \tilde{\delta}_{\{k_i\}} \Big[& U_{\uparrow\downarrow}^{\{s\}}(k_1,k_2,k_3) + \Phi_{\mathrm{SC},\uparrow\downarrow}^{\{s\}}(k_1+k_2,k_1,k_3) \\ & + \Phi_{\mathrm{plane}}^{\{s\}}(k_3-k_2,k_1,k_2) - \Phi_{\mathrm{axis}}^{\{s\}}(k_1-k_3,k_1,k_2) \Big] \,. \end{aligned} \tag{1.24}$$

The right-hand sides of the flow equations (1.15)–(1.20) now read as follows. As a short-hand notation for the loops,

$$L_{\sigma_1,\sigma_2}^{\{s\}}(p,q) = \partial_\lambda \left[G_{\sigma_1}^{s_1,s_2}(p)\, G_{\sigma_2}^{s_3,s_4}(q) \right]$$

is introduced. Once again, the prime in the measure $d'p$ indicates that the respective momentum integral only runs over the reduced BZ. In the particle-particle channels, one obtains

$$\begin{aligned} \dot{\Phi}_{\mathrm{SC},\sigma}^{\{s\}}(l,q,q') = & \frac{1}{2} \sum_{\{s_i'\}} \int d'p\, W_\sigma^{s_1,s_2,s_1',s_3'}(q,l-q,l/2+p,l/2-p) \\ & \times W_\sigma^{s_4',s_2',s_3,s_4}(l/2-p,l/2+p,q',l-q')\, L_{\sigma,\sigma}^{\{s_i'\}}(l/2+p,l/2-p) \,, \end{aligned} \tag{1.25}$$

$$\begin{aligned} \dot{\Phi}_{\mathrm{SC},\uparrow\downarrow}^{\{s\}}(l,q,q') = & - \sum_{\{s_i'\}} \int d'p\, W_{\uparrow\downarrow}^{s_1,s_2,s_1',s_3'}(q,l-q,l/2+p,l/2-p) \\ & \times W_{\uparrow\downarrow}^{s_2',s_4',s_3,s_4}(l/2+p,l/2-p,q',l-q')\, L_{\uparrow,\downarrow}^{\{s_i'\}}(l/2+p,l/2-p) \,. \end{aligned} \tag{1.26}$$

The flow in the particle-hole channels is governed by

$$\begin{aligned}\dot{\Phi}^{\{s\}}_{K,\uparrow}(l,q,q') = &-\sum_{\{s_i'\}}\int d'p\, W_{\uparrow}^{s_4',s_2,s_4,s_1'}(p+l/2,q',l+q',p-l/2)\\ &\times W_{\uparrow}^{s_1,s_2',s_3',s_3}(q,p-l/2,p+l/2,q-l)\, L^{\{s_i'\}}_{\uparrow,\uparrow}(p-l/2,p+l/2)\\ &-\sum_{\{s_i'\}}\int d'p\, W_{\uparrow\downarrow}^{s_2,s_4',s_4,s_1'}(q',p+l/2,l+q',p-l/2)\\ &\times W_{\uparrow\downarrow}^{s_1,s_2',s_3,s_3'}(q,p-l/2,q-l,p+l/2)\, L^{\{s_i'\}}_{\downarrow,\downarrow}(p-l/2,p+l/2)\,, \end{aligned}\tag{1.27}$$

$$\begin{aligned}\dot{\Phi}^{\{s\}}_{K,\downarrow}(l,q,q') = &-\sum_{\{s_i'\}}\int d'p\, W_{\downarrow}^{s_4',s_2,s_4,s_1'}(p+l/2,q',l+q',p-l/2)\\ &\times W_{\downarrow}^{s_1,s_2',s_3',s_3}(q,p-l/2,p+l/2,q-l)\, L^{\{s_i'\}}_{\downarrow,\downarrow}(p-l/2,p+l/2)\\ &-\sum_{\{s_i'\}}\int d'p\, W_{\uparrow\downarrow}^{s_4',s_2,s_1',s_4}(p+l/2,q',p-l/2,l+q')\\ &\times W_{\uparrow\downarrow}^{s_2',s_1,s_3',s_3}(p-l/2,q,p+l/2,q-l)\, L^{\{s_i'\}}_{\uparrow,\uparrow}(p-l/2,p+l/2)\,, \end{aligned}\tag{1.28}$$

$$\begin{aligned}\dot{\Phi}^{\{s\}}_{\text{plane}}(l,q,q') = &-\sum_{\{s_i'\}}\int d'p\, W_{\uparrow\downarrow}^{s_4',s_2,s_3,s_1'}(p+l/2,q',l+q',p-l/2)\\ &\times W_{\uparrow\downarrow}^{s_1,s_2',s_3',s_4}(q,p-l/2,p+l/2,q-l)\, L^{\{s_i'\}}_{\downarrow,\uparrow}(p-l/2,p+l/2)\,, \end{aligned}\tag{1.29}$$

$$\begin{aligned}\dot{\Phi}^{\{s\}}_{\text{axis}}(l,q,q') = &\sum_{\{s_i'\}}\int d'p\, W_{\uparrow\downarrow}^{s_4',s_2,s_1',s_4}(p+l/2,q',p-l/2,q'+l)\\ &\times W_{\uparrow}^{s_1,s_2',s_3',s_3}(q,p-l/2,p+l/2,q-l)\, L^{\{s_i'\}}_{\uparrow,\uparrow}(p-l/2,p+l/2)\\ &+\sum_{\{s_i'\}}\int d'p\, W_{\downarrow}^{s_4',s_2,s_4,s_1'}(p+l/2,q',l+q',p-l/2)\\ &\times W_{\uparrow\downarrow}^{s_1,s_2',s_3,s_3'}(q,p-l/2,q-l,p+l/2)\, L^{\{s_i'\}}_{\downarrow,\downarrow}(p-l/2,p+l/2)\,. \end{aligned}\tag{1.30}$$

Expressed in Nambu space, the flow equations for the self-energy read as

$$\begin{aligned}\partial_\lambda \Sigma_{\uparrow}^{s_1 s_2}(k_1,k_2) = &-\sum_{s_1' s_2'}\int d'p\, S_{\uparrow}^{s_1' s_2'}(p)\, W_{\uparrow}^{s_1,s_2',s_1',s_2}(k_1,p,p,k_2)\\ &+\sum_{s_1' s_2'}\int d'p\, S_{\downarrow}^{s_1' s_2'}(p)\, W_{\uparrow\downarrow}^{s_1,s_2',s_2,s_1'}(k_1,p,k_2,p) \end{aligned}\tag{1.31}$$

and

$$\partial_\lambda \Sigma_\downarrow^{s_1 s_2}(k_1,k_2) = -\sum_{s_1' s_2'} \int d'p\, S_\downarrow^{s_1' s_2'}(p)\, W_\downarrow^{s_1,s_2',s_1',s_2}(k_1,p,p,k_2) + \sum_{s_1' s_2'} \int d'p\, S_\uparrow^{s_1' s_2'}(p)\, W_{\uparrow\downarrow}^{s_2',s_1,s_1',s_2}(p,k_1,p,k_2)\,. \tag{1.32}$$

1.4.3. Improved parametrization

In the present form, this channel decomposition would already allow for a reduction of computational effort if all three momentum and frequency variables were discretized. This would, however, rather be an approximation simplifying the numerics than a decomposition into physically meaningful channels. Namely, Φ_K and Φ_{axis} both contain S_z^2 and CDW contributions. In a physically meaningful channel decomposition that allows for sensible further approximations, S_z^2 and CDW contributions should appear in different channels. In the following, this will be accomplished by decomposing the single-channel coupling functions into spin-normal and spin-anomalous contributions and then linearly recombining the spin-normal parts.

Let me first decompose Φ_{axis} into its spin-normal and spin-anomalous parts

$$\Phi_{\text{axis}\pm}^{\{s\}}(l,p,q) = \frac{1}{2}\left[\Phi_{\text{axis}}^{\{s\}}(l,p,q) \pm \Phi_{\text{axis}}^{\{\bar{s}\}}(-l,q,p)\right]\,,$$

where $\{\bar{s}\} = (s_2, s_1, s_4, s_3)$. Their scale derivatives can be cast into the form

$$\begin{aligned}
\dot{\Phi}^{\{s\}}_{\mathrm{axis}\pm}(l,q,q') = \frac{1}{2}\sum_{\{s'_i\}}\int d'p\, W^{s'_4,s_2,s'_1,s_4}_{\uparrow\downarrow}(p+l/2,q',p-l/2,q'+l) \\
\times W^{s_1,s'_2,s'_3,s_3}_{\uparrow}(q,p-l/2,p+l/2,q-l)\, L^{\{s'_i\}}_{\uparrow,\uparrow}(p-l/2,p+l/2) \\
\pm \frac{1}{2}\sum_{\{s'_i\}}\int d'p\, W^{s_2,s'_4,s_4,s'_1}_{\uparrow\downarrow}(q',p+l/2,q'+l,p-l/2) \\
\times W^{s_1,s'_2,s'_3,s_3}_{\downarrow}(q,p-l/2,p+l/2,q-l)\, L^{\{s'_i\}}_{\downarrow,\downarrow}(p-l/2,p+l/2) \\
+ \frac{1}{2}\sum_{\{s'_i\}}\int d'p\, W^{s'_4,s_2,s_4,s'_1}_{\downarrow}(p+l/2,q',q'+l,p-l/2) \\
\times W^{s_1,s'_2,s_3,s'_3}_{\uparrow\downarrow}(q,p-l/2,q-l,p+l/2)\, L^{\{s'_i\}}_{\downarrow,\downarrow}(p-l/2,p+l/2) \\
\pm \frac{1}{2}\sum_{\{s'_i\}}\int d'p\, W^{s'_4,s_2,s_4,s'_1}_{\uparrow}(p+l/2,q',q'+l,p-l/2) \\
\times W^{s'_2,s_1,s'_3,s_3}_{\uparrow\downarrow}(p-l/2,q,p+l/2,q-l)\, L^{\{s'_i\}}_{\uparrow,\uparrow}(p-l/2,p+l/2)\,. \qquad (1.33)
\end{aligned}$$

Likewise, one may introduce spin-normal and spin-anomalous coupling functions

$$\Phi^{\{s\}}_{K\pm}(l,p,q) = \frac{1}{2}\left[\Phi^{\{s\}}_{K,\uparrow}(l,p,q) \pm \Phi^{\{\bar{s}\}}_{K,\downarrow}(l,p,q)\right]$$

for the K channels. Their scale derivative can be obtained by adding or subtracting the

flow equations (1.27) and (1.28), respectively, i.e.

$$\begin{aligned}
\dot{\Phi}^{\{s\}}_{K,\pm}(l,q,q') = &-\frac{1}{2}\sum_{\{s_i'\}}\int d'p\, W_{\uparrow}^{s_4',s_2,s_4,s_1'}(p+l/2,q',l+q',p-l/2)\\
&\times W_{\uparrow}^{s_1,s_2',s_3',s_3}(q,p-l/2,p+l/2,q-l)\, L_{\uparrow,\uparrow}^{\{s_i'\}}(p-l/2,p+l/2)\\
&\mp\frac{1}{2}\sum_{\{s_i'\}}\int d'p\, W_{\downarrow}^{s_4',s_2,s_4,s_1'}(p+l/2,q',l+q',p-l/2)\\
&\times W_{\downarrow}^{s_1,s_2',s_3',s_3}(q,p-l/2,p+l/2,q-l)\, L_{\downarrow,\downarrow}^{\{s_i'\}}(p-l/2,p+l/2)\\
&-\frac{1}{2}\sum_{\{s_i'\}}\int d'p\, W_{\uparrow\downarrow}^{s_2,s_4',s_4,s_1'}(q',p+l/2,l+q',p-l/2)\\
&\times W_{\uparrow\downarrow}^{s_1,s_2',s_3,s_3'}(q,p-l/2,q-l,p+l/2)\, L_{\downarrow,\downarrow}^{\{s_i'\}}(p-l/2,p+l/2)\\
&\mp\frac{1}{2}\sum_{\{s_i'\}}\int d'p\, W_{\uparrow\downarrow}^{s_4',s_2,s_1',s_4}(p+l/2,q',p-l/2,l+q')\\
&\times W_{\uparrow\downarrow}^{s_2',s_1,s_3',s_3}(p-l/2,q,p+l/2,q-l)\, L_{\uparrow,\uparrow}^{\{s_i'\}}(p-l/2,p+l/2)\,, \qquad (1.34)
\end{aligned}$$

S_z^2 and CDW contributions are spin-normal and can be obtained as

$$\begin{aligned}
\Phi_z^{\{s\}}(l,p,q) &= \Phi_{K+}^{\{s\}}(l,p,q) - \Phi_{\text{axis}+}^{\{s\}}(l,p,q)\,,\\
\Phi_{\text{CDW}}^{\{s\}}(l,p,q) &= \Phi_{K+}^{\{s\}}(l,p,q) + \Phi_{\text{axis}+}^{\{s\}}(l,p,q)\,,
\end{aligned}$$

respectively, as illustrated by Figs. 1.3(a),(b). With the shorthand notations

$$W_{\pm\sigma}^{\{s\}}(k_1,k_2,k_3,k_4) = W_{\uparrow\downarrow}^{\{s\}}(k_1,k_2,k_3,k_4) \pm W_{\sigma}^{\{\tilde{s}\}}(k_1,k_2,k_4,k_3)\,, \qquad (1.35)$$

the flow equations of these new single-channel coupling functions read as

$$\begin{aligned}
\dot{\Phi}^{\{s\}}_{\text{CDW}}(l,q,q') = &-\frac{1}{2}\sum_{\{s_i'\}}\int d'p\, L_{\uparrow,\uparrow}^{\{s_i'\}}(p-l/2,p+l/2)\\
&\times W_{-\uparrow}^{s_2',s_1,s_3',s_3}(p-l/2,q,p+l/2,q-l)\, W_{-\uparrow}^{s_4',s_2,s_1',s_4}(p+l/2,q',p-l/2,q'+l)\\
&-\frac{1}{2}\sum_{\{s_i'\}}\int d'p\, L_{\downarrow,\downarrow}^{\{s_i'\}}(p-l/2,p+l/2)\\
&\times W_{-\downarrow}^{s_1,s_2',s_3,s_3'}(q,p-l/2,q-l,p+l/2)\, W_{-\downarrow}^{s_2,s_4',s_4,s_1'}(q',p+l/2,q'+l,p-l/2)
\end{aligned} \qquad (1.36)$$

and

$$\begin{aligned}\dot{\Phi}_z^{\{s\}}(l,q,q') = &-\frac{1}{2}\sum_{\{s_i'\}}\int d'p\, L_{\uparrow,\uparrow}^{\{s_i'\}}(p-l/2,p+l/2)\\ &\times W_{+\uparrow}^{s_2',s_1,s_3',s_3}(p-l/2,q,p+l/2,q-l)\, W_{+\uparrow}^{s_4',s_2,s_1',s_4}(p+l/2,q',p-l/2,q'+l)\\ &-\frac{1}{2}\sum_{\{s_i'\}}\int d'p\, L_{\downarrow,\downarrow}^{\{s_i'\}}(p-l/2,p+l/2)\\ &\times W_{+\downarrow}^{s_1,s_2',s_3,s_3'}(q,p-l/2,q-l,p+l/2)\, W_{+\downarrow}^{s_2,s_4',s_4,s_1'}(q',p+l/2,q'+l,p-l/2) \quad (1.37)\end{aligned}$$

Summarizing, in a more physical parametrization the single-channel coupling functions $W_\uparrow$, $W_\downarrow$ and $W_{\uparrow\downarrow}$ are decomposed into the following channels

$$\begin{aligned}W_\uparrow(K_1,K_2,K_3,K_4) = \tilde{\delta}_{\{k_i\}}\Big[&U_\uparrow^{\{s\}}(k_1,k_2,k_3)+\Phi_{\mathrm{SC},\uparrow}^{\{s\}}(k_1+k_2,k_1,k_3)\\ &-\frac{1}{2}\Phi_{\mathrm{CDW}}^{\{s\}}(k_1-k_3,k_1,k_2)-\frac{1}{2}\Phi_z^{\{s\}}(k_1-k_3,k_1,k_2)\\ &-\Phi_{K-}^{\{s\}}(k_1-k_3,k_1,k_2)+\frac{1}{2}\Phi_{\mathrm{CDW}}^{\{\tilde{s}\}}(k_3-k_2,k_1,k_2)\\ &+\frac{1}{2}\Phi_z^{\{\tilde{s}\}}(k_3-k_2,k_1,k_2)+\Phi_{K-}^{\{\tilde{s}\}}(k_3-k_2,k_1,k_2)\Big]\,,\end{aligned}$$

$$\begin{aligned}W_\downarrow(K_1,K_2,K_3,K_4) = \tilde{\delta}_{\{k_i\}}\Big[&U_\downarrow^{\{s\}}(k_1,k_2,k_3)+\Phi_{\mathrm{SC},\downarrow}^{\{s\}}(k_1+k_2,k_1,k_3)\\ &-\frac{1}{2}\Phi_{\mathrm{CDW}}^{\{s\}}(k_1-k_3,k_1,k_2)-\frac{1}{2}\Phi_z^{\{s\}}(k_1-k_3,k_1,k_2)\\ &+\Phi_{K-}^{\{s\}}(k_1-k_3,k_1,k_2)+\frac{1}{2}\Phi_{\mathrm{CDW}}^{\{\tilde{s}\}}(k_3-k_2,k_1,k_2)\\ &+\frac{1}{2}\Phi_z^{\{\tilde{s}\}}(k_3-k_2,k_1,k_2)-\Phi_{K-}^{\{\tilde{s}\}}(k_3-k_2,k_1,k_2)\Big]\end{aligned}$$

and

$$\begin{aligned}W_{\uparrow\downarrow}(K_1,K_2,K_3,K_4) = \tilde{\delta}_{\{k_i\}}\Big[&U_{\uparrow\downarrow}^{\{s\}}(k_1,k_2,k_3)+\Phi_{\mathrm{SC},\uparrow\downarrow}^{\{s\}}(k_1+k_2,k_1,k_3)\\ &+\Phi_{\mathrm{plane}}^{\{s\}}(k_3-k_2,k_1,k_2)-\frac{1}{2}\Phi_{\mathrm{CDW}}^{\{s\}}(k_1-k_3,k_1,k_2)\\ &+\frac{1}{2}\Phi_z^{\{s\}}(k_1-k_3,k_1,k_2)-\Phi_{\mathrm{axis}-}^{\{s\}}(k_1-k_3,k_1,k_2)\Big]\,.\end{aligned}$$

The scale dependence of Φ_{CDW}, Φ_z, Φ_{K-} and $\Phi_{\mathrm{axis}-}$ is governed by the flow equations (1.36), (1.37), (1.34) and (1.33) In contrast, the single-channel coupling functions $\Phi_{\mathrm{SC},\sigma}$, $\Phi_{\mathrm{SC},\uparrow\downarrow}$ and Φ_{plane} still flow according to Eqs. (1.25), (1.26) and (1.29). In a way similar to the above extraction of CDW and S_z^2 contributions, Φ_{plane} could be decomposed into (spin-normal) $S_x^2+S_y^2$ and (spin-anomalous) S_xS_y terms. Also singlet, triplet

and anomalous pairing terms could be extracted from $\Phi_{\mathrm{SC},\uparrow}$, $\Phi_{\mathrm{SC},\downarrow}$ and $\Phi_{\mathrm{SC},\uparrow\downarrow}$. But in the absence of further symmetries this would result in even lengthier expressions and I therefore refrain from performing this decomposition for the general case here. For the symmetries of Chapter 4.2.1, however, this will be done in Chapter 4.2.2.

Summarizing, the channel decomposition presented here paves the road to an efficient (approximate) parametrization of the interaction resulting in numerically tractable flow equations as in Chapter 4.4.3, where an exchange parametrization will be employed. The group-theoretic view on exchange parametrizations presented in Section 1.2.3 also applies to the above flow equations for collinear spin ordering. For the present chapter, the channel decomposition shall be left in this general form as it might be useful also in other contexts. By dropping the Nambu indices and extending the momentum integrals to the full BZ, for example, it can also be applied to problems without breaking of the translational symmetry, e.g. with just a spin-splitting term. The Kane-Mele-Hubbard model [80–82], for example, might be an interesting candidate for such a study (see remark in the Conclusions on page 174).

1.5. Summary

In this chapter, fRG flow equations for parametrization schemes used in the remainder of this thesis have been provided. Approximations specific to the model and/or to the numerical implementation will then be made in the respective following chapters. Since all RG flows in this work will be inside U(1) symmetric phases, I have recapitulated the general RG flow equations for charge-conserving theories at the beginning of this chapter. For the instability analyses of Chapter 3, these flow equations can be further simplified by exploiting the spin rotation symmetry. Despite these simplifications, an unbiased discretization of these flow equations would still be a formidable task for a numerical viewpoint. Therefore, a channel decomposition [24,56] can be very helpful for integration of these flow equations.

Up to that point, only results from the literature have been recapitulated (for a review, see Ref. [19]). As a new result, I have then presented a group-theoretical discussion of exchange parametrizations, which shines light on the truncation of the form-factor expansion in Refs. [24–26]. In Chapters 4 and 5, flows into AF phases will be considered. First, this requires an efficient parametrization of the flow equation for phases of collinear spin ordering. After a parametrization exploiting the remaining $\mathrm{U}_z(1)$ symmetry has been given and after the corresponding flow equations and the global SU(2) Ward identity have been derived, the fRG flow has been decomposed into different channels. The breaking of the SU(2) symmetry then splits the magnetic channel into radial and Goldstone parts as well as spin-anomalous terms. Also in the pairing channels there are spin-anomalous contributions resulting for the splitting of triplet-pairing terms. These

distinctions are not yet fully respected in the first attempt of a channel decomposition in Section 1.4.2. But after decomposing the coupling functions further into spin-normal and spin-anomalous parts, the normal parts could be recombined to physically meaningful channels in Section 1.4.3. While the flow equations in this latter form will be used in Chapter 4, they may also be useful for other models with a spin splitting term.

Chapter 2.

Extensions for Multiband Models

In this chapter, some nontrivial properties of multiband models are discussed on a formal level. First, the point-group behavior of the vertex functions is discussed and related to the choice of different Bloch bases. I will show that, for a large class of multiband models and in a band language, there always exist Bloch bases, in which the vertex functions transform trivially under all point-group operations. Moreover, I will give a prescription how an effective action for low-energy degrees of freedom can be calculated. These low-energy degrees of freedom usually constitute the conduction band(s). Due to virtual fluctuations in the high-energy sector, e.g. in the valence bands, such an effective action acquires three-particle and higher terms. While these terms have been neglected in previous multiband fRG studies, this chapter concludes with an extension of the conventional level-two truncation of the fRG flow equations, which partly takes the three-particle term of the effective action into account.

Parts of this chapter have previously been published in Ref. [83, 84] and [59].

In the first chapter, the fRG formalism has been laid out for fermionic fields with momentum and spin quantum numbers. Of course, the above results also apply in the presence of additional fermionic flavors, if the corresponding quantum numbers are understood as tacitly included in the momentum quantum numbers. In the context of correlated electrons in a solid, such additional flavor indices usually appear as band indices in models that include more than one electronic orbital per unit cell. While the low-energy physics of the cuprate superconductors with only one conduction band may in essence

be described by a single-band model, other materials of interest have multiple (possibly entangled) Fermi surfaces and therfore require a multiband description. Moreover, in an attempt to push the frontiers of fRG methods further in a more quantitative direction, one may also want to include degrees of freedom further away from the Fermi surface. fRG studies of multiband Hubbard models therefore seem appealing. In the fRG literature, a number of multiband studies can be found including work on multiorbital models of the high-T_c CuO planes, [41] on graphene systems, [28–31,33,68] the pnictides, [34–40] or other two-dimensional systems. [42–44]

In these works, the respective model Hamiltonians are given in a second-quantized language with field operators corresponding to fairly localized Wannier states. Generically, these states already hybridize at the one-particle level. For the numerical implementation of the RG flow equations, it may however be helpful to work in a basis of *Bloch* states that do *not* hybridize. In such a basis, the one-particle part of the Hamiltonian then contains the band dispersion. (Even in the recently developed SMFRG approach, [33,43,44] which considers the interaction in the orbital instead of in the band picture, fermionic loops in the diagrams are evaluated in the band picture.) In the band picture, the multiband nature of the model may give rise to important effects. Since the orbital content of the bands depends on momentum, the transformation to the band picture renders a Hubbard interaction momentum-dependent. This effect dubbed *orbital makeup* [52] or *matrix element effect* [43] may have a considerable impact on the phase diagrams of extended Hubbard models, as pointed out in Refs. [41–43] and also in the following chapter. In the first section of this chapter, the formulation of multiband models in a second-quantization language is reviewed. Furthermore, I will comment on the freedom in choosing the basis set and on orbital makeup effects.

On a technical level, multiband fRG studies pose additional challenges compared to the single-band case. In the one-band Hubbard model on a square lattice, for example, the point-group symmetries can straightforwardly be exploited, since its vertex functions behave trivial under all point-group operations. For multiple orbitals per unit cell, however, this does no more hold in general and the point-group properties of the vertex functions are basis-dependent. In particular, the orbital quantum numbers are affected by a point-group operation in general. In the second section of this chapter, I will show that, for a large class of multiband models, the phases of the Bloch basis states in the band picture can be fixed such that the vertex functions transform trivially under all point-group operations. This way, the point-group symmetries of the model can be exploited as in the single-band case.

In order to reduce the computational effort, it may be advantageous to derive an effective action for the conduction band(s) which is then treated with fRG or another low-energy solver. Such a derivation will be given in the third section. In the resulting effective action, also three-particle and higher terms occur. They are generated by virtual fluctuations in the bands with higher energies. In the fourth section of this chapter,

I will present an approach which partly incorporates these contributions into the RG flow equations.

2.1. General tight-binding model

Let us now start form a general many-particle Hamiltonian

$$H = H_0 + \sum_{n=2}^{m} H_n^{\text{int}}$$

for electrons in some solid in D dimensions with a one-particle part H_0 and two- up to m-particle interaction terms H_n^{int}. (Although bare three-particle and higher interactions are generically absent, i.e. although one usually has $m = 2$, some statements that will be made in the following hold as well if these higher-order interaction terms are present.)

2.1.1. Wannier basis

Suppose that, from an *ab initio* method, we have a basis set of (fairly well localized) Wannier functions at hand. If the above model Hamiltonian describes l of these orbitals per unit cell, these states can be labeled in the following way. The one-particle state

$$|\psi_a^\alpha(\mathbf{R})\rangle$$

is associated with the αth orbital in the direct unit cell with center $\mathbf{R}$. This convention seems not to be very widespread in the literature, but has the advantage that the position quantum numbers $\mathbf{R}$ of Wannier orbitals corresponding to electronic orbitals on different atoms all live on the same Bravais lattice. The subscript a denotes a collection of other quantum numbers, which usually include the spin projection. Note that the position $\mathbf{R}$ plays the role of a quantum number and should not be confused with the argument $\mathbf{r}$ of the wavefunction $\langle \mathbf{r} | \psi_a^\alpha(\mathbf{R}) \rangle$ in position representation. In proceeding towards a second quantization language, Slater determinant n-particle states

$$\left|\psi_{a_1}^{\alpha_1}(\mathbf{R}_1) \dots \psi_{a_n}^{\alpha_n}(\mathbf{R}_n)\right\rangle$$

are written as excitations of the vacuum $|0\rangle$ with $\Psi_a^\alpha(\mathbf{R})\,|0\rangle = 0$ according to

$$\left|\psi_{a_1}^{\alpha_1}(\mathbf{R}_1) \dots \psi_{a_n}^{\alpha_n}(\mathbf{R}_n)\right\rangle = \Psi_{a_1}^{\alpha_1\dagger}(\mathbf{R}_1) \dots \Psi_{a_n}^{\alpha_n\dagger}(\mathbf{R}_n)\,|0\rangle \ .$$

The field operators $\Psi_a^\alpha(\mathbf{R})$ and $\Psi_a^{\alpha\dagger}(\mathbf{R})$ obey the canonical commutation relations for fermions and consequently

$$\Psi_{a_1}^{\alpha_1}(\mathbf{R}_1) \left|\psi_{a_1}^{\alpha_1}(\mathbf{R}_1)\, \psi_{a_2}^{\alpha_2}(\mathbf{R}_2) \dots \psi_{a_n}^{\alpha_n}(\mathbf{R}_n)\right\rangle = \left|\psi_{a_2}^{\alpha_2}(\mathbf{R}_2) \dots \psi_{a_n}^{\alpha_n}(\mathbf{R}_n)\right\rangle \ .$$

In a second-quantized language, the Hamiltonian now reads as [85]

$$\begin{aligned} H = & \sum_{a_1,a_2} \sum_{\alpha_1,\alpha_2} \sum_{\mathbf{R}_1,\mathbf{R}_2} \mathcal{T}\left(a_1,\alpha_1,\mathbf{R}_1;a_2,\alpha_2,\mathbf{R}_2\right) \Psi_{a_1}^{\alpha_1\dagger}(\mathbf{R}_1)\, \Psi_{a_2}^{\alpha_2}(\mathbf{R}_2) \\ & + \sum_{n=2}^{m} \sum_{a_1,\ldots,a_{2n}} \sum_{\alpha_1,\ldots,\alpha_{2n}} \sum_{\mathbf{R}_1,\ldots,\mathbf{R}_{2n}} \mathcal{U}_n\left(a_1,\alpha_1,\mathbf{R}_1;\ldots;a_{2n},\alpha_{2n},\mathbf{R}_{2n}\right) \\ & \times \Psi_{a_1}^{\alpha_1\dagger}(\mathbf{R}_1)\ldots\Psi_{a_n}^{\alpha_n\dagger}(\mathbf{R}_n)\, \Psi_{a_{n+1}}^{\alpha_{n+1}}(\mathbf{R}_{n+1})\ldots\Psi_{a_{2n}}^{\alpha_{2n}}(\mathbf{R}_{2n}) \end{aligned}$$

with the vertex functions

$$\begin{aligned} \mathcal{T}\left(a_1,\alpha_1,\mathbf{R}_1;a_2,\alpha_2,\mathbf{R}_2\right) &= \left\langle \psi_{a_1}^{\alpha_1}(\mathbf{R}_1)\right| H_0 \left|\psi_{a_2}^{\alpha_2}(\mathbf{R}_2)\right\rangle \\ \mathcal{U}_n\left(a_1,\alpha_1,\mathbf{R}_1\,;\ldots;a_{2n},\alpha_{2n},\mathbf{R}_{2n}\right) &= \\ &= \left\langle \psi_{a_1}^{\alpha_1}(\mathbf{R}_1)\ldots\psi_{a_n}^{\alpha_n}(\mathbf{R}_n)\right| H_n^{\text{int}} \left|\psi_{a_{2n}}^{\alpha_{2n}}(\mathbf{R}_{2n})\ldots\psi_{a_{n+1}}^{\alpha_{n+1}}(\mathbf{R}_{n+1})\right\rangle . \end{aligned}$$

Clearly, the precise form of these vertex functions depends on the choice of the basis. If a fairly localized Wannier basis has been chosen, long-ranged terms in the vertex functions are typically negligible. (In the two-particle part, this corresponds to a screening of a Coulomb interaction between the electrons.) Note that, in general, the one-particle vertex function $\mathcal{T}$ contains hopping terms between different species of orbitals.

2.1.2. Hybridizing and non-hybridizing Bloch bases

Let us now switch to reciprocal space, i.e. to the basis of Bloch states

$$|\phi_a^\alpha(\mathbf{k})\rangle = \sum_{\mathbf{R}} e^{i\mathbf{k}\cdot\mathbf{R}}\, |\psi_a^\alpha(\mathbf{R})\rangle = \left[\sum_{\mathbf{R}} e^{i\mathbf{k}\cdot\mathbf{R}}\, \Psi_a^{\alpha\dagger}(\mathbf{R})\right] |0\rangle = \Psi_a^{\alpha\dagger}(\mathbf{k})\,|0\rangle$$

with wavevectors $\mathbf{k}$ in the first Brillouin zone (BZ) $\mathbb{B}$ and new field operators $\Psi_a^\alpha(\mathbf{k})$. The sum over $\mathbf{R}$ in the Fourier transform defining these new fields runs over the centers of the unit cells of the direct lattice. In this new basis, the Hamiltonian reads as

$$H = \sum_a \int_{\mathbb{B}} d\mathbf{k}\, \Psi_a^\dagger(\mathbf{k})\, \mathcal{H}_0(\mathbf{k})\, \Psi_a(\mathbf{k}) + H_{\text{int}}\left[\Psi^\dagger,\Psi\right] . \tag{2.1}$$

The one-particle part is given in matrix notation with l-component pseudo-spinors $\Psi_a(\mathbf{k})$, called *orbitors* in the following. In Eq. (2.1), I have assumed that the quadratic (one-particle) part $\mathcal{H}_0$ of the Hamiltonian does not depend on these additional quantum numbers. For example, if a denotes the spin-projection quantum number, $\mathcal{H}_0$ is independent of this quantum number for a SU(2) symmetric theory. If the SU(2) invariance is broken, it may be advantageous to include components with different spin-projection quantum numbers into the orbitor, i.e. in the quantum numbers α instead of in a.

The interaction with coupling functions $\mathcal{V}$ now reads as

$$H_{\text{int}} = \sum_{n=2}^{m} \int_{\mathbb{B}} d\mathbf{k}_1 \dots d\mathbf{k}_{2n}\ \mathcal{V}^{\alpha_1,\dots,\alpha_{2n}}_{a_1,\dots,a_{2n}}(\mathbf{k}_1,\dots,\mathbf{k}_n;\mathbf{k}_{n+1},\dots,\mathbf{k}_{2n}) \\ \times \Psi^{\alpha_1\,\dagger}_{a_1}(\mathbf{k}_1)\dots\Psi^{\alpha_n\,\dagger}_{a_n}(\mathbf{k}_n)\ \Psi^{\alpha_{n+1}}_{a_{n+1}}(\mathbf{k}_{n+1})\dots\Psi^{\alpha_{2n}}_{a_{2n}}(\mathbf{k}_{2n})\,,$$

where the summation over the orbital indices α_i and other quantum numbers a_i is implicit.

For the evaluation of observables or the calculation of Feynman diagrams as they, e.g., appear on the right-hand side of RG flow equations, it seems rewarding to work in a basis in which $\mathcal{H}_0(\mathbf{k})$ is diagonal. This way, the effort invested in index summations at internal legs of vertices can be reduced.[1] This is accomplished by a unitary transformation $u(\mathbf{k})$ of the orbitor $\Psi_a(\mathbf{k})$ in the orbital picture to the band picture with pseudo-spinors

$$\boldsymbol{\chi}_a(\mathbf{k}) = u(\mathbf{k})\,\Psi_a(\mathbf{k})\,,$$

where $u(\mathbf{k})$ is a $l \times l$ matrix with components $u_{\alpha\beta}$ relating the βth orbital to the αth band. The hybridizing one-particle Bloch basis states are consequently transformed to non-hybridizing ones

$$|\chi^{\alpha}_a(\mathbf{k})\rangle = \sum_{\beta} u_{\alpha,\beta}(\mathbf{k})\ \left|\phi^{\beta}_a(\mathbf{k})\right\rangle\ .$$

The dispersion of the αth band is then given by the component $\mathcal{B}_{\alpha\alpha}(\mathbf{k})$ of the diagonal matrix

$$\mathcal{B}(\mathbf{k}) = u(\mathbf{k})\,\mathcal{H}_0(\mathbf{k})\,u^{\dagger}(\mathbf{k})$$

in the quadratic part

$$H_0 = \sum_a \int d\mathbf{k}\,\boldsymbol{\chi}^{\dagger}_a(\mathbf{k})\,\mathcal{B}(\mathbf{k})\,\boldsymbol{\chi}_a(\mathbf{k})$$

of the Hamiltonian. Let us now rewrite also the interacting part of the Hamiltonian in the band language. In terms of the new fields $\boldsymbol{\chi}$, it reads as

$$H_{\text{int}} = \sum_{n=2}^{m} \int_{\mathbb{B}} d\mathbf{k}_1 \dots d\mathbf{k}_{2n}\ \mathcal{F}^{\alpha_1,\dots,\alpha_{2n}}_{a_1,\dots,a_{2n}}(\mathbf{k}_1,\dots,\mathbf{k}_n;\mathbf{k}_{n+1},\dots,\mathbf{k}_{2n}) \\ \times \boldsymbol{\chi}^{\alpha_1\,\dagger}_{a_1}(\mathbf{k}_1)\dots\boldsymbol{\chi}^{\alpha_n\,\dagger}_{a_n}(\mathbf{k}_n)\ \boldsymbol{\chi}^{\alpha_{n+1}}_{a_{n+1}}(\mathbf{k}_{n+1})\dots\boldsymbol{\chi}^{\alpha_{2n}}_{a_{2n}}(\mathbf{k}_{2n})$$

with the n-particle coupling function

$$\mathcal{F}^{\alpha_1,\dots,\alpha_{2n}}_{a_1,\dots,a_{2n}}(\mathbf{k}_1,\dots,\mathbf{k}_n;\mathbf{k}_{n+1},\dots,\mathbf{k}_{2n}) = \mathcal{V}^{\beta_1,\dots,\beta_{2n}}_{a_1,\dots,a_{2n}}(\mathbf{k}_1,\dots,\mathbf{k}_n;\mathbf{k}_{n+1},\dots,\mathbf{k}_{2n}) \\ \times u_{\alpha_1\beta_1}(\mathbf{k}_1)\dots u_{\alpha_n\beta_n}(\mathbf{k}_n)\,u_{\alpha_{n+1}\beta_{n+1}}(\mathbf{k}_{n+1})^*\dots u_{\alpha_{2n}\beta_{2n}}(\mathbf{k}_{2n})^*\,. \tag{2.2}$$

[1] For other reasons, fRG calculations in the orbital language can still be viable and maybe even preferable in some cases, cf. for example Refs. [33, 43, 44].

One can observe that the momentum dependence of the n-particle coupling function is modulated by the (momentum-dependent) transformation matrix elements $u_{\alpha\beta}(\mathbf{k})$. In particular, if the interaction is completely wavevector-independent in the orbital language, a nontrivial momentum dependence emerges in the band picture. An on-site Hubbard term, for example, is then rendered nonlocal by this so-called *orbital makeup*, [52] which may have a considerable impact on the phase diagram of multiband models as the ones discussed in this thesis. Moreover, it is also believed to account for the differences between the phase diagrams of extended Hubbard models on the honeycomb and the kagome lattices. [42, 43] In addition, it lends a non-trivial behavior under point-group operations to the interaction. In Section 2.2, I will discuss how this behavior can be simplified.

In this place, one might also want to perform an inverse Fourier transform on the basis states $|\chi_a^\alpha\rangle$, at least for some bands α in the low-energy sector. This would lead to *non-hybridizing* Wannier states. The localization of these new states should, however, be expected to be worse than for the hybridizing Wannier states $|\Psi\rangle$. This, e.g., also happens when 8-band models for iron arsenides in the basis of both Fe3d and As4p Wannier states are reduced to 5-band models with d-like Wannier orbitals on the Fe sites. These low-energy effective orbitals typically extend somewhat more on the As sites, and hence are less strongly localized than the previous Fe orbitals.

I will henceforth use the following nomenclature. Instead of Wannier or Bloch states, I will also speak of real and reciprocal space descriptions, respectively. The expansion in states which do not hybridize at the one-particle level will be referred to as the *band language*, while in the *orbital language* these states hybridize. In this place, note that renormalizations in the self-energy may alter the dispersion and the orbital content of the bands. Therefore, the non-hybridizing Bloch basis of the quadratic part of an effective action at lower scales may differ from the non-hybridizing basis of the bare Hamiltonian. By switching from the operator to the functional integral formalism, it is easy to verify that the following statements made for the bare, normally ordered Hamiltonian also apply to a renormalized interaction.

The basis transformations considered here correspond to the multiplication of the Bloch states or field operators in reciprocal space by a phase, i.e.

$$\Psi_a^\alpha(\mathbf{k}) \to e^{i\vartheta_\alpha(\mathbf{k})}\, \Psi_a^\alpha(\mathbf{k})$$

in the orbital language and

$$\boldsymbol{\chi}_a^\alpha(\mathbf{k}) \to e^{i\varphi_\alpha(\mathbf{k})}\, \boldsymbol{\chi}_a^\alpha(\mathbf{k})$$

in the band language. The latter freedom is sometimes referred to as a $\mathbf{k}$-local U(1) invariance of the electronic structure. Since these transformations both correspond to convolution operations in real space, they may significantly affect the localization properties of both hybridizing and non-hybridizing Wannier states. Therefore, an interpretation in real space has to be made with care, keeping these phases in mind.

In the following, only phase transformations that are independent of the additional quantum numbers a will be considered. One might be tempted to call these transformations a Bloch regauging. I will avoid using this term, since the vertex functions in a second-quantized language transform nontrivially. Therefore, there is no redundancy of the state description and the above transformations are strictly speaking not gauge transformations.

2.2. Point-group symmetries and basis transformations

2.2.1. Motivation

In the single-band $2D$ Hubbard model on a square lattice, the coupling functions of the bare and the effective action transform trivially under a point-group operation. Namely, under such a transformation, the momentum quantum numbers $\mathbf{k}_i$ are mapped to their rotated counterparts $R_{\hat{O}}\mathbf{k}_i$, where $R_{\hat{O}}$ denotes the rotation matrix corresponding to the point-group operation $\hat{O} \in C_{4v}$. (These rotation matrices then form a faithful representation of the point group.) The coupling functions of the single-band Hubbard model then take on the same values for $\mathbf{k}_i$ and $R_{\hat{O}}\mathbf{k}_i$. Therefore, the point-group symmetries can be exploited in a fRG calculation.

In multiband models, this generally does not hold for the following reasons. First of all, if there is more than one atom per unit cell, a point-group operation may map some of these atoms onto one another. Moreover, the Wannier states, in terms of which the model is formulated, may transform nontrivially under some point-group operations. In Appendix B, two such models with fourfold and sixfold symmetries will be discussed. At present, there has been a series of fRG studies of multiband models working in the band picture for graphene systems, [28–31, 68] the pnictides, [34–39] or other two-dimensional systems. [41, 42, 44] In some of those works, the point-group symmetries have been exploited already, however without discussing the underlying formal structures. For a general multiband model for interacting fermions, however, this issue may require some care. Before embarking on this task, let me note in passing that there are other RG studies that work in the orbital picture. [33, 43, 44, 86] For those studies, the transformation behavior in the band language discussed below is less relevant, but the symmetry properties in the orbital picture described in the following subsection will still apply.

As a starting point, let me recapitulate that in a second-quantization language, a many-particle Hamiltonian is expressed in terms of field operators which are *auxiliary* quantities. However, the presence or absence of a physical symmetry manifests itself in *observable* quantities. Although the energy of the system is such an observable, the vertex functions of a many-particle model are auxiliary quantities in general, since they

play the role of coefficients in an expansion in auxiliary quantities. Of course, one should in principle be able to find transformation rules according to which the physical symmetries manifest themselves in auxiliary quantities such as the vertex functions. This is an issue related to the possible nontrivial transformation properties of specific wavefunctions in elementary quantum mechanics, e.g. in the case of rotational symmetry, while the observables should reflect the symmetry in a trivial way. Another textbook example similar to the discussion below is the behavior of the Dirac 4-spinor under Lorentz-transformations which leads to a Lorentz invariant Lagrangian. Below the corresponding transformation for the field operators in a multiorbital problem is constructed, such that the Hamiltonian (or the Lagrangian) density in the orbital picture and later in the band picture remains invariant under point-group operations.

For symmetries other than those in the point group, symmetry constraints on fermionic vertex functions have been derived from such transformation rules in the fRG literature, [24, 48, 58] particle-hole and time-reversal symmetries being examples. In these cases, the corresponding symmetries could be implemented due to a simple form of these constraints. At this point, however, it is not clear why also the point-group transformation rules of the vertex functions should take on a simple form which would allow for a reduction of the numerical effort. Since we are dealing with auxiliary quantities, even further complications may arise. If a theory is expressed in auxiliary quantities, there may be *gauge or basis transformations* affecting the auxiliary, but not the observable quantities. Here, these transformations are basis transformation between Bloch states with different phase factors and the corresponding sets of Wannier orbitals. Hence, these transformations have the character of basis rather than of gauge transformations, since not only the fields, but also the vertex functions will be affected. The precise form of the point-group transformation rules for the vertex functions may consequently be basis-dependent in general.

Despite the equivalence of all possible bases, one of them may be more convenient than another in a particular context. The choice of maximally localized Wannier functions, for example, may be very helpful. [87] For a second quantized tight-binding Hamiltonian, the precise form of the vertex functions depends on the Wannier basis chosen. In particular, weakly localized Wannier orbitals will result in long-range hopping terms. One may therefore wonder, whether the phase of the Bloch state in the band language can be fixed in such a way that the point-group transformation rules for the vertex functions take on a simple form. This would allow for further progress and make the symmetry explicit. In the following, I will show that, for a large class of tight-binding models, there always exists a *natural Bloch basis* with transformation rules for the vertex functions that only affect the momentum quantum numbers. This will be done for a general point group $\mathcal{G}$. In real space, the choice of the phases of the Bloch states corresponds to the above mentioned freedom in the localization properties of Wannier functions. Therefore, the interpretation of a real-space formulation requires some care.

2.2.2. Point-group transformations

Suppose that transformation rules for the orbitors in reciprocal space are of the form

$$\Psi_a(\mathbf{k}) \xrightarrow{\hat{O}} \Psi'_a(R_{\hat{O}}\mathbf{k}) = M_{\hat{O}}(\mathbf{k})\,\Psi_a(\mathbf{k})\,, \quad \hat{O} \in \mathcal{G}$$

with l-dimensional unitary representation matrices $M_{\hat{O}}$ of the point group $\mathcal{G}$. In general, these matrices are wavevector-dependent, as will be explained further below. They must obey the group law

$$M_{\hat{C}}(\mathbf{k}) = M_{\hat{B}}(R_{\hat{A}}\mathbf{k})\,M_{\hat{A}}(\mathbf{k}) \quad \text{for} \quad \hat{C} = \hat{B}\hat{A}\,. \tag{2.3}$$

Let me first discuss the transformation behavior of the quadratic part of the Hamiltonian. Under a point-group operation $\hat{O}$, the one-particle Hamiltonian density

$$\Psi^\dagger_a(\mathbf{k})\,\mathcal{H}_0(\mathbf{k})\,\Psi_a(\mathbf{k})$$

gets mapped to

$$\Psi'^\dagger_a(R_{\hat{O}}\mathbf{k})\,\mathcal{H}_0(R_{\hat{O}}\mathbf{k})\,\Psi'_a(R_{\hat{O}}\mathbf{k}) = \Psi^\dagger_a(\mathbf{k})\,M^\dagger_{\hat{O}}(\mathbf{k})\,\mathcal{H}_0(R_{\hat{O}}\mathbf{k})\,M_{\hat{O}}(\mathbf{k})\,\Psi_a(\mathbf{k})\,.$$

If there now exists a set of representation matrices $M_{\hat{O}}(\mathbf{k})$ with the property

$$\mathcal{H}_0(R_{\hat{O}}\mathbf{k}) = M_{\hat{O}}(\mathbf{k})\,\mathcal{H}_0(\mathbf{k})\,M^\dagger_{\hat{O}}(\mathbf{k}) \quad \forall\,\hat{O} \in \mathcal{G}\,, \tag{2.4}$$

the one-particle Hamiltonian density is point-group symmetric, since the representation matrices then cancel. In the presence of interactions, point-group symmetry consequently requires the existence of a set of representation matrices that fulfill both Eq. (2.4) and

$$\begin{aligned}
&\mathcal{V}^{\alpha_1,\ldots,\alpha_{2n}}_{a_1,\ldots,a_{2n}}(R_{\hat{O}}\mathbf{k}_1,\ldots,R_{\hat{O}}\mathbf{k}_n;R_{\hat{O}}\mathbf{k}_{n+1},\ldots,R_{\hat{O}}\mathbf{k}_{2n}) \\
&= \sum_{\beta_1,\ldots,\beta_{2n}} \left[\prod_{j=1}^{n} (M_{\hat{O}})_{\alpha_j,\beta_j}(\mathbf{k}_j) \left(M^\dagger_{\hat{O}}\right)_{\beta_{j+n},\alpha_{j+n}}(\mathbf{k}_{j+n})\right] \mathcal{V}^{\beta_1,\ldots,\beta_{2n}}_{a_1,\ldots,a_{2n}}(\mathbf{k}_1,\ldots,\mathbf{k}_n;\mathbf{k}_{n+1},\ldots,\mathbf{k}_{2n})\,.
\end{aligned} \tag{2.5}$$

Clearly, the Hamiltonians for the Emery model and the graphene tight-binding model in Appendix B are point-group invariant as their coupling functions fulfill these relations. If this transformation rule affects orbitor components with different spin orientations in a nontrivial way, one might expect that the (fermionic) orbitor gets multiplied by -1 under a rotation by 2π. However, for a charge-conserving theory, such an additional phase will always cancel and can hence safely be dropped.

In the above description, point-group symmetry manifests itself in the relations (2.4) and (2.5) for the coupling functions in a second-quantized language. The precise form

of the representation matrices in these equations depends, of course, on the basis. For example, under a basis transformation

$$\begin{aligned}
\Psi_a^\alpha(\mathbf{k}) &\to e^{i\vartheta_\alpha(\mathbf{k})}\,\Psi_a^\alpha(\mathbf{k})\,,\\
\left(\mathcal{H}_0(\mathbf{k})\right)_{\alpha,\beta} &\to e^{i\vartheta_\alpha(\mathbf{k})}\,\left(\mathcal{H}_0(\mathbf{k})\right)_{\alpha,\beta}\,e^{-i\vartheta_\beta(\mathbf{k})}\\
\mathcal{V}^{\alpha_1,\ldots,\alpha_{2n}}_{a_1,\ldots,a_{2n}}(\mathbf{k}_1,\ldots,\mathbf{k}_{2n}) &\to e^{i\vartheta_{\alpha_1}(\mathbf{k})}\ldots e^{i\vartheta_{\alpha_n}(\mathbf{k})}\,\mathcal{V}^{\alpha_1,\ldots,\alpha_{2n}}_{a_1,\ldots,a_{2n}}(\mathbf{k}_1,\ldots,\mathbf{k}_{2n})\,e^{-i\vartheta_{\alpha_{n+1}}(\mathbf{k})}\ldots e^{-i\vartheta_{\alpha_{2n}}(\mathbf{k})}
\end{aligned}$$

in the orbital language, momentum-independent representation matrices $M_{\hat{O}}$ may be rendered momentum-dependent according to

$$\left(M_{\hat{O}}(\mathbf{k})\right)_{\alpha,\beta} \to e^{i\vartheta_\alpha(R_{\hat{O}}\mathbf{k})}\,\left(M_{\hat{O}}(\mathbf{k})\right)_{\alpha,\beta}\,e^{-i\vartheta_\beta(\mathbf{k})}\,. \tag{2.6}$$

As one may easily verify, this transformation does not affect the group law in Eq. (2.3). A multiband model of the type given in Eq. (2.1) is therefore invariant under point-group operations irrespective of the choice of the phases $\vartheta_\alpha(\mathbf{k})$.

One may now wonder whether Eqs. (2.4) and (2.5) can be derived with postulating vanishing commutators as a starting point. This can be accomplished as follows. For a given $\mathcal{G}$-symmetric Hamiltonian, there exists a set of unitary operators $D_{\hat{O}}$ which is isomorphic to the point group $\mathcal{G}$. They act on an arbitrary one-particle state $|\psi\rangle$ with wave function $\langle\mathbf{r}|\psi\rangle$ in position representation according to

$$\langle\,\mathbf{r}\,|D_{\hat{O}}|\,\psi\,\rangle = \left\langle\, R_{\hat{O}}^{-1}\mathbf{r}\,\right|\,\psi\,\rangle\,.$$

If we require the Bloch states to transform as

$$D_{\hat{O}}\,|\phi_a^\alpha(\mathbf{k})\rangle = \sum_\beta \left(M_{\hat{O}}^\dagger\right)_{\alpha,\beta}(\mathbf{k})\,\left|\phi_a^\beta(R_{\hat{O}}\mathbf{k})\right\rangle\,, \tag{2.7}$$

where the above representation matrices $M_{\hat{O}}(\mathbf{k})$ are given by

$$\left(M_{\hat{O}}(\mathbf{k})\right)_{\alpha,\beta} = \int d\mathbf{r}\;\langle R_{\hat{O}}\mathbf{r}\,|\phi_a^\alpha(R_{\hat{O}}\mathbf{k})\rangle\,\left\langle\,\phi_a^\beta(\mathbf{k})\right|\,\mathbf{r}\,\rangle$$

for arbitrary a. Under a phase transformation of the hybridizing Bloch basis, Eq. (2.6) is recovered from this formula. For a point-group symmetric model, the representation operators $D_{\hat{O}}$ commute with the Hamiltonian

$$[D_{\hat{O}}, H] = 0 \quad \forall\,\hat{O} \in \mathcal{G} \tag{2.8}$$

and with its coupling functions which are complex numbers. Consequently, the point-group symmetries must be encoded in the behavior of the field operators under

$$\Psi_a(\mathbf{k}) \to D_{\hat{O}}\,\Psi_a(\mathbf{k})\,D_{\hat{O}}^\dagger\,.$$

From Eq. (2.7), it follows that

$$D_{\hat{O}}\,\Psi_a(\mathbf{k})\,D_{\hat{O}}^\dagger = M_{\hat{O}}^\dagger(\mathbf{k})\,\Psi_a(R_{\hat{O}}\mathbf{k})\,,$$

since the vacuum reference state $|0\rangle = D_{\hat{O}}|0\rangle$ is mapped onto itself under all point-group operations. Together with Eq. (2.8), this implies the validity of Eqs. (2.4) and (2.5).

2.2.3. Basis transformations in the band language

Let us now look at the general tight-binding model of Section 2.1 in the band language, i.e. let us switch from orbitors $\Psi_a(\mathbf{k})$ to band pseudo-spinors $\boldsymbol{\chi}_a(\mathbf{k}) = u(\mathbf{k})\,\Psi_a(\mathbf{k})$. The orbital-to-band transformation $u(\mathbf{k})$ is chosen such that it renders the one-particle coupling-function

$$\mathcal{B}(\mathbf{k}) = u(\mathbf{k})\,\mathcal{H}_0(\mathbf{k})\,u^\dagger(\mathbf{k})\,,$$

diagonal. Since the eigenvalues of $\mathcal{H}_0$ will be invariant under a unitary transformation and since we have such a transformation on the right-hand side of Eq. (2.4), the band labels can be chosen such that

$$\mathcal{B}(\mathbf{k}) = \mathcal{B}(R_{\hat{O}}\mathbf{k}) \tag{2.9}$$

holds. So the point-group symmetry of the Hamiltonian already implies that the band dispersion transforms trivially under $\mathbf{k} \to R_{\hat{O}}\mathbf{k}$. In the following, the bands will always be labeled in a way that guarantees Eq. (2.9).

Let me ignore the interactions for a moment. Then different (unitary) representation matrices $\tilde{M}_{\hat{O}}(\mathbf{k})$ could have been chosen in Eq. (2.4), if

$$\tilde{M}_{\hat{O}}(\mathbf{k}) = M_{\hat{O}}(\mathbf{k})\,A_{\hat{O}}(\mathbf{k}) \tag{2.10}$$

with a unitary matrix $A_{\hat{O}}(\mathbf{k})$ commuting with $\mathcal{H}_0(R_{\hat{O}}\mathbf{k})$. Note that replacing $M_{\hat{O}}(\mathbf{k})$ by $\tilde{M}_{\hat{O}}(\mathbf{k})$ may violate the transformation rule (2.5) for $H_{\rm int}$. I will now show that the two l-dimensional representations of $\mathcal{G}$ with representation matrices $M_{\hat{O}}(\mathbf{k})$ and $\tilde{M}_{\hat{O}}(\mathbf{k})$, respectively, are connected by a basis transformation between basis sets of non-hybridizing Bloch states. Such a transformation corresponds to a different choice of the eigenvectors of $\mathcal{H}_0(\mathbf{k})$, i.e. the orbital-to-band matrix $u_{\alpha\beta}(\mathbf{k})$ is substituted by $\tilde{u}_{\alpha\beta}(\mathbf{k}) = e^{-i\varphi_\alpha(\mathbf{k})}\,u_{\alpha\beta}(\mathbf{k})$. Due to momentum conservation, the one-particle coupling function $\mathcal{B}$ in the band language remains unaffected by such transformations. This may be interpreted as an *emergent* local U(1) gauge symmetry at a Fermi liquid fixed point. [88] It should however be emphasized that, away from such a fixed point, this gauge symmetry is violated or that, in other words, the coupling functions of a non-vanishing interaction term may change under a basis transformation.

Clearly, the point-group symmetry Eq. (2.9) of the band dispersion implies

$$\mathcal{H}_0(\mathbf{k}) = u^\dagger(\mathbf{k})\,u(R_{\hat{O}}\mathbf{k})\;\mathcal{H}_0(R_{\hat{O}}\mathbf{k})\;u^\dagger(R_{\hat{O}}\mathbf{k})\,u(\mathbf{k})$$

and therefore Eq. (2.4) can be satisfied with representation matrices

$$M_{\hat{O}}(\mathbf{k}) = u^\dagger(R_{\hat{O}}\mathbf{k})\,u(\mathbf{k})\,. \tag{2.11}$$

On the other hand, changing the phase of the bands gives rise to representation matrices

$$\tilde{M}_{\hat{O}}(\mathbf{k}) = u^\dagger(R_{\hat{O}}\mathbf{k})\,P_{\hat{O}}(\mathbf{k})\,u(\mathbf{k})\,, \tag{2.12}$$

where

$$(P_{\hat{O}})_{\alpha\beta}(\mathbf{k}) = \delta_{\alpha\beta}\, e^{i\left[\varphi_\beta(R_{\hat{O}}\mathbf{k}) - \varphi_\beta(\mathbf{k})\right]}\,.$$

Being a product of unitary matrices, the $\tilde{M}_{\hat{O}}(\mathbf{k})$ are themselves unitary. It is now straightforward to show that the mapping given by Eq. (2.12) is an isomorphism between two l-dimensional representations of $\mathcal{G}$. Namely, the group law (2.3) also holds for the new representation matrices in Eq. (2.12) for arbitrary phases $\varphi_\beta(\mathbf{k})$, since

$$P_{\hat{B}}(\mathbf{k})\, P_{\hat{A}}(R_{\hat{B}}\mathbf{k}) = P_{\hat{C}}(\mathbf{k}) \quad \text{for} \quad \hat{C} = \hat{B}\hat{A}\,.$$

Furthermore, one finds that Eq. (2.10) is fulfilled for

$$A_{\hat{O}}(\mathbf{k}) = u^\dagger(\mathbf{k})\, P_{\hat{O}}(\mathbf{k})\, u(\mathbf{k})\,.$$

As far as the one-particle Hamiltonian is concerned, a basis transformation $u(\mathbf{k}) \to \tilde{u}(\mathbf{k})$ just maps a representation of $\mathcal{G}$ with matrices $M_{\hat{O}}(\mathbf{k}) = u^\dagger(R_{\hat{O}}\mathbf{k})\, u(\mathbf{k})$ onto one with matrices $\tilde{M}_{\hat{O}}(\mathbf{k}) = \tilde{u}^\dagger(R_{\hat{O}}\mathbf{k})\, \tilde{u}(\mathbf{k})$. This implies that, for any choice of the $\varphi_\beta(\mathbf{k})$, there exists an l-dimensional representation of $\mathcal{G}$, with which the orbital-to-band matrix transforms under a point-group operation, i.e.

$$\tilde{u}(\mathbf{k}) = \tilde{u}(R_{\hat{O}}\mathbf{k})\, \tilde{M}_{\hat{O}}(\mathbf{k})\,, \quad \forall\, \hat{O} \in \mathcal{G}\,.$$

The one-particle coupling function $\mathcal{H}_0(\mathbf{k})$ in the orbital language may be transformed with each of these representations under $\mathbf{k} \to R_{\hat{O}}\mathbf{k}$.

Now we are in a position to address the question of a sensible fixing of the phases of the bands in the presence of interactions. Changing these phases then replaces $M_{\hat{O}}(\mathbf{k})$ by $\tilde{M}_{\hat{O}}(\mathbf{k})$ in the transformation rule (2.4) for the one-particle Hamiltonian, but the transformation rule (2.5) for the interactions may not hold with the new representation matrices $\tilde{M}_{\hat{O}}(\mathbf{k})$ in general. A particular basis of non-hybridizing Bloch states corresponding to $u(\mathbf{k})$ shall henceforth be called *natural* if also H_{int} remains invariant under

$$\Psi_a(\mathbf{k}) \to \Psi'_a(R_{\hat{O}}\mathbf{k}) = u^\dagger(R_{\hat{O}}\mathbf{k})\, u(\mathbf{k})\, \Psi_a(\mathbf{k})$$

for all operations $\hat{O} \in \mathcal{G}$. This means that, if one finds a given Hamiltonian to transform according to Eqs. (2.4) and (2.5) with representation matrices $M_{\hat{O}}(\mathbf{k})$, in natural Bloch basis

$$u(R_{\hat{O}}\mathbf{k}) = u(\mathbf{k})\, M^\dagger_{\hat{O}}(\mathbf{k}) \tag{2.13}$$

must be fulfilled. Formally, this equation is equivalent to Eq. (2.11). However, a condition on $u(\mathbf{k})$ is imposed for given representation matrices $M_{\hat{O}}(\mathbf{k})$ here.

That such a natural basis must always exist, can be seen as follows. When $\mathcal{H}_0(R_{\hat{O}}\mathbf{k})$ in Eq. (2.4) is diagonalized, the symmetry of the band dispersion (2.9) implies that $\mathcal{H}_0(\mathbf{k})$ is as well diagonalized by $u(R_{\hat{O}}\mathbf{k})\, M_{\hat{O}}(\mathbf{k})$. The group law (2.3) then ensures that $u(R_{\hat{O}}\mathbf{k})$ is unique for given $u(\mathbf{k})$ within a natural gauge, which therefore can be identified as a

possible choice of $u(\mathbf{k})$ for given $u(R_{\hat{O}}\mathbf{k})$. If $u(\mathbf{k})$ is given at some point $\mathbf{k} = \mathbf{q}$, the group law (2.3) then ensures that, within a natural basis, $u(\mathbf{k})$ is uniquely defined on the star of $\mathbf{q}$, i.e. at $\mathbf{k} = R_{\hat{O}}\mathbf{q}\ \forall \hat{O} \in \mathcal{G}$. For a particular model, however, there are infinitely many natural bases corresponding to different l-dimensional representations that all satisfy Eqs. (2.4) and (2.5). Namely, if we start from a natural basis and perform a basis transformation

$$u_{\alpha,\beta}(\mathbf{k}) \to u_{\alpha,\beta}(\mathbf{k})\, e^{-i\varphi_\beta(\mathbf{k})}\,, \quad \text{where} \quad \varphi_\beta(R_{\hat{O}}\mathbf{k}) = \varphi_\beta(\mathbf{k}) \quad \forall\, \hat{O} \in \mathcal{G}\,,$$

the properties of a natural basis are preserved.

2.2.4. Properties of the coupling functions in a natural basis

For the examples of the Emery model and for graphene in Appendix B, one can see that, expressed in a natural basis, the coupling functions of the interaction transform trivially under all point-group operations. In this place, one may probably wonder whether this also holds for the general Hamiltonian discussed in this section. Let us therefore look at the transformation properties of the coupling functions $\mathcal{F}$ of the interaction in Eq. (2.2), substitute $\mathbf{k}_i$ by $R_{\hat{O}}\mathbf{k}_i$ and insert Eqs. (2.5) and (2.13). The representation matrices then cancel and therefore the n-particle coupling function indeed transforms trivially, i.e.

$$\mathcal{F}^{\alpha_1,\ldots,\alpha_{2n}}_{a_1,\ldots,a_{2n}}(R_{\hat{O}}\mathbf{k}_1,\ldots,R_{\hat{O}}\mathbf{k}_n;R_{\hat{O}}\mathbf{k}_{n+1},\ldots,R_{\hat{O}}\mathbf{k}_{2n}) = \mathcal{F}^{\alpha_1,\ldots,\alpha_{2n}}_{a_1,\ldots,a_{2n}}(\mathbf{k}_1,\ldots,\mathbf{k}_n;\mathbf{k}_{n+1},\ldots,\mathbf{k}_{2n})\,.$$

Consequently, the full Hamiltonian is invariant under

$$\boldsymbol{\chi}_\sigma(\mathbf{k}) \to \boldsymbol{\chi}'_\sigma(R_{\hat{O}}\mathbf{k}) = \boldsymbol{\chi}_\sigma(\mathbf{k})\,. \tag{2.14}$$

This corresponds to the trivial point-group behavior of the natural basis states

$$D_{\hat{O}}\,|\chi^\alpha_a(\mathbf{k})\rangle = |\chi^\alpha_a(R_{\hat{O}}\mathbf{k})\rangle\ , \tag{2.15}$$

which follows from Eqs. (2.7) and (2.13).

As already mentioned earlier, the above vertex functions in the Hamiltonian also directly enter in the bare action in a functional integral formulation, since the Hamiltonian has been given in a normally ordered form. One may therefore easily switch between the functional integral and the operator formalism. In a functional integral language, the invariance of the Hamiltonian under point-group transformations translates to a trivial point-group behavior of all coupling functions of the action and the generating functionals of amputated Green's function and one-particle irreducible vertices. This way, the point-group symmetry can be exploited straightforwardly in a fRG approach.

Of course, an RG flow of the self-energy may lead to a hybridization of the bands in the effective action at a lower scale λ. One may then switch to a Bloch basis with elements

that are not hybridized by the renormalized action. This corresponds to *renormalized bands* with fields

$$\boldsymbol{\eta}_a(\mathbf{k}) = u^\lambda(\mathbf{k})\, \Psi_a(\mathbf{k})$$

related to the orbitors by a scale-dependent transformation $u^\lambda(\mathbf{k})$. (Here, I have assumed that the trivial dependence of the self-energy on the additional quantum numbers a is protected by some symmetry. For example, this is the case if these a corresponds to spin-projection quantum numbers and if the model is SU(2) symmetric.) The above calculations can be repeated for the renormalized vertex functions and consequently there also exist natural bases for the renormalized bands.

Also in cases where a natural basis seems a suboptimal choice, its existence has consequences that may simplify analytical and/or numerical calculations. Let us therefore start from a natural basis with states $|\chi_a^\alpha(\mathbf{k})\rangle$ and switch to a non-natural one with states

$$|\eta_a^\alpha(\mathbf{k})\rangle = e^{i\varphi_\alpha(\mathbf{k})}\, |\chi_a^\alpha(\mathbf{k})\rangle = \boldsymbol{\eta}_a^{\alpha\dagger}(\mathbf{k})\, |0\rangle \tag{2.16}$$

and pseudo-spinor fields $\boldsymbol{\eta}_a(\mathbf{k})$. If there are degeneracies in the bands at some points, also non-hybridizing Bloch states exist that violate Eq. (2.16). Namely, at these points, the degenerate bands may get mixed. At all other points, Eq. (2.16) is of course still respected. We will refer to such a band basis as an *awkward* one. This name seems already justified since band degeneracies typically occur at singular points, and since the transformation from natural to awkward Bloch states would hence be discontinuous at the band degeneracies. (Note, however, that this does not imply the continuity of the orbital-to-band transformation for non-awkward states on the whole BZ.) In addition, awkward Bloch states may have other pathological properties, as will become clear in the following.

But let us first look at the point-group properties in non-awkward non-natural bases. Transforming Eqs. (2.14) and (2.15) according to Eq. (2.16) yields

$$D_{\hat{O}}\, |\eta_a^\alpha(\mathbf{k})\rangle = e^{i\left[\varphi_\alpha(\mathbf{k}) - \varphi_\alpha(R_{\hat{O}}\mathbf{k})\right]}\, |\eta_a^\alpha(R_{\hat{O}}\mathbf{k})\rangle\ ,$$

and

$$\boldsymbol{\eta}_a(\mathbf{k}) \to \boldsymbol{\eta}'_a(R_{\hat{O}}\mathbf{k}) = N_{\hat{O}}(\mathbf{k})\, \boldsymbol{\eta}_a(\mathbf{k})\,, \qquad \left(N_{\hat{O}}(\mathbf{k})\right)_{\alpha\beta} = \delta_{\alpha\beta}\, e^{i\left[\varphi_\alpha(R_{\hat{O}}\mathbf{k}) - \varphi_\alpha(\mathbf{k})\right]}$$

respectively. So non-awkward non-hybridizing Bloch states with arbitrarily chosen φ_α in Eq. (2.16) acquire a phase factor under a point-group operation. Hence, the representation matrices $M_{\hat{O}}(\mathbf{k})$ in the orbital language can be said to have *diagonal* counterparts $N_{\hat{O}}(\mathbf{k})$ in the band language with a non-awkward basis or, in other words, non-awkward bands transform with one-dimensional representations of the point group. At points, where the bands are non-degenerate, the latter statement is already well known (cf. Chapter 8-4 of Ref. [74]) without the notion of a natural basis. For a further discussion and an alternative proof of the existence of a natural gauge in the absence of degeneracies away from points of high symmetry, the reader shall be referred to Appendix B.3.

In a similar way as for the fields, the orbital-to-band transformation matrix v corresponding to the non-awkward states of Eq. (2.16) transforms with a phase factor according to

$$v(R_{\hat{O}}\mathbf{k}) = N_{\hat{O}}(\mathbf{k})\, v(\mathbf{k})\, M^{\dagger}_{\hat{O}}(\mathbf{k})\,,$$

which follows straightforwardly from Eq. (2.13). Together with Eqs. (2.2) and (2.5), this implies that the n-particle coupling function enjoys a rather simple point-group behavior, namely

$$\begin{aligned}
&\mathcal{F}^{\alpha_1,\ldots,\alpha_{2n}}_{a_1,\ldots,a_{2n}}(R_{\hat{O}}\mathbf{k}_1,\ldots,R_{\hat{O}}\mathbf{k}_n;R_{\hat{O}}\mathbf{k}_{n+1},\ldots,R_{\hat{O}}\mathbf{k}_{2n}) \\
&= \exp\left\{ i\sum_{j=1}^{2n} s_j \left[\varphi_{\alpha_j}(R_{\hat{O}}\mathbf{k}_j) - \varphi_{\alpha_j}(\mathbf{k}_j)\right]\right\} \mathcal{F}^{\alpha_1,\ldots,\alpha_{2n}}_{a_1,\ldots,a_{2n}}(\mathbf{k}_1,\ldots,\mathbf{k}_n;\mathbf{k}_{n+1},\ldots,\mathbf{k}_{2n}) \qquad (2.17)\\
&= \sum_{\beta_1,\ldots,\beta_{2n}} \left[\prod_{j=1}^{n} (N_{\hat{O}})_{\alpha_j,\beta_j}(\mathbf{k}_j) \left(N^{\dagger}_{\hat{O}}\right)_{\beta_{j+n},\alpha_{j+n}}(\mathbf{k}_{j+n})\right] \mathcal{F}^{\beta_1,\ldots,\beta_{2n}}_{a_1,\ldots,a_{2n}}(\mathbf{k}_1,\ldots,\mathbf{k}_n;\mathbf{k}_{n+1},\ldots,\mathbf{k}_{2n})\,,
\end{aligned}$$

where $s_j = +1$ for $j \leq n$ and $s_j = -1$ for $j > n$. The non-natural basis sets for the Emery model and graphene given in Appendix B.1.3 and B.2.2, respectively, are non-awkward and hence enjoy these properties.

If one finds a way how to deal with the phases in Eq. (2.17), it may also be convenient to work in a non-awkward, non-natural basis. This approach was pursued in fRG studies [34–40, 42, 44] of multiband models with Fermi surface patching. In awkward bases, Eq. (2.17) would be violated at points with band degeneracies *away* from the origin (or at other points of high symmetry), justifying the name chosen for those bases. In practice, working in a non-natural band basis may hence require a careful treatment of such band degeneracies. If there is only a degeneracy at the origin, the transformation rule in Eq. (2.17) still holds, since it is trivially fulfilled at this point.

2.2.5. Construction of a natural Bloch basis

Having established these results, I will now comment on more practical aspects of a natural fixing of the phases of the bands for a given model. In doing so, one has to fix l phases, one for each band. In contrast, the condition (2.13) for a natural basis corresponds to l^2 constraints for l variables. Hence, there must be some redundancy, as a natural basis must exist as shown above. (The reason for this redundancy lies in the diagonalizability of $u(\mathbf{k})$, which therefore has only l *independent* entries.)

If no zeros appear in $u(\mathbf{k})$, the phases of the band can be fixed to a natural basis by taking an arbitrary row in Eq. (2.13), i.e. by choosing an arbitrary orbital index. For the example of graphene, the orbital-to-band matrix has no zeros and hence one may proceed in this way. In the case of the Emery model without oxygen-oxygen hopping,

however, the flat band has no d-orbital component and hence the first row of Eq. (2.13) only fixes the phases of the other bands. If one allows for oxygen-oxygen hopping, as in Chapter 3.2, the situation is different. Then there is no pure p-band any more, and all entries in $u_{\alpha 1}(\mathbf{k})$ are non-zero except at the origin, were Eq. (2.13) is trivial. The first line $u_{\beta 1}(R_{\hat{O}}\mathbf{k}) = u_{\beta 1}(\mathbf{k})$ can then be fulfilled by requiring

$$u_{\beta 1}(\mathbf{k}) \ \in \mathbb{R}, > 0 \quad \forall \beta, \mathbf{k}\,,$$

as the u can be chosen real.

For the general case, the following construction scheme seems appropriate.

i) Select a minimal sector $\mathbb{S}$ of the BZ $\mathbb{B}$, i.e. the smallest set of points from which $\mathbb{B}$ can be generated according to

$$\mathbb{B} = \left\{ \mathbf{p} \,\middle|\, \mathbf{p} = R_{\hat{O}}\mathbf{q}, \mathbf{q} \in \mathbb{S}, \hat{O} \in \mathcal{G} \right\} .$$

For C_{4v}, for example, $\mathbb{S}$ corresponds to 1/8 of the BZ.

ii) Choose the band phases in the orbital-to-band transformation $u(\mathbf{k})$ arbitrarily on $\mathbb{S}$.

iii) Determine $u(R_{\hat{O}}\mathbf{k})$ from $u(\mathbf{k})$ for $\mathbf{k} \in \mathbb{S}$ via Eq. (2.13). Since $M_{\hat{O}}(\mathbf{k}) = 1$ for $\hat{O}\mathbf{k} = \mathbf{k}$, this scheme is free of inconsistencies.

Let us now have a brief look at the locality of the basis states, which plays an important role in dynamical mean-field theory and its extensions. Under a transformation from a non-natural to a natural Bloch basis, there seems to be no generic tendency in the localization properties of the corresponding (non-hybridizing) Wannier states. These latter states are simply obtained from the respective Bloch basis by a Fourier transformation. A fast decay of the hopping parameters with increasing distance may be regarded as a hallmark of their locality. Since the band dispersion is invariant under this transformation, the coefficients of its hopping-parameter expansion remain unaffected, and the localization properties seem not to change much in this picture.

2.3. Effective action for low-energy modes

Now the foundations are laid for proceeding towards an effective one-band action for modes near the Fermi level. This implies integrating out high-energy modes. From now on, I will work in the functional integral language with a general multiband action $\mathcal{A}$. For the remainder of this chapter, the above discussed point-group symmetries are of minor importance, but may become helpful when the expressions given in the following are evaluated.

2.3.1. Integrating out high-energy modes

Consider first the generating functional W of the connected Green's functions

$$W[\bar{\eta},\eta] = -\ln\left[\int \mathcal{D}(\bar{\chi},\chi)\, e^{-\mathcal{A}[\bar{\chi},\chi]} e^{(\bar{\eta},\chi)+(\bar{\chi},\eta)}\right]$$

with source fields η. Since the focus is on the low-energy properties of the system, the upper-band components of these sources can then be set to zero, *before* derivatives with respect to the source fields are taken. In the band language, the fermionic fields and the quadratic part $\mathcal{A}^{(2)}$ of the action can be decomposed into low and high-energy parts

$$\mathcal{A}^{(2)}[\bar{\chi},\chi] = (\bar{\chi}, D\chi) = (\bar{\chi}_+, D_+\chi_+) + (\bar{\chi}_-, D_-\chi_-)\,,$$

with

$$\chi = \chi_+ + \chi_-\,, \quad D = D_+ + D_-\,.$$

Therefore, the covariance splitting formula [58] applies, which gives rise to the following form of the one-band effective action $\mathcal{A}_{\text{eff}}$ for the low-energy modes

$$\begin{aligned}\mathcal{A}_{\text{eff}}[\bar{\chi}_-,\chi_-] &= (\bar{\chi}_-, D_-\chi_-) + \mathcal{V}[\bar{\chi_-},\chi_-]\,,\\ e^{-\mathcal{V}[\bar{\chi_-},\chi_-]} &= \int \mathcal{D}(\bar{\chi}_+,\chi_+)\, e^{-(\bar{\chi}_+, D_+\chi_+)}\, e^{-\mathcal{A}^{(4)}[\bar{\chi}_+ + \bar{\chi}_-, \chi_+ + \chi_-]}\,,\end{aligned} \tag{2.18}$$

which leads to

$$W[\bar{\eta}_-,\eta_-] = -\ln\left[\int \mathcal{D}(\bar{\chi}_-,\chi_-)\, e^{-\mathcal{A}_{\text{eff}}[\bar{\chi}_-,\chi_-]}\, e^{(\bar{\eta}_-,\chi_-)+(\bar{\chi}_-,\eta_-)}\right].$$

The effective interaction $\mathcal{V}$ contains a functional integral over the high-energy part of the fields with measure $\mathcal{D}(\bar{\chi}_+,\chi_+)$ and corresponds to the generating functional of amputated connected Greens functions, as used in the Polchinski renormalization group scheme [89] (for comprehensive reviews of the various generating functionals in the fRG context, see e.g. Refs. [20, 90, 91]). This means that the parameters of the effective low-energy action are given by these amputated connected Green's functions. In the special case of Eq. (2.18), however, only the high-energy modes have been integrated out. Thus, in the diagrammatic expansion of the expansion coefficients in the low-energy fields χ_- and $\bar{\chi}_-$, the propagators on internal lines are restricted to the high-energy sector, whereas external legs live at low energies. Before commenting on viable approximations for $\mathcal{A}_{\text{eff}}$, I would like to recall that the amputated connected Greens functions can be recovered from one-particle irreducible (1PI) diagrams by drawing all tree diagrams with 1PI vertices. In the present case, the internal lines of these tree diagrams are high-energy propagators.

For assessing the low-energy properties of a multiband model, the following seems appealing as a general strategy. In a first step, $\mathcal{A}_{\text{eff}}$ is calculated. Since the Fermi surface

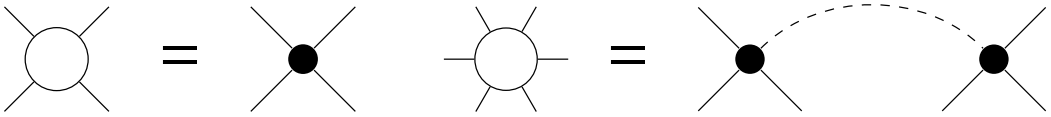

(a) Two-particle vertex (b) Three-particle vertex

Figure 2.1.: Two- (a) and three-particle vertex (b) of $\mathcal{A}_{\text{eff}}$ for the effective one-band model as considered in the three-particle truncation. Small filled vertices correspond to the bare interaction $\mathcal{A}^{(4)}$, whereas the vertices of $\mathcal{A}_{\text{eff}}$ on the left hand sides are denoted by empty circles. Solid lines represent low and dashed lines high-energy modes. There are no propagators attached to the external legs. Self-energy effects will be neglected.

does not intersect with the bands in the high-energy sector, the diagrams that appear in Eq. (2.18) need no infrared regularization and therefore the low-energy effective action can be evaluated perturbatively for sufficiently small values of the bare interaction. In a second step, the effective action for the low-energy modes is treated by a method of choice – in this thesis the fRG. The bare low-energy action $\mathcal{A}_{\text{eff}}$ then imposes an initial condition on the RG flow.

For an instability analysis, the effective interaction of the low-energy model is the object of prime interest. The simplest truncation of the effective action would then consist in dropping all three-particle and higher terms. Then the four-point term $\mathcal{A}^{(4)}_{\text{eff}}$ in the effective action can be computed in perturbation theory in the interactions with high-energy legs. In lowest order, i.e. in zeroth order in the interactions with high-energy legs or first order in the bare interactions irrespective of energy scales, $\mathcal{A}^{(4)}_{\text{eff}}$ is just the bare interaction of the fields in the low-energy sector, decorated with orbital makeup. In the following, this truncation will be called *conventional*. It is the standard that has been employed e.g. in all fRG studies of unconventional pairing in the iron pnictides so far, and it is used implicitly if the one-band Hubbard model is chosen as a description for the high-T_c cuprates. Since solving the conventionally truncated low-energy theory diagrammatically captures (possibly singular) diagrams with both internal lines in the low-energy window, it appears to be the simplest truncation suited for an RG instability analysis.

In next order, i.e. second order in the bare high-energy interactions, one gets various diagrams. On one hand, there are self-energy Hartree- and Fock-like contributions on the external legs. Further, there are one-loop corrections with both lines in the high-energy sector. As already mentioned, these are non-singular one-loop terms, since all internal lines lie significantly away from the Fermi level. I will call the scheme that keeps these terms the *high-energy perturbation theory* (hePT) truncation. In an attempt to solve the low-energy theory diagrammatically, one will capture one-loop corrections for the effective interaction that have both propagator lines in the high-energy sector and that are already included in $\mathcal{A}^{(4)}_{\text{eff}}$, and corrections with both lines in the low-energy

sector, coming from the perturbation expansion in $\mathcal{A}_{\text{eff}}^{(4)}$. What is not included are 'mixed' diagrams with one internal line in the high-energy sector and one line in the low-energy window. Looking at the energy denominators of these lines, these excluded mixed contributions should be potentially more important than those with two internal high-energy propagators captured in the hePT truncation.

One could now go on and include further orders in the bare interactions as corrections to $\mathcal{A}_{\text{eff}}^{(4)}$. It is however clear that, in these higher-order diagrams, all internal lines will be high-energy propagators. Hence, these corrections do not include the missing mixed diagrams, and thus I will not proceed in discussing these corrections any further here. In principle, they can be summed up using RG schemes, as described in Ref. [92].

So the next useful extension should follow another path in improving the truncation of the effective action. Hence, the three-particle term in the effective action shall now be kept. In the tree-diagram expansion of $\mathcal{A}_{\text{eff}}$, such a three-particle term is generated in second order in the 1PI two-particle vertices of the high-energy model. Here those 1PI vertices will be replaced by the lowest order, i.e. by the bare interactions, as shown in Fig. 2.1(b). This means that possible high-energy renormalizations of the two-particle interactions by additional high-energy processes are deliberately excluded. As argued above, these corrections with additional high-energy propagators should however be smaller due to the energy separation of the bands. I will call this approximation level *three-particle* truncation. Furthermore, one may drop self-energy corrections in order to avoid double counting of some contributions that are already included in *ab initio* calculated values for the parameters of the model. In this approximation, the quadratic part and the bare two-particle couplings remain unrenormalized, whereas a three-particle term depicted in Fig. 2.1(b) is generated. For the effective action, one then obtains

$$\begin{aligned}
\mathcal{A}_{\text{eff}}[\bar{\chi}_-, \chi_-] &= \left(\mathcal{A}^{(2)} + \mathcal{A}^{(4)}\right)[\bar{\chi}_-, \chi_-] + \mathcal{A}_{\text{eff}}^{(6)}[\bar{\chi}_-, \chi_-] \\
\mathcal{A}_{\text{eff}}^{(6)}[\bar{\chi}_-, \chi_-] &= -\frac{1}{36}\int d\xi_1 \ldots d\xi_6 \; F^{(6)}(\boldsymbol{\xi})\, \bar{\chi}_-(\xi_1)\bar{\chi}_-(\xi_2)\bar{\chi}_-(\xi_3)\chi_-(\xi_4)\chi_-(\xi_5)\chi_-(\xi_6)\,,
\end{aligned}$$

$\xi_i = (k_i, \sigma_i)$ being a short-hand notation for the quantum numbers of the fields. The precise form of the six-point coupling function $F^{(6)}$ will be given in Eq. (2.21) in Section 2.4.2. Now, if the low-energy theory was treated perturbatively, one would obtain contributions with two legs of the three-particle vertex folded together by a low-energy propagator line. As the three-particle term came about by joining two legs of two two-particle interactions by a high-energy propagator line, this will effectively bring in those missing diagrams with two internal propagators – one in the high-energy and one in the low-energy sector.

Let me note in passing that the constrained RPA method used for computing effective Hubbard interaction parameters [93, 94] can be understood as an infinite order resummation of the mixed diagrams included in the three-particle truncation. Resummation within hePT, i.e. without any internal lines in the low-energy sector, would presumably

result in much less reduction of the on-site repulsion. On the other hand, just keeping the three-particle term still does not capture the full cRPA series, as pure powers of mixed loops (i.e. bubbles with one high-energy and one low-energy line) included in the cRPA are not contained in the RPA series generated from the three-particle truncation of the effective action. This can be seen from constructing bubble sums with the elements of Fig. 2.1(b) by contracting low-energy lines. There is a mixed diagram in second order in the bare interactions, but in third order or fourth order one has to add a pure low-energy loop between two mixed loops. So, while some orders in the mixed diagrams are still missing, including the three-particle term seems to lead in the right direction. On the other hand, in contrast to the cRPA, the three-particle truncation does not neglect vertex corrections or particle-particle diagrams. The question how the cRPA series is to be understood in terms of the effective action has recently been discussed by C. Honerkamp in Ref. [95]. In that publication, the cRPA is extended to a multi-channel constrained fRG method within the Wick-ordered scheme.

2.3.2. Parametrization of multiband interactions

In order to make progress, the interaction term $\mathcal{A}^{(4)}$ of the bare multiband action should be parametrized in a way that distinguishes between high- and low-energy modes. This will then allow for giving explicit expressions for the vertex functions of the effective low-energy action $\mathcal{A}_{\text{eff}}$.

Upon the orbital-to-band transformation, the coupling function in the orbital language gets multiplied by a product of wavevector-dependent transformation matrix elements $u_{\alpha,\beta}(\mathbf{k})$, which decorates the interaction with orbital makeup. $\mathcal{A}^{(4)}$ is now rewritten in terms of the fields χ in the band language

$$\mathcal{A}^{(4)}[\bar{\chi},\chi] = \frac{1}{4}\sum_{\{X_i\}} F(X_1,X_2,X_3,X_4)\ \bar{\chi}(X_1)\,\bar{\chi}(X_2)\,\chi(X_3)\,\chi(X_4)$$

and the interaction is decomposed according to the band indices of the external legs. Since only models with one conduction band are discussed in this thesis, the band indices for the low-energy modes will be suppressed in the notation.

This yields

$$
\begin{aligned}
F(X_1,X_2,X_3,X_4) = \mathfrak{A}_{X_1,X_2}\mathfrak{A}_{X_3,X_4}\Bigg[& F_4(\xi_1,\xi_2,\xi_3,\xi_4)\,\delta_{\boldsymbol{\alpha},0000} + \sum_{\boldsymbol{\beta}} F_0^{\boldsymbol{\beta}}(\xi_1,\xi_2,\xi_3,\xi_4)\,\delta_{\boldsymbol{\alpha},\boldsymbol{\beta}} \\
& + \sum_{\beta_1,\beta_2} F_{2\to 0}^{\beta_1,\beta_2}(\xi_1,\xi_2,\xi_3,\xi_4)\,\delta_{\boldsymbol{\alpha},(\beta_1,\beta_2,0,0)} \\
& + \sum_{\beta_3,\beta_4} F_{0\to 2}^{\beta_3,\beta_4}(\xi_1,\xi_2,\xi_3,\xi_4)\,\delta_{\boldsymbol{\alpha},(0,0,\beta_3,\beta_4)} \\
& + \sum_{\beta_2,\beta_3} 4F_{1\to 1}^{\beta_2,\beta_3}(\xi_1,\xi_2,\xi_3,\xi_4)\,\delta_{\boldsymbol{\alpha},(0,\beta_2,\beta_3,0)} \\
& + \sum_{\beta} 2F_{2\to 1}^{\beta}(\xi_1,\xi_2,\xi_3,\xi_4)\,\delta_{\boldsymbol{\alpha},(\beta,0,0,0)} \\
& + \sum_{\beta_2,\beta_3,\beta_4} 2F_{0\to 1}^{\beta_2,\beta_3,\beta_4}(\xi_1,\xi_2,\xi_3,\xi_4)\,\delta_{\boldsymbol{\alpha},(0,\beta_2,\beta_3,\beta_4)} \\
& + \sum_{\beta} 2F_{1\to 2}^{\beta}(\xi_1,\xi_2,\xi_3,\xi_4)\,\delta_{\boldsymbol{\alpha},(0,0,0,\beta)} \\
& + \sum_{\beta_1,\beta_2,\beta_3} 2F_{1\to 0}^{\beta_1,\beta_2,\beta_3}(\xi_1,\xi_2,\xi_3,\xi_4)\,\delta_{\boldsymbol{\alpha},(\beta_1,\beta_2,\beta_3,0)}\Bigg]\,,
\end{aligned}
$$

where ξ_i denotes (k_i,σ_i) and $X_i = (\alpha_i,\xi_i)$ and where the two-point antisymmetrization operator $\mathfrak{A}$ has been defined as $\mathfrak{A}_{a,b}f(a,b) = [f(a,b) - f(b,a)]/2$.

Hermiticity of the Hamiltonian in the band language requires that the terms F_4, F_0, $F_{1\to 1}$ must obey

$$
\begin{aligned}
F_4(\xi_1,\xi_2,\xi_3,\xi_4) &= F_4^*(\xi_4,\xi_3,\xi_2,\xi_1) \\
F_0^{\boldsymbol{\beta}}(\xi_1,\xi_2,\xi_3,\xi_4) &= F_0^{\tilde{\boldsymbol{\beta}}^*}(\xi_4,\xi_3,\xi_2,\xi_1) \\
F_{1\to 1}^{\beta_2,\beta_3}(\xi_1,\xi_2,\xi_3,\xi_4) &= F_{1\to 1}^{\beta_3,\beta_2\,*}(\xi_4,\xi_3,\xi_2,\xi_1)\,,
\end{aligned}
\tag{2.19}
$$

where $\tilde{\boldsymbol{\beta}} = (\beta_4,\beta_3,\beta_2,\beta_1)$. For the other terms, one obtains the following relations:

$$
\begin{aligned}
F_2^{\beta,\gamma}(\xi_1,\xi_2,\xi_3,\xi_4) :&= F_{0\to 2}^{\beta,\gamma}(\xi_1,\xi_2,\xi_3,\xi_4) = F_{2\to 0}^{\gamma,\beta\,*}(\xi_4,\xi_3,\xi_2,\xi_1) \\
F_3^{\beta}(\xi_1,\xi_2,\xi_3,\xi_4) :&= F_{2\to 1}^{\beta}(\xi_1,\xi_2,\xi_3,\xi_4) = F_{1\to 2}^{\beta\,*}(\xi_4,\xi_3,\xi_2,\xi_1) \\
F_1^{\beta_1,\beta_2,\beta_3}(\xi_1,\xi_2,\xi_3,\xi_4) :&= F_{1\to 0}^{\beta_1,\beta_2,\beta_3}(\xi_1,\xi_2,\xi_3,\xi_4) = F_{0\to 1}^{\beta_3,\beta_2,\beta_1\,*}(\xi_4,\xi_3,\xi_2,\xi_1)\,.
\end{aligned}
$$

Moreover, the antisymmetry constraint

$$
F_X(\xi_1,\xi_2,\xi_3,\xi_4) = -F_X(\xi_2,\xi_1,\xi_3,\xi_4) = -F_X(\xi_1,\xi_2,\xi_4,\xi_3)
$$

for $X = 4,0,2$ reflects the anticommuting nature of the Grassmann fields. Let me now introduce the shorthand notations

$$
D_{\boldsymbol{\sigma}} = \delta_{\sigma_1,\sigma_4}\delta_{\sigma_2,\sigma_3} \qquad \text{and} \qquad E_{\boldsymbol{\sigma}} = \delta_{\sigma_1,\sigma_3}\delta_{\sigma_2,\sigma_4}
$$

for the spin dependence of SU(2) invariant vertices and

$$\delta_k = \delta\left(k_1 + k_2 - k_3 - k_4\right)$$

for the δ-function which ensures energy and momentum conservation. According to Eq. (1.6), the coupling functions F_X with $X = 0, 2, 4$ can be written as

$$F_X(\xi_1, \xi_2, \xi_3, \xi_4) = \delta_k \left[E_{\boldsymbol{\sigma}} V_X(k_2, k_1, k_3) - D_{\boldsymbol{\sigma}} V_X(k_1, k_2, k_3)\right] , \tag{2.20}$$

with the constraint $V_X(k_1, k_2, k_3) = V_X(k_2, k_1, k_3 - k_1 - k_2)$ arising from the Pauli principle. For vertices with three legs in the high-energy sector and one band at low energies, however, one of the symmetry constraints is violated and one only has $F_3(\xi_1, \xi_2, \xi_3, \xi_4) = -F_3(\xi_1, \xi_2, \xi_4, \xi_3)$. This still allows for the parameterization

$$F_3^{\beta}(\xi_1, \xi_2, \xi_3, \xi_4) = \delta_k \left[E_{\boldsymbol{\sigma}} V_3^{\beta}(k_1, k_2, k_4) - D_{\boldsymbol{\sigma}} V_3^{\beta}(k_1, k_2, k_3)\right] ,$$

but now, in contrast to the vertices V_X considered before, a Pauli-principle constraint for V_3 is absent. Similarly, one may parametrize the vertices with one leg at low energies and the other three ones in the high-energy sector

$$F_1^{\beta_1,\beta_2,\beta_3}(\xi_1, \xi_2, \xi_3, \xi_4) = \delta_k \left[E_{\boldsymbol{\sigma}} V_1^{\beta_1,\beta_2,\beta_3}(k_1, k_2, k_4) - D_{\boldsymbol{\sigma}} V_1^{\beta_1,\beta_2,\beta_3}(k_1, k_2, k_3)\right] .$$

Finally, there are no antisymmetry relations for $F_{1\to1}$, which gives rise to the parameterization

$$F_{1\to1}^{\beta,\gamma}(\xi_1, \xi_2, \xi_3, \xi_4) = \delta_k \left[E_{\boldsymbol{\sigma}} V_{1\to1,E}^{\beta,\gamma}(k_1, k_2, k_3) - D_{\boldsymbol{\sigma}} V_{1\to1,D}^{\beta,\gamma}(k_1, k_2, k_3)\right] .$$

2.4. Three-particle feedback

Let me now return to the issue of the diagrams with mixed loops. As argued above, dropping all effective interactions higher than the two-particle (four-point) term ignores these possibly important contributions. Therefore, the effective action $\mathcal{A}_{\text{eff}}$ for the low-energy modes should also be considered in the three-particle truncation. In the following, I will discuss how a an extension of the fRG level-two truncation can bring in the missing mixed diagrams.

Starting from the exact flow equation (1.2) for the generating functional Γ_- of the one-particle irreducible (1PI) vertex functions related to $W[\bar{\eta}_-, \eta_-]$ by a Legendre transformation in the low-energy fields, one obtains an infinite hierarchy of differential equations for the 1PI vertices as described in Chapter 1.1.2. The subscript of Γ_- reminds us that only low-energy degrees of freedom are integrated out, while the high-energy modes have been absorbed in the initial conditions. At this point, I would like to point out that

there is no simple relation between Γ_- and the Legendre transform Γ of $W[\bar{\eta}, \eta]$. In the former case, information about correlations in the high-energy sector is lost and the one-particle irreducibility only holds regarding propagators in the low-energy sector. In the latter, namely the full multiband case, however, the band-index summation on the internal lines of 1PI diagrams runs over all bands.

In order to make progress, the hierarchy of flow equations needs to be truncated at some point. In the conventional truncation scheme, one neglects the three-particle vertex completely [58]. In the so-called Katanin scheme [71] three-particle contributions that are generated during the RG flow are partly fed back into the flow equation for the two-particle vertex. Both established truncation schemes are however not suited for a non-vanishing initial three-particle vertex. So its impact on the flow poses a conceptually new problem.

2.4.1. General remarks

In an fRG flow, keeping track of the three-particle term in arbitrary order in the bare interactions or even of higher terms are hard tasks that have recently been addressed in the context of the Wick-ordered scheme [95]. But still, the numerical integration of the resulting flow equations for realistic models can be excessively demanding in practice. Therefore, a simpler fRG truncation scheme beyond the conventional level-two truncation shall be used in the following. The approximations underlying this scheme are neglecting four-particle and higher interactions and assuming that the three-particle vertex does not flow in the weak coupling regime. Then the three-particle interaction is just given by the product of two 1PI two-particle vertices, connected by a high-energy propagator as depicted in the diagram Fig. 2.1(b). If the three-particle vertex is then fed back into the two-particle flow equation for the low-energy theory, the missing diagrams appear on the right-hand side with one high-energy and one single-scale low-energy line as shown in Fig. 2.2. In this truncation, two-loop contributions are neglected. Note that in Refs. [51, 96] also two-loop terms have been considered. However, that has only been done for the case of an initially vanishing three-particle vertex and purely local bare interactions.

Before deriving the flow equations in this truncation, I will qualitatively discuss the first two diagrams in Fig. 2.2, which constitute the feedback term. Their precise form shall be given the following subsection. Strikingly, the diagrams with self-energy insertions in Fig. 2.2 get disconnected when the high-energy line is cut. But this should not lead to confusion. Since we are dealing with an effective low-energy action, one-particle irreducibility only holds regarding lines on the low-energy modes. If self-energy effects are neglected, the extra term in the flow equation for the two-particle vertex is just identical to the scale derivative of the sum of second-order diagrams in the bare interaction that

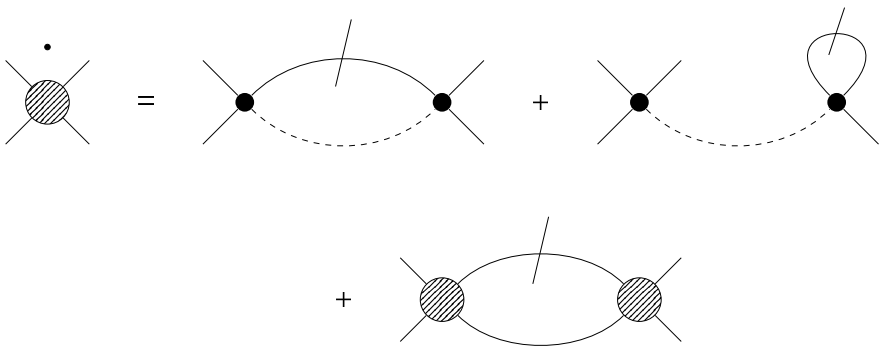

Figure 2.2.: Effective flow equation in the low-energy problem for the one-particle irreducible two-particle vertex including the feedback term re-expressed in terms of the bare couplings. The dashed line stands for propagators in the upper band.

have one internal line in the high-energy sector and another in the low-energy sector. In the infrared, these diagrams stay regular but will be larger compared to second-order diagrams with all internal lines in the high-energy sector provided that the high-energy modes are sufficiently gapped. I will therefore neglect those smaller hePT diagrams and restrict the terms in the effective interactions to the tree level in the high-energy modes.

In the following, three levels of approximation are distinguished:

1. Ignoring the three-particle vertex completely. In this approximation the only multiband effects are the signatures of orbital makeup. In the following, it will be referred to as the *conventional* truncation of the RG flow equations.

2. Including the *three-particle feedback* (3PF) term in one-loop fRG and using the flow equation depicted in Fig. 2.2.

3. Adding the mixed-band diagrams in the limit $\lambda \to 0$ to the initial condition for the flow of the low-energy model. This approximation will henceforth be referred to as *constrained perturbation theory* (cPT). It may be regarded as a simplification of the 3PF truncation that is easier to handle numerically. This simplification should be applicable if the mixed diagrams are already close to their infrared value at scales at which the lower-band diagrams only have induced a small renormalization of the initial couplings.

In Chapter 3.1.4, the fRG results in these three approximation will be compared. If one recalls that the LDA-derived dispersion of the two-orbital model underlying those calculations already contains interaction effects on a certain level, the band-flip self-energy insertion diagram (second term on the right hand side in the diagrammatic equation in Fig. 2.2) should potentially be neglected in order to avoid double counting. Its impact

is however not important, as will be commented on at the end of Chapter 3.1.4.

2.4.2. Leading one-loop corrections to the level-two flow equations

Now I derive the leading one-loop corrections to the level-two RG flow equations in the symmetric phase following the prescription given in the preceeding subsection. Self-energy effects will be neglected as well as the the flow of the three-particle vertex. Therefore, only the two-particle flow equation matters here. Let me recapitulate that the fRG is applied as a low-energy solver after the high-energy modes have been integrated out. So if the three-particle function was ignored, the flow of the effective two-particle vertex $F_4(\xi_1, \xi_2, \xi_3, \xi_4)$ is governed by the flow equation Eq. (1.5) where $f = F_4$.

If the three-particle feedback is taken into account in as a further step, a new term δF_4 appears, i.e.

$$\begin{aligned}\partial_\lambda F_4(\xi_1, \xi_2, \xi_3, \xi_4) = \mathcal{F}_{\mathrm{pp}}(\xi_1, \xi_2, \xi_3, \xi_4) + \mathcal{F}_{\mathrm{ph}}(\xi_1, \xi_2, \xi_3, \xi_4) - \mathcal{F}_{\mathrm{ph}}(\xi_1, \xi_2, \xi_4, \xi_3) \\ + \delta F_4(\xi_1, \xi_2, \xi_3, \xi_4)\,, \\ \delta F_4(\xi_1, \xi_2, \xi_3, \xi_4) = -\frac{1}{2}\int d\eta_1\, d\eta_2\; S(\eta_1, \eta_2)\, F^{(6)}(\eta_1, \xi_1, \xi_2, \eta_2, \xi_3, \xi_4)\,,\end{aligned}$$

S denoting the single-scale propagator $S = \dot{G} - G\dot{\Sigma}G$ with self-energy Σ. Since we are in the symmetric phase, these correction terms can as well be parametrized as

$$\begin{aligned}\delta F_4(\xi_1, \xi_2, \xi_3, \xi_4) = [\delta V_4(k_1, k_2, k_3)\, \delta_{\sigma_1,\sigma_4}\delta_{\sigma_2,\sigma_3} - \delta V_4(k_2, k_1, k_3)\, \delta_{\sigma_1,\sigma_3}\delta_{\sigma_2,\sigma_4}] \\ \times\, \delta(k_1 + k_2 - k_3 - k_4)\,.\end{aligned}$$

according to Eq. (1.6), i.e. δV_4 appears as a correction to V_4 in the flow equations (1.7-1.9). The three-particle term $F^{(6)}$ stems two two-particle vertices F_3^β each with one high-energy and three low-energy legs, which are connected by a high-energy line with band index β. In the following, the coupling functions V_4 and V_3^β are assumed to be real as in the case of the models discussed in the next chapter. In second order in the bare interaction, the three-particle coupling function is given by

$$\begin{aligned}F^{(6)}(\xi_1 \ldots \xi_6) = -9\, \mathfrak{A}_{\xi_1,\xi_2,\xi_3}\mathfrak{A}_{\xi_4,\xi_5,\xi_6} \sum_\beta \int d\eta_1\, d\eta_2\; G_{+\beta}(\eta_1, \eta_2)\, F_3^\beta(\eta_1, \xi_2, \xi_4, \xi_5) \\ \times\, F_3^\beta(\eta_2, \xi_6, \xi_3, \xi_1)\,, \qquad (2.21)\end{aligned}$$

where $G_{+\beta}$ denotes the propagator for the high-energy modes and where the three-point antisymmetrization operator

$$\mathfrak{A}_{a,b,c} f(a, b, c) = \frac{1}{3!}\sum_\pi P_\pi\, f\,(\pi(a), \pi(b), \pi(c))\,.$$

is given by the difference of the sums of cyclic ($P_\pi = 1$) and anti-cyclic ($P_\pi = -1$) permutations π. These antisymmetrization operators give rise to self-energy insertion and one-loop diagrams $\delta F_4 = \delta f_{\mathrm{SE}} + \delta f_{\mathrm{loop}}$. The former contain the *band-flip self-energy*

$$\Sigma_{\pm,\beta}(\xi_1,\xi_2) = \delta(\xi_1-\xi_2)\int d\eta_1\, d\eta_2\, F_3^\beta(\xi_1,\eta_1,\eta_2,\xi_2)\, S(\eta_1,\eta_2)$$

and read as

$$\delta f_{\mathrm{SE}}(\xi_1,\xi_2,\xi_3,\xi_4) = \sum_\beta \int d\eta_3\, d\eta_4\, G_+(\eta_3,\eta_4)\Big[\mathfrak{A}_{\xi_1,\xi_2} F_3^\beta(\eta_3,\xi_2,\xi_3,\xi_4)\,\Sigma_{\pm,\beta}(\eta_4,\xi_1) + \mathfrak{A}_{\xi_3,\xi_4} F_3^\beta(\eta_4,\xi_3,\xi_2,\xi_1)\,\Sigma_{\pm,\beta}(\eta_3,\xi_4)\Big]\,.$$

Due to symmetries, this expression can again be parameterized as

$$\delta f_{\mathrm{SE}}(\xi_1,\xi_2,\xi_3,\xi_4) = \delta_k\,\left[E_{\boldsymbol{\sigma}}\, V_{\mathrm{SE}}(k_2,k_1,k_3) - D_{\boldsymbol{\sigma}}\, V_{\mathrm{SE}}(k_1,k_2,k_3)\right]\,,$$

where V_{SE} is subject to the same symmetry constraint

$$V_{\mathrm{SE}}(k_1,k_2,k_3) = V_{\mathrm{SE}}(k_2,k_1,k_1+k_2-k_3)$$

as V. With the short-hand notation

$$\tilde\Sigma_\beta^\pm(k) = G_{+\beta}(k)\int dq\, S(q)\left[V_3^\beta(k,q,k) - 2V_3^\beta(k,q,q)\right]\,,$$

one obtains

$$\begin{aligned} V_{\mathrm{SE}}(k_1,k_2,k_3) = \sum_\beta\; & V_3^\beta(k_1,k_2,k_3)\,\tilde\Sigma_\beta^\pm(k_1) + V_3^\beta(k_2,k_1,k_1+k_2-k_3)\,\tilde\Sigma_\beta^\pm(k_2) \\ & + V_3^\beta(k_1+k_2-k_3,k_3,k_2)\,\tilde\Sigma_\beta^\pm(k_1+k_2-k_3) \\ & + V_3^\beta(k_3,k_1+k_2-k_3,k_1)\,\tilde\Sigma_\beta^\pm(k_3)\,. \end{aligned}$$

The one-loop part, which is also parametrized as

$$\delta f_{\mathrm{loop}}(\xi_1,\xi_2,\xi_3,\xi_4) = \delta_k\,\left[E_{\boldsymbol{\sigma}}\, V_{\mathrm{loop}}(k_2,k_1,k_3) - D_{\boldsymbol{\sigma}}\, V_{\mathrm{loop}}(k_1,k_2,k_3)\right]$$

comprises particle-particle, crossed and direct particle-hole diagrams

$$V_{\mathrm{loop}}(k_1,k_2,k_3) = \mathcal{R}_{\mathrm{pp}}(k_1,k_2,k_3) + \mathcal{R}_{\mathrm{ph}}^{\mathrm{cr}}(k_1,k_2,k_3) + \mathcal{R}_{\mathrm{ph}}^{\mathrm{d}}(k_1,k_2,k_3)\,. \tag{2.22}$$

Since V_3 obeys no symmetry constraint, the particle-particle contribution

$$\mathcal{R}_{\mathrm{pp}}(k_1,k_2,k_3) = -\sum_\beta \int dq\, S(q)\, G_{+\beta}(l-q)\Big[V_3^\beta(l-q,q,k_1)\,V_3^\beta(l-q,q,l-k_3) + V_3^\beta(l-q,q,k_2)\,V_3^\beta(l-q,q,k_3)\Big]_{l=k_1+k_2}$$

consists of two terms that otherwise would coincide. The crossed particle-hole terms

$$\begin{aligned}\mathcal{R}_{\mathrm{ph}}^{\mathrm{cr}}(k_1,k_2,k_3) = &-\sum_\beta \int dq\, S(q)\, G_{+\beta}(l+q)\, V_3^\beta(l+q,k_1,q)\, V_3^\beta(l+q,k_2-l,q)\Big|_{l=k_3-k_1} \\ &-\sum_\beta \int dq\, S(q)\, G_{+\beta}(l+q)\, V_3^\beta(l+q,k_2,q)\, V_3^\beta(l+q,k_3,q)\Big|_{l=k_1-k_3}\end{aligned} \tag{2.23}$$

behave likewise. The direct particle-hole diagrams read as

$$\begin{aligned}\mathcal{R}_{\mathrm{ph}}^{\mathrm{d}}(k_1,k_2,k_3) = &-\sum_\beta \int dq\, S(q)\, G_{+\beta}(l+q) \Big[-2V_3^\beta(l+q,k_1,k_1+l)\, V_3^\beta(l+q,k_3,k_2) \\ &+ V_3^\beta(l+q,k_1,k_1+l)\, V_3^\beta(l+q,k_3,q) + V_3^\beta(l+q,k_1,q)\, V_3^\beta(l+q,k_3,k_2)\Big]_{l=k_2-k_3} \\ &-\sum_\beta \int dq\, S(q)\, G_{+\beta}(l+q) \Big[-2V_3^\beta(l+q,k_2,k_3)\, V_3^\beta(l+q,k_1-l,k_1) \\ &+ V_3^\beta(l+q,k_2,k_1-l)\, V_3^\beta(l+q,k_3,q) \\ &+V_3^\beta(l+q,k_2,q)\, V_3^\beta(l+q,k_1-l,k_1)\Big]_{l=k_3-k_2}\,.\end{aligned} \tag{2.24}$$

2.4.3. Estimating two-loop corrections

In this subsection, an argument will be given, why not going beyond the above corrections, i.e. why dropping the renormalization of the three-particle vertex itself, may suffice. If its renormalization could not be dropped, a correction term would have to be added to the constant three-particle vertex as in Fig. 2.3(a). By integrating and then iterating the flow equation for the three-particle vertex, this renormalization induced term can be expressed as a sum of diagrams containing the two-particle and constant three-particle vertices only up to arbitrary order. Note that the constant part of the three-particle vertex is of second order in the four-point couplings. In leading, i.e. third order, one obtains two one-loop terms depicted in Fig. 2.3(b). One of these diagrams includes only four-point vertices and would as well be present in the absence of an initial three-particle term while the other one contains this initial three-particle interaction. When the right-hand side of Fig. 2.3(b) is now fed back into the flow equation for the four-point vertex, diagrams with overlapping and non-overlapping loops arise. If one had started the fRG analysis directly from the full action $\left(\mathcal{A}^{(2)}+\mathcal{A}^{(4)}\right)[\bar{\chi},\chi]$ instead of the effective low-energy action $\mathcal{A}_{\mathrm{eff}}$ and kept the band indices as variables attached to the legs of the vertices, the overlapping ones would be neglected in the Katanin truncation. So they shall be dropped in the present treatment as well.

One then ends up with the correction terms depicted in Fig. 2.4. The first and the third one can be merged with the one-loop terms in Fig. 2.2 leading to a Katanin substitution

(a) Full vertex

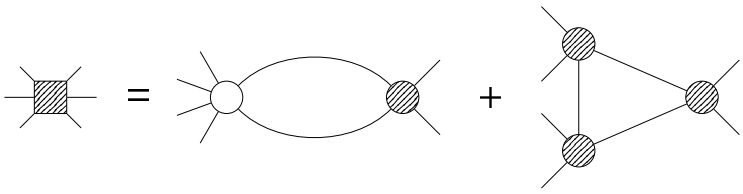

(b) Leading corrections

Figure 2.3.: (a) Full (scale-dependent) vertex (hatched circle) written as a sum of its initial value (empty circle) and a renormalization induced correction term (hatched square). (b) Leading order result for the correction term.

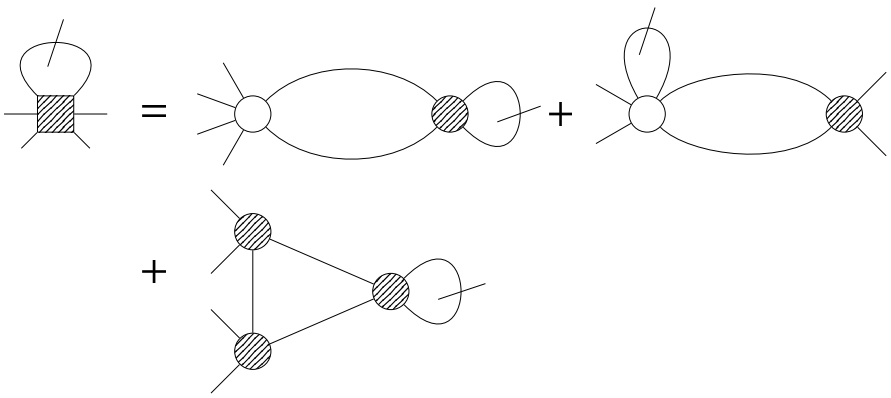

Figure 2.4.: Leading corrections to flow equation in Fig. 2.2. Diagrams with overlapping loops have been neglected.

$S \to \dot{G}$ both in the low-energy term and in the one-loop feedback. Since self-energy effects will be neglected for all RG flows with 3PF in this thesis, this substitution will not affect the results presented here.

The second diagram in Fig. 2.4, however, requires more care. I now proceed with giving upper estimates for the remaining correction term and the one-loop feedback and low-energy terms in Fig. 2.2. If the frequency dependence of the coupling functions is dropped, all Matsubara sums can be evaluated analytically giving rise to the following rules for an estimate.

- The four-point coupling functions V_3^β and V at scale λ are replaced by their maximal value g_3 and g_-, respectively.

- Mixed loops including a scale derivative are replaced by a factor $4\pi^2(\epsilon_+\lambda)^{-1}$, where ϵ_+ denotes the minimal energy of the high-energy bands. The band-flip self-energy diagrams are assumed to behave likewise.

- Lower-band loops with and without a scale derivative are replaced by $4\pi^2\lambda^{-2}$ and $4\pi^2\lambda^{-1}$, respectively.

At all scales the correction term depicted in Fig. 2.4 should be small compared to the the low-energy term, which implies

$$4\pi^2 g_3^2 \ll g_-\epsilon_+ \,. \tag{2.25}$$

Note that the orbital makeup reduces the value of the bare coupling functions and may therefore finally allow for the omission of the correction term. At scales at which the one-loop feedback term flows, the one-loop feedback should prevail against two-loop corrections, i.e. $4\pi^2 g_- \ll \lambda$. Together with the condition Eq. (2.25), this requires the cutoff λ to be much larger than g_3^2/ϵ_+. At lower scales $\lambda \ll g_-^2\epsilon_+/g_3^2$, however, the mixed one-loop diagrams eventually saturate and the feedback term becomes negligible compared to the low-energy loop term that may finally drive the flow to a strong-coupling fixed point. The crossover region between these two regimes should be small, as long as the inequality (2.25) holds. So a one-loop fRG approach should suffice to qualitatively discuss the impact of the three-particle term on the critical scale for d-wave superconductivity, for example.

Finally, a comment on the relation of the flows of the 1PI functionals Γ for all bands and Γ_- for the conduction bands seems to be in order. If self-energy effects are neglected completely, the four-point vertex of Γ_- is equal to the four-point vertex of Γ with all external legs on the low-energy bands, since they both must lead to the same four-point correlation functions for the low-energy modes. If one now considers the flow of Γ for an energy shell cutoff in the usual truncation and in addition forces all four-point vertices with at least one leg on the high-energy bands not to flow, the one-loop feedback in the flow of Γ_- is recovered. In the RG flow of Γ, the most relevant correction term to this approximation consists of the diagram with the internal lines on the low-energy bands and three external legs on the low and one on the high-energy bands. If this correction is fed back into the flow of the vertex with all external legs on the lower bands, the feedback correction term is equivalent to the second diagram in Fig. 2.4 in leading order. As soon as self-energy effects are taken into account, however, this correspondence breaks down.

2.5. Summary

In this chapter, several new formal results for multiband models could be established. First of all, the point-group symmetries of a large class of multiband models have been discussed — in the orbital as well as in the band language. In the orbital language, not only the momentum, but also the orbital quantum numbers transform with representation matrices of the point group. Under a transformation from one basis of hybridizing Bloch functions to another, these representation matrices are mapped onto equivalent ones with a different momentum dependence.

If one now switches to the band language, the band dispersion transforms trivially under all point-group operations. On a one-particle level, this gives rise to an invariance under a transformation to another basis set of non-hybridizing Bloch states, reflecting the arbitrariness of the phases of eigenvectors. Such a transformation corresponds to an isomorphism between representations matrices in the orbital language. The interactions, however, may not transform in the same way in two such representations. In the band language, this implies that the interaction can be more conveniently expressed in some bases. I have shown that the vertex functions of the interactions simply transform by a rotation of their momentum arguments for such a *natural basis*, without additional phases or a reordering of the bands. The fixing of the band phases for the natural basis may render the vertex functions discontinuous at momenta on symmetry elements such as inversion centers, mirror axes or planes. However, if one finds a way how to deal with these discontinuities, the point-group symmetries can now be exploited in the numerical calculation of Feynman diagrams.

This way, the computational effort of fRG studies may be lowered considerably, as in Chapter 3.3, where the renormalized interaction of the Emery model shows a trivial C_{4v} behavior in a natural Bloch basis. Further possible applications include two-dimensional systems with a sixfold symmetry such as multilayer graphene [29–31] and electrons on a kagome lattice. [42,43] Let me also express the hope that the concepts of orbitors and natural Bloch bases may also be helpful in the context of other analytical or numerical many-particle methods. This should be possible for perturbative and self-consistent methods, where vertex functions are an important building block.

For a further reduction of the computational effort, it seems advantageous to start form an effective action obtained from the full multiband model by integrating out the bands at outside a low-energy window, which usually includes the conduction band(s), perturbatively. A parametrization that respects this (formally arbitrary) distinction between high- and low-energy degrees of freedom has been given in the third section of this chapter, where also the conventional, hePT and three-particle truncations of the perturbative expansion have been introduced. Even if the effective action is calculated for a single conduction band, it still shows multiband features in all these truncations. Namely, the

two-particle interaction is decorated by orbital makeup already in the conventional truncation. Moreover, three-particle and higher-order terms induced by virtual fluctuations outside the low-energy window appear. In the conventional and hePT truncation these terms are however omitted. Four-particle and higher-order terms are always neglected in this thesis. In the literature, the three-particle term has not been captured so far, and therefore its impact on the flow poses a conceptually new problem.

In the fourth section of this chapter, a new fRG truncation for multiband systems has been proposed, where the three-particle term is fed back into the flow equation for the two-particle vertex. This way, virtual excitations outside the low-energy window are partly taken into account. The conventional treatment, in contrast, completely neglects virtual excitations involving both high- and low-energy modes once one has switched to the low-energy theory. The new 3PF approach considers them up to second order in perturbation theory within a frame of larger energies around such a low-energy window. On the formal level, this is achieved by a one-loop fRG treatment of an effective action for the low-energy modes, which is truncated *after* (i.e. keeps) the three-particle interactions generated by the high-energy modes. Of course the low-energy theory could also be solved using a different method than fRG, and also here the three-particle term of the effective interactions may play a role. In the RG flow in the low-energy window, the three-particle vertex gives rise to mixed one-loop diagrams with one low-energy and one high-energy leg. Actually, a part of these diagrams is summed up in the cRPA framework currently used in *ab initio* calculations. [93, 94] (A recently proposed fRG approach to constrained summations [95] generalizes both the three-particle feedback scheme and cRPA.) The correlation functions of high-energy modes are no longer kept track of in the three-particle feedback scheme. This considerably reduces the required numerical resources compared to a 'full' fRG approach with an extended energy window.

Chapter 3.

Instability Analyses of Multiband Models

This chapter is devoted to numerical fRG instability analyses of multiband models. Since there is only one conduction band in the high-T_c cuprates, weakly coupled models for the CuO planes of these materials are well-suited as a testbed for multiband fRG methods. In a simple two-band model, the impact of a three-particle term generated by virtual fluctuations in the valence band on the RG flow of the conduction band degrees of freedom is studied and found to be potentially important. An instability analysis of the Emery model within a new channel-decomposed approach follows. While the three-particle term is found to be negligible, orbital makeup effects quantitatively play a role in the Emery model. By virtue of the new channel-decomposed approach, a deformation of the d-wave pairing gap is found. This is not an intrinsic multiband effect, but has not been observed in previous channel-decomposed fRG studies with an exchange parametrization of the interaction.

Parts of this chapter have previously been published in Ref. [84] and [59].

Now we are in a position, where the findings of the previous chapter can be applied in numerical studies of multiband models. In assessing a given material, one may first perform *ab initio* calculations and then cut out an energy window around the Fermi surface, for which an effective model can then be formulated. By choosing a narrow low-energy window, one should be able to account for the more universal features of the low-temperature physics. The two-dimensional single-band Hubbard model, for

example, can be regarded as a standard model for the high-T_c cuprate materials at low temperatures. [97,98] In the case of the iron-based superconductors, a recently proposed S_4 symmetric Hamiltonian [99] may probably serve as such a minimal model.

Widening the low-energy window should then bring in more of the material characteristics. For the cuprate superconductors, various multi-band models have been proposed (see, for example, Refs. [53,54,100]). In the case of the iron pnictides, four- and five-band models with *ab initio* parameters have been used also in a number of fRG studies [37–39], while a recently derived eight-band model [101, 102] seems to qualitatively account for some of the differences in the phases diagrams of LaOFeAs and SmOFeAs. [103]

One may now wonder about the role of multiband effects that appear beyond minimal models. Models for the CuO planes of cuprate materials seem to be a good testbed for exploring such effects, since the cuprates only have one Fermi surface and since models with multiple Fermi surfaces pose additional challenges. This chapter is therefore devoted to multiband Hubbard models that have initially been proposed for the cuprates. The above described truncations of the RG flow equations, however, require sufficiently weak coupling strengths, which is probably unrealistic for the real cuprates. The focus in this chapter therefore rather lies on the methodology than on quantitative predictions for real materials.

First, the impact of the three-particle feedback will be investigated for a two-band model [54] in a simplified approach. Then multiband effects will be studied in the three-band Emery model. [53,54] This will be done within a new channel-decomposed fRG approach, which does *not* resort to a form-factor expansion. This way, it also keeps track of effects that are not of multiband nature, but were hard to resolve in previous studies.

3.1. Three-particle feedback in a simplified fRG approach

3.1.1. Two-band model

In order to have some kind of minimal multiband model, it seems appealing to consider a two-orbital Hamiltonian, with one of the two resulting band crossing the Fermi level, while the other one is separated by an energy gap. Moreover, the coupling functions of this model should transform trivially under operations in the point group of the underlying lattice. The structure of the model used in this section is borrowed from an (effective) two-orbital model derived for high-T_c cuprates, more precisely for the $sp\sigma$ and $dp\sigma$ orbitals residing on the Copper atoms. The one-particle Hamiltonian from the

local density approximation (LDA) band structure of $YBa_2Cu_3O_7$ [54] is extended by inter- and intra-orbital interactions of strengths U and U', viz.

$$\begin{aligned} H =& \sum_{\sigma} \int d\mathbf{k} \begin{pmatrix} f^\dagger_{\mathbf{k},+,\sigma} & f^\dagger_{\mathbf{k},-,\sigma} \end{pmatrix} \begin{pmatrix} A_{\mathbf{k}} & C_{\mathbf{k}} \\ C_{\mathbf{k}} & B_{\mathbf{k}} \end{pmatrix} \begin{pmatrix} f_{\mathbf{k},+,\sigma} \\ f_{\mathbf{k},-,\sigma} \end{pmatrix} \\ &+ \frac{U}{2} \sum_{i,\alpha,\sigma} : n_{i,\alpha,\sigma} n_{i,\alpha,-\sigma} : + \frac{U'}{2} \sum_{i,\alpha,\sigma,\sigma'} : n_{i,\alpha,\sigma} n_{i,-\alpha,\sigma'} : , \end{aligned} \tag{3.1}$$

there $: \cdots :$ denotes normal ordering. Here, $f_{\mathbf{k},\alpha,\sigma}$ and $n_{i,\alpha,\sigma} = f^\dagger_{i,\alpha,\sigma} f_{i,\alpha,\sigma}$ denote the annihilation operator of an electron with momentum $\mathbf{k}$, orbital α and spin orientation σ and the density of such a fermion at site i, respectively. The non-interacting part of the Hamiltonian is given by

$$\begin{aligned} A_{\mathbf{k}} &= \Delta E + \left(1 - u^+_{\mathbf{k}}\right) w_s \,, \quad B_{\mathbf{k}} = \left(1 - u^+_{\mathbf{k}}\right) w_d \,, \\ C_{\mathbf{k}} &= -u^-_{\mathbf{k}} \sqrt{w_d w_s} \,, \quad u^\pm_{\mathbf{k}} = \frac{1}{2} \left(\cos k_y \pm \cos k_x\right) \,, \end{aligned}$$

ΔE being the band separation and w_s and w_d the widths of the dispersion of the s- and d-orbitals, respectively. Of course, other interactions terms like a Hund's rule or non-local terms could be added, but this does not play any role for the considerations that follow.

Let me again point out, that this model is studied as a simple test case for the development of a fRG approach to multiband systems. The goal is not to make predictions for a specific material that hold on a quantitative level. Regarding $YBa_2Cu_3O_7$, the results presented in this section should indeed only be taken with a grain of salt. The reason for this is threefold: First of all, a multiorbital tight-binding model of the cuprates should include orbitals on the oxygen atoms, as they are of some importance in the strong coupling case. [16] Moreover, the two-orbital model given above does not allow for the description of Varma currents [104] and other types of intra-unit cell order [105]. Furthermore, the fRG approach for fermions used in this work is only viable as long as the renormalized interaction stays weak, whereas, in the cuprates, realistic values for the bare interaction are already large compared to the bandwidth. Also other parameters will not always be chosen according to ab initio calculations in the following.

Let us now switch to an imaginary-time functional integral formalism with Grassmann fields $\bar{\psi}_{k,\alpha,\sigma}$ and $\psi_{k,\alpha,\sigma}$ corresponding to the operators $f^\dagger_{\mathbf{k},\alpha,\sigma}$ and $f_{\mathbf{k},\alpha,\sigma}$. These fields depend on the $1+2$ momentum $k = (k_0, \mathbf{k})$ with Matsubara frequency k_0.

Diagonalization of the quadratic part $\mathcal{A}^{(2)}$ of the action corresponding to Eq. (3.1) yields bands with energies

$$E_{\mathbf{k},\pm} = \frac{1}{2} \left[A_{\mathbf{k}} + B_{\mathbf{k}} \pm \sqrt{\left(A_{\mathbf{k}} - B_{\mathbf{k}}\right)^2 + 4 C^2_{\mathbf{k}}} \right] \,,$$

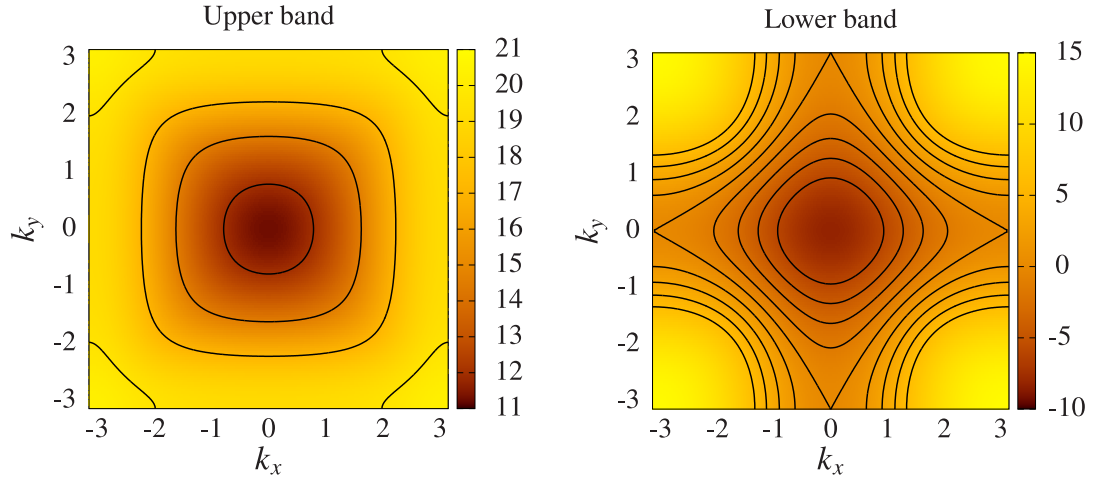

(a) Valence band (b) Conduction band

Figure 3.1.: Band structure of the two-band model for $\Delta E = 1.7\, w_d$ and $w_s = 0.39\, w_d$ at van-Hove filling. The lower band in (b) is the conduction band. The colorbars on the sides indicate the band energy. This choice of parameters underlies the RG flow in Fig. 3.3.

which are shown in Fig. 3.1. In the following, I will work in a parameter range where the lower of the two bands cuts the Fermi level, while the upper band is entirely above the Fermi level. In the terminology of subsection 2.3.1, the lower and upper band constitute the low- and high-energy sector, respectively. This simple two-band set-up may serve as minimal model for more complex situations in with many, possibly entangled bands in both high-energy and low-energy sector.

The equation for the unitary transformation from orbitals ψ to bands χ labeled by $\alpha = \pm$ reads as

$$\psi_{k,\alpha,\sigma} = \alpha d_{\mathbf{k}} \chi_{k,\alpha,\sigma} + c_{\mathbf{k}} \chi_{k,-\alpha,\sigma} \tag{3.2}$$

with

$$d_{\mathbf{k}} = \frac{N_{\mathbf{k}}}{2}\left(A_{\mathbf{k}} - B_{\mathbf{k}} + \sqrt{(A_{\mathbf{k}} - B_{\mathbf{k}})^2 + 4C_{\mathbf{k}}^2}\right), \quad c_{\mathbf{k}} = N_{\mathbf{k}} C_{\mathbf{k}},$$

where $N_{\mathbf{k}}$ normalizes the transformation to a unitary one. The inverse of this transformation gives the orbital amplitudes $\alpha d_{\mathbf{k}}$ and $c_{\mathbf{k}}$ for the band fields $\chi_{k,\alpha,\sigma}$. By transforming from orbitals to bands according to Eq. (3.2), one obtains four factors of $d_{\mathbf{k},\alpha,\sigma}$ or $c_{\mathbf{k},\alpha,\sigma}$ multiplying the interaction parameters U and U' acting as orbital makeup.

Parametrization of the interaction For the parametrization of the interaction, one can exploit more symmetries than in the general case of subsection 2.3.2: In the orbital picture, the interaction is invariant under a band-index flip. Since the trace of the matrix of the orbital-to-band transformation Eq. (3.2) vanishes, this property also holds in the

band language, giving rise to the following identities

$$\begin{aligned}
F_+(\xi_1,\xi_2,\xi_3,\xi_4) &= F_-(\xi_1,\xi_2,\xi_3,\xi_4)\\
F_{+\to-}(\xi_1,\xi_2,\xi_3,\xi_4) &= F_{-\to+}(\xi_1,\xi_2,\xi_3,\xi_4)\\
F_{\pm\to\pm}(\xi_1,\xi_2,\xi_3,\xi_4) &= F_{\pm\to\pm}(\xi_2,\xi_1,\xi_4,\xi_3)\\
F_{-\to\pm}(\xi_1,\xi_2,\xi_3,\xi_4) &= F_{+\to\pm}(\xi_1,\xi_2,\xi_3,\xi_4)\\
F_{\pm\to-}(\xi_1,\xi_2,\xi_3,\xi_4) &= F_{\pm\to+}(\xi_1,\xi_2,\xi_3,\xi_4)\,.
\end{aligned}$$

The symmetry constraint

$$V^{(D,E)}_{\pm\to\pm}(k_1,k_2,k_3) = V^{(D,E)}_{\pm\to\pm}(k_2,k_1,k_3-k_1-k_2)$$

reflects the behavior under a band-index flip. I now give explicit expressions for the coupling functions

$$V_-(k_1,k_2,k_3) = U\left(\prod_i d_{\mathbf{k}_i} + \prod_i c_{\mathbf{k}_i}\right) + U'\left(d_{\mathbf{k}_1}c_{\mathbf{k}_2}c_{\mathbf{k}_3}d_{\mathbf{k}_4} + c_{\mathbf{k}_1}d_{\mathbf{k}_2}d_{\mathbf{k}_3}c_{\mathbf{k}_4}\right) \tag{3.3}$$

$$\begin{aligned}
V_2(k_1,k_2,k_3) &= U\left(d_{\mathbf{k}_1}d_{\mathbf{k}_2}c_{\mathbf{k}_3}c_{\mathbf{k}_4} + c_{\mathbf{k}_1}c_{\mathbf{k}_2}d_{\mathbf{k}_3}d_{\mathbf{k}_4}\right) - U'\left(d_{\mathbf{k}_1}c_{\mathbf{k}_2}d_{\mathbf{k}_3}c_{\mathbf{k}_4} + c_{\mathbf{k}_1}d_{\mathbf{k}_2}c_{\mathbf{k}_3}d_{\mathbf{k}_4}\right)\\
V^{(D)}_{\pm\to\pm}(k_1,k_2,k_3) &= U\left(d_{\mathbf{k}_1}c_{\mathbf{k}_2}c_{\mathbf{k}_3}d_{\mathbf{k}_4} + c_{\mathbf{k}_1}d_{\mathbf{k}_2}d_{\mathbf{k}_3}c_{\mathbf{k}_4}\right) + U'\left(\prod_i d_{\mathbf{k}_i} + \prod_i c_{\mathbf{k}_i}\right)\\
V^{(E)}_{\pm\to\pm}(k_1,k_2,k_3) &= U\left(d_{\mathbf{k}_1}c_{\mathbf{k}_2}c_{\mathbf{k}_3}d_{\mathbf{k}_4} + c_{\mathbf{k}_1}d_{\mathbf{k}_2}d_{\mathbf{k}_3}c_{\mathbf{k}_4}\right) - U'\left(c_{\mathbf{k}_1}c_{\mathbf{k}_2}d_{\mathbf{k}_3}d_{\mathbf{k}_4} + d_{\mathbf{k}_1}d_{\mathbf{k}_2}c_{\mathbf{k}_3}c_{\mathbf{k}_4}\right)\\
V_3(k_1,k_2,k_3) &= U\left(d_{\mathbf{k}_1}c_{\mathbf{k}_2}c_{\mathbf{k}_3}c_{\mathbf{k}_4} - c_{\mathbf{k}_1}d_{\mathbf{k}_2}d_{\mathbf{k}_3}d_{\mathbf{k}_4}\right) + U'\left(d_{\mathbf{k}_1}d_{\mathbf{k}_2}d_{\mathbf{k}_3}c_{\mathbf{k}_4} - c_{\mathbf{k}_1}c_{\mathbf{k}_2}c_{\mathbf{k}_3}d_{\mathbf{k}_4}\right)\,.
\end{aligned} \tag{3.4}$$

So the bare interaction can be expressed in terms of 5 independent functions of three $1+2$-momenta by exploiting its symmetries.

3.1.2. RG setup: Two-patch approximation

One may now proceed with the second step of solving the low-energy model, which will be done by a fRG flow here. This will clarify the differences between the various levels of approximations. I now introduce a multiplicative infrared (IR) cutoff on the lower band by replacing D_- by $D_- R_\lambda^{-1}$, where R_λ denotes a regulator function. In this section, the regulator function is chosen according to the so-called Ω-scheme

$$R_\lambda(\xi,\xi') = \delta(\xi-\xi')\,\frac{k_0^2}{k_0^2+\lambda^2}\,. \tag{3.5}$$

Employed by Husemann and Salmhofer [24], it does not completely suppress contributions from the Fermi surface at nonzero λ and therefore allows one to take a possible

ferromagnetic instability into account. Moreover, a pure frequency cutoff with $R_\lambda = 0$ at $k_0 = 0$ circumvents Fermi-surface-renormalization issues [19], since the full propagator reads as

$$G = R_\lambda \left[Q + \Sigma R_\lambda\right]^{-1} ,$$

Σ being the self-energy. So self-energy effects may be neglected *without* ignoring the most relevant terms.

In order to make the resulting numerical calculations more feasible, and as the main purpose of this section is to get a first picture of the effects due to the higher truncation, the so called two-patch approximation is now employed. This approximation has been used in the context of the one-band Hubbard model [106, 107] and the iron pnictides [108].

Just as for the one-band Hubbard model, the dispersion of the lower band of the model Hamiltonian in Eq. (3.1) has saddle points at $\mathbf{k} = A = (0, \pi)$ and $B = (\pi, 0)$. If the system is now considered at van Hove filling, A and B lie on the Fermi surface. At zero temperature, the low-energy properties then are dominated by contributions of a small vicinity around these saddle points. The internal momenta in the lower-band diagrams are therefore restricted to two small patches around A and B. In the following, self-energy effects and the frequency dependence of the coupling functions will be neglected. In the one-loop diagrams, the momentum integral then only enters in the bare bubbles

$$\Phi_{\mathrm{pp}}(l) = \sum_{p_0} \int_{\mathrm{patch}} d\mathbf{p}\, G_-(p)\, G_-(l-p)$$
$$\Phi_{\mathrm{ph}}(l) = \sum_{p_0} \int_{\mathrm{patch}} d\mathbf{p}\, G_-(p)\, G_-(l+p)\,.$$

For zero temperature, the Matsubara sum is evaluated analytically for $l_0 = 0$ and the two-patch approximation restricts the transfer momenta $\mathbf{l}$ to $\mathbf{0}$ or $\hat{\boldsymbol{\pi}} = (\pi, \pi)$. In our truncation, the fRG analysis can now be restricted to four running couplings depicted in Fig. 3.2, namely

$$g_1 = V_-(A,B,B) = V_-(B,A,A)$$
$$g_2 = V_-(A,B,A) = V_-(B,A,B)$$
$$g_3 = V_-(A,A,B) = V_-(B,B,A)$$
$$g_4 = V_-(A,A,A) = V_-(B,B,B)\,.$$

This reduces the computational cost of the RG flow drastically. In the conventional truncation, the initial conditions for these couplings are obtained from transforming the intra- and interorbital interactions from the bare Hamiltonian into the band language. The corresponding expression have already been given in Eq. (3.3). The hePT diagram (with all internal lines on the upper band) will be neglected in the following. If the 3PF is included in the RG flow, one also has to look at the diagrams with mixed loops. In

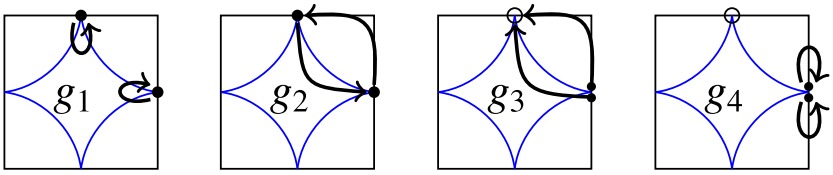

Figure 3.2.: The four running couplings g_1 to g_4 for the conduction band in two-patch approximation. The blue lines represent the Fermi surface.

these loops, however, also regions away from the Fermi surface contribute significantly. Therefore, the loop integrals in the mixed-band diagrams will be taken over the whole Brillouin zone.

Let me now return to the loops with both lines on the lower band. In the case of the one-band Hubbard model, the cutoff can be chosen such that the resulting loop integrals can be evaluated analytically and do not depend on the patch size [109]. However, that cutoff scheme is only viable in a small neighborhood around the saddle points whereas the cutoff needs to be defined on the entire Brillouin zone in order to consider the 3PF. To the author's knowledge, only momentum shell cutoff schemes have been used for the two-patch model while a frequency cutoff is used in this section.

The flow equations in the two-patch approximation read as

$$\dot{g}_1 = \delta V_-(A,B,B) + d_1\left(g_1^2+g_3^2\right) + 2d_2\left(g_2-g_1\right)g_4 - d_3\left(g_1^2+g_2^2\right) \tag{3.6}$$
$$\dot{g}_2 = \delta V_-(A,B,A) + d_1 g_2\left(g_1-g_2\right) + 2d_2 g_2 g_4 - 2d_3 g_1 g_2 \tag{3.7}$$
$$\dot{g}_3 = \delta V_-(A,A,B) - 2d_0 g_3 g_4 + 2d_1 g_3\left(2g_1-g_2\right) \tag{3.8}$$
$$\dot{g}_4 = \delta V_-(A,A,A) - d_0\left(g_3^2+g_4^2\right) + d_2\left(g_2^2+2g_1g_2-2g_1^2+g_4^2\right)\,, \tag{3.9}$$

where the dot denotes a derivative with respect to λ. The three-particle feedback leads to correction terms δV_- that do not occur in two-patch studies of one-band systems. They have been given in Chapter 2.4.2. The integration over the patches in the loops

$$d_0 = \dot{\Phi}_{\mathrm{pp}}(\mathbf{0})\,, \quad d_1 = \dot{\Phi}_{\mathrm{ph}}(\hat{\boldsymbol{\pi}})\,,$$
$$d_2 = \dot{\Phi}_{\mathrm{ph}}(\mathbf{0})\,, \quad d_3 = -\dot{\Phi}_{\mathrm{pp}}(\hat{\boldsymbol{\pi}})$$

are performed numerically using an adaptive routine [110]. The different levels of approximation introduced in Chapter 2.4.1 now imply the following:

1. *Conventional truncation.* Neglecting δV_- and initializing the g_is by the respective values of the coupling function V_- at $\lambda = \infty$.

2. *Three-particle feedback.* Keeping δV_- and initializing the g_is by the respective values of V_-.

3. *Constrained perturbation theory.* Neglecting δV_- and initializing the g_is by the respective values of $V_- + \Delta V_-$, where $\Delta V_- = -\int_0^\infty d\lambda\, \delta V_-$ denotes the sum of all second-order mixed-band diagrams.

In all the cases considered in this section, an abrupt flow to strong coupling at some critical scale λ_{crit} can be observed. In the two-patch approximation, the flow equations of the couplings to external source fields for s- and d-wave superconductivity ($\alpha_{s\text{SC}}$ and $\alpha_{d\text{SC}}$, respectively), anti-ferromagnetism (α_{AF}) and ferromagnetism (α_{FM}) take the simple forms

$$\begin{aligned}
\dot{\alpha}_{s\text{SC}} &= -2d_0\,(g_3 + g_4)\,\alpha_{s\text{SC}} \\
\dot{\alpha}_{d\text{SC}} &= -2d_0\,(g_4 - g_3)\,\alpha_{d\text{SC}} \\
\dot{\alpha}_{\text{AF}} &= +2d_1\,(g_1 + g_3)\,\alpha_{\text{AF}} \\
\dot{\alpha}_{\text{FM}} &= +2d_2\,(g_2 + g_4)\,\alpha_{\text{FM}}\,.
\end{aligned}$$

These couplings also appear in the expressions for the corresponding susceptibilities and determine which ordering tendency grows fastest at the critical scale, i.e. is the leading instability at λ_{crit}.

3.1.3. Flows without a three-particle term: Impact of orbital makeup and competition of FM and dSC instabilities

In this subsection, I will discuss the impact of orbital makeup when the three-particle feedback is neglected.

Let me first consider the case of vanishing inter-orbital interaction, $U' = 0$. In that case, according to Eq. (3.3) all four couplings take on the same value U_{eff} at the beginning of the flow. Since $d_k^2 + c_k^2 = 1$, these couplings are smaller than the intra-orbital coupling U. Moreover, in an expansion of the lower band dispersion around the saddle points, the lower-band dispersion is equivalent to the dispersion of the one-band t-t' Hubbard model up to second order with effective parameters t and t' for nearest and second-neighbor hopping. So for $U' = 0$ and in the conventional truncation, where the upper band does not enter, the one-band t-t' model in a two-patch approximation is recovered, albeit with a reduced U. (Moreover, a smooth frequency cutoff is used here and not a momentum-shell cutoff as in previous two-patch studies.)

Let me now characterize the nature of the flow in the absence of a three-particle term. Characteristic curves for the flow of the couplings g_i in the conventional truncation can be seen in Figs. 3.3 and 3.4. For zero second-neighbor hopping $t' = 0$, the Fermi surface is perfectly nested, giving rise to antiferromagnetism as the leading instability. For small but nonzero t', the most important loops in the flow equations Eqs. (3.6)-(3.9) are d_0

and d_1. Therefore d_2 and d_3 can be neglected at first. In this approximation, g_4 is decreased by d_0 while the d_1 term in Eq. (3.8) prevents g_3 from being renormalized to zero. This allows for a sign change of g_4, after which the growth of d_0 drives the system to a d-wave superconducting dSC instability corresponding to a strong-coupling fixed point with $g_4 \to -\infty$ and $g_1, g_2, g_3 \to +\infty$. This instability is in full agreement with the findings of previous two-patch studies. [106] If one now increases t', the particle-hole diagrams with zero wavevector transfer become more important, i.e. the d_2 terms cannot be neglected any more. In particular, the last term in Eq. (3.9) hampers the sign change of g_4, which now occurs at a lower scale, leading to a lower critical scale. Moreover, g_2 is now renormalized to zero instead of diverging to $+\infty$. Thus we have an altered strong-coupling fixed point, but still with $g_3 \to +\infty$, $g_4 \to -\infty$, corresponding to a d-wave pairing instability. This distinction was absent in traditional two-patch studies [106,107] in which the growth of d_2 in the flow was hampered by the choice of the cutoff function. Katanin and Kampf have included such contributions in a momentum-shell approach. [109] They find a similar strong-coupling fixed point with non-diverging g_2 which however corresponds to an antiferromagnetic instability. In N-patch flows, there would be a smooth crossover from the fixed point with $g_2 \to \infty$ to the one with $g_2 \to 0$.

If the dispersion is varied further by increasing t', d_2 grows even more strongly. Eventually, it prevents a sign change of g_4 and therefore excludes d-wave superconductivity. Then the flow corresponds to a FM instability. Conversely, the negative values of g_4 at lower t' in the d-wave regime prohibit ferromagnetism, since the d_2 terms in Eqs. (3.6)-(3.7) depend linearly on this parameter. This reflects the mutual exclusion of the FM and dSC instabilities. Along the separatrix between these two regimes, all four running couplings flow to zero. This suggests that the critical scale drops to zero from both sides, which implies the existence of a quantum critical line between the two phases. In an N-patch study, however, the situation is more involved and both instabilities may occur simultaneously. Unfortunately, the region around the separatrix is unaccessible in our calculations due to an excessive number of function calls required for numerical integration of the loops. In Fig. 3.5, the phase diagram of this model obtained in the conventional truncation is depicted. In the d-wave regime, a reduction of the interaction strength to U_{eff} leads to a lower critical scale.

Let us now turn to the case of non-vanishing inter-orbital coupling, where one has $g_1 = g_4 > g_2 = g_3$ at the initial scale. From Table 3.2, one can see that this detuning leads to a lower critical scale in the dSC regime, as the inter-orbital interaction suppresses $g_3 - g_4$ in the initial condition while $g_3 + g_4$ remains unchanged.

Before the d-wave regime is analyzed in further detail, let us briefly look at the band structure for parameters given for $YBa_2Cu_3O_7$ in Ref. [54]. For such a system, however, van Hove filling is not close to the experimental situation, since it corresponds to a filling factor of about 0.19. The result should therefore not be taken as a realistic prediction

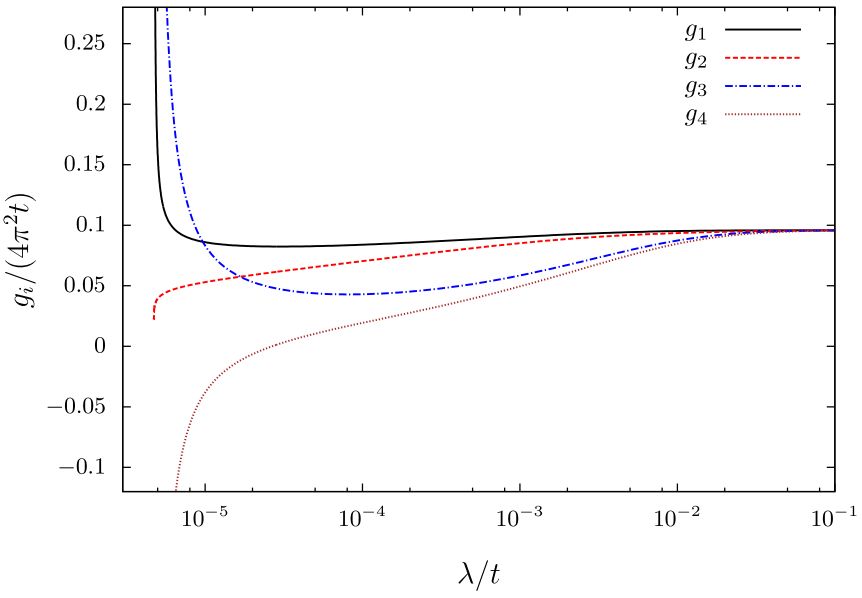

(a) $U' = 0$

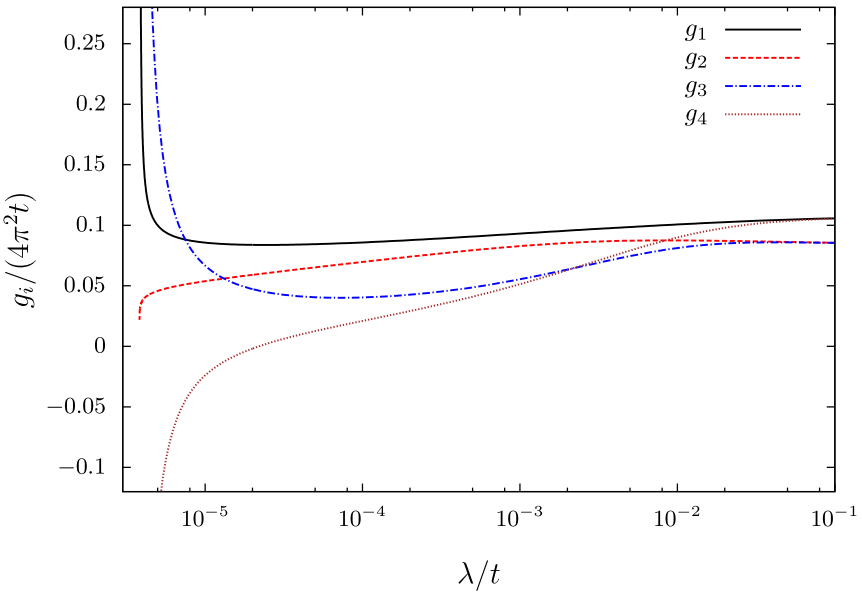

(b) $U' = 0.3U$

Figure 3.3.: Flow in the low-energy model for $\Delta E = 1.70\, w_d$, $w_s = 0.39\, w_d$, $U = 0.03 \cdot 4\pi^2 w_d$, $U' = 0$ (a) and $U' = 0.3U$ (b) in the conventional truncation. The two-patch couplings are depicted as solid (g_1), dashed (g_2), dashed-dotted (g_3) and dotted lines (g_4). The band-flip self-energy term in the feedback has not been taken into account.

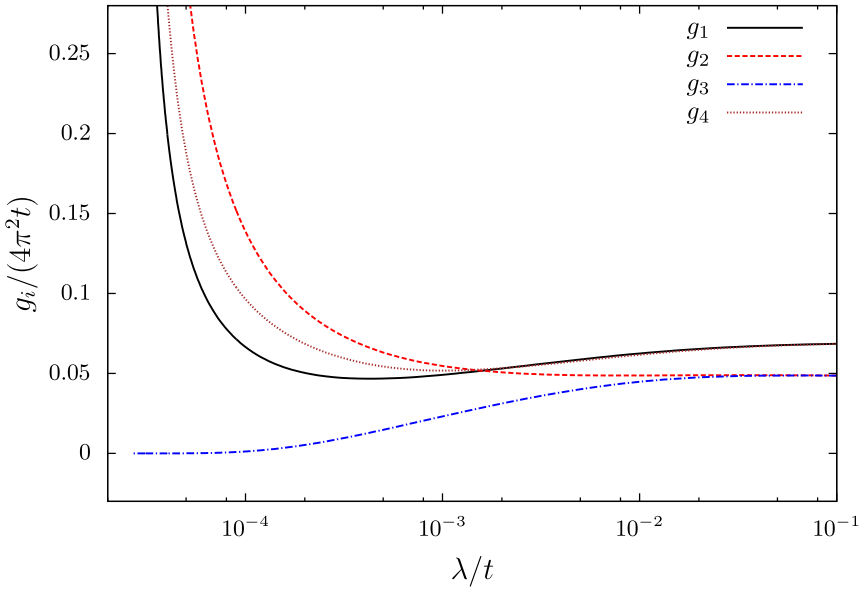

Figure 3.4.: Flow without band-flip self-energy term for $\Delta E = 0.57\, w_d$, $w_s = 2.07\, w_d$, $U = 0.03 \cdot 4\pi^2 w_d$, $U' = 0.3U$ at in the conventional truncation. Line styles as in Fig. 3.3.

$\Delta E/w_d$	w_s/w_d	n_{low}	c_{max}/U	t/w_d	$-t'/t$	FIG.
1.70	0.39	0.415	$2.81 \cdot 10^{-2}$	0.223	0.264	3.3
0.57	2.07	0.192	$3.73 \cdot 10^{-2}$	0.317	0.492	3.4

Table 3.1.: Different parameter sets for the dispersion analyzed in this section. The lower-band filling factor $\int_{\mathrm{BZ}} d\mathbf{k}\, \Theta[-E_-(\mathbf{k})]/(4\pi^2)$ is denoted by n_{low} and the maximal hybridization matrix element by $c_{\mathrm{max}} = \max_{\mathbf{k}} c_{\mathbf{k}}$.

for this material. In Fig. 3.4, the flow approaches a FM fixed point in the conventional truncation. This will also hold for the other truncations with 3PF and cPT.

3.1.4. Inclusion of the three-particle term

Let us now turn our attention to the three-particle feedback in the 3PF and cPT flows in Figs. 3.6 and 3.7. Once again, let me emphasize that the model parameters will be varied in order to clarify the differences between the truncation schemes discussed above and may not always correspond to an experimentally realistic situation.

One can observe a flow to a dSC strong-coupling fixed point over a wide parameter range irrespective of the presence of inter-orbital interactions. This pairing instability occurs for all three truncation schemes considered. The critical scale, however, is enhanced by the three-particle feedback. As can be seen from Table 3.2 and also Fig. 3.8, this

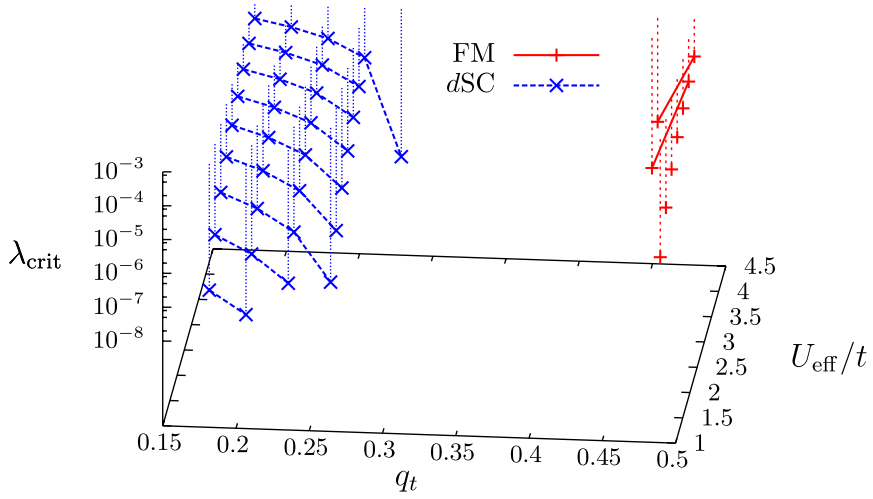

Figure 3.5.: Phase diagram of the t-t' Hubbard model in two-patch approximation, conventional truncation, with $q_t = -t'/t$. Points that correspond to the same value of U_{eff} are connected by a line. The region around the separatrix between the dSC and FM instabilities is inaccessible in the approach pursued here, since the numerical integration of the loops gets too cumbersome.

	conventional		3PF		cPT	
FIG.	$\lambda_{\text{crit},1}/t$		$\lambda_{\text{crit},2}/t$		$\lambda_{\text{crit},3}/t$	
3.3a)	$4.73 \cdot 10^{-6}$	dSC	$1.28 \cdot 10^{-5}$	dSC	$1.32 \cdot 10^{-5}$	dSC
3.3b)	$3.83 \cdot 10^{-6}$	dSC	$8.69 \cdot 10^{-6}$	dSC	$8.93 \cdot 10^{-6}$	dSC
3.4	$3.76 \cdot 10^{-5}$	FM	$3.58 \cdot 10^{-5}$	FM	$3.58 \cdot 10^{-5}$	FM

Table 3.2.: Critical scale λ_{crit} and leading instability for different levels of approximation.

enhancement can easily be a factor of two, at least in the parameter range of small critical scales. One can observe that λ_{crit} only differs weakly between the 3PF and cPT flows. Figs. 3.6 and 3.7 illustrate that first the mixed-band diagrams flow to a value close to their infrared limit before the lower-band diagrams start to grow significantly. (All other ratios of the couplings that are not shown in Figs. 3.6 and 3.7 behave indeed likewise.) This separation of scales is enhanced or might be even induced by a two-patch approximation. It ensures that the two-loop correction term discussed in Appendix 2.4.3 remains negligible and also holds in the ferromagnetic case and for Fig. 3.8.

The question now is whether the three-particle feedback on the critical scale can be related to characteristic properties of the band structure such as band curvatures. For this purpose, I consider ΔV_{-} terms in the initial condition with cPT corrections for small hybridization $c_{\mathbf{k}}$ as in the case of Fig. 3.6. If for simplicity U' is then sent to zero, the bare coupling functions V_{-} and V_3 Eqs. (3.3) and (3.4) read in leading order in the hybridization

$$V_{-}(k_1,k_2,k_3) \approx U \prod_i d_{\mathbf{k}_i}$$
$$V_3(k_1,k_2,k_3) \approx -U c_{\mathbf{k}_1} d_{\mathbf{k}_2} d_{\mathbf{k}_3} d_{\mathbf{k}_4} \,.$$

This corresponds to taking only the on-site interaction in the d-orbital into account. Since $U' = 0$, the self-energy insertion contributions to all four running couplings take on the same value and the direct particle-hole diagrams (2.24) vanish. In the diagrams in Eq. (2.22), the hybridization $c_{\mathbf{k}}$ appears only inside the integrand whereas the external legs of momentum $\mathbf{k}$ have a factor $d_{\mathbf{k}}$, which in contrast to $c_{\mathbf{k}}$ is invariant under a spatial rotation by $\pi/2$. This implies that the particle-particle contributions to $\Delta V_{-}(A,A,B)$ and $\Delta V_{-}(A,A,A)$ are of equal size, whereas the crossed particle-hole diagrams give different contributions. The latter can be seen as follows: After calculating the Matsubara sum for $\lambda = 0$, the integral in Eq. (2.23) reads as

$$\int_{\mathrm{BZ}} d\mathbf{q}\; c^2_{\mathbf{l}+\mathbf{q}}\, d^2_{\mathbf{q}}\; \left[E_{+}(\mathbf{q}+\mathbf{l}) - E_{-}(\mathbf{q})\right]^{-1} \Theta\left(-E_{-}(\mathbf{q})\right) \,, \tag{3.10}$$

with the Heaviside function $\Theta(x)$. For $\Delta V_{-}(A,A,A)$, which renormalizes g_4, one has $\mathbf{l} = 0$ and for $\Delta V_{-}(A,A,B)$, which renormalizes g_3, the transfer momentum is $\mathbf{l} = \hat{\boldsymbol{\pi}}$. Since both bands have a curvature with the same sign in our model and since E_{+} is always positive, the denominator in the integrand of Eq. (3.10) should take on smaller values for $\mathbf{l} = 0$ than for $\mathbf{l} = \hat{\boldsymbol{\pi}}$ on a large phase space region centered around $\mathbf{q} = 0$. One might therefore expect a suppression of $g_3 - g_4$. This argument, however, ignores the momentum dependence of the orbital weight completely. Whilst being zero along the diagonals of the BZ, the hybridization matrix elements $c_{\mathbf{q}}$ have their maximal value close to the saddle points of the lower band. This weakens the effect of the band curvature on $g_3 - g_4$, in particular if the hybridization shows plateau-like structures centered around the van Hove points as for the parameters underlying the flow in Fig. 3.6. At these points, however, the four-fold rotation symmetry of the dispersion gives rise to identical

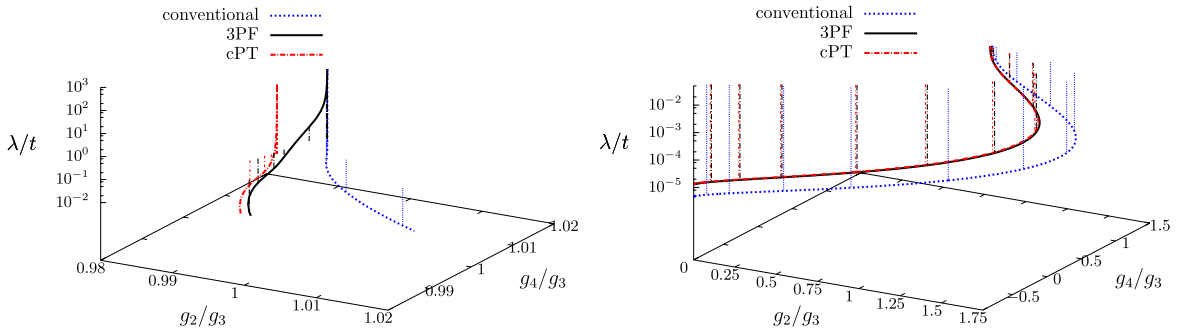

(a) High scales (b) Low scales

Figure 3.6.: Flows in the low-energy model for $\Delta E = 1.70\, w_d$, $w_s = 0.39\, w_d$, $U = 0.03 \cdot 4\pi^2 w_d$, $U' = 0$ at the different approximation levels. The interaction has been projected to the g_2/g_3-g_4/g_3 plane, while the z-direction corresponds to the scale. The impulse-type vertical lines have been added for clearness and have no physical meaning. The initial flow for high scales is shown on the left hand side in (a). Here one can see that the RG flow with 3PF has the same initial condition for the g_is as the conventional truncation, but approaches quickly the values with cPT corrections in the early flow. On the right hand side, the continuation of the flow at lower scales is depicted. The 3PF and cPT curves are basically equivalent and have a higher critical scale than in the conventional truncation. The ratio g_2/g_3 flows to zero, corresponding to the second d-wave pairing fixed point discussed in Section 3.1.3. The band-flip self-energy term in the feedback has not been taken into account.

denominators of the loop integrand in Eq. (3.10) for $\mathbf{l} = 0$ and $\mathbf{l} = \hat{\boldsymbol{\pi}}$. Hence, the effect of band curvatures that one might expect ignoring orbital makeup effects should play a minor role in such a case. In contrast, the phase space weight imposed by the orbital makeup may lead to an enhancement of $g_3 - g_4$, even for weak hybridization as in the case of Fig. 3.6. For larger values of the hybridization, the situation is yet more involved, as terms with opposite signs compete. So far, I have discussed the cPT contributions of ΔV_- to $g_3 - g_4$. They have been found to be quite sensitive to the orbital makeup.

The question now is how they affect the critical scale: On average, ΔV_- suppresses the couplings g_i while the difference $g_3 - g_4$ may be enhanced or lowered depending on the orbital makeup. In general, smaller initial values of the couplings give rise to lower critical scales while a larger value of the d-wave coupling $g_3 - g_4$ promotes a sign change of g_4 at higher scales. So for enhanced d-wave coupling, one has to deal with two counteracting tendencies and it is *a priori* not clear which one prevails, whereas a suppression of λ_{crit} is to be expected if $g_3 - g_4$ is lowered. In Fig. 3.7, they lead to a surprisingly large enhancement of λ_{crit}. Indeed, $g_3 - g_4$ gets larger when the three-particle feedback is taken into account, but if contributions from d_2 and d_3 in the flow equations Eqs. (3.6)-(3.9) are neglected, the critical scales obtained the conventional and cPT truncations virtually coincide. Moreover, their values are increased by orders of magnitude without the d_2 and d_3 terms. This points out the importance of those

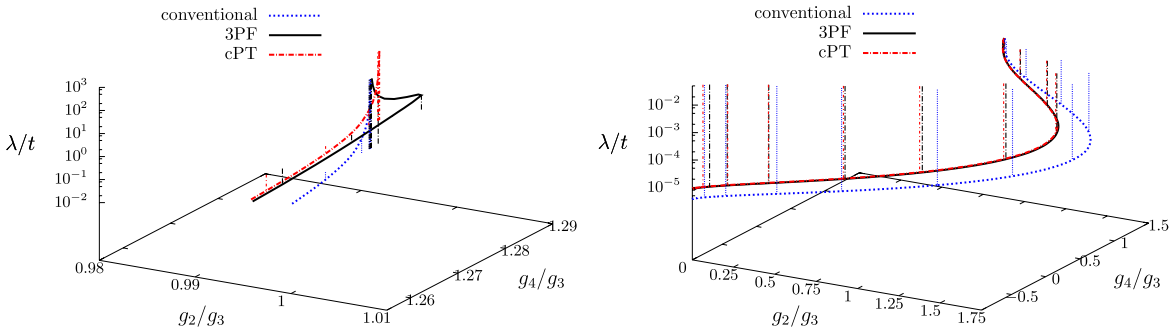

(a) High scales (b) Low scales

Figure 3.7.: Same as in Fig. 3.6, but for $U' = 0.3U$.

terms and their interplay with the three-particle feedback for the dispersion underlying Fig. 3.6.

In Fig. 3.7, $g_3 - g_4$ is suppressed by ΔV_-. Without the d_2 and d_3 terms, this would only change the critical scale by values below the level of accuracy, while λ_{crit} is significantly enhanced if those terms are taken into account. As for the flow to a ferromagnetic instability in Fig. 3.4, one finds that the three-particle term is of minor importance for the corresponding parameters.

Finally, I investigate the impact of the band separation ΔE on the critical scale as depicted in Fig. 3.8. Lower values of ΔE correspond to a larger ratio $-t'/t$ and therefore to a lower critical scale in the dSC regime. One can observe that for band separations smaller than $1.70\, w_d$, the three-particle feedback substantially enhances the critical scale. In particular, when the critical scale gets small due to the competition with the FM channel, the three-particle term can change the result by an order of magnitude. This indicates that these corrections may play a role in situations with competing ordering tendencies. Deep in the d-wave regime, or also on the FM side, the impact of the three-particle term is only of quantitative nature. Since the behavior at small dSC critical scales mainly stems from the interplay of the three-particle feedback and the d_2 loop, it should result from the increasing contribution of d_2 that one has to encounter when ΔE is lowered. The inclusion of the band-flip self-energy term only leads to slight changes of the critical scale and does not affect the results of Fig. 3.8 on a qualitative level.

3.2. Three vs. single-band description

Let me now switch from a two-band to the three-band Emery model. The latter includes also p-orbitals on the oxygen atoms, which are important in the strong-coupling case [111] and for potential loop currents. [104, 105] Since the atoms, and hence the centers of the

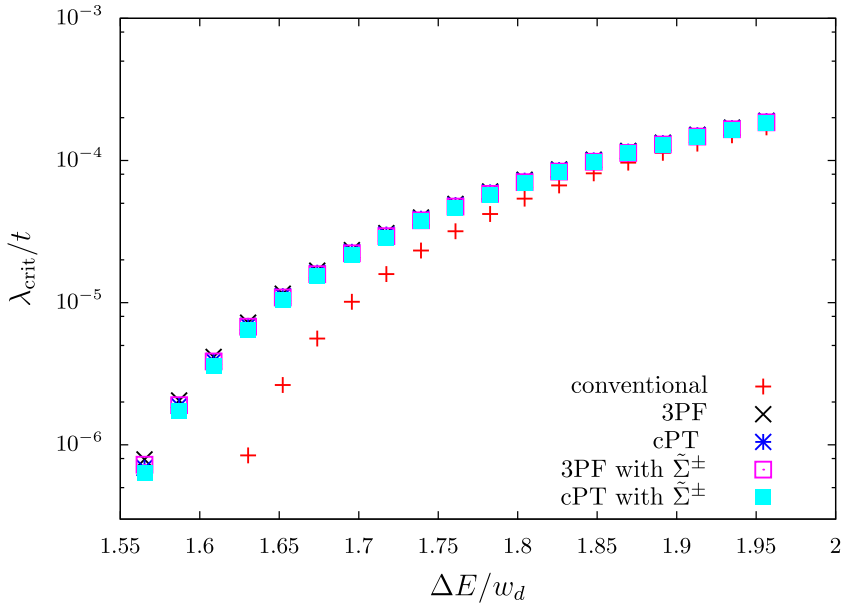

Figure 3.8.: Critical scale λ_{crit} for $w_s = 0.39\,w_d$, $U = 0.03 \cdot 4\pi^2 w_d$, $U' = 0.3U$ as a function of ΔE, in the dSC regime. In the legend, "with $\tilde{\Sigma}^{\pm}$" indicates that the values of the respective curves have been calculated with band-flip self-energy contributions included.

Wannier states included in the model, now reside in different locations in the unit cell, this make the form of the coupling functions more complicated (see Chapter 2.2 and Appendix B.1). At weak coupling and close to van-Hove filling, the three-band Emery model can be systematically related to the single-band Hubbard model with effective parameters. So before studying the Emery model numerically in the next section, I will elaborate on this relationship.

3.2.1. Emery model

Let me start with giving the Emery Hamiltonian. [53, 54] It reads as

$$H = \sum_{\mathbf{k},\sigma} \Psi_\sigma^\dagger(\mathbf{k}) \left(\mathcal{H}_0 - \mu\right) \Psi_\sigma(\mathbf{k}) + : H_{\mathrm{int}} :,$$

where $\mathbf{k}$ denotes the 2D-momentum, μ the chemical potential and σ the spin index and where the interaction term H_{int} enters in normally ordered form. The annihilation operators $d_\sigma(\mathbf{k})$ for the Cu $3d$-orbitals and $p_{x,\sigma}(\mathbf{k}), p_{y,\sigma}(\mathbf{k})$ for the oxygen $2p$-orbitals form the components of the orbital pseudo-spinor

$$\Psi_\sigma(\mathbf{k}) = \begin{pmatrix} d_\sigma(\mathbf{k}) \\ p_{x,\sigma}(\mathbf{k}) \\ p_{y,\sigma}(\mathbf{k}) \end{pmatrix}.$$

Here and throughout the lattice constant (i.e. the spacing between neighboring Copper atoms) is set to unity. The one-particle part of H is then determined by the matrix

$$\mathcal{H}_0 = \begin{pmatrix} \epsilon_d & t_{pd}\, s_x & t_{pd}\, s_y \\ t_{pd}\, s_x & \epsilon_p + t_{pp}\, c_x & 2t_{pp}\, s_x s_y \\ t_{pd}\, s_y & 2t_{pp}\, s_x s_y & \epsilon_p + t_{pp}\, c_y \end{pmatrix} , \tag{3.11}$$
$$s_{x,y} = \sin\left(k_{x,y}/2\right) , \quad c_{x,y} = \cos\left(k_{x,y}\right) ,$$

with on-site energies ϵ_d, ϵ_p and hopping integrals t_{pp}, t_{pd}. LDA-values of these parameters [55] for La_2CuO_4 are used as a starting point. The importance of the oxygen-oxygen hopping t_{pp} has been extensively discussed [5, 7–9, 54] for the strong coupling case. At weak coupling, in its absence the leading instability of the system would correspond to commensurate AFM due to perfect nesting. In the improper basis chosen here, $\mathcal{H}_0$ is not 2π-periodic due to the $s_{x/y}$-entries, but real-valued. In Appendix B.1.1, this is discussed in further detail in the absense of oxygen-oxygen hopping. It is easy to verify that the statements made for vanishing t_{pp} also hold in the presence of oxygen-oxygen hopping. As pointed out in Appendix B.1.1, all momenta still must be folded back to the first Brillouin zone.

In addition to this one-particle Hamiltonian, a short-ranged interaction term

$$\begin{aligned} H_{\text{int}} = U_d \sum_i n_{d,\uparrow}(\mathbf{R}_i)\, n_{d,\downarrow}(\mathbf{R}_i) + U_p \sum_j n_{p,\uparrow}(\mathbf{R}_j)\, n_{p,\downarrow}(\mathbf{R}_j) \\ + U_{pd} \sum_{\langle ij \rangle} n_d(\mathbf{R}_i)\, n_p(\mathbf{R}_j) + U_{pp} \sum_{\langle jj' \rangle} n_p(\mathbf{R}_j)\, n_p(\mathbf{R}_{j'}) , \end{aligned}$$

is considered, where the brackets $\langle ij \rangle$ and $\langle jj' \rangle$ indicate that the sum only runs over neighboring orbitals of the respective types. The results in the following section are restricted to weak interaction strengths, i.e. the typical energy scales of the interaction are about one order of magnitude below the values given in Ref. [55] for La_2CuO_4. Interaction terms involving the oxygen p-orbitals are weak compared the the dominating U_d-term and are thus often neglected in the literature (see Ref. [9] for example).

Within the fermionic fRG approach pursued in the following, it turns out to be advantageous to write the quadratic part of the Hamiltonian in its diagonalized form, i.e. in terms of bands instead of orbitals. The field operators then correspond to Bloch states that do not get mixed by the one-particle part of the Hamiltonian. The band dispersion of the Emery model is depicted in Fig. 3.9 for typical parameter values. The chemical potential μ is chosen to values around van-Hove filling μ_{vH} where the Fermi surface touches the saddle points at $(0, \pi)$ and $(\pi, 0)$ of the uppermost band. One then obtains one conduction band which is separated from two valence bands by an energy gap of about four times its width. Through the orbital weight imposed by the unitary transformation from the orbital to the band picture, the interaction acquires a nontrivial momentum dependence, dubbed *orbital makeup* [52] by some authors (cf. Chapter 2.1.2 for a quantitative

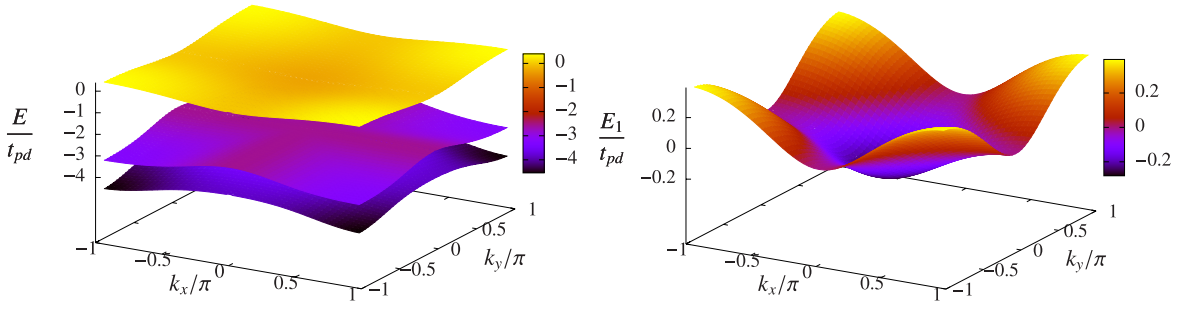

(a) All bands (b) Blow up for the conduction band

Figure 3.9.: Bandstructure (a) of the Emery model for the dispersion parameters given in Tab. 3.3 and at van-Hove filling and a blow-up for the conduction band (b).

description). From the form of the one-particle Hamiltonian Eq. (3.11), one finds that the hybridization of the d- and p-orbitals grows from the center to the boundary of the Brioullin zone.

3.2.2. Effective one-band Hubbard model

In principle, an appropriate low-energy solver could be directly applied to the full three-band model. Such a solver would effectively resum diagrams up to infinite order, even if the underlying concept is of non-perturbative nature. The result of such a resummation at weak to moderate coupling will be dominated by diagrams with internal legs on the conduction band. It should therefore suffice to treat the valence bands perturbatively only up to a certain order. Such an approach has been layed out in Chapter 2.3.1, where a prescription for the calculation of an effective action $\mathcal{A}_{\text{eff}}$ for the conduction band has been given. In the following section, RG flows starting from $\mathcal{A}_{\text{eff}}$ will be considered both in the conventional and in the 3PF truncation.

One may now wonder what features of the effective one-band actions play a major role at low temperatures. If this question can be answered, these features could be incorporated into a simpler, effective single-band model. In the conventional truncation, the (t, t') one-band Hubbard model seems to be a good candidate for such an effective low-energy model. The corresponding Hamiltonian reads as

$$H = \left[t \sum_{\langle ij \rangle, \sigma} c^\dagger_{\sigma,i} c_{\sigma,j} + t' \sum_{\langle\langle ij \rangle\rangle, \sigma} c^\dagger_{\sigma,i} c_{\sigma,j} + \text{h.c.} \right] + U_{\text{eff}} \sum_i : n_{\uparrow,i}\, n_{\downarrow,i} : , \tag{3.12}$$

where $n_{\sigma,i} = c^\dagger_{\sigma,i} c_{\sigma,i}$ and where $\langle\langle ij \rangle\rangle$ indicates that the sum runs over second neighbors.

Before I give a prescription how the effective parameters t, t' and U_{eff} can be calculated, I will briefly elaborate on the differences between the effective action Eq. (2.18) for the conduction band and the effective one-band Hamiltonian Eq. (3.12). The frequency dependence of the action corresponding to Eq. (3.12) will of course be trivial in contrast to the frequency dependence in $\mathcal{A}_{\text{eff}}$ which is generated by integrating out the valence bands. Throughout this chapter, I will, however, project to zero frequency and hence such effects are not discussed. Recently, frequency-dependent RG flows have been analyzed for the two-dimensional one-band Hubbard model. [25, 26] In this context, also frequency-dependent multiorbital effects appear to be worth further study.

As far as the momentum dependence is concerned, the Hamiltonian Eq. (3.12) is short-ranged in the sense that all terms are either on-site or describe hopping between first and second neighbors at most. In contrast, $\mathcal{A}_{\text{eff}}$ may contain quite long-ranged terms both in the dispersion and in the two-particle interaction. At van-Hove filling, the restriction to only two hopping integrals in Eq. (3.12) can be justified in the spirit of a gradient expansion. Since the density of states diverges at the saddle points $A = (0, \pi)$ and $B = (\pi, 0)$, the integrals over momenta of internal lines in a perturbation expansion will be dominated by a small region around these saddle points. Consequently, in leading order in an expansion around the van-Hove points, the exact and an approximate dispersion should coincide. Since a $k_x k_y$-term is forbidden by symmetries, only two expansion coefficients remain in leading (second) order. They can be expressed in terms of effective first and second neighbor hoppings t and t'.

Away from van-Hove filling, the situation may be more involved and hopping terms between non-neighboring unit cells of the direct lattice may be needed for an effective model. Since this corresponds to Wannier functions that have support on more than one unit cell, such a description is not really of tight-binding type. The effective two-particle interaction will also bear traces of the multiorbital character of the underlying model. More precisely, the orbital makeup renders the interaction nonlocal. Whether this feature plays a role for the low-energy physics remains a question to be answered by applying a low-energy solver.

Before doing so, I now give a prescription according to which the effective Hubbard parameters t, t' and U_{eff} can be calculated. From the comments made above, a gradient expansion around the saddle points of the dispersion appears natural as a guiding principle. So the calculation of t and t' is straightforward.

For the interaction, I proceed as follows. First, let $U(k_1, k_2, k_3)$ denote the bare coupling function that appears in the symmetric parametrization (1.6) of the effective two-particle interaction for the conduction band. and further assume a basis of Bloch states that ensures a trivial behavior of this coupling function under C_{4v} operations. In Chapter 2.2, it has been shown that such a Bloch basis exists. Note that this property is nontrivial, since the oxygen p-orbitals are mapped onto one another upon a rotation of $\pi/2$.

As a second step, the two-particle interaction is expanded around the saddle-points. In leading order, one then again obtains the four two-particle couplings of the two-patch approximation, namely

$$\begin{aligned} g_1 &= U(A,B,B) = U(B,A,A) \\ g_2 &= U(A,B,A) = U(B,A,B) \\ g_3 &= U(A,A,B) = U(B,B,A) \\ g_4 &= U(A,A,A) = U(B,B,B)\,. \end{aligned}$$

For the Hubbard model, all four two-patch couplings g_i are equal to U_{eff}. For given $\mathcal{A}_{\text{eff}}^{(4)}$, the average of the two-patch couplings $U_{\text{eff}} = \sum_i g_i/4$ is therefore taken as the effective Hubbard interaction, while the hopping parameters t and t' are calculated from a gradient expansion. This means that the parameters of the one-band Hubbard model are chosen such that it has a common two-patch approximation with $\mathcal{A}_{\text{eff}}$ and that the hopping terms are further restricted to neighboring unit cells and the interaction to an on-site density-density term in the effective one-band Hamiltonian. Note that, in contrast to the famous work by Zhang and Rice, [111] which has been tailored rather for the strong-coupling case, this method is non-perturbative in the hybridization between the orbitals.

3.2.3. Classification of multiband effects

We are now in a position for a classification of multiorbital effects. Clearly, if one has a full model [in the present case $\mathcal{A}_{\text{eff}}$ given in Eq. (2.18)] and an effective one-orbital Hamiltonian [e.g. the Hubbard Hamiltonian in Eq. (3.12)], effects contained in the full, but not in the effective model are of multiorbital character. Of course, the multiorbital nature cannot be attributed to a certain effect without referring to a prescription according to which the full model is mapped to its effective single-orbital counterpart. So, in the following, multiorbital effects will be classified with respect to the above prescription based on a gradient expansion around the saddle points of the dispersion.

In this picture, multiorbital effects decay into three classes, namely

i) effects resulting from the three-particle interaction, and other higher-order vertices generated by the high-energy bands,

ii) orbital-makeup effects, in particular a detuning of the two-patch couplings g_i,

iii) hopping between non-neighboring unit cells.

The three-particle and higher-order vertices responsible for the effects listed as i) appear as (perturbative) corrections as described in Chapter 2.3.1 and in Chapter 2.4. Since

these corrections also contain internal loops with valence-band propagators, they are in general frequency-dependent. Throughout this thesis, four-particle and higher-order terms are neglected as well as contributions with closed valence-band loops (see Fig. 2.1 for the remaining diagrams). Since then only tree-diagrams of bare vertices in the perturbative expansion of $\mathcal{V}$ (i.e. diagrams that are reducible to bare vertices by cutting one internal line) are included, the two- and three particle interaction terms of $\mathcal{A}_{\text{eff}}$ are frequency-independent in this approximation. Hence, the frequency dependence of $\mathcal{A}_{\text{eff}}$ is completely neglected in this chapter.

In the following, the three-particle term of $\mathcal{A}_{\text{eff}}$ will be either neglected or fed back into the flow equation of the two-particle vertex using the 3PF extended truncation of the fRG flow equations introduced in Chapter 2.4. It will turn out to play a minor role due to the large gap between the conduction band and the valence bands.

As far as orbital makeup effects are concerned, the discussion will thus be restricted to the two-particle interaction although the three-particle term obviously bears signatures of orbital makeup. Deviations of the two-particle interaction from the on-site Hubbard type manifest themselves in a detuning of the two-patch couplings g_i and in a nontrivial momentum dependence also away from the saddle points of the dispersion. These effects have been listed as ii) above. This implies that orbital makeup effects can be partly understood with the help of the flow equations (3.6-3.9) in the two-patch approximation. By looking at the bare one-particle part Eq. (3.11) of the Emery Hamiltonian, however, one can observe that the hybridization between the d and p orbitals is stronger at the saddle points than in other parts of the Brillouin zone. For example, at the origin in k-space, there is no hybridization at all. Therefore, there is a pronounced momentum dependence which may lead to effects that cannot be captured in the two-patch approximation.

The effective action $\mathcal{A}_{\text{eff}}$ and the effective single-orbital Hamiltonian H_{eff} also differ in their quadratic parts. If the dispersion of the conduction band in the former is expanded around its saddle points, also hopping terms between non-neighboring unit cells appear in the coefficients in subleading orders. As already mentioned, these longer-range hopping integrals do not fit well into a tight-binding picture, as this would correspond to Wannier functions with long tails. Since the conduction band is predominantly of d-orbital character, the hybridization with oxygen p-orbitals can be said to create such tails. Assuming that the single-band Hubbard model provides a good description, one may expect hopping between non-neighboring unit cells to play a minor role for the Emery model at weak coupling.

t_{pp}	$\epsilon_p - \epsilon_d$	U_d	U_p	U_{pd}	U_{pp}
$0.5\,t_{pd}$	$-2.77\,t_{pd}$	$0.385\,t_{pd}$	$U_d/8$	$U_d/16$	0

Table 3.3.: Generic parameter set with $t_{pd} > 0$. The values for the dispersion are chosen according to Ref. [55], while the interactions parameters given in that work have been lowered by a factor of $1/20$. The parameters of the corresponding one-band Hubbard model are $t = 9.8 \cdot 10^{-2}\,t_{pd}$, $t' = -0.26\,t$ and $U_{\text{eff}} = 2.73\,t$.

3.3. Instability analysis of the Emery model

In this section, an instability analysis is performed in order to obtain an approximate zero-temperature phase diagram of the Emery model. The parameters in the Emery Hamiltonian will be varied around the generic values in Tab. 3.3 and the chemical potential will take on values around van-Hove filling. All considered filling factors will then be on the hole-doped side. As before, a Ω-scheme multiplicative regulator [cf. Eq. (3.5)] is employed, in order to take also a possible Stoner instability and phases with loop-currents [104, 105] into account. The parameter range considered, however, the antiferromagnetism (AFM) and d-wave superconductivity (dSC) are found to be the leading instabilities. First, the RG flow will be run in the conventional truncation, i.e. without the three-particle feedback. The stability of the results against variation of those parameters and against three-particle feedback is then tested. Finally, the Emery model is compared to the corresponding one-band Hubbard model.

3.3.1. fRG Implementation

Due to the nontrivial momentum dependence of the bare interaction, an fRG approach beyond the traditional Fermi surface patching [23] seems desirable. Therefore, I will resort to a channel decomposition of the flow equations. Based on ideas of Jutta Ortloff, who has implemented a precursor algorithm [67], I present a new channel-decomposed approach that differs from the form-factor expansion (FFE) of Refs. [24–26, 33, 43, 44] in the following way: Instead of employing a FFE, all three momenta of the single-channels coupling functions $\Phi_{\text{SC}}, \Phi_{\text{M}}$ and Φ_{K} introduced in Chapter 1.2.2 are patched directly while all frequencies are projected to zero. The fermionic momenta are then put on a much coarser grid than the bosonic ones. The finest resolution is only used for the bosonic momenta around potential divergencies and for the internal loop momenta close to the Fermi surface. If not indicated otherwise, I use 6×6 fermionic quadratic patches and a bosonic resolution of 18×18 and of 126×126 patches away from and close to possible ordering vectors, respectively. The Pauli principle, point-group and particle-hole symmetries reduce the number of independent couplings further. Note that, close to the transition from $d_{x^2-y^2}$-wave SC to ferromagnetism in the one-band Hubbard model,

this resolution would be still too coarse in the fermionic momenta. [67] The parameters considered in this section, however, lie far away from such a transition and a deformation of the form factors at low energies should at least qualitatively be captured within the present approach.

Since the frequencies are projected to zero, the Matsubara sums over internal frequencies can be performed analytically as in Ref. [112]. For the Ω-scheme regularization employed in this work, the remaining two-dimensional loop integrals are numerically challenging. They can be efficiently calculated using an adaptive routine. [110] For different patches, these loop integrals are evaluated in parallel using OpenMP and then stored. When the diagrams are subsequently assembled, their calculation is again OpenMP parallelized for different external momenta. Note that this algorithm does not scale properly with a large number of CPU. Within a shared-memory approach, the code will drown in cache-level misses with increasing non-uniformity of the memory architecture. In a distributed memory approach, one should as well expect massive communication overhead prohibiting the usage of large clusters. Therefore, extensions to frequency-dependent vertices and to self-energy feedback are not straightforward tasks.

External fields breaking the U(1), SU(2) and/or space group symmetries are sent to zero right from the beginning. The resulting decrease of computational effort, however, comes with a price. The limit of vanishing external fields is only physical *after* the thermodynamic limit has been performed. Consequently, spontaneous breaking of a symmetry manifests itself in a flow to strong coupling. The flow is therefore stopped when the maximum of the coupling functions reaches $7.7\,t_{pd}$, and the stopping scale λ_c is interpreted as an estimate for the critical scale of the respective instability.[1] Note that this stopping condition is rather weak, since $7.7\,t_{pd}$ corresponds to about thirteen times the bandwidth of the conduction band. In comparison, in Ref. [24], the flow is stopped once the interactions exceed 2.5 times the bandwidth. For the present subsection, I have not chosen a stronger stopping condition in order to keep track of the strong competition of AFM and dSC instabilities that will be discussed in the following subsection.

3.3.2. Nature of the leading instability

For the generic parameters in Tab. 3.3 and at van-Hove filling, one can observe a flow to strong coupling at about $\lambda_\mathrm{c} = 2.9 \cdot 10^{-3}\,t_{pd}$, which roughly corresponds to 50 K for $t_{pd} = 1.3\,\mathrm{eV}$. In order to determine the nature of this instability, the coupling functions Φ_SC, Φ_M and Φ_K are diagonalized at the stopping scale. The largest of the eigenvalues of these three coupling functions is then attributed to the leading instability, which is

[1] As for a conventional momentum shell cutoff, the particle-particle susceptibility in the Ω-scheme diverges at a scale $\lambda_\mathrm{c} \propto e^{-1/(U\rho_0)}$ for a BCS-type interaction of strength U and a constant density of states ρ_0 near the Fermi level. Therefore, λ_c is proportional to the BCS critical temperature.

characterized by an optimized form factor given by the corresponding eigenvector (see Chapter 1.2.3 for further details).

For the parameter sets considered in the following, the most relevant eigenvalues in the pairing and the magnetic channels compete. Let me first describe the results for the generic parameter set of Tab. 3.3 and at van-Hove filling. The optimized form factors for this parameter set are depicted in Fig. 3.10. In the pairing channel, contributions with total wavevector $\mathbf{l} = 0$ dominate clearly. The optimized form factor corresponds to a $d_{x^2-y^2}$-wave, with peaks that are a little broader than for $f_d = \cos(q_x) - \cos(q_y)$ (cf. Fig. 3.10(b)). I will comment on the admixture of higher harmonics to this optimized form factor further below. In the magnetic channel, the optimized form factor corresponds to a deformed s-wave with small admixtures of higher harmonics. For the generic parameter set, one finds slightly incommensurate magnetic ordering vectors on the boundary of the Brillouin zone. Inequivalent IRs of C_{4v} may hence mix. In the case of the generic parameter set of Tab. 3.3, one can indeed observe small admixtures of other IRs to the s-wave contributions of the optimized form factor. For example, a small $d_{x^2-y^2}$-wave admixture is clearly visible.

Other types of instabilities such as a Pomeranchuk instability [21, 113–116] and the formation of different types of loop currents [104, 105, 117] do not participate in the competition of the most relevant instabilities. For the former type of ordering, the results presented here are in agreement with Ref. [116], where the experimentally observed nematic tendency [118–121] in cuprate materials appears to be of strong-coupling nature. Similarly, the absence of loop currents is not surprising in a weak-coupling scenario, since the critical interaction strengths are found to be quite large in mean-field calculations. [105]

At van-Hove filling, one can expect that it is possible to tune the Emery model to a Stoner-like ferromagnetic instability by raising the value of t_{pp}. For the parameter sets considered in this work, however, ferromagnetism is not found to prevail over other ordering tendencies. I hence conclude that a Stoner instability only occurs for oxygen-oxygen hopping parameters that are far away from the generic value of t_{pp} in Tab. 3.3.

At the stopping scale, I also consider a FFE of the full coupling function V obtained within the new approach outlined in Section 3.3.1 for comparison. This expansion is truncated behind the most slowly varying form factors. Note that this should not be confused with the results obtained from RG flow equations in an exchange parametrization, as mixing between different irreducible representations of C_{4v} and the admixture of higher harmonics are taken into account in the integration of the flow equations. The propagator D_d of $d_{x^2-y^2}$-wave Copper pairs rescaled by the square strength of the fermion-boson interaction then reads as

$$D_d(l) = \int d\mathbf{q}\, d\mathbf{q}'\, f_d(l/2-q)\, f_d(l/2-q')\; V(q, l-q, q')|_{q_0=q_0'=l_0/2}\ ,$$

where $f_d(k) = \cos(k_x) - \cos(k_y)$. In the following, I will simply refer to D_d as a bosonic propagator despite the rescaling by an energy-squared factor. Likewise, the propagator of the magnetic s-wave exchange-boson is obtained as

$$M_s(l) = \int d\mathbf{q}\, d\mathbf{q}'\, f_s(l/2+q)\, f_s(-l/2+q')\; V(q,q',l+q)|_{q_0=-q_0'=-l_0/2}\ ,$$

with $f_s(k) = 1$. Note that this FFE is only viable if the basis of Bloch states is properly chosen such that V is invariant under all point-group transformations of the lattice.

In Fig. 3.11, $D_d(l)$ and $M_s(l)$ are depicted for the generic parameter set in Tab. 3.3 at the stopping scale. Both $d_{x^2-y^2}$-wave Cooper-pair and magnetic s-wave propagators show peaks with values close to the corresponding eigenvalues of the coupling functions of the respective channel. Since the dSC peak is quite sharp while the incommensurate peaks of the magnetic propagator have a broader width, $d_{x^2-y^2}$-wave superconductivity might prevail in a situation where the two most relevant instabilities are closely competing. In any case, the system is in a regime of two competing, mutually reinforcing instabilities. In this place, I would like to recapitulate that a quite weak stopping condition is used. Therefore, if the magnetic and pairing channels are still of comparable strength at the stopping scale, these two channels are then indeed closely competing and this competition itself might have some physical content.

In Ref. [23], the parameter-space region of strong AFM-dSC competition was dubbed the *saddle-point regime* and interpreted as an insulating spin-liquid phase. It may also contain a region of homogeneous coexistence as described for the iron pnictides in Ref. [122]. It is likely that a large part of this regime has a non-vanishing superconducting gap. Unfortunately, order parameters are not directly accessible within the present instability analysis. In a recent fRG approach to the one-band Hubbard model using rebosonization techniques, [64] it has however been found that pairing is avoided inside the antiferromagnetic phase. This is not surprising, since at least parts of the Fermi surface are gapped away once spontaneous symmetry-breaking in one channel sets in, which hampers symmetry-breaking in the other channels. A very recent purely fermionic study on the fRG flow of the repulsive single-band Hubbard model into the superconducting phase is in full agreement with this picture. [50] In that work, a non-vanishing pairing gap is indeed found in a large subregion of the saddle-point regime. So a putative coexistence phase should be considerably smaller than the saddle-point regime. In principle, a two-order-parameter mean-field approach is viable below the stopping scale, [22] but of course such a treatment is not free of bias.

In the following, the character of the instability will turn out to be quite robust against slight variations of the parameters. The stopping scale is then found to be sensitive to the chemical potential μ and to the diagonal oxygen-oxygen hopping t_{pp}. This latter dependence is already rather smooth, if the oxygen-oxygen hopping is not to far away from its generic value. So the behavior around the generic parameters suggests that

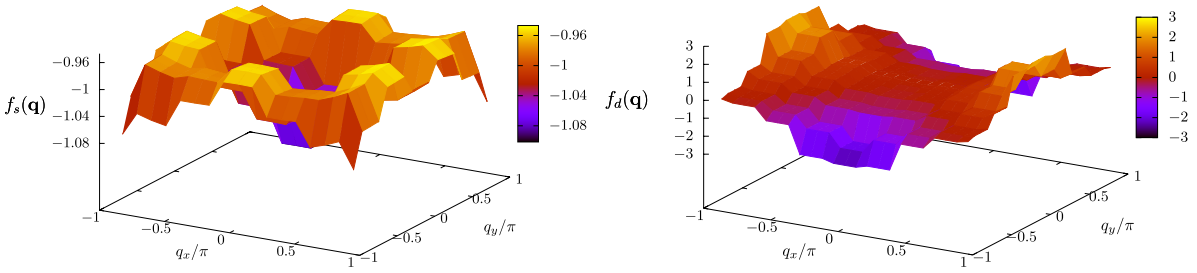

(a) Pairing d-wave (b) Magnetic s-wave

Figure 3.10.: Optimized from factors f_d and f_s as functions of the 'fermionic' wavevector $\mathbf{q}$. These form factors are obtained as eigenvectors corresponding to the most relevant eigenvalues for the generic parameter set of Tab. 3.3 at the stopping scale in the pairing and magnetic channels, respectively. Note that both optimized form factors are close to the most slowly varying basis functions of the respective irreducible representation of C_{4v}. Due to the incommensurability of the ordering vector, f_s in (a) shows slight admixtures of other irreducible representations.

the system is close to a first-order phase transition between AFM and dSC, as second-order transition would probably go along with a kink of the critical scale. Since the RG stopping scale is an upper estimate for the critical scale, such a kink may however be hidden. For the one-band Hubbard model close to van-Hove filling, a similar behavior has been observed. [22–24]

3.3.3. Doping dependence

The system also stays in the saddle-point regime when the doping level is slightly varied. In Fig. 3.12, the stopping scale for the parameters in Tab. 3.3 is plotted as a function of μ (+-markers). In the following, the hole filling factor is defined as the number of holes per unit cell and spin orientation that have been doped into the originally half-filled conduction band, or, more formally,

$$n_\mathrm{h} = \frac{1}{2} - \int d\mathbf{k}\, \Theta\left[\mu - \epsilon(\mathbf{k})\right] , \tag{3.13}$$

where $\epsilon(\mathbf{k})$ and $\Theta(x)$ denote the dispersion of the conduction band and the Heaviside step function, respectively. Note that n_h may differ for the dispersions of the Emery model and the single-band model with effective parameters calculated according to Section 3.2.2. In the following, all values of n_h will be for the Emery model.

The doping level varies between $n_\mathrm{h} = 6.5 \cdot 10^{-2}$ and $14.3 \cdot 10^{-2}$ and at van-Hove filling the filling factor is 0.115. Between half-filling ($n_\mathrm{h} = 0$) and van-Hove filling, the stopping scale only varies slightly. The AFM and dSC instabilities are closely competing, except

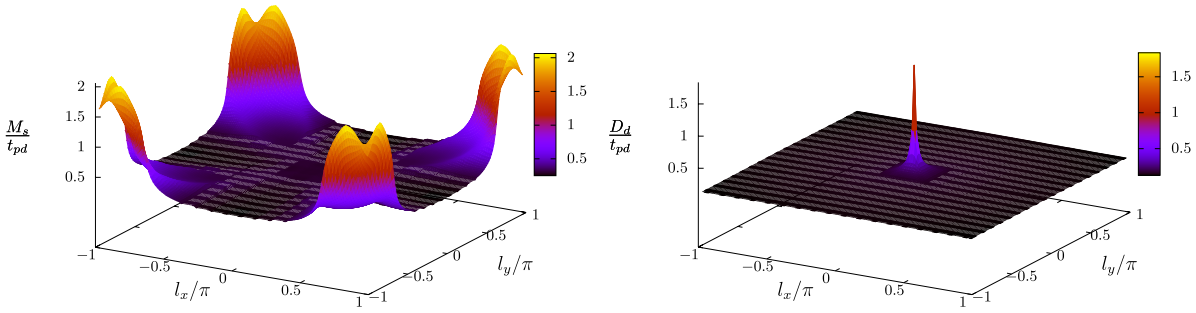

(a) Magnetic s-wave (b) Pairing d-wave

Figure 3.11.: Bosonic propagators at zero frequency corresponding to the most slowly varying basis functions for s-wave magnetism (a) and $d_{x^2-y^2}$-wave Cooper pairs (b) at the stopping scale for the parameters in Tab. 3.3, as functions of the bosonic wavevector $\mathbf{l}$.

$(\mu_{\mathrm{vH}} - \mu)/t_{pd} \cdot 10^3$	-15.4	-7.69	-3.85	0	3.85	7.69
$n_{\mathrm{h}} \cdot 10^2$	6.5	8.7	9.9	11.5	13.1	14.3

Table 3.4.: Filling factors n_{h} defined as in Eq. (3.13) for the parameters set in Tab. 3.3.

for $n_{\mathrm{h}} < 0.09$, where AFM clearly prevails. At hole doping beyond van-Hove filling, the stopping scale decreases rapidly and the tendency to $d_{x^2-y^2}$-wave pairing gets a little stronger. Qualitatively, this behavior is analogous to the hole-doped one-band Hubbard model. [23]

The enhanced $d_{x^2-y^2}$-wave pairing at hole doping beyond van-Hove filling, however, comes with a broadening of the $d_{x^2-y^2}$-wave form factor at the van-Hove points as can be seen from Fig. 3.13. Moreover, the magnetic s-wave propagator is of interest. It is depicted in Fig. 3.14 at varying hole doping. For $n_{\mathrm{h}} \leq 0.09$, it shows a peak at the commensurate ordering vector $\mathbf{l} = (\pi, \pi)$. At about van-Hove filling, the commensurate peak of M_s is split into four ones at incommensurate ordering vectors. The deviation of the ordering vector from (π, π) then increases with hole doping, corresponding to the shift of Fermi surface segments at high density of states.

The highly incommensurate peaks at $n_{\mathrm{h}} = 0.14$ (i.e. at hole doping significantly beyond van-Hove filling) still allow the Kohn-Luttinger effect to generate an attractive d-wave pairing component. This however goes along with a strong deformation of the form factor f_d for d-wave pairing (see Fig. 3.13). Such a simultaneous occurrence of incommensurability in the magnetic channel and a deformation of the fermion-boson vertex in the Cooper channel has already been observed in the one-band (t, t') Hubbard model [67] and may be explained as follows. Consider a singlet Copper pair with momenta $(\mathbf{k}, -\mathbf{k})$ scattered to $(\mathbf{k}', -\mathbf{k}')$ by the interaction in the Cooper channel which shall be mimicked by a one-loop particle-particle diagram with two spin-channel vertices. If these vertices

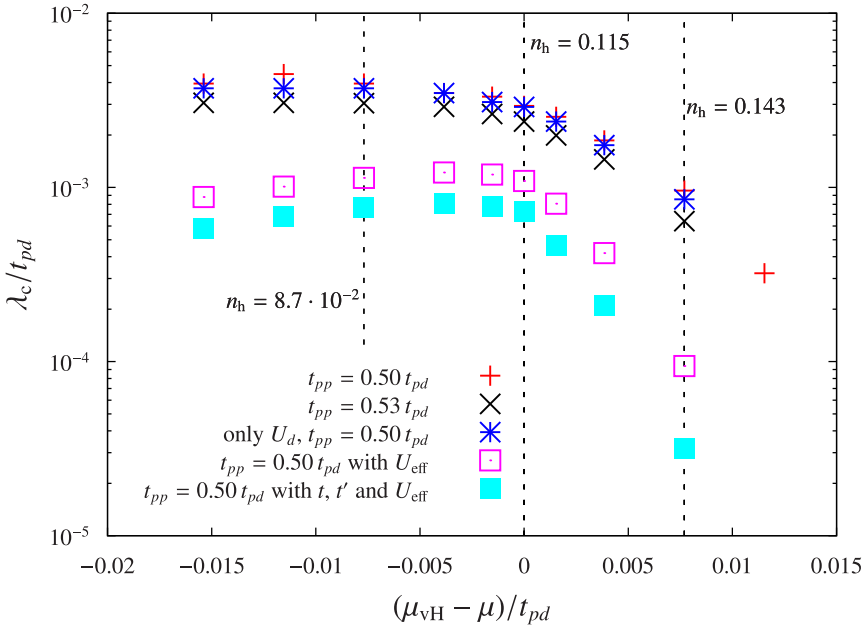

Figure 3.12.: Doping dependence of the stopping scale around van-Hove filling. The curve with +-markers is for the generic parameter set in Tab. 3.3, and the one with x-markers is for $t_{pp} = 0.53 t_{pd}$ while all over parameters are left unchanged. The star-like markers depict the stopping scales for an interaction with a U_d-term only. The other two curves are for effective models: Empty squares represent data for an effective on-site Hubbard interaction with the full dispersion of the Emery model for the generic parameter set. Filled square markers are for the effective t-t'-U_{eff} Hubbard model. The corresponding hole-fillings n_{h} can be found in Tab. 3.4. Note that these values are only for the Emery model and not necessarily for the single-band Hubbard model.

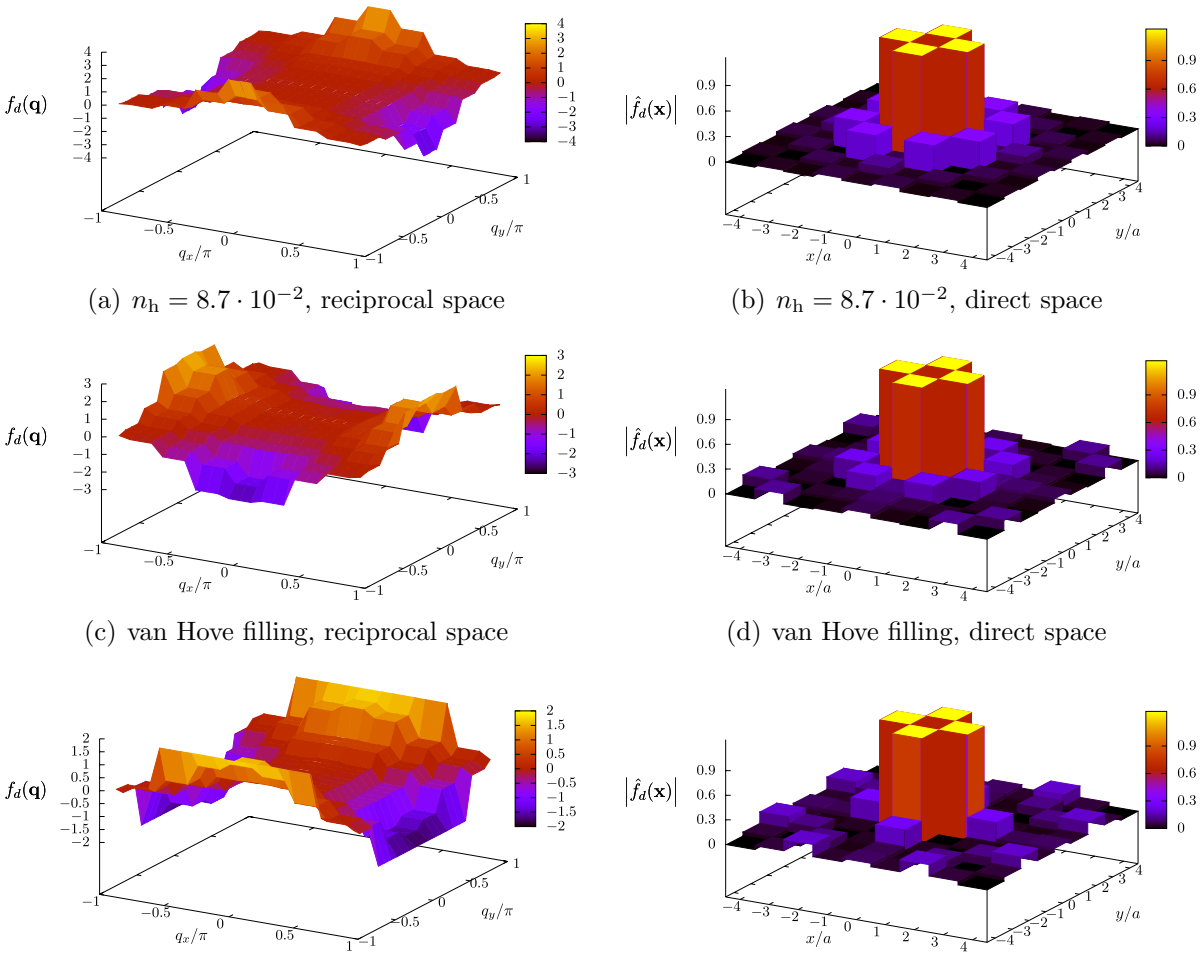

(a) $n_\mathrm{h} = 8.7 \cdot 10^{-2}$, reciprocal space

(b) $n_\mathrm{h} = 8.7 \cdot 10^{-2}$, direct space

(c) van Hove filling, reciprocal space

(d) van Hove filling, direct space

(e) $n_\mathrm{h} = 0.14$, reciprocal space

(f) $n_\mathrm{h} = 0.14$, direct space

Figure 3.13.: Deformation of the optimized $d_{x^2-y^2}$-wave form factor $f_d(\mathbf{q})$ in the Cooper channel at the stopping scale (a),(c),(e) and the absolute value of its Fourier components $\hat{f}_d(\mathbf{x})$ on the real lattice obtained from FFT (b),(d),(f). The central row (c),(d) is for van-Hove filling and the upper and lower ones for $n_\mathrm{h} = 8.7 \cdot 10^{-2}$ (a),(b) and for $n_\mathrm{h} = 0.14$ (e),(f), respectively. All other parameters are chosen as in Tab. 3.3. The form factors have been normalized to $\int dq\ |f_d(q)|^2 = 1$. $f_d(\mathbf{q})$ gets broadened at the saddle points with increasing hole doping. The (discrete) direct-space coordinate corresponds to the distance of two electrons forming a Cooper pair. For all three filling factors considered here, the main contribution to the pairing comes from electrons residing on neighboring sites, which corresponds to $f_d = \cos(q_x) - \cos(q_y)$ in reciprocal space. Admixtures of higher harmonics are present in all three cases and get shifted away from the origin at hole doping beyond van-Hove filling.

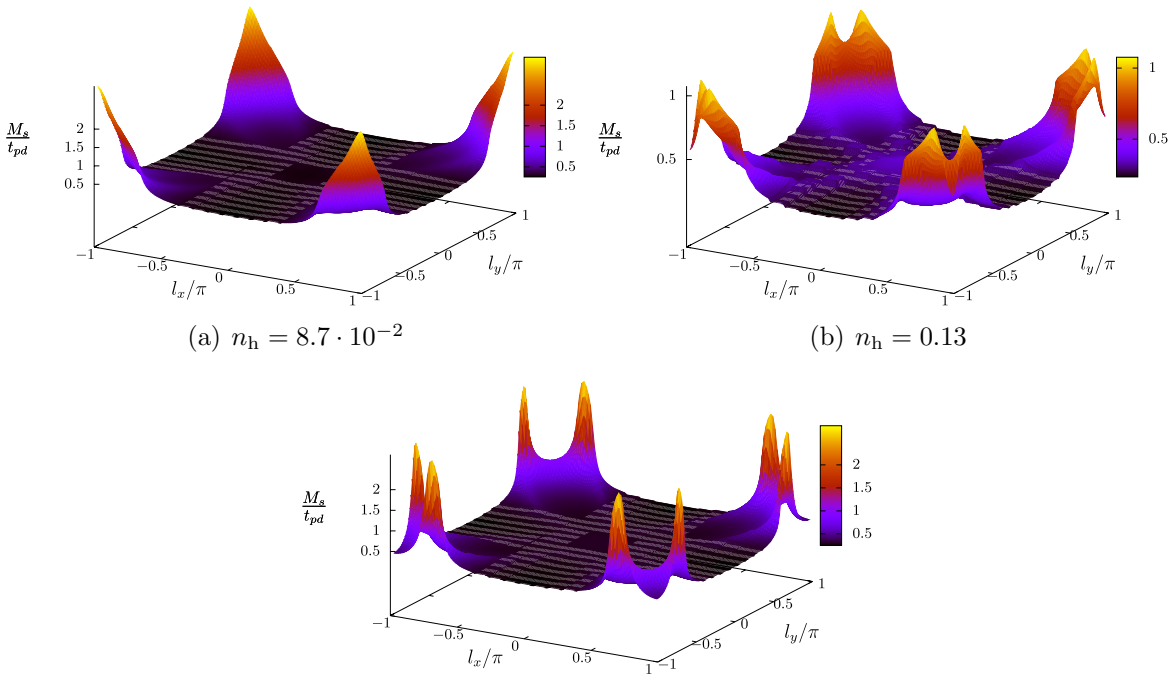

(a) $n_\mathrm{h} = 8.7 \cdot 10^{-2}$

(b) $n_\mathrm{h} = 0.13$

(c) $n_\mathrm{h} = 0.14$

Figure 3.14.: Magnetic s-wave propagator as function of the bosonic wavevector $\mathbf{l}$ at the stopping scale for $n_\mathrm{h} = 8.7{\cdot}10^{-2}$ (a), $n_\mathrm{h} = 0.13$ (b) and $n_\mathrm{h} = 0.14$ (c). All other parameters are chosen as in Tab. 3.3.

have their peaks at transfer momentum $\mathbf{l} = \mathbf{Q} = (\pi, \pi)$, the main contribution to the Cooper channel comes from $\mathbf{k}' = \mathbf{k}$. For incommensurate ordering vectors, the important contributions come from $\mathbf{k}' = \mathbf{k}$ as well as from $\mathbf{k}' = \mathbf{k} + \mathbf{Q}_i + \mathbf{Q}_j$, where i and j may correspond to all possible combinations of the ordering vectors. The dependence of fermion-boson vertex in the Cooper channel on the fermionic momenta is hence smeared out around $(0, \pi)$ and $(\pi, 0)$ resulting in a broadening of the form factor. A shoulder-like broadening of the peaks of M_s would give rise to the same effect in a similar way.

While higher harmonics do not contribute at the so-called anti-nodal points $(0, \pi)$ and $(\pi, 0)$, they may change the slope of the gap at the nodal points. Such an occurrence of multiple energy scales for the gap has been observed in Raman spectroscopy [123] and angle-resolved photoemission spectroscopy [124] experiments. In contrast to the results for weak coupling presented here, Ref. [123] suggests decreasing contributions of higher harmonics with hole doping. This may be due to the strong-coupling nature of real cuprate materials.

As the Fourier transform of the form factor in the pairing channel corresponds to the distribution of the distance between the electrons forming a Cooper pair, deviations from the $\cos(q_x) - \cos(q_y)$-form may also be analyzed in real space (see lower row in Fig. 3.13). One should, however, be aware that an interpretation in real space requires some care, since basis sets of Wannier functions may strongly differ in their localization properties (cf. Chapter 2.1.1). The position argument in the real-space form factors then corresponds to the relative distance between the constituents of such a pair, i.e. the two electrons or holes involved. Note that this distance can be resolved up to only n sites in all directions for $2n \times 2n$ fermionic patches. Therefore the flow for some parameters has been studied with a resolution of 8×8 fermionic and 24×24 or 120×120 bosonic patches away from and close to possible ordering vectors, respectively. The results are displayed in Fig. 3.13. One can observe that the most important contribution corresponds to a $\cos(q_x) - \cos(q_y)$-form. But already at van-Hove filling, an admixture of higher harmonics is visible, which partly get shifted further away from the origin at hole doping beyond van-Hove filling. A thorough discussion of the minor contributions corresponding to Cooper pairing beyond nearest neighbors may require a resolution higher than 8×8 fermionic patches.

Before I analyze the impact of the t_{pp}-hopping parameter, a remark on the effects of the coupling between the different channels seems to be in order. These effects go far beyond the spin-fluctuation induced generation of an attractive pairing interaction. In particular, if the magnetic propagator was calculated within RPA, i.e. if the Cooper and forward-scattering channels were neglected in the flow, the stopping scale would be about one decade higher. Moreover, the magnetic propagator would be less sharply peaked. This behavior can be attributed to the feedback of the Cooper on the magnetic channel, which hampers antiferromagnetism before the $d_{x^2-y^2}$-wave pairing interaction gets attractive. On a qualitative level, this effect is already captured in the flow equations

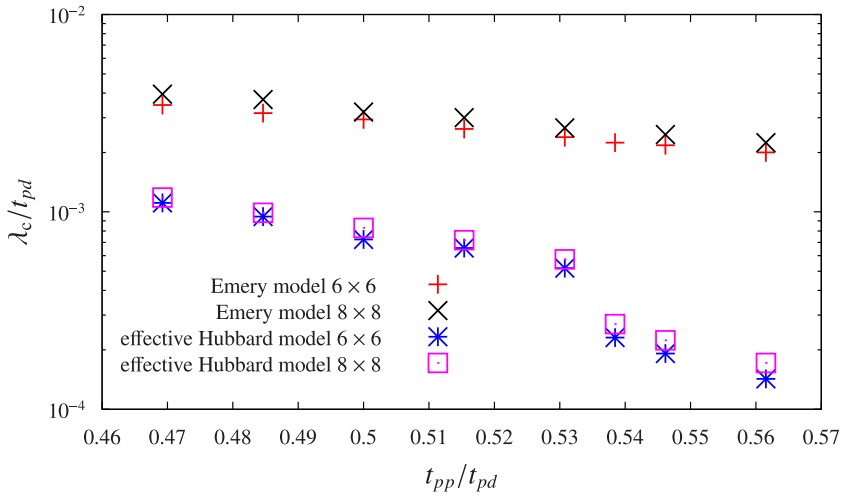

Figure 3.15.: Variation of the stopping scale with t_{pp} at van-Hove filling. All other parameters are chosen according to Tab. 3.3. The $d_{x^2-y^2}$-wave pairing tendency increases with t_{pp}/t_{pd}.

(3.6-3.9) in two-patch approximation.

3.3.4. Dependence on hopping-between the p-orbitals

So far, I have only investigated the impact of doping away from van-Hove filling, but not the interplay between μ and t_{pp}. If, in this spirit, the hopping between the p-orbitals is now changed to $t_{pp} = 0.53\,t_{pd}$, the effective second-neighbor hopping in the conduction band gets stronger and the tendency to $d_{x^2-y^2}$-wave pairing should be enhanced. Indeed, the flow can now be attributed to the saddle point regime for all filling factors considered. The corresponding curve in Fig. 3.12 (x-markers), however, looks similar to the one for $t_{pp} = 0.50\,t_{pd}$ except for the insignificantly lower stopping scale. Moreover, at hole doping beyond van-Hove filling and at $t_{pp} = 0.53\,t_{pd}$, the tendency to dSC is only slightly enhanced compared to $t_{pp} = 0.5\,t_{pd}$. It therefore seems that a considerable region of the parameter space has to be attributed to the saddle-point regime as for the one-band Hubbard model in Ref. [23].

In Fig. 3.15, the dependence of the stopping scale on t_{pp} is depicted for van-Hove filling both for 6×6 and for 8×8 fermionic patches. The curves for the two resolutions almost coincide, indicating that 6×6 fermionic patches are sufficient. The stopping scale behaves as follows:

For the Emery model, a decrease of λ_c with increasing t_{pp} of less than one decade can be observed. Such a behavior is quite generic as, in the absence of orbital makeup, a more rounded Fermi surface depresses the stopping scale in other models. [41] Once t_{pp} exceeds

$0.54\,t_{pd}$, the flow to strong coupling bears rather the signatures of pure $d_{x^2-y^2}$-wave pairing than of the saddle-point regime. For the one-band Hubbard model with effective parameters, however, the situation is different: The stopping scales are much lower and drop abruptly as soon as the system enters the pure dSC regime at about $t_{pp} = 0.54\,t_{pd}$. This is apparently caused by an abrupt growth of the hybridization at the saddle points which reduces the effective interaction strength U_{eff}. Comparing the Emery model to its effective one-band Hubbard counterpart, one finds that orbital-makeup effects in the Emery model partly counteract the decrease of λ_{c} with a more rounded Fermi surface and that they prevent the stopping scale from dropping abruptly.

In Ref. [41], a similar behavior as been found for multiband models only involving orbitals on the Copper atoms. Also the DCQMC results of Ref. [12] support this conjecture. Namely, the critical temperature is found to increase with the value of t_{pp} in that work. At first glance, this seems to contradict fRG results discussed here. However, the calculations in Ref. [12] have been performed at strong coupling, where the orbital makeup seems to overcompensate the effect of the more rounded Fermi surface observed at weak coupling. Of course, this argument is not fully stringent, since, at strong coupling, mechanisms may be at work that do not occur in a perturbative picture.

3.3.5. Discussion of multiband effects

Let us now look at multiband effects more systematically. So far, I have discussed results for the full Emery model as given by the parameters in Tab. 3.3 and variations of t_{pp} and μ in a conventional truncation of the flow equations, i.e. without a three-particle term. If the feedback of this term is taken into account within the truncation proposed in Chapter 2.4, only insignificant changes of the stopping scale are found. Moreover, the tendency to dSC is slightly enhanced between half-filling and van-Hove filling, so that the system stays in the saddle point regime down to $n_{\text{h}} = 6.5 \cdot 10^{-2}$, as can be seen from the phase diagrams depicted in Fig. 3.16. Such minor modifications of the phase diagram seem quite surprising as those feedback terms had a great impact on the phase diagram of the two-band model of Section 3.1.4. Such a behavior of the three-particle feedback may, however, may be an artefact of the two-patch approach pursued in that section. Namely, the two-patch approximation only allows for a small number of strong-coupling fixed points, which results in a mutual exclusion of the Cooper and Stoner instabilities. Moreover, in the Emery model, the large gap between the conduction band and the valence bands results in a flat momentum structure of the diagrams corresponding to three-particle feedback terms. In a frequency-resolved study, the three-particle feedback may however play a more important role.

Before elaborating on other multiband effects, I now discuss the role of the oxygen p-orbitals in the two-particle interaction. First, let us look at the impact of a U_{pp}-term,

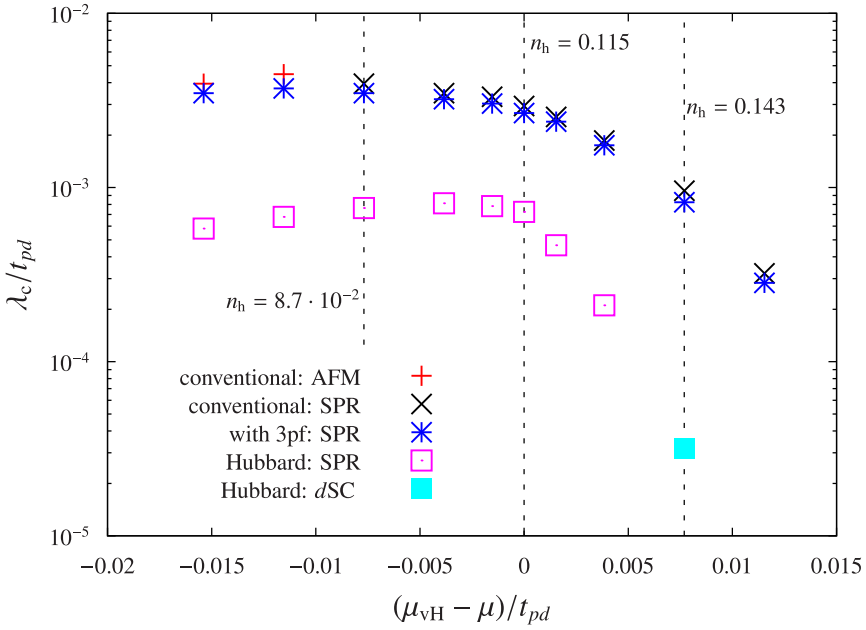

Figure 3.16.: Phase diagrams for the generic parameter set of Tab. 3.3 with and without three-particle feedback (3pf) and for the corresponding one-band Hubbard model. Large parts of these phase diagrams can be attributed to the saddle-point regime (SPR).

which should be absent according to Ref. [55]. Upon variation of U_{pp} from zero to $0.1\,U_d$, the stopping scale only changes insignificantly and the systems stays in the saddle-point regime.

In a second step, I will now discuss the role of the interaction terms involving legs on the p-orbitals. More precisely, I will compare the result for the full Emery model to what is obtained if all interaction terms except U_d are ignored. Note that this interaction is still non-local in the band language, and that it is therefore different from an on-site Hubbard term. Data points for this level of approximation with dispersion parameters according to Tab. 3.3 are represented by stars in Fig. 3.12. These points almost coincide with the ones for the full interaction (+-symbols). Therefore interaction terms involving the p-orbitals only slightly affect the stopping scale.

However, this does not mean that these terms do not have any impact at all. Actually, the tendency to AFM is enhanced if the p-orbital interaction terms are neglected. In particular, between half filling and van-Hove filling, the flow to strong coupling shows features of an AFM-instability rather than of the saddle-point regime. A form factor deformation above van-Hove filling still occurs, but this effect is a little weaker without U_p and U_{pd}. One may now try to understand the enhancement of the AFM tendency by considering the two-patch couplings g_i in the ultraviolet. For the full interaction g_1, g_2 and g_4 have the same value of about $0.269\,t_{pd}$ while g_3 is lowered by a few percent to $0.264\,t_{pd}$. For an interaction involving the d-orbital only, in contrast, $g_1 = g_4 = g_2 =$

$0.255\,t_{pd}$ and g_3 is now enhanced to $0.257\,t_{pd}$. So there is an overall decrease of the two-patch couplings and their detuning differs from the case of full interaction, resulting in a relative increase of the d-wave pairing and the AFM components of the interaction in the two-patch approximation, $g_3 - g_4$ and $g_1 + g_3$, respectively. Apparently, a lowering of the stopping scale induced by the former is compensated by the latter and, as a net effect, the AFM tendency gets stronger.

I now continue with the discussion of the other multiband effects that have been listed in Section 3.2.3. First, the two-particle interaction for the conduction band is replaced by an on-site Hubbard interaction, leaving the dispersion unchanged. The interaction strength U_{eff} is chosen to be the average of the two-patch couplings that correspond to the full interaction. From the open squares in Fig. 3.12, one can see that the stopping scale is significantly lowered in this approximation. As the detuning of the two-patch couplings is rather small on this level of approximation, phase-space regions away from the saddle points must play some (minor) role even at van-Hove filling. Since the hybridization of p- and d-orbitals is strongest at the saddle points, the contributions of those regions to the diagrams on the right-hand side of the flow equations are underestimated by an on-site interaction with strength U_{eff}. Therefore a flow to strong coupling occurs at lower scales for an effective Hubbard interaction.

One may therefore wonder, whether another prescription for choosing U_{eff} might give results that are more close to those for the three-band model. Since the hybridization between d and p-orbitals is strongest at the saddle points and since the U_p and U_{pd} interactions are of minor importance, the choice $U_{\text{eff}} = U_d$ seems appealing as well. If one were to follow this alternative prescription, the stopping scale of the effective model would overshoot the value for the original model by roughly a factor of two. This is not surprising, since the averaged interaction strength of the two models then already differs at the saddle points. Moreover, the prescription $U_{\text{eff}} = U_d$ can be regarded as the leading-order result of a gradient expansion around $\mathbf{k} = (0, 0)$. However, this is inconsistent with the expansion around the saddle points of the conduction band underlying the calculation of the effective hopping parameters t and t'. Therefore, I continue to use the prescription given in Section 3.2.2, since the approach seems to be the most systematic one.

The suppression of orbital makeup then generically lowers the stopping scale. Away from van-Hove filling (in particular at hole doping beyond), this lowering is more pronounced as the gradient expansion gets worse. Moreover, for an effective Hubbard interaction, the system stays in the saddle-point regime for all filling factors considered. There are now several possible mechanisms giving rise to the enhanced tendency to dSC between half filling and van-Hove filling. As the attractive $d_{x^2-y^2}$-wave pairing component is generated by fluctuations in the magnetic channel, this enhancement may simply be caused by the lowering of the stopping scale. Furthermore, a detuning of the two-patch couplings that hampers the dSC instability is now absent. Let us note in passing that

the broadening of the $d_{x^2-y^2}$-wave form factors around the saddle points is still restricted to hole doping beyond van-Hove filling.

Let us finally consider the t, t', U_{eff} one-band Hubbard model (filled squares in Fig. 3.12), i.e. also the dispersion is now approximated by the leading-order result of a gradient expansion around the saddle points. Compared to the previous data set, the stopping scale is again lowered by almost a factor of two at van-Hove filling. Away from van-Hove filling, this depression of λ_c again grows. At hole doping beyond van-Hove filling, this effect is more pronounced between half filling and van-Hove filling and at about $n_h = 0.14$ the system enters the pure dSC regime. Again, a form factor deformation occurs at van-Hove filling and larger hole doping. Compared to the original model, the stopping scale is a factor between five and ten too low. Hence, long-range hopping terms in the effective action for the conduction band play a significant role, since they enhance the stopping scale.

3.4. Summary

In this Chapter, I have presented fRG instability analyses of multiband models for the CuO planes of the high-T_c cuprate materials. Once again, I should point out that these models are considered at (probably unrealistically) weak coupling, where a perturbative, purely fermionic fRG approach can be applied. Consequently, the key results of this chapter are of methodological nature rather than predictions for real materials.

In the first section of this chapter, a simple two-orbital model has been analyzed. In order to understand the impact of the three-particle terms in the effective action $\mathcal{A}_{\text{eff}}$ for the conduction band, RG flows with three-particle feedback (3PF) and with corrections to the bare two-particle interaction obtained from constrained perturbation theory (cPT) have been studied within a two-patch approximation. In both cases, the stopping scale is changed significantly in a similar way. Mixed one-loop diagrams with one internal leg in the high- and one in the low-energy sector saturate at scales at which the flow of the low-energy loops is still negligible in two-patch approximation. The cPT and 3PF corrections to the conventional fRG truncation hence virtually yield the same results. In Section 3.1.3, the two-patch RG flow has been found to be governed by the mutual exclusion of d-wave pairing and a Stoner instability, resulting in a great sensitivity to the initial conditions, i.e. to the couplings in the ultraviolet. Therefore the strong impact of the three-particle term observed in the numerical results of Section 3.1.4 appears to be a possible artefact of the two-patch approximation.

Indeed, the impact of the three-particle term is negligible for the Emery model studied in Section 3.3 within a new channel-decomposed treatment. Since this approach keeps track of a large number of running couplings, d-wave pairing and Stoner ferromagnetism

do not mutually exclude one another. Therefore, the stopping scale is not sensitive to small changes of the bare two-particle couplings. The mixed diagrams generated by the three-particle term consequently play a minor role, since, for zero loop frequencies, these diagram are small due to the large gap between the valence bands and the conduction band. (In a frequency-resolved study these diagrams may have a greater impact.) So the numerical results for the Emery model can be regarded as the central findings of this chapter. These include both multiband effects and effects that are not intrinsically of multiband nature and that can also be observed in the single-band Hubbard model.

In the former category, orbital makeup effects beyond a detuning of the two-patch couplings and long-range hopping terms in the dispersion of the conduction band dominate. Together, these two features enhance the stopping scale by about one order of magnitude. Having the greater impact, the orbital makeup pushes the stopping scale to higher values by enhancing the interaction away from the saddle-points of conduction band. In Section 3.2.2, a systematic prescription for the calculation of the effective Hubbard parameters at weak coupling has been given with a gradient expansion around these saddle points as a guiding principle. The value of U_{eff} obtained in this way underestimates the interaction strength away from the Fermi surface and at low density of states, while it only averages the two-patch couplings at the important van-Hove points of the dispersion. This way, the effective Hubbard model gives results that qualitatively agree with those for the Emery model close to van-Hove filling. On a more quantitative level, also momentum-space regions away from the van-Hove points play a role, which results in a strong impact of the orbital makeup.

Mentioning that also other multiband effects may matter in a frequency-resolved study, I now turn to the discussion of properties that can be observed both in the three-band Emery and in the single-band effective Hubbard model. The new fRG approach presented in Section 3.3.1 is suited for the resolution of incommensurate ordering tendencies. At van-Hove filling and hole doping beyond, such tendencies are observable in the magnetic channel where the incommensurability increases with hole doping. This also feeds back on the pairing channel giving rise to a broadening of $d_{x^2-y^2}$-wave form factor at the van-Hove points.

Both for the Emery and the corresponding effective one-band Hubbard model, a considerable region of the parameter space can be attributed to the saddle-point regime, where d-wave pairing and antiferromagnetism strongly compete and mutually reinforce each other. Unfortunately, the present instability analyses lack directly accessible measurable quantities in potentially symmetry-broken phases which would facilitate the interpretation of such a behavior. In order to find a sharp phase boundary or a coexistence phase between AFM and dSC, it would be advantageous to enter the symmetry-broken phases within a purely fermionic approach. For the multiband models of this chapter, I refrain from the formidable task of explicitly breaking the U(1) and/or SU(2) symmetries. For the one-band Hubbard model, fermionic flows have been continued into the superfluid

phase. [47–51,57] Parametrization questions and the exact fRG solution of reduced mean-field models for the AFM phase will be addressed in the following chapter, where also an extension for a perfectly nested two-pocket model beyond the mean-field level will be given. Moreover, as recently suggested by Giering and Salmhofer, [26] the parameters of an effective partially bosonized theory may be derived within a purely fermionic RG flow, whereas symmetry-broken phases are entered within a mixed flow. Such an approach has been applied to the one-band Hubbard model, where rebosonization techniques are used to describe the generation of d-wave pairing from spin-fluctuations. [61–64]

Such issues left aside, the strong-coupling nature of *ab initio* parameter sets still prevents a thorough discussion of the applicability of weak-coupling approach pursued here. Namely, interaction parameters have been chosen one decade smaller than typical literature values for cuprate materials. However, the Emery model at weak coupling is shown to have the same leading instabilities as the one-band Hubbard model. This way, the present study complements the strong-coupling VCA study by Kiesel *et al.* in Ref. [16]. Moreover, it has turned out to form a good, rather simple testbed for the new discretization scheme presented here. This scheme may be carried over to other, more complicated multiband systems where a weak-coupling approach is indeed realistic. Candidates would be the iron superconductors or strontium ruthenates (for a recent SMFRG study, see Ref. [44]), both with three and more Fermi surfaces.

Chapter 4.

fRG Flows into Antiferromagnetically Ordered Phases

In this chapter parametrization questions for fRG flows into antiferromagnetically ordered phases are addressed. First an exactly solvable reduced mean-field model is studied. For more general models with perfect nesting, a hierarchy of approximations is devised. These approximation levels start from neglecting time-reversal breaking interactions in the channel decomposed flow equations. I then resort to an exchange parametrization and, in a further step, only s-wave contributions are retained. Finally, also interaction terms that violate momentum conservation are neglected. In RPA, the mean-field results are then still recovered from the resulting flow equations.

Parts of this chapter, in particular of Section 4.1, have previously been published in Ref. [60].

Although the instability analyses of the preceeding chapter could provide a qualitative picture for the phase diagrams of the respective models, they lack predictions for measurable quantities. While these calculations yield estimates for the critical scale and for the gap shapes, they do not give any result for the gap size. This is not a deficiency of fRG in general, but rather the price paid for staying in the symmetric phase during the flow.

In a series of publications, [61–64] spontaneous symmetry breaking in the two-dimensional Hubbard model has been addressed within mixed fRG flow with fermionic and bosonic

fields corresponding to Cooper pairs and antiferromagnetic (AF) exchange bosons. While the effective action in those works contains Mexican hat potentials for the zero-momentum sectors of the order parameter fields with scale-dependent parameters, the momentum dependence is strongly approximated. In Refs. [125, 126], the U(1) symmetry has been broken explicitly in a mixed fermion-boson approach to the superfluid phase of the attractive Hubbard model. These mixed approaches are complemented by purely fermionic fRG studies of phases of broken symmetry, where a small symmetry-breaking term with an external seed field is added to the bare action in order to trigger the symmetry breaking. This way, the fRG can reproduce the solution of reduced mean-field models for pairing [48,57] and charge-density wave (CDW) [45,46] ordering exactly within an extended one-loop truncation. [71] For singlet superfluids, studies beyond mean-field have been undertaken within this truncation [47, 49, 50] and, very recently, at the two-loop level. [51]

Antiferromagnetically ordered phases have not been studied so far within a purely fermionic framework. These phases, however, play an important role in the phase diagrams of pnictide and cuprate unconventional superconductors and therefore seem to be worth further further study. In particular, being able to calculate not only pairing, but also AF gaps within an fRG approach would be an appealing long-term goal. In practice, however, a number of issues needs to be resolved first.

In order to first build up some intuition, a reduced mean-field model for AF ordering is studied in the first section of this chapter. For a system with a perfectly nested dispersion, parametrization questions are addressed in a second section. In Chapter 1.4, channel-decomposed fRG flow equations for AF phases have been provided, which will be the starting point for fRG calculations beyond mean field. Exact symmetry constraints on the single-channel coupling functions of this approach are given in Section 4.2.2. Due to the presence of Nambu indices, the integration of the flow equations then still would require large computational resources without further approximations. In particular, approximations that reduce the number of independent channels and simplify the Nambu-index dependence of the interaction can be expected to considerably decrease the computational effort.

Clearly, the breaking of the continuous SU(2) symmetry must still be present in a physically meaningful approximation for the interaction, as the Goldstone theorem applies. More precisely, it requires terms of $S_x^2 + S_y^2$ type to diverge in the limit of a vanishing seed field, while radial contributions of S_z^2 type are to be expected to be kept regular through the opening of the gap. Interaction terms breaking the discrete translational and time-reversal[1] symmetries, in contrast, seem to play a minor role, as momentum non-conserving interactions are absent in the fRG flow of the reduced CDW mean-field model. [45] A similar behavior can be expected in the AF case, as the translational invari-

[1] Note that, at the two-particle level, time-reversal invariance does not necessarily imply SU(2) invariance.

ance is only broken at microscopic scales. The same argument holds for the time-reversal behavior, which will be explained in Section 4.2.3.

In the following, a hierarchy of approximations will be devised, where the computational effort is lowered at each step. As a guiding principle, the breaking of the continuous SU(2) symmetry in the interaction is taken into account at all levels of approximation, whereas the breaking of discrete symmetries in the interaction is successively neglected. In this spirit, time-reversal breaking interactions are omitted in Section 4.2.3.

Subsequently, an exchange parametrization is employed in the third section, where only fermion-boson vertices with a slow variation in momentum and frequency are retained. As a further step, interaction terms that are not of s-wave type are discarded in the fourth section. In Section 4.4.2, I show that the resulting flow equations reproduce the mean-field gap equation at the RPA level. This result is not affected if also momentum non-conserving terms are neglected. This is done in Section 4.4.3, where numerically tractable reduced flow equations are given. At this final level of approximation, interaction terms breaking the discrete symmetries are completely neglected, while the breaking of the SU(2) symmetry is still taken into account in the two-particle vertex.

4.1. Mean-field model for commensurate antiferromagnetism

Before discussing more complicated cases, a simple mean-field model for fermions on a D-dimensional lattice with infinitely long-ranged staggered (i.e. antiferromagnetic) spin-spin interactions shall be studied. More precisely, I will consider lattice fermions on a D-dimensional torus with circumference L in all directions and take the limit $L \to \infty$. The staggering is characterized by a wavevector $\mathbf{Q}$, which does not need to be specified in full detail. However, for simplicity, let me restrict the following analysis to commensurate ordering vectors $\mathbf{Q}$. The action then reads as

$$\mathcal{A} = \int dk\, \bar{\psi}_\sigma(k)\, (ik_0 - \epsilon_{\mathbf{k}})\, \psi_\sigma(k) + \frac{J}{\Omega}\, \mathbf{S}_Q \cdot \mathbf{S}_{-Q}\,, \tag{4.1}$$

where $Q = (0, \mathbf{Q})$, $J > 0$ and $\mathbf{S}_Q = \int dk\, \bar{\boldsymbol{\psi}}(k)\, \boldsymbol{\tau}\, \boldsymbol{\psi}(k+Q)$ with the vector $\boldsymbol{\tau}$ of the Pauli matrices. Later, also perfect particle-hole nesting entailed by a fermionic lattice dispersion with the property $\epsilon_{\mathbf{k}} = -\epsilon_{\mathbf{k}+\mathbf{Q}}$ will be assumed. This assumption is not crucial for the validity of the scheme, but makes the solution of the flow equations much simpler. Note that the interaction term in Eq. (4.1) contains in total only two k-summations, i.e., the frequency- and momentum structure of the interaction is strongly or doubly restricted compared to the general translationally invariant case with three summations for momenta and frequencies. Its strength is renormalized by the $1 + D$-dimensional volume $\Omega = \beta L^D$ at temperature $1/\beta$. In the following, we will consider

the RG flow in the limit $\Omega \to \infty$, which corresponds to the thermodynamic limit and/or zero temperature.

4.1.1. Parametrization

In order to break both SU(2) and translational invariance, a spin-antisymmetric term $-\Delta \mathbf{S}^z_Q$ is added to the quadratic part of the bare action. In the collinear spin parametrization of Chapter 1.3.1, the quartic part of Eq. (4.1) corresponds to the following coupling functions in the ultraviolet:

$$\begin{aligned} V^\infty_\uparrow &= \frac{2J}{\Omega} \left[\delta\left(k_2 - k_3 + Q\right) - \delta\left(k_1 - k_3 + Q\right)\right] \delta_{\{k_i\}}\,, \\ V^\infty_\downarrow &= \frac{2J}{\Omega} \left[\delta\left(k_2 - k_3 + Q\right) - \delta\left(k_1 - k_3 + Q\right)\right] \delta_{\{k_i\}}\,, \\ V^\infty_{\uparrow\downarrow} &= \frac{2J}{\Omega} \left[2\delta\left(k_2 - k_3 + Q\right) + \delta\left(k_1 - k_3 + Q\right)\right] \delta_{\{k_i\}}\,. \end{aligned}$$

Here, the superscript denotes the scale and I have introduced $\delta(p-q) = \Omega\, \delta_{p_0,q_0} \delta_{\mathbf{p},\mathbf{q}}$ and

$$\delta_{\{k_i\}} = \delta\left(k_1 + k_2 - k_3 - k_4\right)$$

as a short-hand notation for an energy- and momentum-conserving δ function.

Here and throughout, a pseudo-continuous notation will be used, i.e. momentum and frequency integrals $\int dk$ are interpreted as a summation $\Omega^{-1} \sum_k$ over the discrete momenta of the finite system at finite temperature in the thermodynamic limit $L \to \infty$ and send $\beta \to \infty$ for zero-temperature calculations. As pointed out in Refs. [45, 57], only diagrams in one channel contribute in reduced mean-field theories. For a multi-channel reduced mean-field interaction, these channels may couple on the RPA level as in Ref. [48], while box and vertex-correction diagrams do not contribute to the renormalized interaction. In all these studies, the Katanin truncation [71] of the fRG flow equations is exact. In the case considered here, particle-particle diagrams and diagrams with overlapping loops vanish in the thermodynamic limit since the square of a δ function brings in an extra factor Ω in non-overlapping particle-hole loops. Particle-hole ladders are therefore of first order in Ω^{-1} just as the bare interaction. In the thermodynamic limit, only these first-order contributions to the renormalized interaction survive and hence a Bethe-Salpether equation

$$\begin{aligned} f^\lambda(\xi_1, \xi_2, \xi_3, \xi_4) = -\mathcal{A}_{\xi_3,\xi_4} \int d\eta_1 \cdot\cdot\, d\eta_4\, G^\lambda(\eta_1, \eta_2) \\ \times G^\lambda(\eta_3, \eta_4)\, f^\infty(\eta_4, \xi_2, \xi_3, \eta_1)\, f^\lambda(\xi_1, \eta_2, \eta_3, \xi_4) \end{aligned} \tag{4.2}$$

holds, where the operator $\mathcal{A}$ antisymmetrizes the coupling function according to

$$\mathcal{A}_{\xi_1,\xi_2} h(\xi_1, \xi_2) = \left[h\left(\xi_1, \xi_2\right) - h\left(\xi_2, \xi_1\right)\right]/2\,.$$

All diagrams not resummed by this equation are at least of second order in Ω^{-1}. Note that the Bethe-Salpether equation (4.2) holds without any further assumption for the dispersion such as perfect nesting. Similarly, only contributions to the self-energy of zeroth order in Ω^{-1} are retained in the thermodynamic limit.

For broken translational invariance, contributions to the interaction that violate momentum conservation are generated during the flow in general. In the thermodynamic limit, however, such interaction terms vanish due to the restricted momentum dependence of the bare interaction. The renormalized interaction can therefore be parametrized by four couplings

$$\begin{aligned} V_{\uparrow}^{\lambda} &= J_{\uparrow}^{\lambda} \left[\delta\left(k_2 - k_3 + Q\right) - \delta\left(k_1 - k_3 + Q\right)\right] \delta_{\{k_i\}}/\Omega\,, \\ V_{\downarrow}^{\lambda} &= J_{\downarrow}^{\lambda} \left[\delta\left(k_2 - k_3 + Q\right) - \delta\left(k_1 - k_3 + Q\right)\right] \delta_{\{k_i\}}/\Omega\,, \\ V_{\uparrow\downarrow}^{\lambda} &= \left[J_{xy}^{\lambda}\delta\left(k_2 - k_3 + Q\right) + J_{13}^{\lambda}\delta\left(k_1 - k_3 + Q\right)\right] \delta_{\{k_i\}}/\Omega\,. \end{aligned} \tag{4.3}$$

In the SU(2) symmetric case, these couplings fulfill the constraints $J_{\uparrow} = J_{\downarrow} = J_{xy} - J_{13}$ [cf. Eq. (1.11)]. In the absence of a density-density term in the interaction, we further have $J_{xy} = 2J_{13}$.

4.1.2. Flow equations

From the ultraviolet values $J_{\uparrow}^{\infty} = J_{\downarrow}^{\infty} = 2J$, $J_{xy}^{\infty} = 4J$ and $J_{13}^{\infty} = 2J$ these couplings flow according to

$$\dot{J}_{\uparrow} = -J_{\uparrow}^2 \dot{B}_{\uparrow\uparrow} - J_{13}^2 \dot{B}_{\downarrow\downarrow}\,, \tag{4.4}$$

$$\dot{J}_{\downarrow} = -J_{\downarrow}^2 \dot{B}_{\downarrow\downarrow} - J_{13}^2 \dot{B}_{\uparrow\uparrow}\,, \tag{4.5}$$

$$\dot{J}_{13} = -J_{13}\left(J_{\uparrow}\dot{B}_{\uparrow\uparrow} + J_{\downarrow}\dot{B}_{\downarrow\downarrow}\right)\,, \tag{4.6}$$

$$\dot{J}_{xy} = -J_{xy}^2 \dot{B}_{\downarrow\uparrow}\,, \tag{4.7}$$

with the dots denoting scale derivatives. For convenience, we have now suppressed the scale dependence in the notation. The particle-hole bubble

$$B_{\sigma_1\sigma_2} = \frac{1}{\Omega}\int dk\, dk' \left[G_{\sigma_1}(k,k')\, G_{\sigma_2}(k'+Q, k+Q) + G_{\sigma_1}(k,k'+Q)\, G_{\sigma_2}(k'+Q,k)\right]$$

corresponds to a trace in Nambu space with spinors

$$\mathbf{\Psi}_{\sigma}(k) = \begin{pmatrix} \psi_{\sigma}(k) \\ \psi_{\sigma}(k+Q) \end{pmatrix}\,. \tag{4.8}$$

The restricted momentum dependence of the interaction leaves the momentum-conserving component of the self-energy unchanged during the flow. For the remaining anomalous[2]

[2]Throughout this Chapter, the adjective 'anomalous' refers to the momentum non-conserving components of the one-particle propagator [off-diagonal components in Nambu representation Eq. (4.8)].

components, the flow equations read as

$$\Sigma_\sigma(k,k') = \Sigma_\sigma\,\delta(k-k'+Q)\,,$$
$$\dot{\Sigma}_\uparrow = -J_\uparrow A_\uparrow + J_z A_\downarrow\,, \tag{4.9}$$
$$\dot{\Sigma}_\downarrow = -J_\downarrow A_\downarrow + J_z A_\uparrow\,, \tag{4.10}$$

with

$$A_\sigma = \frac{1}{\Omega}\int dk\,dk'\,S_\sigma(k,k')\,\delta(k-k'+Q)$$

being the anomalous tadpole bubble. Note that if one had only broken the translational, but not the spin symmetry, the loop integrals A_σ and $\dot{B}_{\sigma_1\sigma_2}$ in the flow equations (4.4)–(4.10) would not depend on the spin indices and the number of independent couplings would be reduced to one according to $J_\uparrow = J_\downarrow = J_{xy} - J_z = J_z$ in the absence of a density-density term in the bare interaction .

If the symmetry-breaking term in the bare action is antisymmetric under a spin flip as in our case, the property $-\Sigma_\downarrow = \Sigma_\uparrow =: \Delta$ is preserved in the flow. We thus have $B_{\uparrow\uparrow} = B_{\downarrow\downarrow}$, $A_\uparrow = -A_\downarrow$, and $J_\uparrow = J_\downarrow = J_z$ and thus the flow equations (4.5) and (4.10) become redundant. This way, the interaction now remains invariant under spin flips. For the following discussion, it seems preferable to work with the coupling constants $J_{\mathrm{CDW}} = J_\uparrow - J_{13}$ and $J_z = J_\uparrow + J_{13}$. The flow equations to be solved finally read as

$$\dot{J}_{\mathrm{CDW}} = +J_{\mathrm{CDW}}^2\dot{B}_{\uparrow\uparrow}\,, \tag{4.11}$$
$$\dot{J}_z = -J_z^2\dot{B}_{\uparrow\uparrow}\,, \tag{4.12}$$
$$\dot{J}_{xy} = -J_{xy}^2\dot{B}_{\downarrow\uparrow}\,, \tag{4.13}$$
$$\dot{\Delta} = -J_z A_\uparrow\,. \tag{4.14}$$

Note that the flows of the in-plane coupling J_{xy} and the CDW coupling J_{CDW} do not feed back on the flow of Δ and J_z. This behavior is similar to the reduced BCS model, [57] where the flows of the amplitude vertex and the gap decouple from the flow of the Goldstone vertex as well. Indeed, J_{xy} will turn out to account for the Goldstone modes further below. For the action given in Eq. (4.1), we have $J_{\mathrm{CDW}}^\infty = 0$ and hence this coupling constant will vanish at any scale. If one were to add a CDW mean-field term in the interaction of Eq. (4.1), i.e. if one were to choose $J_\uparrow^\infty > J_{13}^\infty$, this term would behave like an irrelevant coupling down to the critical scale and can be expected to remain small when the gap Δ opens. Since J_{CDW} does not feed back on the remaining flow equations (4.12)–(4.14), the presence of a CDW mean-field term in the ultraviolet will not change the flow of the other couplings. In particular, it does not degenerate anomalous contributions to the interaction.

So far, no specific assumption for the dispersion has been made. In the following, I will only consider the case of perfect nesting $\epsilon_{\mathbf{k}} = -\epsilon_{\mathbf{k}+\mathbf{Q}}$ in order to simplify the integration

of the loops.[3] Since the anomalous self-energy $\Sigma_\sigma = \pm\Delta$ is independent of k, we may write in Nambu representation

$$\boldsymbol{G}_\sigma(k,k') = \boldsymbol{G}_\sigma(k)\,\delta(k-k')\,,$$
$$\boldsymbol{G}_\sigma(k) = \frac{\chi}{k_0^2+\epsilon_{\mathbf{k}}^2+\chi^2\Sigma_\sigma^2}\begin{pmatrix} -ik_0-\epsilon_{\mathbf{k}} & -\chi\Sigma_\sigma \\ -\chi\Sigma_\sigma & -ik_0+\epsilon_{\mathbf{k}}\end{pmatrix},$$

with a sharp energy-shell regulator $\chi = \Theta(|\epsilon_{\mathbf{k}}|-\lambda)$. One can observe that this propagator is of the form given in Eq. (4.25) with a constant anomalous self-energy Δ and vanishing normal components of the self-energy.

The expressions for the loops are now evaluated as follows. The Matsubara sums are performed analytically and Morris' lemma [127]

$$\delta(x-\lambda)\,f\left(\Theta(x-\lambda),\lambda\right) = \delta(x-\lambda)\int_0^1 dt\, f(t,x)$$

for a function f of the Heaviside function is used to evaluate such functions at their jumps. In order to have a lean notation, let me now define

$$E = \sqrt{\epsilon^2+\chi^2\Delta^2}\,,\quad t = \tanh\left(\frac{E}{2T}\right),\quad t' = \left[2T\cosh^2\left(\frac{E}{2T}\right)\right]^{-1},$$

where T denotes the temperature. Calculating the Matsubara sum analytically, one obtains for the particle-hole bubble with opposite spins

$$\dot{B}_{\downarrow\uparrow} = -\partial_\lambda\int d\mathbf{k}\,\chi\,\frac{t}{2E} = \rho_\lambda\frac{t}{2E}\bigg|_{\epsilon=\lambda,\chi=1} + \dot{\Delta}\Delta\int_\lambda^W d\epsilon\,\rho_\epsilon\left[\frac{t}{E^3}-\frac{t'}{E^2}\right],$$

whereas the equal-spin bubble reads as

$$\dot{B}_{\uparrow\uparrow} = \dot{B}_{\uparrow\downarrow} + \partial_\lambda\int d\mathbf{k}\,\chi\,\Delta^2\left(\frac{t}{2E^3}-\frac{t'}{2E^2}\right)$$
$$= \rho_\lambda\left(\frac{t\,\lambda^2}{2E^3}+\frac{\Delta^2\,t'}{2E^2}\right)_{\epsilon=\lambda,\chi=1} + \dot{\Delta}\Delta\int_\lambda^W d\epsilon\,\rho_\epsilon\left[3\left(\frac{t}{E^3}-\frac{t'}{E^2}\right)\frac{\epsilon^2}{E^2}+\frac{t\,t'\Delta^2}{TE^3}\right].$$

Here, momentum integrals have been replaced by energy integrals with the density of states ρ_ϵ and ultraviolet cutoff W. For the tadpole bubble, Morris' lemma yields

$$A_\uparrow = \rho_\lambda\,\Delta\frac{t}{2E}\bigg|_{\epsilon=\lambda,\chi=1}.$$

If spin symmetry was restored, we would have to encounter a flow to strong coupling, since then $\dot{\Delta}=0$ and hence $\dot{B}_{\sigma_1\sigma_2}>0$.

[3] If this perfect-nesting condition is violated by a chemical potential, a behavior similar to Ref. [46] is to be expected. A potential first-order phase transition may then be assessed by introducing a counterterm in the RG flow.

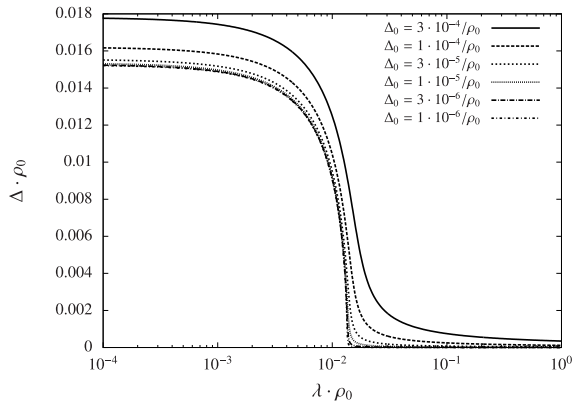

(a) Gap

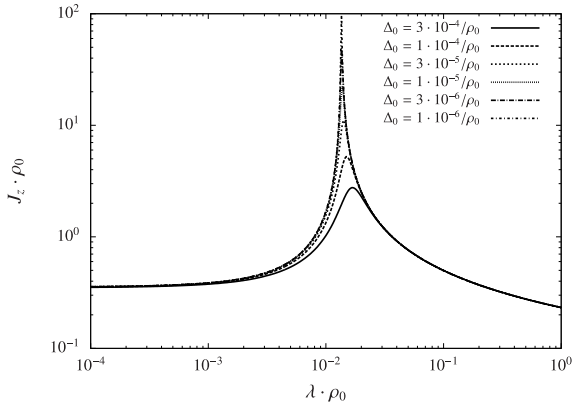

(b) Radial vertex

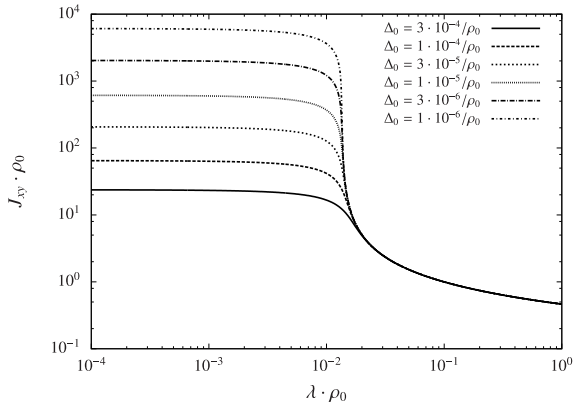

(c) Goldstone vertex

Figure 4.1.: Flow of Δ (a), J_z (b) and J_{xy} (c) according to Eqs. (4.12), (4.14), and (4.18) for zero temperature, perfect nesting and a constant density of states ρ_0 ($W = 2/\rho_0$, $J = 0.1/\rho_0$). Instead of the flow equation (4.13) for J_{xy}, the formal solution (4.18) has been used in order to avoid numerical complications in (c).

In Fig. 4.1, the flow of Δ, J_z, and J_{xy} is depicted for perfect nesting, zero temperature and a constant density of states ρ_0. At a critical scale $\lambda_{\text{crit}} \propto e^{-1/(4J\rho_0)}$ (about $10^{-2}/\rho_0$ in the case considered here), the coupling constants of the interaction grow and the gap opens. At lower scales, J_z is then depressed by this gap while J_{xy} continues to grow. The growth of J_z slightly above the critical scale occurs as a remnant of the AF instability encountered in an SU(2)-symmetric flow. If Δ_0 is sent to zero, the infrared values of J_z and Δ saturate, whereas J_{xy} grows without bound in the infrared.

4.1.3. Exact solution

The flow equations (4.12) and (4.13) can be formally solved to reproduce the RPA result

$$J_z = \frac{4J}{1 + 4J\, B_{\uparrow\uparrow}}\,, \tag{4.15}$$

$$J_{xy} = \frac{4J}{1 + 4J\, B_{\uparrow\downarrow}}\,. \tag{4.16}$$

The gap equation for the anomalous part of the propagator can now be derived if the tadpole is recast as

$$A_\uparrow = -\dot{\Delta}\, B_{\uparrow\uparrow} + \frac{1}{\Omega}\int dk\, dk'\, \dot{G}_\uparrow(k,k')\, \delta(k - k' + Q)\,.$$

Inserting Eq. (4.15) into (4.14) and integrating then yields the following gap equation:

$$\Delta - \Delta_0 = -\frac{4J}{\Omega}\int dk\, dk'\, G_\uparrow(k,k')\, \delta(k - k' + Q) = -4J\, B_{\uparrow\downarrow}\, \Delta\,, \tag{4.17}$$

which can as well be obtained from a self-consistent mean-field ansatz. For zero temperature, perfect nesting and a constant density of states, the gap behaves as $\Delta \propto e^{-1/(4J\rho_0)}$. Since we now have

$$J_{xy} = 4J\, \Delta/\Delta_0\,, \tag{4.18}$$

J_{xy} diverges for $\Delta_0, \lambda \to 0$ and can thus be interpreted as a Goldstone vertex. J_z, however, remains finite in the infrared and therefore corresponds to radial fluctuations of the staggered magnetization. The divergence of J_{xy} for vanishing Δ_0 also directly follows from the Ward identity Eq. (1.12), which simplifies to

$$\Delta - \Delta_0 = -\Delta_0\, J_{xy}\, B_{\uparrow\downarrow}\,. \tag{4.19}$$

4.2. Parametrization in the presence of perfect nesting

In an attempt to go beyond a mean-field approach, one is left with the full channel-decomposed flow equations of Chapter 1.4.3. Due to the Nambu-index dependence of

the coupling functions, a direct discretization of their arguments would still be far too costly. Therefore additional symmetries, such as the one stemming form a perfectly nested dispersion should be exploited in the parametrization of the coupling functions. In this section, I will therefore discuss these symmetries for a general action of the form

$$\begin{aligned}\mathcal{A}[\bar{\psi},\psi] = &\sum_{\sigma}\int dk\, dk'\, \bar{\psi}_\sigma(k)\, C_\sigma(k,k')\, \psi_\sigma(k') \\ &+ \frac{1}{4}\int d\xi_1 \ldots d\xi_4\, f(\xi_1,\xi_2,\xi_3,\xi_4)\; \bar{\psi}(\xi_1)\,\bar{\psi}(\xi_2)\,\psi(\xi_3)\,\psi(\xi_4)\,, \end{aligned} \tag{4.20}$$

before incorporating them into the parametrization.

4.2.1. Symmetries

Often, the Hubbard model at half-filling and with hopping only between nearest neighbors is said to be particle-hole symmetric [128]. The underlying notion of a particle-hole transformation, however, differs from the one used in this work and in Refs. [24–26]. Namely, in the former case, this transformation is defined in an operator language, while in the latter a functional integral language is used. In agreement with Refs. [24–26], I define the particle-hole transformation as the mapping

$$\bar{\psi}_\sigma(k) \to i\psi_\sigma(k)\,, \qquad \psi_\sigma(k) \to i\bar{\psi}_\sigma(k)\,.$$

Note that, in real space, this corresponds to

$$\bar{\psi}_\sigma(x) \to i\psi_\sigma(-x)\,, \qquad \psi_\sigma(x) \to i\bar{\psi}_\sigma(-x) \qquad x = (\tau,\mathbf{R})\,,$$

where the position $\mathbf{R}$ and imaginary time τ undergo a sign-change under this transformation. One can now observe that the action $\mathcal{A}$ in Eq. (4.20) is particle-hole symmetric if

$$C_\sigma(k,k') = C_\sigma(k',k)\,, \qquad f(\xi_1,\xi_2,\xi_3,\xi_4) = f(\xi_4,\xi_3,\xi_2,\xi_1)\,. \tag{4.21}$$

In the first of these constraints, the Pauli principle is already included. The second one, however, is complemented by the Pauli constraint

$$f(\xi_1,\xi_2,\xi_3,\xi_4) = -f(\xi_2,\xi_1,\xi_3,\xi_4) = -f(\xi_1,\xi_2,\xi_4,\xi_3)\,.$$

Whenever the term 'particle-hole symmetry' (PHS) is used in the following, this refers to the relations in Eq. (4.21). The Hubbard model, for example, is particle-hole symmetric in this sense — even for nonvanishing second-neighbor hopping. This illustrates that PHS according to Eq. (4.21) does not imply perfect nesting, which may be protected by another symmetry.

In a fRG framework, symmetries can only be exploited if they can be formulated in terms of symmetry constraints on the coupling functions, Eq. (4.21) being an example thereof. Hence, it seems worthwhile to look for such a constraint on the coupling

functions that arises from perfect nesting. This constraint could then be used in a further parametrization of the coupling functions. For the perfectly nested Hubbard model with

$$\begin{aligned} C_\sigma(k,k') &= \{ik_0 - 2t\,[\cos(k_x)+\cos(k_y)]\}\,\delta(k-k') - \tau^z\Delta\,\delta(k-k'+Q) \\ f(\xi_1,\xi_2,\xi_3,\xi_4) &= U\,\delta(k_1+k_2-k_3-k_4)\,(\delta_{\sigma_1,\sigma_4}\delta_{\sigma_2,\sigma_3} - \delta_{\sigma_1,\sigma_3}\delta_{\sigma_2,\sigma_4}) \end{aligned}$$

and $Q=(0,(\pi,\pi))$ one indeed finds that

$$C_\sigma(k,k') = -C^*_{-\sigma}(k+Q,k'+Q)\,, \tag{4.22}$$

$$f(\xi_1,\xi_2,\xi_3,\xi_4) = f^*(\tilde{\xi}_1,\tilde{\xi}_2,\tilde{\xi}_3,\tilde{\xi}_4)\,, \tag{4.23}$$

where $\tilde{\xi}_i = (-\sigma_i, k_i+Q)$. In the language of Refs. [128,129], this corresponds to flipping the components of the pseudospinors

$$\Psi^s_{\mathrm{p}}(k) = \begin{pmatrix} \psi^s_\uparrow(k) \\ \bar{\psi}^{-s}_\downarrow(-k) \end{pmatrix}.$$

This symmetry constitutes a subgroup of the 'hidden' SU(2) pseudospin symmetry. Since a general pseudospin rotation mixes ingoing and outgoing fields, fully exploiting this hidden symmetry in the parametrization of the interaction represents a challenging task, which I leave for future work. These symmetry constraints still hold in the presence of a nonvanishing antiferromagnetic seed field Δ. But as soon as a second-neighbor hopping term $t'\cos(k_x)\cos(k_y)\,\delta(k-k')$, which violates perfect nesting, is added in the quadratic part of the action, Eq. (4.22) is violated as well. Once met by the bare action, the constraints in Eqs. (4.22) and (4.23) are preserved by the flow equations (1.15)–(1.20) for the interaction and (1.21) and (1.22) for the self-energy. For the spin-independent coupling functions, the second of these constraints translates to

$$\begin{aligned} V_\uparrow(k_1,k_2,k_3,k_4) &= V^*_\downarrow(k_1+Q,k_2+Q,k_3+Q,k_4+Q)\,, \\ V_{\uparrow\downarrow}(k_1,k_2,k_3,k_4) &= V^*_{\uparrow\downarrow}(k_2+Q,k_1+Q,k_4+Q,k_3+Q)\,, \end{aligned}$$

while the first implies a form

$$\begin{aligned} C_\uparrow(k) &= \Delta(k)\,\tau^x + (ik_0 - \epsilon_{\mathrm{s}}(k)) - \epsilon_{\mathrm{a}}(k)\,\tau^z \\ C_\downarrow(k) &= -\Delta^*(k)\,\tau^x + (ik_0 + \epsilon^*_{\mathrm{s}}(k)) - \epsilon^*_{\mathrm{a}}(k)\,\tau^z \end{aligned} \tag{4.24}$$

of the quadratic part of the action in Nambu space with spinors according to Eq. (4.8). In the following, I will refer to this symmetry as to the pseudospin-flip symmetry (PFS). For a bare action with a perfectly nested dispersion, $\epsilon_{\mathrm{s}}=0$ and hence the Nambu-symmetric part of the self-energy is created during the flow. In Nambu space, this corresponds to a propagator of the form

$$\begin{aligned} G_\uparrow(k) = {} & \frac{1}{k_0^2 + 2ik_0\epsilon_{\mathrm{s}}(k) - \epsilon_{\mathrm{s}}(k)^2 + \epsilon_{\mathrm{a}}(k)^2 + \Delta(k)^2} \\ & \times \begin{pmatrix} -ik_0 + \epsilon_{\mathrm{s}}(k) - \epsilon_{\mathrm{a}}(k) & -\Delta(k) \\ -\Delta(k) & -ik_0 + \epsilon_{\mathrm{s}}(k) + \epsilon_{\mathrm{a}}(k) \end{pmatrix} \end{aligned} \tag{4.25}$$

for spin up and likewise for spin down with the substitutions $\Delta(k) \to -\Delta^*(k)$, $\epsilon_{\mathrm{s}}(k) \to -\epsilon_{\mathrm{s}}^*(k)$ and $\epsilon_{\mathrm{a}}(k) \to \epsilon_{\mathrm{a}}^*(k)$.

This general PFS symmetric form of the propagator differs from the one in the mean-field case. For one thing, the bare dispersion in ϵ_{a} gets renormalized by contributions of the normal self-energy, which depend on momentum and frequency. Also the anomalous part Δ of the self-energy may show such a dependence. Furthermore, one has to encounter contributions ϵ_{s} to the normal self-energy that are symmetric under a Nambu index flip. As can be seen from the denominator of Eq. (4.25), a nonvanishing value of ϵ_{s} might give rise to a Fermi surface reconstruction, since it may cause zeros of the dominator in the presence of an antiferromagnetic gap. Keeping track of this effect may, however, require a good momentum resolution of the self-energy within an unbiased discretization scheme. In the present work, I will therefore have to refrain from such tasks.

In the following, other symmetries will turn out to be useful. Let us again consider an action that is equivalent to a model Hamiltonian. Under frequency-inversion $k_0 \to -k_0$, the coupling functions both in the quadratic and the quartic part of the action are then mapped to their complex conjugates, i.e.

$$\begin{aligned} C_\sigma(\hat{k}, \hat{k}') &= C_\sigma^*(k, k')\,, \\ V_\uparrow(\hat{k}_1, \hat{k}_2, \hat{k}_3, \hat{k}_4) &= V_\uparrow^*(k_1, k_2, k_3, k_4)\,, \\ V_{\uparrow\downarrow}(\hat{k}_1, \hat{k}_2, \hat{k}_3, \hat{k}_4) &= V_{\uparrow\downarrow}^*(k_1, k_2, k_3, k_4)\,, \end{aligned}$$

where $\hat{k} = (-k_0, \mathbf{k})$. This symmetry is as well preserved by the flow equations (1.15)–(1.22). The point-group symmetries give rise to the constraints

$$\begin{aligned} C_\sigma(R_{\hat{O}}k, R_{\hat{O}}k') &= C_\sigma(k, k')\,, \\ V_\uparrow(R_{\hat{O}}k_1, R_{\hat{O}}k_2, R_{\hat{O}}k_3, R_{\hat{O}}k_4) &= V_\uparrow(k_1, k_2, k_3, k_4)\,, \\ V_{\uparrow\downarrow}(R_{\hat{O}}k_1, R_{\hat{O}}k_2, R_{\hat{O}}k_3, R_{\hat{O}}k_4) &= V_{\uparrow\downarrow}(k_1, k_2, k_3, k_4)\,, \end{aligned}$$

where $R_{\hat{O}}$ denotes the representation matrix corresponding to the $\hat{O}$ in the point group $\mathcal{G}$. (For a more general discussion of point-group symmetries, see Chapter 2.2.) Here and throughout this chapter, I will assume that the parity operation $\mathbf{k} \to -\mathbf{k}$ is contained in $\mathcal{G}$.

Before I proceed further, let me briefly elaborate on the behavior under time reversal, which corresponds to the transformation

$$\psi_\sigma(x) \to i\sigma\bar{\psi}_{-\sigma}(-\tau, \mathbf{R})\,, \quad \bar{\psi}_\sigma(x) \to i\sigma\psi_{-\sigma}(-\tau, \mathbf{R})$$

(cf. Refs. [48, 130]). For the coupling functions, this translates to

$$\begin{aligned} C_{-\sigma}(k'^{\mathcal{T}}, k^{\mathcal{T}}) &\to C_\sigma(k, k')\,, \\ V_\uparrow(k_4^{\mathcal{T}}, k_3^{\mathcal{T}}, k_2^{\mathcal{T}}, k_1^{\mathcal{T}}) &\to V_\downarrow(k_1, k_2, k_3, k_4)\,, \\ V_{\uparrow\downarrow}(k_4^{\mathcal{T}}, k_3^{\mathcal{T}}, k_2^{\mathcal{T}}, k_1^{\mathcal{T}}) &\to V_{\uparrow\downarrow}(k_1, k_2, k_3, k_4)\,, \end{aligned}$$

where $k^{\mathcal{T}} = (k_0, -\mathbf{k})$. One can observe that, in the presence of PHS and parity invariance, the time-reversal operation acts on the interaction just as a spin-flip. Clearly, a finite AF gap $\Delta(k)$ breaks time-reversal invariance in the quadratic part of the action and consequently also in the renormalized interaction.

Note however that, in the absence of such a gap, SU(2) invariance would impose stronger constraints on the interaction than time-reversal symmetry, as the SU(2) constraint (1.11) contains more than spin-flip invariance. As an approximation, one may hence enforce spin-flip invariance in the interaction without completely eliminating the signatures of the SU(2) breaking. This approximation will be further discussed in Section 4.2.3.

4.2.2. Application to the channel decomposition

In this subsection, constraints on the single-channel coupling functions imposed by particle-hole, PFS and frequency-inversion symmetries and the Pauli principle are derived. These symmetries are preserved in the RG flow equations in Chapter 1.4.2 and 1.4.3 and should therefore be respected by an approximate parametrization. In the following, I will first give symmetry constraints on the coupling functions of Chapter 1.4.2 before discussing the physically more meaningful coupling functions of the improved channel decomposition of Chapter 1.4.3.

For the $W_\uparrow$ part of the interaction, the PHS leads to

$$\Phi^{\{s\}}_{\mathrm{SC},\sigma}(l,p,q) = \Phi^{\{\hat{s}\}}_{\mathrm{SC},\sigma}(l,q,p) \tag{4.26}$$

$$\Phi^{\{s\}}_{K\sigma}(l,p,q) = \Phi^{\{\hat{s}\}}_{K\sigma}(-l,p-l,q+l)\,, \tag{4.27}$$

$\{\hat{s}\}$ being a short-hand notation for $(s_3 s_4 s_1 s_2)$. For the $W_{\uparrow\downarrow}$ part, PHS yields

$$\Phi^{\{s\}}_{\mathrm{SC},\uparrow\downarrow}(l,p,q) = \Phi^{\{\hat{s}\}}_{\mathrm{SC},\uparrow\downarrow}(l,q,p) \tag{4.28}$$

$$\Phi^{\{s\}}_{\mathrm{plane}}(l,p,q) = \Phi^{\{\hat{s}\}}_{\mathrm{plane}}(l,q+l,p-l) \tag{4.29}$$

$$\Phi^{\{s\}}_{\mathrm{axis}}(l,p,q) = \Phi^{\{\hat{s}\}}_{\mathrm{axis}}(-l,p-l,q+l)\,. \tag{4.30}$$

Moreover, the Pauli-principle constraint on $W_\uparrow$ translates to

$$\Phi^{\{s\}}_{\mathrm{SC},\sigma}(l,p,q) = -\Phi^{\{\tilde{s}\}}_{\mathrm{SC},\sigma}(l,l-p,q) = \Phi^{\{\bar{s}\}}_{\mathrm{SC},\sigma}(l,l-p,l-q) \tag{4.31}$$

$$\Phi^{\{s\}\sigma}_{K}(l,p,q) = \Phi^{\{\bar{s}\}}_{K\sigma}(-l,q,p)\,, \tag{4.32}$$

where $\{\bar{s}\} = (s_2 s_1 s_4 s_3)$ and $\{\tilde{s}\} = (s_1 s_2 s_4 s_3)$. Note that Φ_K does not have the full antisymmetry of $W_\uparrow$, since it already enters in an antisymmetrizing form in Eq. (1.23).

The PFS symmetry relates $W_\uparrow$ and $W_\downarrow$ according to

$$\Phi^{\{s\}}_{\mathrm{SC},\uparrow}(l,p,q) = \Phi^{\{-s\}}_{\mathrm{SC},\downarrow}(l,p,q)^*$$
$$\Phi^{\{s\}}_{K\uparrow}(l,p,q) = \Phi^{\{-s\}}_{K\downarrow}(l,p,q)^*$$

and it imposes the constraints

$$\Phi^{\{s\}}_{\mathrm{SC},\uparrow\downarrow}(l,p,q) = \Phi^{\{-\bar{s}\}}_{\mathrm{SC},\uparrow\downarrow}(l,l-p,l-q)^* \tag{4.33}$$
$$\Phi^{\{s\}}_{\mathrm{plane}}(l,p,q) = \Phi^{\{-\bar{s}\}}_{\mathrm{plane}}(-l,q,p)^* \tag{4.34}$$
$$\Phi^{\{s\}}_{\mathrm{axis}}(l,p,q) = \Phi^{\{-\bar{s}\}}_{\mathrm{axis}}(-l,q,p)^* \tag{4.35}$$

on the single-channel coupling functions of $W_{\uparrow\downarrow}$.

Let me now decompose the coupling functions Φ_K and Φ_{axis} into time-reversal invariant and time-reversal breaking parts. Recall that, under a spin-flip operation, the multi-channel coupling functions transform according to

$$W^{\{s\}}_\uparrow(k_1,k_2,k_3,k_4) \to W^{\{s\}}_\downarrow(k_1,k_2,k_3,k_4) = W^{-\{s\}}_\uparrow(k_1,k_2,k_3,k_4)^*\,,$$
$$W^{\{s\}}_{\uparrow\downarrow}(k_1,k_2,k_3,k_4) \to W^{\{\bar{s}\}}_{\uparrow\downarrow}(k_2,k_1,k_4,k_3) = W^{-\{s\}}_{\uparrow\downarrow}(k_1,k_2,k_3,k_4)^*\,,$$

where the equal signs stem from the PFS symmetry. If Φ_K is now decomposed into its time-reversal invariant and time-reversal breaking parts, as in Chapter 1.4.3, one obtains

PHS	$\Phi^{\{s\}}_{K\pm}(l,p,q) = \Phi^{\{\hat{s}\}}_{K\pm}(-l,p-l,q+l)\,,$
Pauli	$\Phi^{\{s\}}_{K\pm}(l,p,q) = \Phi^{\{\bar{s}\}}_{K\pm}(-l,q,p)\,,$
PFS	$\Phi^{\{s\}}_{K\pm}(l,p,q) = \pm\Phi^{\{-s\}}_{K\pm}(l,p,q)^*\,.$

Likewise, the constraints for the axial channel read as

PHS	$\Phi^{\{s\}}_{\mathrm{axis}\pm}(l,p,q) = \Phi^{\{\hat{s}\}}_{\mathrm{axis}\pm}(-l,p-l,q+l)$
	$\Phi^{\{s\}}_{\mathrm{axis}\pm}(l,p,q) = \pm\Phi^{\{\bar{s}\}}_{\mathrm{axis}\pm}(-l,q,p)\,,$
PFS	$\Phi^{\{s\}}_{\mathrm{axis}\pm}(l,p,q) = \pm\Phi^{\{-s\}}_{\mathrm{axis}\pm}(l,p,q)^*\,,$

where the second of these identities holds by construction. Note also the sign in that equation, which differs from the above case of $\Phi_{K\pm}$. These properties translate to the CDW coupling functions as follows

PHS	$\Phi^{\{s\}}_{\mathrm{CDW}}(l,p,q) = \Phi^{\{\hat{s}\}}_{\mathrm{CDW}}(-l,p-l,q+l)\,,$
Pauli	$\Phi^{\{s\}}_{\mathrm{CDW}}(l,p,q) = \Phi^{\{\bar{s}\}}_{\mathrm{CDW}}(-l,q,p)\,,$
PFS	$\Phi^{\{s\}}_{\mathrm{CDW}}(l,p,q) = \Phi^{\{-s\}}_{\mathrm{CDW}}(l,p,q)^*\,,$

while the S_z^2 channel must respect the constraints

$$\begin{aligned}
&\text{PHS} && \Phi_z^{\{s\}}(l,p,q) = \Phi_z^{\{\hat{s}\}}(-l,p-l,q+l)\,,\\
&\text{Pauli} && \Phi_z^{\{s\}}(l,p,q) = \Phi_z^{\{\bar{s}\}}(-l,q,p)\,,\\
&\text{PFS} && \Phi_z^{\{s\}}(l,p,q) = \Phi_z^{\{-s\}}(l,p,q)^*\,.
\end{aligned}$$

For the following discussion, it appears worthwhile to also decompose the coupling functions of the pairing channels into time-reversal invariant and time-reversal breaking parts with new coupling functions

$$\begin{aligned}
\Phi_{\mathrm{SC},\uparrow\pm}^{\{s\}}(l,p,q) &= \frac{1}{2}\left[\Phi_{\mathrm{SC},\uparrow}^{\{s\}}(l,p,q) \pm \Phi_{\mathrm{SC},\downarrow}^{\{s\}}(l,p,q)\right]\\
&= \frac{1}{2}\left[\Phi_{\mathrm{SC},\uparrow}^{\{s\}}(l,p,q) \pm \Phi_{\mathrm{SC},\uparrow}^{\{-s\}}(l,p,q)^*\right]\,,\\
\Phi_{\mathrm{SC}\pm}^{\{s\}}(l,p,q) &= \frac{1}{2}\left[\Phi_{\mathrm{SC}\uparrow\downarrow}^{\{s\}}(l,p,q) \pm \Phi_{\mathrm{SC}\uparrow\downarrow}^{\{\bar{s}\}}(l,l-p,l-q)\right]\,.
\end{aligned}$$

Singlet and non-singlet pairing terms can now be projected out of the time-reversal invariant part of $\Phi_{\mathrm{SC},\uparrow\downarrow}$ according to

$$\begin{aligned}
\Phi_{\mathrm{singlet}}^{\{s\}}(l,p,q) &= \frac{1}{2}\left[\Phi_{\mathrm{SC}+}^{\{s\}}(l,p,q) + \Phi_{\mathrm{SC}+}^{\{\tilde{s}\}}(l,p,l-q)\right]\,,\\
\Phi_{\mathrm{nsing}\uparrow\downarrow}^{\{s\}}(l,p,q) &= \frac{1}{2}\left[\Phi_{\mathrm{SC}+}^{\{s\}}(l,p,q) - \Phi_{\mathrm{SC}+}^{\{\tilde{s}\}}(l,p,l-q)\right]\,.
\end{aligned}$$

While $\Phi_{\mathrm{SC},\uparrow+}$ already constitutes a triplet pairing interaction, the non-singlet coupling function $\Phi_{\mathrm{nsing}\uparrow\downarrow}^{\{s\}}$ contains triplet and anomalous terms. Since only singlet pairing contributions will be retained in the following, I refrain from a further decomposition of the latter coupling function in this work.

For the new pairing coupling functions, one obtains the following symmetry constraints. On the time-reversal breaking side, one has

$$\begin{aligned}
&\text{PHS} && \Phi_{\mathrm{SC},\uparrow-}^{\{s\}}(l,p,q) = \Phi_{\mathrm{SC},\uparrow-}^{\{\hat{s}\}}(l,q,p)\,,\\
&\text{Pauli} && \Phi_{\mathrm{SC},\uparrow-}^{\{s\}}(l,p,q) = -\Phi_{\mathrm{SC},\uparrow-}^{(s_2,s_1,s_3,s_4)}(l,l-p,q) = \Phi_{\mathrm{SC},\uparrow-}^{\{\bar{s}\}}(l,l-p,l-q)\,,\\
&\text{PFS} && \Phi_{\mathrm{SC},\uparrow-}^{\{s\}}(l,p,q) = -\Phi_{\mathrm{SC},\uparrow-}^{\{-s\}}(l,p,q)^*
\end{aligned}$$

and

$$\begin{aligned}
&\text{PHS} && \Phi_{\mathrm{SC}-}^{\{s\}}(l,p,q) = \Phi_{\mathrm{SC}-}^{\{\hat{s}\}}(l,q,p)\,,\\
& && \Phi_{\mathrm{SC}-}^{\{s\}}(l,p,q) = -\Phi_{\mathrm{SC}-}^{\{\bar{s}\}}(l,l-p,l-q)\,,\\
&\text{PFS} && \Phi_{\mathrm{SC}-}^{\{s\}}(l,p,q) = -\Phi_{\mathrm{SC}-}^{\{-s\}}(l,p,q)^*\,.
\end{aligned}$$

For the triplet contributions, the symmetry constraints read as

$$\begin{aligned}
&\text{PHS} && \Phi^{\{s\}}_{\mathrm{SC},\uparrow+}(l,p,q) = \Phi^{\{\hat{s}\}}_{\mathrm{SC},\uparrow+}(l,q,p)\,,\\
&\text{Pauli} && \Phi^{\{s\}}_{\mathrm{SC},\uparrow+}(l,p,q) = \Phi^{\{\bar{s}\}}_{\mathrm{SC},\uparrow+}(l,l-p,l-q) = -\Phi^{\{\bar{s}\}}_{\mathrm{SC},\uparrow+}(l,p,l-q)\,,\\
&\text{PFS} && \Phi^{\{s\}}_{\mathrm{SC},\uparrow+}(l,p,q) = \Phi^{\{-s\}}_{\mathrm{SC},\uparrow+}(l,p,q)^*
\end{aligned}$$

and

$$\begin{aligned}
&\text{PHS} && \Phi^{\{s\}}_{\mathrm{nsign}\uparrow\downarrow}(l,p,q) = \Phi^{\{\hat{s}\}}_{\mathrm{nsing}\uparrow\downarrow}(l,q,p)\,,\\
& && \Phi^{\{s\}}_{\mathrm{nsing}\uparrow\downarrow}(l,p,q) = \Phi^{\{\bar{s}\}}_{\mathrm{nsing}\uparrow\downarrow}(l,l-p,l-q) = -\Phi^{\{\bar{s}\}}_{\mathrm{nsing}\uparrow\downarrow}(l,p,l-q)\,,\\
&\text{PFS} && \Phi^{\{s\}}_{\mathrm{nsing}\uparrow\downarrow}(l,p,q) = \Phi^{\{-s\}}_{\mathrm{nsing}\uparrow\downarrow}(l,p,q)^*
\end{aligned}$$

for the non-singlet part, while one has

$$\begin{aligned}
&\text{PHS} && \Phi^{\{s\}}_{\mathrm{singlet}}(l,p,q) = \Phi^{\{\hat{s}\}}_{\mathrm{singlet}}(l,q,p)\,,\\
& && \Phi^{\{s\}}_{\mathrm{singlet}}(l,p,q) = \Phi^{\{\bar{s}\}}_{\mathrm{singlet}}(l,l-p,l-q) = \Phi^{\{\bar{s}\}}_{\mathrm{singlet}}(l,p,l-q)\,,\\
&\text{PFS} && \Phi^{\{s\}}_{\mathrm{singlet}}(l,p,q) = \Phi^{\{-s\}}_{\mathrm{singlet}}(l,p,q)^*
\end{aligned}$$

for the singlet-pairing channel.

Finally, let me also decompose the magnetic in-plane channel into time-reversal invariant and time-reversal breaking parts

$$\Phi^{\{s\}}_{xy\pm}(l,p,q) = \frac{1}{2}\left[\Phi^{\{s\}}_{xy}(l,p,q) \pm \Phi^{\{\bar{s}\}}_{xy}(-l,q,p)\right]\,,$$

corresponding to $S^2_x + S^2_y$ and S_xS_y terms, respectively. They fulfill the symmetry constraints

$$\begin{aligned}
&\text{PHS} && \Phi^{\{s\}}_{xy\pm}(l,p,q) = \Phi^{\{\hat{s}\}}_{xy\pm}(l,q+l,p-l)\\
& && \Phi^{\{s\}}_{xy\pm}(l,p,q) = \pm\Phi^{\{\bar{s}\}}_{xy\pm}(-l,q,p)\,,\\
&\text{PFS} && \Phi^{\{s\}}_{xy\pm}(l,p,q) = \pm\Phi^{\{-s\}}_{xy\pm}(l,p,q)^*\,.
\end{aligned}$$

4.2.3. Time-normal approximation

Typically, the bare interaction is time-reversal invariant. In the presence of PHS and parity inversion, this is equivalent to spin-flip invariance, i.e.

$$\begin{aligned}
U^{\{s\}}_{\uparrow}(k_1,k_2,k_3) &= U^{\{s\}}_{\downarrow}(k_1,k_2,k_3)\,,\\
U^{\{s\}}_{\uparrow\downarrow}(k_1,k_2,k_3) &= U^{\{\bar{s}\}}_{\uparrow\downarrow}(k_2,k_1,k_1+k_2-k_3)
\end{aligned}$$

holds. In order to avoid confusion with a full SU(2) invariance in the interaction, I will henceforth speak of time-reversal invariance instead of spin-flip invariance. This distinction is physically important, as time-reversal symmetry is a discrete one, while a SU(2) symmetry would be continuous.

At the mean-field level, time-reversal breaking interactions are absent. Such terms are however generated during the RG flow if the interaction is not of reduced-mean-field type (see Chapter 1.4.3). In a first attempt to enter the AF phase within a fRG framework beyond mean field, neglecting the time-reversal breaking interactions may be a decent approximation. In the following, I will call this the time-normal approximation.

There are various reasons for resorting to it.

i.) For the special case of an antiferromagnet, a spin flip just shifts the pattern for the alignment of the spins by one lattice constant, while the magnetization would change sign in a ferromagnet. Therefore, the sign of the staggered magnetization is only fixed arbitrarily, while, in contrast, the sign of the magnetization in a ferromagnet is physically meaningful. In other words, spontaneous symmetry breaking towards an AF phase selects an axis for the alignment of the spins. Their orientation along this axis, however, has no relevance on a macroscopic level. Consequently, one may expect spin-flip antisymmetric interaction terms to have a minor impact.

ii.) Moreover, the breaking of the continuous symmetries can be expected to have a greater impact on the fRG flow than for the discrete ones, as the Goldstone theorem only applies in the former case.

iii.) In Appendix C.2, time-reversal breaking contributions to the interaction with zero momentum and frequency transfer are shown to vanish in random-phase approximation in the case of the Hubbard model at half-filling. For the Chubukov model studied in Chapter 5, it appears unlikely that such terms should play a major role.

Note that the time-normal approximation does not involve any approximations at the one-particle level, where the time-reversal still remains broken.

As will become clear in the following, the fRG flow in time-normal approximations still contains a number of features that are not included in the mean-field picture. It seems an appealing strategy to first study these new features and to include time-reversal breaking contributions to the interaction in a further step. While the former is the subject of the remainder of this thesis, the latter will be left for future studies.

In time-normal approximation, the remaining spin-symmetry group for the interaction is $\mathrm{G_t} = \mathrm{U}_z(1) \times \mathrm{Z}_2$, which has a preferred axis, but no preferred orientation along this axis. The Z_2 symmetry rules out such a preferred orientation. It stems from the spin-flip

invariance enforced by omitting contributions to the renormalized interaction that would violate the conditions

$$W_{\uparrow}^{\{s\}}(k_1,k_2,k_3,k_4) = W_{\downarrow}^{\{s\}}(k_1,k_2,k_3,k_4)\,,$$
$$W_{\uparrow\downarrow}^{\{s\}}(k_1,k_2,k_3,k_4) = W_{\uparrow\downarrow}^{\{\bar{s}\}}(k_2,k_1,k_4,k_3)\,,$$

where $\bar{s} = (s_2, s_1, s_4, s_3)$. This Z_2 invariance is, however, not enforced on the one-particle level.[4]

In addition to the time-normal approximation, triplet and anomalous pairing tendencies will be discarded here, since they appear to play a minor role in the presence of perfect nesting. In other words, the single-channel coupling functions $\Phi_{\mathrm{SC},\uparrow\pm}$, $\Phi_{\mathrm{SC}-}$, Φ_{K-}, $\Phi_{\mathrm{axis}-}$ and Φ_{xy-} are neglected. The remaining interaction terms read as

$$\begin{aligned} W_{\uparrow}(k_1,k_2,k_3,k_4)^{\{s\}} = \tilde{\delta}_{\{k_i\}} \Big[& U_{\uparrow}^{\{s\}}(k_1,k_2,k_3) - \frac{1}{2}\Phi_{\mathrm{CDW}}^{\{s\}}(k_1-k_3,k_1,k_2) \\ & - \frac{1}{2}\Phi_{z}^{\{s\}}(k_1-k_3,k_1,k_2) + \frac{1}{2}\Phi_{\mathrm{CDW}}^{\{\tilde{s}\}}(k_3-k_2,k_1,k_2) \\ & + \frac{1}{2}\Phi_{z}^{\{\tilde{s}\}}(k_3-k_2,k_1,k_2)\Big]\,, \end{aligned}$$

$$\begin{aligned} W_{\uparrow\downarrow}^{\{s\}}(k_1,k_2,k_3,k_4) = \tilde{\delta}_{\{k_i\}} \Big[& U_{\uparrow\downarrow}^{\{s\}}(k_1,k_2,k_3) + \Phi_{\mathrm{singlet}}^{\{s\}}(k_1+k_2,k_1,k_3) \\ & + \Phi_{xy+}^{\{s\}}(k_3-k_2,k_1,k_2) - \frac{1}{2}\Phi_{\mathrm{CDW}}^{\{s\}}(k_1-k_3,k_1,k_2) \\ & + \frac{1}{2}\Phi_{z}^{\{s\}}(k_1-k_3,k_1,k_2)\Big] \end{aligned}$$

and

$$W_{\uparrow}^{\{s\}}(k_1,k_2,k_3,k_4) = W_{\downarrow}^{\{s\}}(k_1,k_2,k_3,k_4)\,.$$

Consequently, one now has $W_{\pm\uparrow} = W_{\pm\downarrow} \equiv W_{\pm}$ for the shorthand notations introduced in Eq. (1.35) and the single-channel coupling functions feed into these quantities as

$$\begin{aligned} W_{+}^{\{s\}}(k_1,k_2,k_3,k_4) = \tilde{\delta}_{\{k_i\}} \Big[& U_{\uparrow\downarrow}^{\{s\}}(k_1,k_2,k_3) + U_{\uparrow}^{\{\tilde{s}\}}(k_1,k_2,k_4) + \Phi_{\mathrm{singlet}}^{\{s\}}(k_1+k_2,k_1,k_3) \\ & + \Phi_{xy+}^{\{s\}}(k_3-k_2,k_1,k_2) + \Phi_{z}^{\{s\}}(k_1-k_3,k_1,k_2) \\ & - \frac{1}{2}\Phi_{\mathrm{CDW}}^{\{\tilde{s}\}}(k_3-k_2,k_1,k_2) - \frac{1}{2}\Phi_{z}^{\{\tilde{s}\}}(k_3-k_2,k_1,k_2)\Big] \end{aligned}$$

[4] On the one-particle level, $\mathrm{G_t}$ would be equivalent to SU(2) in the sense that a $\mathrm{G_t}$ symmetric one-particle Green's function is automatically SU(2) symmetric.

and

$$W_{-}^{\{s\}}(k_1,k_2,k_3,k_4) = \tilde{\delta}_{\{k_i\}}\Big[U_{\uparrow\downarrow}^{\{s\}}(k_1,k_2,k_3) - U_{\uparrow}^{\{\bar{s}\}}(k_1,k_2,k_4) + \Phi_{\text{singlet}}^{\{s\}}(k_1+k_2,k_1,k_3) + \Phi_{xy+}^{\{s\}}(k_3-k_2,k_1,k_2) - \Phi_{\text{CDW}}^{\{s\}}(k_1-k_3,k_1,k_2) + \frac{1}{2}\Phi_{\text{CDW}}^{\{\tilde{s}\}}(k_3-k_2,k_1,k_2) + \frac{1}{2}\Phi_{z}^{\{\tilde{s}\}}(k_3-k_2,k_1,k_2)\Big]\,.$$

It can easily be verified, that the time-normal approximation gives rise to

$$W_{\pm}^{\{s\}}(k_1,k_2,k_3,k_4) = W_{\pm}^{\{\bar{s}\}}(k_2,k_1,k_4,k_3)\,.$$

The flow equation for the single-channel coupling functions in time-normal approximation can be cast into a simple form, where the loops enter in the spin-symmetrized combinations

$$I_{\text{eq}}^{\{s'\}}(l,p) = \frac{1}{2}\left[G_{\uparrow}^{s_1's_2'}(p-l/2)\,G_{\uparrow}^{s_3's_4'}(p+l/2) + G_{\downarrow}^{s_1's_2'}(p-l/2)\,G_{\downarrow}^{s_3's_4'}(p+l/2)\right],$$
$$I_{\text{op}}^{\{s'\}}(l,p) = \frac{1}{2}\left[G_{\uparrow}^{s_1's_2'}(p-l/2)\,G_{\downarrow}^{s_3's_4'}(p+l/2) + G_{\downarrow}^{s_1's_2'}(p-l/2)\,G_{\uparrow}^{s_3's_4'}(p+l/2)\right],$$
$$J_{\text{op}}^{\{s'\}}(l,p) = \frac{1}{2}\left[G_{\uparrow}^{s_1's_2'}(l/2+p)\,G_{\downarrow}^{s_3's_4'}(l/2-p) + G_{\downarrow}^{s_1's_2'}(l/2+p)\,G_{\uparrow}^{s_3's_4'}(l/2-p)\right].$$

For the singlet-pairing channel, one obtains the flow equation

$$\dot{\Phi}_{\text{singlet}}^{\{s\}}(l,q,q') = -\frac{1}{2}\sum_{\{s'\}}\int d'p\,\dot{J}_{\text{op}}^{\{s'\}}(l,p)\,W_{\uparrow\downarrow}^{s_1,s_2,s_1',s_3'}(q,l-q,l/2+p,l/2-p) \times\left[W_{\uparrow\downarrow}^{s_2',s_4',s_3,s_4}(l/2+p,l/2-p,q',l-q') + W_{\uparrow\downarrow}^{s_4',s_2',s_3,s_4}(l/2-p,l/2+p,q',l-q')\right] \tag{4.36}$$

and for the in-plane magnetic channel

$$\dot{\Phi}_{xy+}^{\{s\}}(l,q,q') = -\sum_{\{s'\}}\int d'p\,\dot{I}_{\text{op}}^{\{s'\}}(l,p)\,W_{\uparrow\downarrow}^{s_4',s_2,s_3,s_1'}(p+l/2,q',l+q',p-l/2) \times W_{\uparrow\downarrow}^{s_1,s_2',s_3',s_4}(q,p-l/2,p+l/2,q-l)\,. \tag{4.37}$$

For the CDW channel, the flow equation reads as

$$\dot{\Phi}_{\text{CDW}}^{\{s\}}(l,q,q') = -\sum_{\{s'\}}\int d'p\,\dot{I}_{\text{eq}}^{\{s'\}}(l,p)\,W_{-}^{s_2',s_1,s_3',s_3}(p-l/2,q,p+l/2,q-l) \times W_{-}^{s_4',s_2,s_1',s_4}(p+l/2,q',p-l/2,q'+l)\,, \tag{4.38}$$

and for the S_z^2 channel one gets

$$\dot{\Phi}_z^{\{s\}}(l,q,q') = -\sum_{\{s'\}} \int d'p\, \dot{I}_{\mathrm{eq}}^{\{s'\}}(l,p)\, W_+^{s_2',s_1,s_3',s_3}(p-l/2,q,p+l/2,q-l) \\ \times W_+^{s_4',s_2,s_1',s_4}(p+l/2,q',p-l/2,q'+l)\,. \tag{4.39}$$

In the following, the self-energy will be decomposed into its spin-symmetric and spin-antisymmetric parts

$$\Sigma_\pm^{s_1 s_2}(k) = \frac{1}{2}\left[\Sigma_\uparrow^{s_1 s_2}(k) \pm \Sigma_\downarrow^{s_1 s_2}(k)\right]\,,$$

which flow according to

$$\dot{\Sigma}_\pm^{s_1 s_2}(k) = -\frac{1}{2}\sum_{s_1' s_2'} \int d'p\, \left[S_\uparrow^{s_1' s_2'}(p) \pm S_\downarrow^{s_1' s_2'}(p)\right] W_\mp^{s_1 s_2' s_2 s_1'}(k,p,k,p)\,. \tag{4.40}$$

Expressed in terms of the quantities defined in Section 4.2.1, Σ_+ contains $\Re\epsilon_\mathrm{s}$, $\Im\epsilon_\mathrm{a}$ and $\Im\Delta$ and Σ_- contains $\Re\Delta$, $\Im\epsilon_\mathrm{s}$ and renormalizations of $\Re\epsilon_\mathrm{a}$.

4.3. Exchange parametrization

In the spirit of Refs. [24–26], one may now resort to an exchange parametrization as described in Chapter 1.2.3. The formalism presented here has been adapted from Ref. [26], where the Hubbard model has been studied in the symmetric phase.

Two slowly varying form factors are already encoded in the Nambu indices. They can be attributed to the two irreducible representations of the Z_2 group, which correspond to basis vectors that are even or odd under a Nambu-index flip. In this chapter, they will be referred to as trivial and sign-changing form factors, respectively. For the Chubukov model studied in Chapter 5, they correspond to s-wave or $s^\pm$-wave, respectively. For the Hubbard model, the trivial form factor is of s-wave and the sign-changing one of $d_{x^2-y^2}$-wave type.[5] Although one may in principle include more form factors, these two slowly varying ones appear suitable for low-energy considerations.

4.3.1. Projection rule and symmetries

In the present case, there is not only one unique way of performing an exchange parametrization. In particular, the dependence of the interaction on the Nambu indices can be

[5] In the latter case of the Hubbard model, the reduced Brillouin zone should be centered around $(0,\pi)$ for simplicity.

treated in various ways and the dependence on the weak momenta and frequencies can either be taken into account within a form-factor expansion as in Ref. [24] and subsequent works, or it may be projected to a single point. In the following, the latter strategy will be pursued. Moreover, it appears sensible to resort to an exchange parametrization which does not contain approximations on the Nambu index dependence. Such approximations can then be freely devised at a later stage in agreement with the symmetries. On a formal level, a single-channel coupling function Φ_P is approximated by the product of fermion-boson vertices $g_\alpha(q,l)$ and exchange propagators $P^{\{s\}}_{\alpha\beta}(l)$, i.e.

$$\Phi^{\{s\}}_P(l,q,q') \approx \sum_{\alpha\beta} g_\alpha(q,l)\, g_\beta(q',l)\, P^{\{s\}}_{\alpha\beta}(l)\,.$$

The indices α and β correspond to bosonic flavors here. In the following, only fermion-boson vertices with a trivial momentum and frequency dependence will be taken into account. Since α and β then take on only one value, they will be suppressed from the notation in the following. Normalizing the momentum- and frequency-independent fermion-boson vertices to unity then gives

$$\Phi^{\{s\}}_P(l,q,q') \approx P^{\{s\}}(l)\,,$$

i.e. for each combination of Nambu indices, the coupling function of a particular channel can then be attributed to a bosonic propagator. The above mentioned trivial and sign-changing form factors then come into play if the exchange propagators are parametrized further. This parametrization will be addressed further below.

More precisely, one may choose

$$\Phi^{\{s\}}_{\text{singlet}}(l,q,q') \approx D^{\{s\}}(l) = \mathcal{P}_{\text{pp}}\left[\Phi^{\{s\}}_{\text{singlet}}\right](l) \tag{4.41}$$

with the projection rule

$$\mathcal{P}_{\text{pp}}\left[\Phi\right](l) = \Phi(l, l/2, l/2)$$

for particle-particle channels. Note that the weak momentum and frequency arguments of Φ are chosen in such a way that unique symmetry constraints on the exchange propagators result from the respective constraints on Φ. These new constraints on the exchange propagators will be given in Section 4.3.2. For the particle-hole channels, the bosonic propagators are defined likewise according to

$$\Phi^{\{s\}}_{\text{CDW}}(l,q,q') \approx N^{\{s\}}(l) = \mathcal{P}_{\text{ph}}\left[\Phi^{\{s\}}_{\text{CDW}}\right](l)\,, \tag{4.42}$$

$$\Phi^{\{s\}}_{xy+}(l,q,q') \approx M^{\{s\}}_{xy}(l) = \mathcal{P}_{\text{ph}}\left[\Phi^{\{s\}}_{xy+}\right](l)\,, \tag{4.43}$$

$$\Phi^{\{s\}}_{z}(l,q,q') \approx M^{\{s\}}_{z}(l) = \mathcal{P}_{\text{ph}}\left[\Phi^{\{s\}}_{z}\right](l)\,. \tag{4.44}$$

The projection rule

$$\mathcal{P}_{\text{ph}}\left[\Phi\right](l) = \Phi(l, l/2, -l/2)$$

for the particle-hole channels differs from $\mathcal{P}_{\mathrm{pp}}$ by a minus sign in the last argument of Φ, which ensures compatibility with the symmetries.

Note that in contrast to Refs. [24–26], not only the weak frequency dependences, but also the weak momentum dependences are projected to a single point through the above projection rule. For the present work, this seems to be an adequate choice, since the Chubukov model discussed in Chapter 5 can be regarded in the light of a gradient expansion around the centers of hole and electron pockets. The physics of the Hubbard model at van Hove filling is dominate by the vicinity of the saddle points $(0,\pi)$ and $(\pi,0)$ of its dispersion and therefore the projection rule resented here may also be applicable in that case. For $l=0$, the weak frequencies and momenta are only considered in leading (zeroth) order in a gradient expansion around these hot-spots.

Of course, different projection rules can be applied for lattice models, such as the form-factor expansion rule of Refs. [24–26] or the Fermi surface projection of Refs. [49–51]. These projection rules all comply with the symmetry constraints on the single-channel coupling functions in Section 4.2.2.

Let us now assume that the bare interaction is time-reversal invariant and only depends on the Nambu indices and not on the momenta. Both the bare interactions of the Hubbard model and of the two-pocket Chubukov model are of this type. In terms of the above defined exchange propagators, the multichannel coupling functions $W_{\uparrow\downarrow}$, W_+ and W_- in time-normal approximation read as

$$\begin{aligned} W^{\{s\}}_{\uparrow\downarrow}(k_1,k_2,k_3) &= U^{\{s\}}_{\uparrow\downarrow} + D^{\{s\}}(k_1+k_2) + M^{\{s\}}_{xy}(k_3-k_2) \\ &\quad + \frac{1}{2}\left[M^{\{s\}}_{z}(k_1-k_3) - N^{\{s\}}(k_1-k_3)\right] , \\ W^{\{s\}}_{+}(k_1,k_2,k_3) &= U^{\{s\}}_{\uparrow\downarrow} - U^{\{s\}}_{\uparrow} + D^{\{s\}}(k_1+k_2) + M^{\{s\}}_{xy}(k_3-k_2) \\ &\quad + M^{\{s\}}_{z}(k_1-k_3) - \frac{1}{2}\left[N^{\{\tilde{s}\}}(k_3-k_2) + M^{\{\tilde{s}\}}_{z}(k_3-k_2)\right] , \\ W^{\{s\}}_{-}(k_1,k_2,k_3) &= U^{\{s\}}_{\uparrow\downarrow} + U^{\{s\}}_{\uparrow} + D^{\{s\}}(k_1+k_2) + M^{\{s\}}_{xy}(k_3-k_2) \\ &\quad - N^{\{s\}}(k_1-k_3) + \frac{1}{2}\left[N^{\{\tilde{s}\}}(k_3-k_2) + M^{\{\tilde{s}\}}_{z}(k_3-k_2)\right] . \end{aligned}$$

The symmetry constraints for the single-channel coupling functions given in Section 4.2.2 translate to the exchange propagators as follows. The PHS imposes the constraints

$$\begin{aligned} D^{\{s\}}(l) &= D^{\{\hat{s}\}}(l) , \\ M^{\{s\}}_{xy}(l) &= M^{\{\hat{s}\}}_{xy}(l) , \\ M^{\{s\}}_{z}(l) &= M^{\{\hat{s}\}}_{z}(-l) , \\ N^{\{s\}}(l) &= N^{\{\hat{s}\}}(-l) , \end{aligned}$$

where $\{\hat{s}\} = (s_3 s_4 s_1 s_2)$. Furthermore, the PFS symmetry gives rise to

$$\begin{aligned} D^{\{s\}}(l) &= D^{\{-s\}}(l)^*\,, \\ M_{xy}^{\{s\}}(l) &= M_{xy}^{\{-s\}}(l)^*\,, \\ M_{z}^{\{s\}}(l) &= M_{z}^{\{-s\}}(l)^*\,, \\ N^{\{s\}}(l) &= N^{\{-s\}}(l)^*\,. \end{aligned}$$

In addition, by construction or by virtue of the Pauli principle, one has

$$\begin{aligned} D^{\{s\}}(l) &= D^{\{\bar{s}\}}(l) = D^{\{\tilde{s}\}}(l)\,, \\ M_{xy}^{\{s\}}(l) &= M_{xy}^{\{\bar{s}\}}(-l)\,, \\ M_{z}^{\{s\}}(l) &= M_{z}^{\{\bar{s}\}}(-l)\,, \\ N^{\{s\}}(l) &= N^{\{\bar{s}\}}(-l) \end{aligned}$$

with $\{\bar{s}\} = (s_2 s_1 s_4 s_3)$ and $\{\tilde{s}\} = (s_1 s_2 s_4 s_3)$.

For the following discussion, I will assume that the point-group of the model contains the parity operation, giving rise to

$$P^{\{s\}}(-l) = P^{\{s\}}(l)^*$$

for all exchange propagators P.

4.3.2. Parametrization of the Nambu-index dependence

We are now in a position, where the dependence on the Nambu indices can be parametrized. I will first parametrize this dependence exactly by applying the above symmetries. In a second step, I will give a prescription how the Nambu-index dependence can be recast within a form-factor expansion.

In the following, a matrix notation for the Nambu indices will be used, where the rows correspond to $(s_1, s_2) = ++,\ --,\ +-$ and $-+$ and likewise for the columns, which correspond to the ingoing legs with Nambu indices s_3 and s_4. For the singlet-pairing channel, the symmetries lead to an exchange propagator of the form

$$D^{\{s\}}(l) = \begin{pmatrix} a_D(l) & d_D(l) & h_D(l) & h_D(l) \\ d_D(l) & a_D(l)^* & h_D(l)^* & h_D(l)^* \\ h_D(l) & h_D(l)^* & b_D(l) & b_D(l) \\ h_D(l) & h_D(l)^* & b_D(l) & b_D(l) \end{pmatrix}$$

with four independent components a_D, b_D, d_D and h_D. This matrix is symmetric due to the PHS and due to the PFS b_D and d_D are real.

P	trivial	sign-changing	mixed	momentum
D	$(\Re a_D + d_D)/2$	$(\Re a_D - d_D)/2$	$\Im a_D$	$\mathbf{l}$
	b_D			$\mathbf{l}+\mathbf{Q}$
	$\Re h_D$		$\Im h_D$	n.c.
M_{xy}	$(a_{xy} + r_{xy})/2$	$(a_{xy} - r_{xy})/2$		$\mathbf{l}$
	$(\Re b_{xy} + d_{xy})/2$	$(\Re b_{xy} - d_{xy})/2$	$\Im b_{xy}$	$\mathbf{l}+\mathbf{Q}$
	$\Re h_{xy}$		$\Im h_{xy}$	n.c.
M_z	$(a_z + b_z)/2$	$(a_z - b_z)/2$		$\mathbf{l}$
	$(d_z + \Re r_z)/2$	$(d_z - \Re r_z)/2$	$\Im r_z$	$\mathbf{l}+\mathbf{Q}$
	$\Re h_z$		$\Im h_z$	n.c.
N	$(a_N + b_N)/2$	$(a_N - b_N)/2$		$\mathbf{l}$
	$(d_N + \Re r_N)/2$	$(d_N - \Re r_N)/2$	$\Im r_N$	$\mathbf{l}+\mathbf{Q}$
	$\Re h_N$		$\Im h_N$	n.c.

Table 4.1.: Classification of the components of the exchange propagators according form factors and ordering momenta in time-normal approximation. The entries in the column with the label 'mixed' correspond to propagators of exchange bosons that are created as a trivial form-factor (particle-particle or particle-hole) pair and that are annihilated as an sign-changing form-factor pair or vice versa. The entry 'n.c.' in the last column stands for momentum non-conserving terms.

Alternatively, the Nambu-index dependence can be attributed to fermion-boson vertices according to

$$D^{\{s\}}(l) = \sum_{m=0,\pi} \sum_{m'=0,\pi} \sum_{n=\pm} \sum_{n'=\pm} g^{s_1 s_2}_{m,n}\, g^{s_3 s_4}_{m',n'}\, D^{nn'}_{mm'}(l)\,,$$

where the fermion-boson vertices $g^{ss'}_{n,m} = f^{ss'}_m\, f^{ss'}_n$ factorize into $f^{ss'}_m$ which accounts for the ordering momentum and the form factors $f^{ss'}_n$. More precisely, one has $f^{ss'}_0 = \delta_{s,s'}$ and $f^{ss'}_\pi = \delta_{s,-s'}$ and the trivial and sign-changing form factors read as $f^{ss'}_+ = 1$ and $f^{ss'}_- = s$, respectively.

In this new language, the combinations $\Re a_D \pm d_D = D^{\pm\pm}_{00}$ correspond to pairing with total momentum around zero and with trivial and sign-changing form factors, respectively. For a systematic classification of the components of the exchange propagators according to form factors and ordering momenta, see Tab. 4.1.

For the magnetic in-plane channel, one gets

$$M^{\{s\}}_{xy}(l) = \begin{pmatrix} a_{xy}(l) & d_{xy}(l) & h_{xy}(l) & h_{xy}(l)^* \\ d_{xy}(l) & a_{xy}(l) & h_{xy}(l) & h_{xy}(l)^* \\ h_{xy}(l) & h_{xy}(l) & b_{xy}(l) & r_{xy}(l) \\ h_{xy}(l)^* & h_{xy}(l)^* & r_{xy}(l) & b_{xy}(l)^* \end{pmatrix},$$

with real a_{xy}, d_{xy} and r_{xy}. Again, PHS requires a symmetric matrix. In this channel,

the form-factor expansion reads as

$$M_{xy}^{\{s\}}(l) = \sum_{m=0,\pi} \sum_{m'=0,\pi} \sum_{n=\pm} \sum_{n'=\pm} g_{m,n}^{s_1 s_4} \, g_{m',n'}^{s_3 s_2} \, (M_{xy})_{mm'}^{nn'}(l) \, .$$

The Goldstone vertex must consequently be contained in the trivial form-factor contribution $(M_{xy})_{\pi\pi}^{++} = (\Re b_{xy} + d_{xy})/2$ for ordering momentum $\mathbf{l} + \mathbf{Q}$.

Similarly, one finds for the CDW and the S_z^2 channel with exchange propagators $P = N, M_z$

$$P^{\{s\}}(l) = \begin{pmatrix} a_P(l) & d_P(l) & h_P(l) & h_P(l)^* \\ d_P(l)^* & a_P(l) & h_P(l) & h_P(l)^* \\ h_P(l)^* & h_P(l)^* & b_P(l) & r_P(l) \\ h_P(l) & h_P(l) & r_P(l)^* & b_P(l) \end{pmatrix} ,$$

where $a_P, b_P, d_P \in \mathbb{R}$. Note that the PHS leads to a Hermitian matrix here and that the form-factor expansion is to be performed according to

$$P^{\{s\}}(l) = \sum_{m=0,\pi} \sum_{m'=0,\pi} \sum_{n=\pm} \sum_{n'=\pm} g_{m,n}^{s_1 s_3} \, g_{m',n'}^{s_2 s_4} \, P_{mm'}^{nn'}(l) \, .$$

The contributions $P_{\pi\pi}^{++} = (d_P + \Re r_P)/2$ corresponding to ordering momentum $\mathbf{l} + \mathbf{Q}$ and a trivial form factor can be expected to be the most important ones. Namely, these contributions constitute the CDW vertex for $P = N$ and the radial vertex for $P = M_z$, which drives the gap.

In time-normal approximation, the exchange propagators of all four channels have contributions corresponding to mixed form factors, as can be seen from Tab. 4.1. Such processes can be thought of a boson being created with a trivial form factor (particle-particle or particle-hole) pair and being annihilated as one with an sign-changing form factor or vice versa. Since these contributions lack a real part, they vanish at $l = 0$ and hence can be expected to be of minor importance. Note that this behavior may however be induced by the time-normal approximation and that such terms play a more important role once time-reversal breaking terms are included. In contrast, the trivial and sign-changing form-factor components of the exchange propagators are however always real in time-normal approximation.

4.3.3. Flow equations and Ward identity

Let us now apply the above projection rule to the flow equations (4.36)–(4.39) of Section 4.2.3. With the help of the auxiliary functions

$$F^{\{s\}}_{\uparrow\downarrow}[P_1,P_2](l,p) = U^{\{s\}}_{\uparrow\downarrow} + P^{\{s\}}_1(l) + P^{\{s\}}_2(p)\,,$$
$$F^{\{s\}}_{\pm}[P_1,P_2,P_3](l,p) = U^{\{s\}}_{\uparrow\downarrow} \mp U^{\{s\}}_{\uparrow} \pm P^{\{s\}}_1(l) + P^{\{s\}}_2(p) \mp \frac{1}{2}P^{\{\tilde{s}\}}_3(p)\,.$$

for the projected interaction, the flow equations for the exchange propagators read as

$$\dot{D}^{\{s\}}(l) = -\sum_{\{s'\}}\int d'p\, \dot{J}^{\{s'\}}_{\rm op}(l,p)\, F^{s_1,s_2,s_1',s_3'}_{\uparrow\downarrow}[D, M_{xy} + (M_z - N)^*/2](l,p)$$
$$\times\, F^{s_2',s_4',s_3,s_4}_{\uparrow\downarrow}[D, \Re M_{xy} + \Re(M_z - N)/2](l,p)\,, \tag{4.45}$$

$$\dot{M}^{\{s\}}_{xy}(l) = -\sum_{\{s'\}}\int d'p\, \dot{I}^{\{s'\}}_{\rm op}(p,l)\, F^{s_4',s_2,s_3,s_1'}_{\uparrow\downarrow}[M_{xy}, D + (M_z - N)/2](l,p)$$
$$\times\, F^{s_1,s_2',s_3',s_4}_{\uparrow\downarrow}[M_{xy}, D + (M_z - N)^*/2](l,p)\,, \tag{4.46}$$

$$\dot{N}^{\{s\}}(l) = -\sum_{\{s'\}}\int d'p\, \dot{I}^{\{s'\}}_{\rm eq}(l,p)\, F^{s_2',s_1,s_3',s_3}_{-}[N^*, D + M_{xy}, M_z + N](l,p)$$
$$\times\, F^{s_4',s_2,s_1',s_4}_{-}[N, D + M_{xy}, M_z + N](l,p)\,, \tag{4.47}$$

and

$$\dot{M}^{\{s\}}_{z}(l) = -\sum_{\{s'\}}\int d'p\, \dot{I}^{\{s'\}}_{\rm eq}(l,p)\, F^{s_2',s_1,s_3',s_3}_{+}[M^*_z, D + M_{xy}, M_z + N](l,p)$$
$$\times\, F^{s_4',s_2,s_1',s_4}_{+}[M_z, D + M_{xy}, M_z + N](l,p)\,. \tag{4.48}$$

These flow equations resemble those in Ref. [26], from which they differ in two respects. In the present case, the exchange propagators depend on Nambu indices and the projected interactions on the loop momenta $\mathbf{p}$. The latter difference is induced by the choice of different projection rules. For a lattice model, one may alternatively project out the exchange propagators as in Ref. [26] and the projected interactions could then be pulled out of the integral over the loop momenta. Nevertheless, propagator-renormalization, vertex-correction and box diagrams appear on the right-hand side of these flow equations (see Fig. 4.2).

In RPA, only the propagator-renormalization diagrams are retained, which do not have bosonic lines inside a closed loop. In other words, P_2 and P_3 are neglected in the

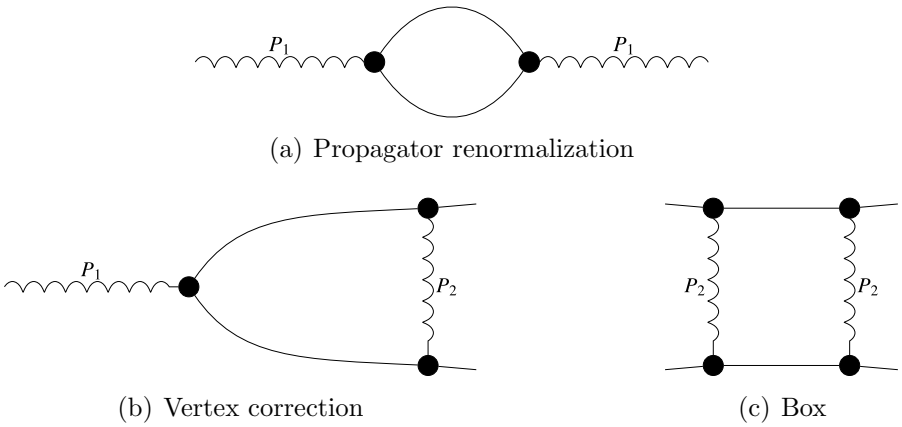

(a) Propagator renormalization

(b) Vertex correction

(c) Box

Figure 4.2.: Diagrams renormalizing an exchange propagator P_1. Straight lines represent quasiparticle propagators, snaked lines exchange propagators and filled black circles correspond to fermion-boson vertices. These diagrams appear on the right-hand side of a flow equation of the form $\dot{P}_1 = F[P_1, P_2] \circ I \circ F[P_1, P_2]$, where P_2 is a linear combination of the exchange propagators of various channels and where I denotes the scale-derivative of the fermionic (particle-particle or particle-hole) loop function.

projected interaction. Exchange propagators of different channels then only couple via the self-energy, indicating that the parametrization used here is indeed a sensible one.

If the flow equation (4.40) for the self-energy is now expressed in terms of these exchange propagators, they feed into its scale derivative

$$\dot{\Sigma}_{\pm}^{s_1 s_2}(k) = -\frac{1}{2} \sum_{s_1' s_2'} \int d'p \, \left[S_{\uparrow}^{s_1' s_2'}(p) \pm S_{\downarrow}^{s_1' s_2'}(p) \right] E_{\mp}^{s_1 s_2' s_2 s_1'}(k,p) \tag{4.49}$$

via the auxiliary functions

$$\begin{aligned} E_{+}^{\{s\}}(k,p) = U_{\uparrow\downarrow}^{\{s\}} - U_{\uparrow}^{\{s\}} + M_z^{\{s\}}(0) + D^{\{s\}}(k+p) + M_{xy}^{\{s\}}(k-p) \\ - \frac{1}{2} \left[N^{\{\tilde{s}\}}(k-p) + M_z^{\{\tilde{s}\}}(k-p) \right] , \end{aligned}$$

and

$$\begin{aligned} E_{-}^{\{s\}}(k,p) = U_{\uparrow\downarrow}^{\{s\}} + U_{\uparrow}^{\{s\}} - N^{\{s\}}(0) + D^{\{s\}}(k+p) + M_{xy}^{\{s\}}(k-p) \\ + \frac{1}{2} \left[N^{\{\tilde{s}\}}(k-p) + M_z^{\{\tilde{s}\}}(k-p) \right] . \end{aligned}$$

One can observe that the flow of the spin-antisymmetric self-energy Σ_{-} and especially of $\Re\Delta$ is driven by $M_z(0)$, which can be expected to dominate the right-hand side of Eq. (4.49) close to the critical scale, opening up the gap. The momentum and frequency dependence of Σ_{-}, in contrast, stems from the other exchange propagators in E_{+}. For the spin-symmetric self-energy, $N(0)$ takes on the role of $M_z(0)$, but these contributions can be expected to be much smaller.

The Nambu-anomalous components $\Re\Delta = \Sigma_{-}^{+-}$ and $\Im\Delta = -i\Sigma_{+}^{+-}$ as well as the Nambu-normal components

$$\Sigma_{\pm\mathrm{s}}(k) = \frac{1}{2}\left[\Sigma_{\pm}^{++}(k) + \Sigma_{\pm}^{--}(k)\right]$$

and

$$\Sigma_{\pm\mathrm{a}}(k) = \frac{1}{2}\left[\Sigma_{\pm}^{++}(k) - \Sigma_{\pm}^{--}(k)\right]$$

of the self-energy feed into the fermionic propagator in Eq. (4.25). As the Nambu-normal components were absent in the RG flow for the reduced mean-field models of Section 4.1, their flow clearly represents a feature beyond the mean-field picture.

Although the remnants of perfect nesting preserve the filling factor, this does not exclude Fermi-surface shifts induced by the zero-frequency components of the normal self-energy. If one has to deal with a low-energy theory as in Chapter 5, these shifts are, however, potentially dangerous as the Fermi momentum may cross the ultraviolet cutoff below which the theory is valid. For a lattice model, such shifts may completely remove the Fermi surface, giving rise to insulating behavior before the antiferromagnetic gap opens. In analogy to Ref. [49], one may therefore introduce a scale-dependent counterterm ξ_{a} in the Nambu-antisymmetric part

$$\Re\epsilon_{\mathrm{a}}(k) = \epsilon_{\mathrm{a,bare}}(\mathbf{k}) + \Sigma_{+\mathrm{a}}(k) - \xi_{\mathrm{a}}\,, \quad \Im\epsilon_{\mathrm{a}}(k) = -i\Sigma_{-\mathrm{a}}(k)\,.$$

The flow of this counterterm would then be fixed by the condition

$$\dot{\xi}_{\mathrm{a}} = \dot{\Sigma}_{+\mathrm{a}}(0)\,.$$

One might also worry about a spin-population imbalance induced by $\Sigma_{-\mathrm{s}}$ at $k^0 = 0$. Introducing a counterterm for the Nambu-symmetric part would however lead to an artificial violation of the WI, as will become clear further below. Without such a counterterms, one has

$$\Re\epsilon_{\mathrm{s}}(k) = \Sigma_{-\mathrm{s}}(k)\,, \quad \Im\epsilon_{\mathrm{s}}(k) = -i\Sigma_{+\mathrm{s}}(k)\,.$$

Since the normal components of the self-energy will be neglected in the numerical calculations in Chapter 5, such also the Nambu-antisymmetric counterterm ξ_{a} will be absent there. Altogether, the Nambu-anomalous components of the self-energy flow according to

$$\begin{aligned}
\Re\dot{\Delta}(k) &= -\frac{1}{2}\sum_{s_1's_2'}\int d'p\,\left[S_{\uparrow}^{s_1's_2'}(p) - S_{\downarrow}^{s_1's_2'}(p)\right]\sum_{s} E_{+}^{ss_2'-ss_1'}(k,p)\,,\\
\Im\dot{\Delta}(k) &= \frac{i}{2}\sum_{s_1's_2'}\int d'p\,\left[S_{\uparrow}^{s_1's_2'}(p) + S_{\downarrow}^{s_1's_2'}(p)\right]\sum_{s} E_{-}^{ss_2'-ss_1'}(k,p)
\end{aligned} \tag{4.50}$$

and its Nambu-normal components are governed by

$$\begin{aligned}
\Re\dot{\epsilon}_{\mathrm{s}}(k) &= -\frac{1}{2}\sum_{s_1's_2'}\int d'p\,\left[S_{\uparrow}^{s_1's_2'}(p) - S_{\downarrow}^{s_1's_2'}(p)\right]\sum_{s} E_{+}^{ss_2'ss_1'}(k,p)\,,\\
\Im\dot{\epsilon}_{\mathrm{s}}(k) &= \frac{i}{2}\sum_{s_1's_2'}\int d'p\,\left[S_{\uparrow}^{s_1's_2'}(p) + S_{\downarrow}^{s_1's_2'}(p)\right]\sum_{s} E_{-}^{ss_2'ss_1'}(k,p)\,,
\end{aligned} \tag{4.51}$$

$$\begin{aligned}\Re\dot{\epsilon}_{\mathrm{a}}(k) &= -\frac{1}{2}\sum_{s_1's_2'}\int d'p\,\left[S_{\uparrow}^{s_1's_2'}(p)+S_{\downarrow}^{s_1's_2'}(p)\right]\sum_{s} s\,E_{-}^{ss_2'ss_1'}(k,p)\,,\\ \Im\dot{\epsilon}_{\mathrm{a}}(k) &= \frac{i}{2}\sum_{s_1's_2'}\int d'p\,\left[S_{\uparrow}^{s_1's_2'}(p)-S_{\downarrow}^{s_1's_2'}(p)\right]\sum_{s} s\,E_{+}^{ss_2'ss_1'}(k,p)\,.\end{aligned} \tag{4.52}$$

Let us now look at the Ward identity (1.12) and assume a nonvanishing bare value Δ_0 of $\Re\Delta$. One can observe that, in contrast to the mean-field case, also the normal components of the self-energy are governed by the WI. For the anomalous self-energy, the WI reads

$$\Re\Delta(k)-\Delta_0 = -\frac{\Delta_0}{2}\int d'p\sum_{s_1,s_2,s_3} I_{\mathrm{op}}^{-s_1,s_2,s_3,s_1}(0,p)\sum_{s_4} E_{\mathrm{WI}}^{s_4,s_2,s_3,-s_4}(k,p)\,, \tag{4.53}$$

where the exchange propagators enter through the function

$$E_{\mathrm{WI}}^{\{s\}}(k,p) = U_{\uparrow\downarrow}^{\{s\}} + M_{xy}^{\{s\}}(0) + D^{\{s\}}(k+p) + \frac{1}{2}\left[M_z^{\{s\}}(k-p) - N^{\{s\}}(k-p)\right]\,.$$

For the normal components of the WI, one obtains

$$\Re\epsilon_{\mathrm{s}}(k) = -\frac{\Delta_0}{2}\int d'p\sum_{s_1,s_2,s_3} I_{\mathrm{op}}^{-s_1,s_2,s_3,s_1}(0,p)\sum_{s_4} E_{\mathrm{WI}}^{s_4,s_2,s_3,s_4}(k,p)\,, \tag{4.54}$$

and

$$\Im\epsilon_{\mathrm{a}}(k) = -\frac{\Delta_0}{2}\int d'p\sum_{s_1,s_2,s_3} I_{\mathrm{op}}^{-s_1,s_2,s_3,s_1}(0,p)\sum_{s_4} s_4\,E_{\mathrm{WI}}^{s_4,s_2,s_3,s_4}(k,p)\,. \tag{4.55}$$

For small Δ_0, $\Re\epsilon_s$ and $\Im\epsilon_a$ can be expected to be weak, since the Goldstone vertex does not feed into the normal WI, as will become clear in Section 4.4.1. Note further that the WI imposes no constraint on the spin-symmetric components $\Im\Delta$, $\Im\epsilon_{\mathrm{s}}$ and $\Re\epsilon_{\mathrm{a}}$ of the self-energy.

With the mean-field results of Section 4.1 in mind, one would expect E_{WI} in Eqs. (4.53)–(4.55) to be dominated by the M_{xy} term for a small seed field Δ_0. More precisely, the Goldstone contributions to $M_{xy}(0)$ then would be of order Δ_0^{-1} in the infrared while the other terms are of higher order in Δ_0. Therefore, the frequency dependence of $\Re\Delta$ should be negligible in the infrared. Note that, in general, this only holds if the above exchange parametrization ansatz with *frequency-independent* fermion-boson vertices is applicable. If this frequency dependence however plays a role, $\Re\Delta$ may acquire a non-negligible frequency dependence as well. In addition, the situation is different at scales where the couplings have not yet saturated to their infrared values, where the frequency dependence of real part of the gap function may play a role.

4.4. Projection to trivial form factors

In the form presented above, the calculation of the right-hand sides of the fRG flow equations (4.45)–(4.49) includes a summation over Nambu indices along internal lines in the corresponding diagrams. In order to gain a deeper understanding of these flow equations, it seems helpful to resort to further approximations for the dependence of the exchange propagators on the Nambu indices.

4.4.1. Flow equations and Ward identity

Let us assume that, in the matrix notation introduced in Section 4.3.1, the bare interaction is of the form

$$U_{\uparrow}^{\{s\}} = 0\,, \qquad U_{\uparrow\downarrow}^{\{s\}} = \begin{pmatrix} U & U & 0 & 0 \\ U & U & 0 & 0 \\ 0 & 0 & U & U \\ 0 & 0 & U & U \end{pmatrix}.$$

This is the case for the Hubbard model and also the interaction of the Chubukov model takes on this form if its bare two-particle couplings are all equal to one another. At perfect nesting, it appears then likely that trivial form-factor contributions to the renormalized interaction play the major role. In particular, symmetry breaking towards antiferromagnetism can be expected to occur so early in the flow that pairing interactions with sign-changing form factors remain negligibly small. Of course, the situation is different if the nesting of the dispersion is imperfect. In that case, a considerable tendency towards unconventional pairing has been observed in instability analyses (see, for example, Refs. [23, 24, 37, 106, 108] and Chapter 3 of this thesis). Sufficiently away from perfect nesting, this finally leads to a competition of the AF and unconventional pairing instabilities.

In order to simplify the flow equations, all components of the exchange propagators with sign-changing form factors are now neglected. For an exchange propagator P, three independent components corresponding to ordering momenta centered around 0 and $\mathbf{Q}$ and to momentum non-conserving processes remain. In the form-factor expansion language of Section 4.3.2, these components are $P^0 = P_{00}^{++}$, $P^\pi = P_{\pi\pi}^{++}$ and $P^{\mathrm{a}} = P_{0\pi}^{++}$, respectively. Note that, for all the channels retained here, $P_{\pi 0}^{++} = P_{0\pi}^{++}$ due to symmetries.

In the singlet-paring channel, the Nambu index dependence of the exchange propagator

then reduces to

$$D^{\{s\}}(l) = \begin{pmatrix} D^0(l) & D^0(l) & D^{\mathrm{a}}(l) & D^{\mathrm{a}}(l) \\ D^0(l) & D^0(l) & D^{\mathrm{a}}(l) & D^{\mathrm{a}}(l) \\ D^{\mathrm{a}}(l) & D^{\mathrm{a}}(l) & D^{\pi}(l) & D^{\pi}(l) \\ D^{\mathrm{a}}(l) & D^{\mathrm{a}}(l) & D^{\pi}(l) & D^{\pi}(l) \end{pmatrix} .$$

The exchange propagators of the CDW and S_z^2 channels are projected to

$$N^{\{s\}}(l) = \begin{pmatrix} N^0(l) & N^{\pi}(l) & N^{\mathrm{a}}(l) & N^{\mathrm{a}}(l) \\ N^{\pi}(l) & N^0(l) & N^{\mathrm{a}}(l) & N^{\mathrm{a}}(l) \\ N^{\mathrm{a}}(l) & N^{\mathrm{a}}(l) & N^0(l) & N^{\pi}(l) \\ N^{\mathrm{a}}(l) & N^{\mathrm{a}}(l) & N^{\pi}(l) & N^0(l) \end{pmatrix}$$

and

$$M_z^{\{s\}}(l) = \begin{pmatrix} M_z^0(l) & M_z^{\pi}(l) & M_z^{\mathrm{a}}(l) & M_z^{\mathrm{a}}(l) \\ M_z^{\pi}(l) & M_z^0(l) & M_z^{\mathrm{a}}(l) & M_z^{\mathrm{a}}(l) \\ M_z^{\mathrm{a}}(l) & M_z^{\mathrm{a}}(l) & M_z^0(l) & M_z^{\pi}(l) \\ M_z^{\mathrm{a}}(l) & M_z^{\mathrm{a}}(l) & M_z^{\pi}(l) & M_z^0(l) \end{pmatrix} ,$$

respectively. In the in-plane channel, one gets

$$M_{xy}^{\{s\}}(l) = \begin{pmatrix} M_{xy}^0(l) & M_{xy}^{\pi}(l) & M_{xy}^{\mathrm{a}}(l) & M_{xy}^{\mathrm{a}}(l) \\ M_{xy}^{\pi}(l) & M_{xy}^0(l) & M_{xy}^{\mathrm{a}}(l) & M_{xy}^{\mathrm{a}}(l) \\ M_{xy}^{\mathrm{a}}(l) & M_{xy}^{\mathrm{a}}(l) & M_{xy}^{\pi}(l) & M_{xy}^0(l) \\ M_{xy}^{\mathrm{a}}(l) & M_{xy}^{\mathrm{a}}(l) & M_{xy}^0(l) & M_{xy}^{\pi}(l) \end{pmatrix}$$

The remnants of perfect nesting now render all components of these propagators real, in agreement with Tab. 4.1.

Together with the symmetries that are already present in the time-normal approximation, all these exchange propagators now respect the relations

$$P^{\{-s\}}(l) = P^{\{s\}}(l) , \quad P^{\{\bar{s}\}}(l) = P^{\{s\}}(l) , \quad P^{\{\hat{s}\}}(l) = P^{\{s\}}(l) . \tag{4.56}$$

Note that the flow equations (4.45)–(4.49) in Section 4.3.3 do not preserve them. Enforcing them therefore requires to project the trivial form-factor components out of the scale derivatives of the exchange propagators in the from given in the flow equations, i.e.

$$\begin{aligned} \dot{D}^{\{s\}}(l) &\approx \frac{1}{4}\left[\dot{D}^{\{s\}}(l) + \dot{D}^{-s_1,-s_2,s_3,s_4}(l) + \dot{D}^{s_1,s_2,-s_3,-s_4}(l) + \dot{D}^{\{-s\}}(l)\right] , \\ \dot{M}_{xy}^{\{s\}}(l) &\approx \frac{1}{4}\left[\dot{M}_{xy}^{\{s\}}(l) + \dot{M}_{xy}^{s_1,-s_2,-s_3,s_4}(l) + \dot{M}_{xy}^{-s_1,s_2,s_3,-s_4}(l) + \dot{M}_{xy}^{\{-s\}}(l)\right] , \\ \dot{N}^{\{s\}}(l) &\approx \frac{1}{4}\left[\dot{N}^{\{s\}}(l) + \dot{N}^{-s_1,s_2,-s_3,s_4}(l) + \dot{N}^{s_1,-s_2,s_3,-s_4}(l) + \dot{N}^{\{-s\}}(l)\right] , \\ \dot{M}_z{}^{\{s\}}(l) &\approx \frac{1}{4}\left[\dot{M}_z{}^{\{s\}}(l) + \dot{M}_z{}^{-s_1,s_2,-s_3,s_4}(l) + \dot{M}_z{}^{s_1,-s_2,s_3,-s_4}(l) + \dot{M}_z{}^{\{-s\}}(l)\right] . \end{aligned}$$

The flow equations (4.45)–(4.49) for the exchange propagators can then be cast into a form which avoids redundant summations over Nambu indices. In these equations, exchange propagators P_1 couple to a linear combination P_2 of other exchange propagators through vertex-correction and box diagrams according to Tab. 4.2. The sixteen configurations of internal Nambu indices in Eqs. (4.45)–(4.49) can be split into three sets such that the projected interaction can be pulled out of the summation over the configurations in one of these sets. These summations yield the three loop functions

$$\begin{aligned}
I^{\pi}_{P_1}(l,p) &= \frac{1}{4}\left[I^{++--}_{P_1}(l,p) + I^{--++}_{P_1}(l,p) + 2I^{+-+-}_{P_1}(l,p)\right] ,\\
I^{0}_{P_1}(l,p) &= \frac{1}{4}\left[I^{++++}_{P_1}(l,p) + I^{----}_{P_1}(l,p) + 2I^{+-+-}_{P_1}(l,p)\right] ,\\
I^{\mathrm{a}}_{P_1}(l,p) &= \frac{1}{4}\left[I^{+-++}_{P_1}(l,p) + I^{+---}_{P_1}(l,p) + I^{+++-}_{P_1}(l,p) + I^{--+-}_{P_1}(l,p)\right] ,
\end{aligned}$$

where the spin orientations along the fermionic lines are given in Tab. 4.2. Note that $G^{ss'} = G^{s's}$ and that hence I^{π} and I^{0} each cover four configurations of Nambu indices, while I^{a} covers eight ones. The PFS relates the particle-hole loops to the particle-particle ones. More precisely, one has

$$J^{\pi}_{\mathrm{op}}(l,p) = -I^{0}_{\mathrm{eq}}(l,p)\,, \quad J^{0}_{\mathrm{op}}(l,p) = -I^{\pi}_{\mathrm{eq}}(l,p)\,, \quad J^{\mathrm{a}}_{\mathrm{op}}(l,p) = -I^{\mathrm{a}}_{\mathrm{eq}}(l,p)\,.$$

The resulting flow equations for the components of P_1 are of the form

$$\begin{aligned}
\dot{P}^{\pi}_1(l) = &-\int d'p\, \dot{I}^{\pi}_{P_1}(l,p)\, \left\{F^{\pi}[P_1,P_2](l,p)\right\}^2 - \int d'p\, \dot{I}^{0}_{P_1}(l,p)\, \left\{F^{\mathrm{a}}[P_1,P_2](l,p)\right\}^2\\
&- 2\int d'p\, \dot{I}^{\mathrm{a}}_{P_1}(l,p)\, F^{\pi}[P_1,P_2](l,p)\, F^{\mathrm{a}}[P_1,P_2](l,p)\,, \qquad (4.57)
\end{aligned}$$

$$\begin{aligned}
\dot{P}^{0}_1(l) = &-\int d'p\, \dot{I}^{0}_{P_1}(l,p)\, \left\{F^{0}[P_1,P_2](l,p)\right\}^2 - \int d'p\, \dot{I}^{\pi}_{P_1}(l,p)\, \left\{F^{\mathrm{a}}[P_1,P_2](l,p)\right\}^2\\
&- 2\int d'p\, \dot{I}^{\mathrm{a}}_{P_1}(l,p)\, F^{0}[P_1,P_2](l,p)\, F^{\mathrm{a}}[P_1,P_2](l,p)\,, \qquad (4.58)
\end{aligned}$$

$$\begin{aligned}
\dot{P}^{\mathrm{a}}_1(l) = &-\int d'p\, \dot{I}^{\mathrm{a}}_{P_1}(l,p)\, \left\{F^{\mathrm{a}}[P_1,P_2](l,p)\right\}^2 - \int d'p\, \dot{I}^{\mathrm{a}}_{P_1}(l,p)\, F^{0}[P_1,P_2](l,p)\, F^{\pi}[P_1,P_2](l,p)\\
&- \int d'p\, \dot{I}^{\pi}_{P_1}(l,p)\, F^{\pi}[P_1,P_2](l,p)\, F^{\mathrm{a}}[P_1,P_2](l,p)\\
&- \int d'p\, \dot{I}^{0}_{P_1}(l,p)\, F^{0}[P_1,P_2](l,p)\, F^{\mathrm{a}}[P_1,P_2](l,p) \qquad (4.59)
\end{aligned}$$

with the functions

$$\begin{aligned}
F^{\pi}[P_1,P_2](l,p) &= 2U + 2P^{\pi}_1(l) + P^{0}_2(p) + P^{\pi}_2(p)\,,\\
F^{0}[P_1,P_2](l,p) &= 2U + 2P^{0}_1(l) + P^{0}_2(p) + P^{\pi}_2(p)\,,\\
F^{\mathrm{a}}[P_1,P_2](l,p) &= 2P^{\mathrm{a}}_1(l) + 2P^{\mathrm{a}}_2(p)
\end{aligned}$$

P_1	P_2	I_{P_1}
$+D$	$(M_z - N)/2 + M_{xy}$	J_{op}
$+M_{xy}$	$(M_z - N)/2 + D$	I_{op}
$+M_z$	$M_{xy} - (M_z + N)/2 + D$	I_{eq}
$-N$	$M_{xy} + (M_z + N)/2 + D$	$-I_{\mathrm{eq}}$

Table 4.2.: Coupling between different channels in the one-loop flow equations (4.57)–(4.59) and spin orientations of the fermionic propagators in the loop.

for the projected interaction. The PFS couples the singlet-pairing and CDW channels, which gives

$$D^{\pi}(l) = -N^{0}(l)\,, \quad D^{0}(l) = -N^{\pi}(l)\,, \quad D^{\mathrm{a}}(l) = -N^{\mathrm{a}}(l)\,.$$

Let us now have a look at different contributions to the self-energy. In Eq. (4.52), only the sign-changing form-factor parts of $M_z(0)$ and $N(0)$, but not their trivial form-factor contributions feed into the flow of the Nambu-antisymmetric self-energy. Moreover, only the sign-changing form-factor contributions to $M_{xy}(0)$ enter in the WI (4.55) for $\Re\epsilon_{\mathrm{a}}$. Since such contributions to the interaction are neglected here, it would not make much sense to consider renormalizations of ϵ_{a}, which will hence be discarded here. In contrast, the trivial form-factor contributions of $M_z^0(0)$ and $M_z^{\mathrm{a}}(0)$ feed into the flow of the Nambu-symmetric part Σ_{s} of the normal self-energy in Eq. (4.51) and trivial form-factor contributions of $M_{xy}(0)$ appear on the right-hand side of the corresponding WI (4.54). It therefore appears sensible to take this part of the self-energy into account here.

In these approximations, the flow equations (4.50) and (4.51) for the remaining contributions of the self-energy can be rewritten with the help of the Nambu-symmetric and Nambu-anomalous single-scale propagators

$$\begin{aligned} S_{\mathrm{s}\pm}(p) &= \frac{1}{4}\left[S_{\uparrow}^{++}(p) + S_{\uparrow}^{--}(p) \pm S_{\downarrow}^{++}(p) \pm S_{\downarrow}^{--}(p)\right]\,, \\ S_{\Delta\pm}(p) &= \frac{1}{2}\left[S_{\uparrow}^{+-}(p) \pm S_{\downarrow}^{+-}(p)\right] \end{aligned}$$

and the auxiliary functions

$$\begin{aligned} E^{\pi}[P_1, P_2, P_3](k,p) &= 2U + 2P_1^{\pi}(0) + P_2^{0}(k-p) + P_3^{0}(k+p) + P_2^{\pi}(k-p) + P_3^{\pi}(k+p)\,, \\ E^{0}[P_1, P_2, P_3](k,p) &= 2U + 2P_1^{0}(0) + P_2^{0}(k-p) + P_3^{0}(k+p) + P_2^{\pi}(k-p) + P_3^{\pi}(k+p)\,, \\ E^{\mathrm{a}}[P_1, P_2, P_3](k,p) &= 2\left[P_1^{\mathrm{a}}(0) + P_2^{\mathrm{a}}(k-p) + P_3^{\mathrm{a}}(k+p)\right] \end{aligned}$$

for the projected interaction. This gives

$$\begin{aligned}\Re\dot{\Delta}(k) = -\int d'p\, \{&S_{\Delta-}(p)\, E^{\pi}[M_z, -(N+M_z)/2 + M_{xy}, D](k,p) \\ &+ S_{\mathrm{s}-}(p)\, E^{\mathrm{a}}[M_z, -(N+M_z)/2 + M_{xy}, D](k,p)\}\,, \\ \Im\dot{\Delta}(k) = i\int d'p\, \{&S_{\Delta+}(p)\, E^{\pi}[-N, (N+M_z)/2 + M_{xy}, D](k,p) \\ &+ S_{\mathrm{s}+}(p)\, E^{\mathrm{a}}[-N, (N+M_z)/2 + M_{xy}, D](k,p)\}\,,\end{aligned} \tag{4.60}$$

$$\begin{aligned}\Re\dot{\epsilon}_{\mathrm{s}}(k) = -\int d'p\, \{&S_{\mathrm{s}-}(p)\, E^{0}[M_z, -(N+M_z)/2 + M_{xy}, D](k,p) \\ &+ S_{\Delta-}(p)\, E^{\mathrm{a}}[M_z, -(N+M_z)/2 + M_{xy}, D](k,p)\}\,, \\ \Im\dot{\epsilon}_{\mathrm{s}}(k) = i\int d'p\, \{&S_{\mathrm{s}+}(p)\, E^{0}[-N, (N+M_z)/2 + M_{xy}, D](k,p) \\ &+ S_{\Delta+}(p)\, E^{\mathrm{a}}[-N, (N+M_z)/2 + M_{xy}, D](k,p)\}\,.\end{aligned} \tag{4.61}$$

One can now observe that, due to the remnants of perfect nesting, $S_{\Delta-}$ and $S_{\mathrm{s}-}$ are real, while $S_{\Delta+}$ and $S_{\mathrm{s}+}$ are purely imaginary. Since the trivial form-factor components of the exchange propagators considered here are all real, the scale derivatives of $\Im\Delta$ and $\Im\Sigma_{\mathrm{s}}$ vanish and the self-energy therefore remains real during the flow. The WI imposes the constraints (4.53) and (4.54) on its remaining components. They simplify to

$$\Re\Delta(k) - \Delta_0 = -2\Delta_0 \int d'p \left[I^{\pi}_{\mathrm{op}}(0,p)\, E^{\pi}_{\mathrm{WI}}(k,p) + I^{\mathrm{a}}_{\mathrm{op}}(0,p)\, E^{\mathrm{a}}_{\mathrm{WI}}(k,p)\right] \tag{4.62}$$

and

$$\Re\epsilon_{\mathrm{s}}(k) = -2\Delta_0 \int d'p \left[I^{\mathrm{a}}_{\mathrm{op}}(0,p)\, E^{0}_{\mathrm{WI}}(k,p) + I^{\pi}_{\mathrm{op}}(0,p)\, E^{\mathrm{a}}_{\mathrm{WI}}(k,p)\right]\,, \tag{4.63}$$

where the exchange propagators are contained in

$$\begin{aligned}E^{0}_{\mathrm{WI}}(k,p) &= 2U + 2M^{0}_{xy}(0) + D^{0}(k+p) + D^{\pi}(k+p) \\ &\quad + \frac{1}{2}\left[M^{0}_{z}(k-p) - N^{0}(k-p) + M^{\pi}_{z}(k-p) - N^{\pi}(k-p)\right]\,, \\ E^{\pi}_{\mathrm{WI}}(k,p) &= 2U + 2M^{\pi}_{xy}(0) + D^{0}(k+p) + D^{\pi}(k+p) \\ &\quad + \frac{1}{2}\left[M^{0}_{z}(k-p) - N^{0}(k-p) + M^{\pi}_{z}(k-p) - N^{\pi}(k-p)\right]\,, \\ E^{\mathrm{a}}_{\mathrm{WI}}(k,p) &= 2\left[M^{\mathrm{a}}_{xy}(0) + D^{\mathrm{a}}(k+p)\right] + M^{\mathrm{a}}_{z}(k-p) - N^{\mathrm{a}}(k-p)\,.\end{aligned}$$

In the limit $\Delta_0 \to 0$, one may expect the right-hand side of Eq. (4.62) to be dominated by $M^{\pi}_{xy}(0)$, which corresponds to the Goldstone vertex. These features would then be reminiscent of the WI (4.19) in mean-field approximation. If the other contributions are negligible in the limit of a vanishing seed field, the momentum and frequency dependence

of the gap then also vanishes and one has $M^{\pi}_{xy}(0) \propto \Delta_0^{-1}$. If one conjectures that all components of the exchange propagators contained in E^0_{WI} and $E^{\mathrm{a}}_{\mathrm{WI}}$ stay regular in the limit $\Delta_0 \to 0$ down to the infrared, $\Re\epsilon_{\mathrm{s}}$ is predicted to vanish in this limit according to Eq. (4.63). For a finite seed field, the k dependence of $\Re\epsilon_{\mathrm{s}}$ may then be much more pronounced that for $\Re\Delta$.

4.4.2. Random phase approximation

Let us now consider the flow equations (4.57)–(4.59) at the RPA level, i.e. neglect P_2. These flow equations then can be cast into the matrix form

$$\dot{\mathbf{P}}(l) = -\mathbf{P}(l)\,\dot{\mathbf{B}}_P(l)\,\mathbf{P}(l) \tag{4.64}$$

with the 2×2 matrices

$$\mathbf{P}(l) = \begin{pmatrix} U + P^0(l) & P^{\mathrm{a}}(l) \\ P^{\mathrm{a}}(l) & U + P^{\pi}(l) \end{pmatrix}, \quad \mathbf{I}_P(l,p) = \begin{pmatrix} 4I^0_P(l,p) & 4I^{\mathrm{a}}_P(l,p) \\ 4I^{\mathrm{a}}_P(l,p) & 4I^{\pi}_P(l,p) \end{pmatrix}$$

and $\mathbf{B}_P(l) = \int d'p\, \mathbf{I}_P(l,p)$. Here P can be D, M_z, M_{xy} or N and the loop functions I_P are those given in Tab. 4.2. The generic RPA flow equation (4.64) is solved by

$$\mathbf{P}(l) = U\left[\mathbf{1} + U\mathbf{B}_P(l)\right]^{-1}, \tag{4.65}$$

where $\mathbf{1}$ denotes the 2×2 unit matrix. This formal solution also fulfills the Bethe-Salpether equation

$$\mathbf{P}(l) = U\left[\mathbf{1} - \mathbf{B}_P(l)\,\mathbf{P}(l)\right].$$

In RPA, diagrams with bosonic lines inside the loops are neglected, i.e. P_2 and P_3 are sent to zero also in E^{π}, E^0 and E^{a} in Eqs. (4.60) and (4.61). The resulting approximate flow equations for the self-energy can also be rewritten in matrix form with

$$\mathbf{\Sigma} = \begin{pmatrix} \epsilon_{\mathrm{s}} \\ \Delta \end{pmatrix}, \quad \mathbf{S} = \begin{pmatrix} S_{\mathrm{s}-} \\ S_{\Delta-} \end{pmatrix},$$

which yields

$$\dot{\mathbf{\Sigma}} = -2\mathbf{M}_z(0) \int d'p\, \mathbf{S}(p)\,. \tag{4.66}$$

Note that the self-energy looses its momentum and frequency dependence at the RPA level. Observe that

$$\int d'p\, \mathbf{S}(p) = \int d'p\, \dot{\mathbf{G}}(p) - \frac{1}{2}\mathbf{B}_{M_z}(0)\,\dot{\mathbf{\Sigma}}\,,$$

where

$$\mathbf{G}(p) = \begin{pmatrix} \frac{1}{4}\left[G^{++}_{\uparrow}(p) + G^{--}_{\uparrow}(p) - G^{++}_{\downarrow}(p) - G^{--}_{\downarrow}(p)\right] \\ \frac{1}{2}\left[G^{+-}_{\uparrow}(p) - G^{+-}_{\downarrow}(p)\right] \end{pmatrix} = \begin{pmatrix} G_{\mathrm{s}-} \\ G_{\Delta-} \end{pmatrix}.$$

Inserting the formal solution (4.65) for M_z into Eq. (4.66) and integrating therefore yields the self-consistency equation

$$\boldsymbol{\Sigma} - \boldsymbol{\Sigma}_0 = -2U \int d'p \, \mathbf{G}(p)$$

for the self-energy, where

$$\boldsymbol{\Sigma}_0 = \begin{pmatrix} 0 \\ \Delta_0 \end{pmatrix} .$$

Expressed in components, it corresponds to two nonlinear integral equations

$$\begin{aligned} \epsilon_\mathrm{s} &= 2U \, \Re \int d'k \, \frac{ik_0 - \epsilon_\mathrm{s}}{k_0^2 + 2ik_0\epsilon_\mathrm{s} - \epsilon_\mathrm{s}^2 + \epsilon_\mathrm{a}(\mathbf{k})^2 + \Delta^2} \, , \\ \Delta - \Delta_0 &= 2U \, \Re \int d'k \, \frac{\Delta}{k_0^2 + 2ik_0\epsilon_\mathrm{s} - \epsilon_\mathrm{s}^2 + \epsilon_\mathrm{a}(\mathbf{k})^2 + \Delta^2} \, . \end{aligned}$$

Clearly, $\epsilon_\mathrm{s} = 0$ solves the first of these two equations due to the odd frequency dependence of the integrand on its right-hand side. At zero temperature, the second equation then reads as

$$\Delta - \Delta_0 = U \, \Delta \int d'\mathbf{k} \, \frac{1}{\sqrt{\epsilon_\mathrm{a}(\mathbf{k})^2 + \Delta^2}} \, . \tag{4.67}$$

But this is the same gap equation (4.19) as in the mean-field picture.

I will now discuss the formal solution of the flow equations in RPA and then elaborate on the fulfillment of the WI. The matrix in Eq. (4.65) can be inverted, which yields

$$\mathbf{P}(l) = \frac{U}{\left[1 + 4UB_P^\pi(l)\right]\left[1 + 4UB_P^0(l)\right] - 16\left[UB_P^\mathrm{a}(l)\right]^2} \begin{pmatrix} 1 + 4UB_P^\pi(l) & -4UB_P^\mathrm{a}(l) \\ -4UB_P^\mathrm{a}(l) & 1 + 4UB_P^0(l) \end{pmatrix} .$$

From the relation

$$\int d'k \, G_\Delta(k) = -2\Delta B_{M_{xy}}^\pi(0)$$

and the gap equation (4.67) one obtains

$$1 + 4UB_{M_{xy}}^\pi(0) = \frac{\Delta_0}{\Delta} \, . \tag{4.68}$$

Moreover, one has

$$B_{M_{xy}}^\mathrm{a}(0) = \epsilon_\mathrm{s}\Delta \int d'p \, \left| k_0^2 + 2ik_0\epsilon_\mathrm{s} - \epsilon_\mathrm{s}^2 + \epsilon_\mathrm{a}^2 + \Delta^2 \right|^{-2} = 0$$

and consequently

$$\mathbf{M}_{xy}(0) = \begin{pmatrix} \frac{U}{1+4UB_\mathrm{op}^0(0)} & 0 \\ 0 & \frac{U}{1+4UB_\mathrm{op}^\pi(l)} \end{pmatrix} = \begin{pmatrix} \frac{U}{1+4UB_\mathrm{op}^0(0)} & 0 \\ 0 & \frac{\Delta U}{\Delta_0} \end{pmatrix} . \tag{4.69}$$

This reflects the Goldstone-vertex nature of $M^{\pi}_{xy}(0)$. Neglecting bosonic lines inside closed loops and setting $\epsilon_{\mathrm{s}} = 0$ leads to

$$\Re\Delta - \Delta_0 = -4\Delta_0\, B^{\pi}_{\mathrm{op}}(0)\, M^{\pi}_{xy}(0)$$

for the WI. By inserting the exact solution (4.69) for the Goldstone vertex, Eq. (4.68) is reproduced, and hence the RPA solution is consistent with the WI. As in Ref. [49] for a singlet superconductor, one may write in leading order in a gradient expansion with coefficients α and β

$$M^{\pi}_{xy}(l) \propto \frac{1}{\Delta_0 + \alpha l_0^2 + \beta \mathbf{l}^2}$$

in the limit $\Delta_0 \to 0$. Beyond RPA, this property appears likely to be preserved by the WI (4.62), provided that M_{xy} remains the only propagator which diverges for a vanishing seed field.

The results presented here are important in a twofold sense.

i.) The flow equations (4.57)–(4.59) contain all contributions to the interaction and the self-energy that are also present at the mean-field level. In addition, they also include some corrections to the mean-field case and contributions that do not feed back on the flow of the mean-field quantities.

ii.) These other contributions do not show additional divergencies in the limit $\Delta_0 \to 0$ and therefore $M^{\pi}_{xy}(0)$ is the only quantity that shows such a divergence.

The time-normal approximation, the exchange parametrization scheme of Section 4.3.1 and the projection to even form factors therefore seem to be decent approximation schemes. At the present stage, however, a divergence of time-reversal breaking interactions in the limit $\Delta_0 \to 0$ has not been ruled out yet. The role of these terms at the RPA level is discussed in Appendix C.2, where they are found to be created from a time-reversal invariant bare interaction by spin-antisymmetric loop functions. This makes their occurrence at least unlikely if it is not prohibited by symmetries. In RPA and at $l = 0$, spin-antisymmetric loop functions only give rise to a nonvanishing value of mixed form-factor terms. It appears unlikely that such terms should play a major role for the Chubukov model discussed in Chapter 5 and in the Hubbard model contributions of this kind are ruled out by the point-group symmetries for zero transfer momentum.

4.4.3. Nambu-normal approximation

The fact that mean-field results can be reproduced from the flow equations (4.57)–(4.59) in RPA does not imply that further approximations in the parametrization of the interaction would spoil this property. As one may easily verify, the mean-field results of

the previous subsection are still recovered if P^0 and P^{a} in the particle-hole channels and D^π and D^{a} are neglected. In other words, one then only keeps momentum-conserving interaction terms with ordering momenta l around 0 in the particle-particle channel and around $\mathbf{Q}$ in the particle-hole channel. One should then also simultaneously neglect $\Re\epsilon_{\mathrm{s}}$, in agreement with the mean-field result. Altogether, this will be called the Nambu-normal approximation in the following. Note that all interaction terms that would violate discrete symmetries are neglected in this approximation, whereas these symmetries are still broken at the one-particle level. The continuous SU(2) symmetry, in contrast, is broken in both the interaction and the quadratic part of the effective action.

In Nambu-normal approximation, one arrives at simpler flow equations for the remaining exchange propagators $D(l) \equiv D^0(l)$, $M_{xy}(l) \equiv M^\pi_{xy}(l)$, $M_z(l) \equiv M^\pi_z(l)$ and $N(l) \equiv N^\pi(l)$. They read as

$$\dot{D}(l) = -\int d'p\, \dot{J}_{\mathrm{op}}(l,p)\, \left\{F'[D, (M_z - N)/2 + M_{xy}](l,p)\right\}^2 , \tag{4.70}$$

$$\dot{M}_{xy}(l) = -\int d'p\, \dot{I}_{\mathrm{op}}(l,p)\, \left\{F'[M_{xy}, (M_z - N)/2 + D](l,p)\right\}^2 , \tag{4.71}$$

$$\dot{N}(l) = -\int d'p\, \dot{I}_{\mathrm{eq}}(l,p)\, \left\{F'[-N, (M_z + N)/2 + M_{xy} + D](l,p)\right\}^2 , \tag{4.72}$$

$$\dot{M}_z(l) = -\int d'p\, \dot{I}_{\mathrm{eq}}(l,p)\, \left\{F'[M_z, -(M_z + N)/2 + M_{xy} + D](l,p)\right\}^2 , \tag{4.73}$$

where

$$F'[P_1, P_2](l,p) = 2U + 2P_1(l) + P_2(p)\,.$$

The flow equation for the self-energy reduces to

$$\dot{\Delta}(k) = -\int d'p\, S_{\Delta-}(p)\, E'[M_z, -(M_z + N)/2 + M_{xy}, D](k,p) \tag{4.74}$$

in Nambu-normal approximation, where

$$E'[P_1, P_2, P_3](k,p) = 2U + 2P_1(0) + P_2(k-p) + P_3(k+p)\,.$$

Due to the PFS, which implies $D = -N$, one of the flow equations for the interaction is redundant. The remaining flow equations to be solved read

$$\dot{D}(l) = \int d'p\, \dot{I}_{\mathrm{eq}}(l,p)\, \left\{F'[D, (M_z + D)/2 + M_{xy}](l,p)\right\}^2 , \tag{4.75}$$

$$\dot{M}_{xy}(l) = -\int d'p\, \dot{I}_{\mathrm{op}}(l,p)\, \left\{F'[M_{xy}, M_z/2 + 3D/2](l,p)\right\}^2 , \tag{4.76}$$

$$\dot{M}_z(l) = -\int d'p\, \dot{I}_{\mathrm{eq}}(l,p)\, \{F'[M_z, -M_z/2 + M_{xy} + 3D/2](l,p)\}^2 \tag{4.77}$$

and

$$\dot{\Delta}(k) = -\int d'p\, S_{\Delta-}(p)\, E'[M_z, (D - M_z)/2 + M_{xy}, D](k,p)\,. \tag{4.78}$$

They are complemented by the reduced WI

$$\Delta(k) - \Delta_0 = -2\Delta_0 \int d'p\, I_{\mathrm{op}}(0,p)\, E'[M_{xy}, (M_z + D)/2, D](k,p) \tag{4.79}$$

and Nambu-normal components of the self-energy are neglected.

Eqs. (4.75)–(4.78) describe the fRG flow in a simple approximation beyond mean-field theory. Corrections to the mean-field picture enter in vertex-correction and box diagrams on their right-hand sides. At the RPA level, such vertex-correction or box diagrams are suppressed and the formal solution of the flow equations fulfills the WI exactly (cf. Section 4.4.2). Beyond RPA, the flow equations have to be solved numerically. The Ward identity (WI) may then be violated due to the one-loop truncation and due to the approximations underlying the parametrization employed. This WI violation may therefore be regarded as a measure of truncation and/or parametrization errors. Note that if the exchange propagator D (and $N = -D$) was neglected, the mean-field results would still be reproduced in RPA. Their impact on the flow of the other exchange propagators and the gap hence clearly represents a feature beyond mean-field theory.

4.5. Summary

In order gain some intuition for more complicated cases, the RG flow of a reduced AF mean-field model has been studied at the beginning of this chapter. This flow can be captured by three running couplings corresponding to radial and Goldstone components of the interaction and the gap. If a CDW reduced mean-field term is added to the bare interaction, there is a fourth nonvanishing coupling constant, which however does not feed back on the flow of the other three. The resulting flow equations can be solved exactly. As one may have expected, the couplings behave as in previous studies [45,48,57] of other mean-field models. The radial coupling J_z shows a pronounced hump at the critical scale, where the gap Δ starts to grow significantly. While the radial coupling and the gap saturate to finite infrared values for small seed fields, the Goldstone coupling J_{xy} diverges, reflecting the masslessness of the Goldstone modes. This can as well be seen from the global SU(2) Ward identity. The RG flow equations reproduce the RPA result for the interaction and the self-consistent gap equation exactly. The generalization to a symmetry-breaking interaction of xxz type in Appendix C.1 is straightforward. In doing so, one finds that the fRG still provides an unbiased description — at least on the mean-field level.

In proceeding towards a fRG approach to AF phases beyond the mean-field picture, a hierarchy of approximations has been applied to the channel decomposed flow equations of Chapter 1.4.3 for models with a perfectly nested dispersion. (For an overview see Fig. 4.3.) The perfect nesting imposes additional symmetry constraints on the coupling functions. They have been discussed in Section 4.2.1, which includes a parametrization of the full quasiparticle propagator. In Section 4.2.3, time-reversal breaking terms have been neglected, which enhances the symmetries of the coupling functions. This results in the simplified flow equations (4.36)–(4.40). Note that the radial and Goldstone vertices still split in this approximation and therefore essential features of the SU(2) breaking are preserved.

In a further step, an exchange parametrization of the remaining time-reversal invariant interaction channels has been employed. The corresponding projection rule in Section 4.3.1 is tailored for low-energy models and should in principle also be applicable to the Hubbard model at van-Hove filling. It projects out exchange propagators corresponding to two slowly varying trivial and sign-changing form factors that are even and odd under a Nambu-index flip, respectively. The dependence of these propagators on the Nambu indices is reduced by the particle-hole, perfect-nesting and Pauli-principle symmetries and the (approximate) time-reversal invariance of the interaction. The form of the resulting flow equations and of the Ward identity in Section 4.3.3 suggests that the parametrization employed is a sensible one.

For a perfectly nested dispersion, interactions with sign-changing form factors (including unconventional pairing tendencies) seem to be of minor importance and therefore such contributions have been neglected in Section 4.4. This again enhances the symmetry and the dependence of the exchange propagators can be completely parametrized, giving rise to the simplified flow equations (4.57)–(4.59). In RPA, these flow equations reproduce the mean-field equation for the gap and the formal RPA solution is fully consistent with the Ward identity.

At the RPA level, momentum non-conserving interactions play a minor role as well as momentum-conserving exchange propagators with ordering momenta centered around $\mathbf{Q}$ and zero in the particle-particle and particle-hole channels, respectively. In particular, these terms do not feed back on the other contributions to the interaction and on the gap in RPA. In Section 4.4.3, also these interactions have been neglected. Due to a hidden symmetry between the particle-particle and particle-hole loops, only three exchange propagators remain, which depend only on one momentum and one frequency variable. The resulting fRG flow equations have to be solved numerically in going beyond the RPA. They are of a similar form as in Refs. [25, 26, 49–51] and therefore the numerical methods used in those works could be adapted in order to integrate them. In doing so, one should keep in mind that the projection rule of Section 4.3.1 is more costly than in Ref. [26], where all exchange propagators could be pulled out of the integrals over the loop momenta on the right-hand sides of the flow equations for the interaction.

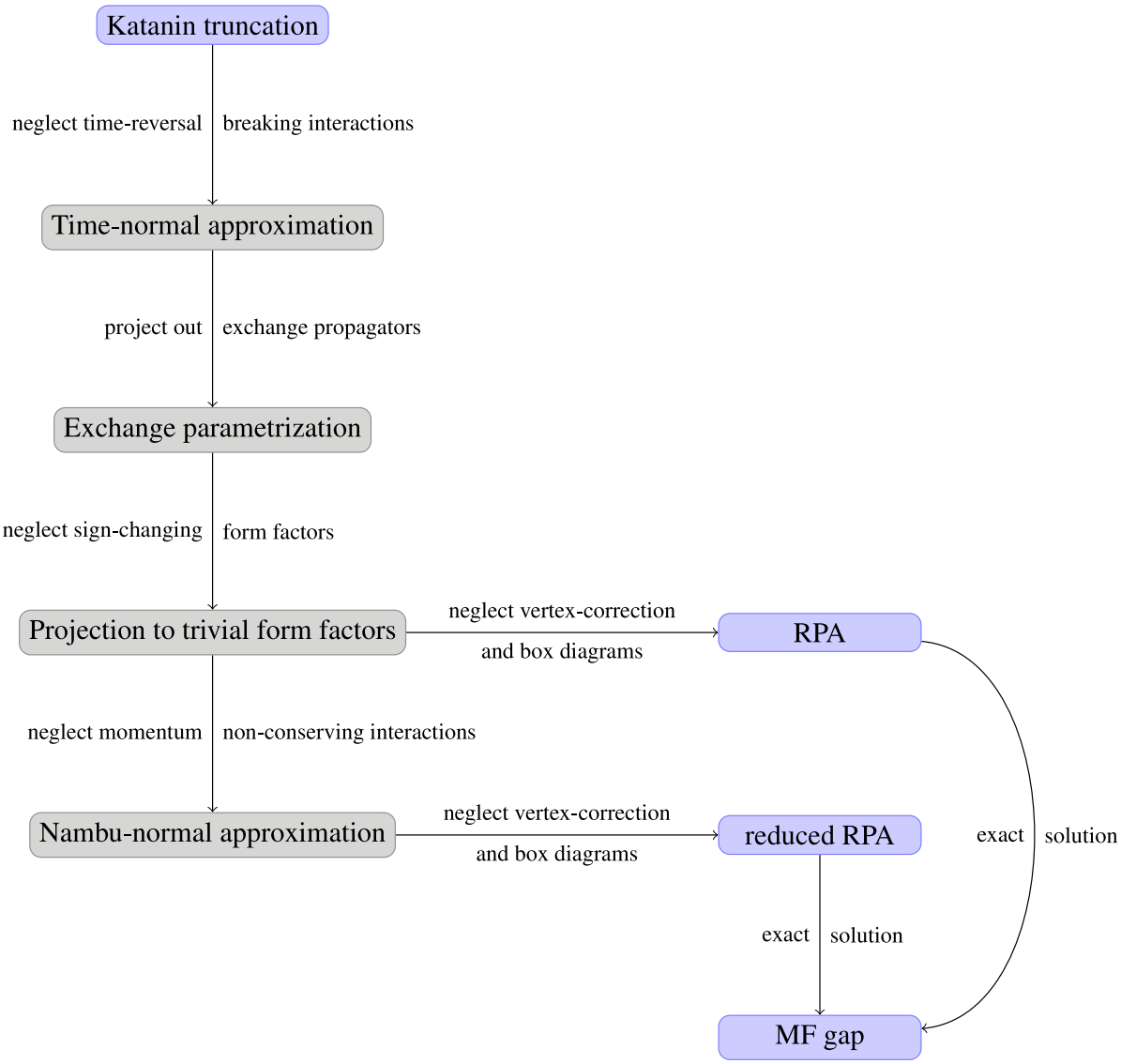

Figure 4.3.: Hierarchy of the approximations employed in this chapter. On the left-hand side, various levels of approximation for the fRG flow are depicted, while the fRG reproduces results also obtained from other methods on the right-hand side.

In order to gain further insight in fRG flows into AF phases, the following long-term strategy seems appropriate. First, the flow equations of Section 4.4.3 should be integrated numerically for a very simple model in order to systematically study the mean-field effects which they capture. This approach may then be carried over to the Hubbard model at half filling and perfect nesting. As further steps, on may successively relax the above approximations, i.e. include sign-changing form-factors and momentum non-conserving and time-reversal breaking interaction terms. The integration of the flow equations can be expected to increase drastically at each of these steps, which would require a well parallelizable implementation.

In the following (last) chapter, the first of the above steps will be undertaken. Namely, the flow equations of Section 4.4.3 will be integrated for the Chubukov model, which enjoys a continuous rotational symmetry.

Chapter 5.

fRG Approach to the SDW Phase of the Chubukov Model

In this chapter, the fRG flow into the spin-density wave phase of a two-pocket model [108] with a quadratic dispersion is studied. The flow equations are implemented in Nambu-normal approximation and the momentum dependence is parametrized. This allows for an extension to numerically more demanding tasks. A significant reduction of the gap compared to mean-field theory is found. The inclusion of the charge-density wave and singlet-pairing channels in the flow equations turns out to be essential. Taking the frequency dependence of the interaction into account improves the fulfillment of the SU(2) *Ward identity, which suggests that the numerical results of this chapter are qualitatively reliable. The remaining violation of the Ward identity, however, reveals that there is still room for an improvement of the parametrization.*

In Chapter 4.4.3, an approximate parametrization for the fRG flow into antiferromagnetic (AF) phases has been given. The resulting flow equations (4.75)-(4.78) seem numerically tractable and reproduce the mean-field gap equation in random-phase approximation (RPA). Their integration will represent a first step beyond the mean-field picture within fRG flows into the AF phase. Of course, one can not *a priori* rule out a potentially strong impact of the underlying approximations on contributions beyond the RPA. If the resulting errors are however really vast, it is likely that the Ward identity (WI) (4.79) is strongly violated, which can be checked at all instances of the flow.

In the derivation of the flow equations, a perfectly nested dispersion has been assumed. As an example of such a model, the repulsive Hubbard model with hopping only between nearest neighbors has already been mentioned in the preceeding chapter. Studying its

flow into the antiferromagnetic phase would complement recent work on the superfluid phase of the repulsive Hubbard model. [50, 51] In order to get some intuition, it seems however preferable to consider a model with a higher symmetry, which will require less computational resources. The Chubukov model [108] proposed for a simple (Wilsonian) RG instability analysis of the iron pnictides enjoys a continuous point-group symmetry and will hence be studied in this chapter. It is introduced in the first section.

It seems advantageous to implement the flow equations (4.75)-(4.78) in a way that allows for an efficient treatment of other models and less approximate parametrizations. Both can be expected to strongly enhance the requirements for computational power and, hence, for the parallelizability of the code. So it appears rewarding to set up a suitable algorithm. This is done in the second subsection, where the momentum dependence of the interaction is parametrized in order to avoid transversing of large pieces of memory randomly. In the third section, this algorithm is applied to the Chubukov model in Nambu-normal approximation. Particular attention is paid to the violation of the WI in this prototypical study. The results for the AF gap are compared to mean-field theory, and the role of the charge-density wave and singlet-pairing channels is discussed.

5.1. Model

Good candidates for a model with a higher symmetry than the Hubbard model are effective low-energy theories, e.g. (extended) g-ology models. In this chapter, a two-pocket model [108] proposed by Chubukov will be considered. Originally, it was conceived for a (Wilsonian) RG study of the competition between spin-density wave (SDW) order and superconductivity in the iron pnictides. Having a purely quadratic dispersion and a simplified momentum dependence of the interactions, this model has an ultraviolet cutoff Λ. The remaining degrees of freedom live on two patches centered around the Γ and the M point in the folded two-dimensional Brillouin zone (BZ) and mimic the band structure close to the Fermi surfaces around these points. (For a pictorial representation of the dispersion, see Fig. 5.1.) In the following, this folded BZ will be referred to as the *full* BZ in order to avoid confusion with the *reduced* BZ, which is bounded by the dashed line in Fig. 5.1(a).

5.1.1. Bare action

The bare action of the Chubukov model will now be expressed in terms of the Nambu spinors $\Psi_\sigma(k)$ in Eq. (4.8) with components $\Psi^s_\sigma(k)$, where the subscript σ denotes the spin-projection. In this case, the Nambu indices s can as well be interpreted as pocket indices, where $s = +1$ and $s = -1$ correspond to the hole pocket at the Γ point and

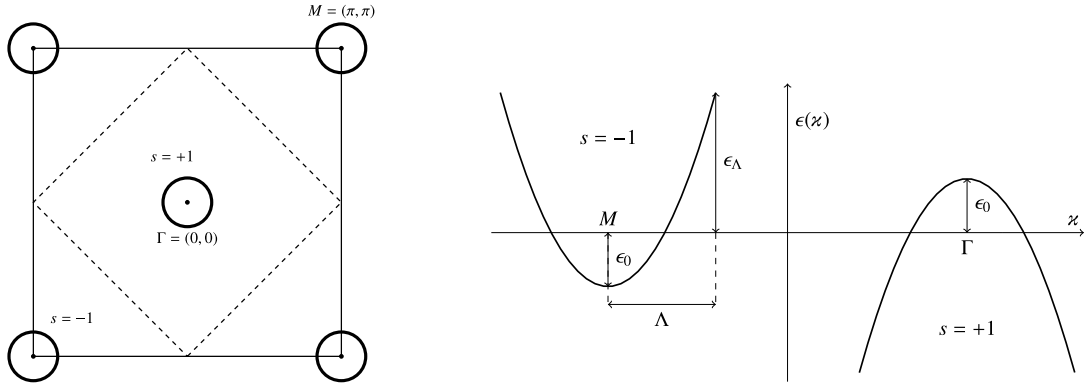

(a) Full BZ (b) Dispersion along the BZ diagonal

Figure 5.1.: Dispersion of the Chubukov model. (a) Fermi surfaces (bold lines) in the full BZ for the physical momentum $\varkappa = \mathbf{k} + (1-s)/2\,(\pi,\pi)$. The dashed line represents the boundary of the *reduced* BZ, on which the momentum quantum number $\mathbf{k}$ is defined. (b) Dispersion as a function of the physical momentum $\varkappa$ along the diagonal of the full BZ. The dispersion is cut off at the energy $\epsilon_\Lambda = \Lambda^2/2 - \epsilon_0$. See text for further explanation.

the electron pocket at the M point, respectively. The momentum quantum numbers $\mathbf{k}$ therefore vary only within the pockets (see also Fig. 5.1.) In Nambu space, the bare action then reads as

$$\mathcal{A} = \sum_\sigma \int_{|\mathbf{k}|\leq\Lambda} dk\, \bar\Psi_\sigma(k)\, C_\sigma(k)\, \Psi_\sigma(k) + \mathcal{A}^{(4)}[\bar\Psi, \Psi]$$

where $C_\sigma(k)$ is of the form given in Eq. (4.24) with

$$\epsilon_{\mathrm{a}}(k) = -\frac{\mathbf{k}^2}{2} + \epsilon_0 \quad \text{and} \quad \epsilon_{\mathrm{s}} = 0\,.$$

In order to trigger the symmetry breaking, a small SDW seed field $\Delta(k) = \Delta_0$ will be introduced. Note that, in two dimensions, this dispersion corresponds to a constant density of states $\rho_0 = 1/(2\pi)$. In the following, $\epsilon_0 > 0$ so that there are two circular Fermi surfaces centered around the M and the Γ point.

The interaction reads as

$$\begin{aligned}\mathcal{A}^{(4)} = -\sum_{s_1\ldots s_4}\sum_{\sigma_1\ldots\sigma_4}\int_{|\mathbf{k}_i|\leq\Lambda} dk_1\ldots dk_4 \bar\Psi^{s_1}_{\sigma_1}(k_1)\,\bar\Psi^{s_2}_{\sigma_2}(k_2)\,\Psi^{s_3}_{\sigma_3}(k_3)\,\Psi^{s_4}_{\sigma_4}(k_4)\,\delta_{\{k\}}\delta_{\sigma_1\sigma_4}\,\delta_{\sigma_2,\sigma_3}\\ \times\Big\{U_1\,\delta_{\mathbf{s},(+--+)} + U_2\,\delta_{\mathbf{s},(-+-+)} + \frac{U_3}{2}\left[\delta_{\mathbf{s},(--++)} + \delta_{\mathbf{s},(++--)}\right]\\ + \frac{U_4}{2}\left[\delta_{\mathbf{s},(++++)} + \delta_{\mathbf{s},(----)}\right]\Big\}\end{aligned}$$

with bare couplings U_i. Both quartic and quadratic part respect the particle-hole and remainders-of-perfect-nesting symmetries discussed in Chapter 4.2.1 and hence the fRG flow equations will preserve these symmetries. In the following, only the case $U_1 = U_2 = U_3 = U_4 = U$ is studied. The interaction then has the same form as a Hubbard interaction expressed in momentum space. The only difference to the Hubbard model in the two-patch approximation then lies in the dispersion, which is isotropic in the present case. (Note that flipping a Nambu index shifts the respective momentum by $\mathbf{Q}$.)

In order to study the flow into the SDW phase, a small symmetry-breaking seed field $\Delta(k) = \Delta_0$ is added to the bare action. This will regularize divergences resulting from the Goldstone modes. The case of the *spontaneous* breaking of the SU(2) and translational symmetries is recovered in the limit $\Delta_0 \to 0$. In practice, this means that Δ_0 is chosen to be small compared to the other energy scales in the bare action. After an infrared frequency or momentum cutoff λ has been removed by the RG flow, Δ_0 may subsequently used as a flow parameter which is sent to zero. [49, 51] However, I will refrain from considering a seed-field flow, since the focus of this chapter rather lies on more basic questions such as the applicability of the Nambu-normal approximation.

From a numerical viewpoint, it is preferable to choose this low-energy continuum model instead of a lattice model for a first fRG study of the AF phase beyond mean field. First, such an effective model may allow for a parametrization of its renormalized coupling functions based on a gradient expansion (see Section 5.2.1). In addition, the C_{4v} symmetry of a 2D lattice model such as the ones used in Refs. [34–39] is promoted to a full circular symmetry, which imposes more severe restrictions on the allowed terms in such a gradient expansion and simplifies the integration over internal momenta in Feynman diagrams. Altogether, this will lead to a drastic reduction of the numerical effort undertaken in a numerical integration of the flow equations.

In Ref. [108], the RG flow of this model has been analyzed in the symmetric phase with momentum and frequency-independent couplings U_1, U_2, U_3 and U_4. This can be regarded a gradient-expansion approach in leading order. Obviously, one has to go beyond this approximation in the symmetry-broken phase, since the violation of the SU(2) Ward identity (1.12) would otherwise be horrendous.

5.1.2. Mean-field gap equation for the Chubukov model

For the case $U_1 = U_2 = U_3 = U_4 \equiv U$ studied in this thesis, the mean-field gap equation

$$\Delta = 2U \int d'k \, \frac{\Delta}{k_0^2 + \epsilon_\mathrm{a}(\mathbf{k})^2 + \Delta^2} = U \int_{|\mathbf{k}|\leq\Lambda} d\mathbf{k} \, \frac{\Delta}{\sqrt{\epsilon_\mathrm{a}(\mathbf{k})^2 + \Delta^2}} \tag{5.1}$$

for antiferromagnetism has the same form as for the Hubbard model at half filling (see, for example, Ref. [131]) and the BCS gap equation. For the AF case, the prime in the measure $d'k$ indicates that the corresponding momentum integral only runs over half the BZ. Since the Chubukov model has a constant density of states $\rho = \rho_0 \equiv 1/(2\pi)$ between $\epsilon_\mathrm{a} = -\epsilon_0$ and $\epsilon_\mathrm{a} = \epsilon_\Lambda \equiv \Lambda^2/2 - \epsilon_0$ and $\rho = 0$ outside this low-energy window, the momentum integral can be performed analytically. This yields

$$\rho_0 U \left[\mathrm{Arsinh}\left(\frac{\epsilon_0}{\Delta}\right) + \mathrm{Arsinh}\left(\frac{\epsilon_\Lambda}{\Delta}\right)\right] = 1\,. \tag{5.2}$$

Clearly, there is no critical interaction strength, i.e. for any positive value of U there will be a finite gap.

Compared to the discussion of the BCS gap equation as it appears in most textbooks, there is an additional ϵ_0-dependent term due to the asymmetry of the dispersion around the Fermi level. In the following, I will show that, for a large cutoff $\epsilon_\Lambda \gg \Delta, \epsilon_0$, this equation has an approximate weak-coupling solution $\Delta \propto \exp\left[-1/(2\rho_0 U)\right]$ reminiscent of BCS theory. Since $\mathrm{Arcsinh}(x) \approx \ln(2x)$ for $x \gg 1$, one obtains

$$\frac{\epsilon_0}{\Delta} \approx \sinh\left[\frac{1}{\rho_0 U} + \ln\left(\frac{\Delta}{2\epsilon_\Lambda}\right)\right]\,.$$

or equivalently

$$1 + \frac{\epsilon_0}{\epsilon_\Lambda}\,\exp\left(\frac{1}{\rho_0 U}\right) \approx \left(\frac{\Delta}{2\epsilon_\Lambda}\right)^2 \exp\left(\frac{2}{\rho_0 U}\right)\,. \tag{5.3}$$

At moderate coupling $U \simeq 1/\rho_0$, let us assume $\epsilon_0 \ll \Delta$ in addition to $\epsilon_0 \ll \epsilon_\Lambda$. In leading order in ϵ_0/Δ, Eq. (5.3) then gives

$$\ln\left(\frac{2\epsilon_\Lambda}{\Delta}\right) \approx \frac{1}{\rho_0 U} - \frac{2\epsilon_0}{\Delta} \approx \frac{1}{\rho_0 U}\,,$$

which is solved by

$$\Delta \approx 2\epsilon_\Lambda \exp\left(-\frac{1}{\rho_0 U}\right)\,. \tag{5.4}$$

Since we are at moderate coupling, this yields a gap of about the size of the cutoff $\Delta \simeq \epsilon_\Lambda$ and consequently the assumption $\Delta \ll \epsilon_\Lambda$ underlying Eq. (5.3) is violated. Therefore Eq. (5.4) fails as an approximate solution.

At weak coupling $U \ll 1/\rho_0$, the 1 in Eq. (5.3) is negligible, which results in

$$\Delta \approx 2\sqrt{\epsilon_\Lambda \epsilon_0}\exp\left(-\frac{1}{2\rho_0 U}\right)\,. \tag{5.5}$$

Indeed, this equation yields $\Delta \ll \sqrt{\epsilon_\Lambda \epsilon_0} \ll \epsilon_\Lambda$, which is consistent with Eq. (5.3). All the numerical calculations in this Chapter will be in a parameter regime, where it is applicable as an approximation formula.

Note that the Chubukov model is not safe against a variation of this ultraviolet cutoff, as the gap grows with $\sqrt{\epsilon_\Lambda}$ at weak coupling. This might be a shortcoming of mean-field theory. If such a behavior can also be observed in the fRG results (or the results obtained from another low-energy solver), this would contradict the concept of an effective low-energy theory, according to which low-energy observables should only vary weakly with the cutoff. For analytical results, one would accordingly expect the leading-order expression of such observables in physical limits to be independent of the ultraviolet cutoff. If this is not the case, either the model itself or the approximations made in the corresponding derivations (or both) seem questionable.

5.2. Numerical implementation

Let us now switch to the implementation of the fRG flow equations (4.75)–(4.78) in Nambu-normal approximation for the Chubukov model. The circular symmetry of this model will be exploited and all calculations will be performed at zero temperature.

5.2.1. Parametrization of the momentum dependence

For the low-energy model under consideration, it seems appealing to parametrize the momentum dependence instead of a brute-force discretization in momentum space. This will considerably lower the numerical effort spent on the integration of the flow equations (4.75)-(4.78) and in principle allows for well parallelizable code (see Section 5.2.2). In order to keep the momentum dependence simple, a frequency cutoff seems preferable to other schemes. An additive frequency regulator will turn out to be a good choice in the following. As in Refs. [49–51], the infrared cutoff λ is implemented by the replacement

$$ik_0 \to ik_0 + R_\lambda(k_0) = i\,\mathrm{sign}(k_0)\,\sqrt{k_0^2 + \lambda^2}$$

in the quadratic part of the bare action in this chapter. One might also consider a multiplicative regulator as in the Ω-scheme of Refs. [24–26], but that cutoff scheme would lead to harder loop integrals on the right-hand sides of the fRG flow equations.

Note that the frequency dependence of the vertices and the self-energy may not be easy to parametrize at finite scales. In the following, a parametrization of the momentum dependence is given, where the coefficients all remain frequency-dependent. This latter dependence is then discretized (see again Section 5.2.2).

Let me first address the momentum dependence of the exchange propagators. In the spirit of a gradient expansion around ordering momenta, one may approximate the

momentum dependence of one of the exchange propagators $P(l)$ by a Lorentzian, i.e.

$$P(l) = \frac{1}{m_P(l_0)\,[1 + n_P(l_0)\,\mathbf{l}^2]}\,, \tag{5.6}$$

with two frequency-dependent parameters. $m_P(l_0)$ corresponds to a bosonic mass and determines the height of the Lorentz peak at $\mathbf{l} = 0$ with width $|n_P(l_0)|^{-1/2}$. Due to the (continuous) rotation symmetry of the model, corrections to this ansatz would appear as even-order terms in $|\mathbf{l}|$ in the denominator.

Neglecting the $\mathbf{l}^2$ term in the denominator would correspond to a frequency-dependent g-ology approach. In a mixed fermion-boson fRG approach to superfluidity in the attractive Hubbard model, gradient terms of radial and Goldstone modes are reminiscent of the above Lorentz decay. [125, 126] Therefore, it seems prudent to at least include the $\mathbf{l}^2$ term in Eq. (5.6). In order to keep the computational cost low, I will not go beyond a Lorentzian in a first attempt of an fRG study in the AF phase beyond mean field. But in the implementation of the RG flow equation used here, the inclusion of higher-order terms does not create parallelization issues in principle. In this context also a superposition of two Lorentzians as suggested in Ref. [26] may be worth considering.

In the following, the gap functions will be projected to zero momentum, i.e.

$$\Delta(k_0) = \Delta(k)|_{\mathbf{k}=0}\,.$$

Note that $\mathbf{k} = 0$ corresponds to considering the gap only at the centers of the pockets, since the Nambu indices play the role of pocket indices and since $\mathbf{k}$ therefore only lives on half the BZ, i.e. only varies *within* the pockets. Of course, also the momentum dependence of the gap would be interesting to study and resolving only its frequency dependence may seem awkward in first place. Looking at the flow equation (4.78) for the self-energy, one can however observe that the frequency and momentum dependence is generated by the dependence of the second and third argument in the square brackets of E'. Since the momentum dependence of these propagators is only taken into account to subleading order in a gradient expansion, and since the self-energy is mainly driven by the radial vertex at $l = 0$, it seems appropriate to neglect the momentum dependence of the self-energy in a first step beyond mean-field. This way, the integrand in Eq. (4.78) remains independent of the angular integration variable, which reduces the three-dimensional integral to a two-dimensional one. Studying the momentum dependence of the self-energy appears however worthwhile if one goes beyond a Lorentzian profile in the exchange propagators.

5.2.2. General setup for the numerics

The integration of the fRG flow equations (4.75)-(4.78) mainly involves two numerical tasks.

i.) Non-linear ordinary differential equations (ODEs) have to be solved. This is done by a fourth-order Runge-Kutta algorithm. [132]

ii.) The integrals on the right-hand sides of the flow equations require efficient quadrature routines. For the integrals over loop momenta and frequencies, different routines from the NAG library [133] are used here. For the frequency integrals, the integration mesh is determined using a special algorithm (see Section 5.2.3).

While the application of the ODE solver in i.) is straightforward, the loop integrals are more difficult to handle. They require the exchange propagators and the self-energy to be given as continuous functions of frequency and momentum. The momentum dependence of the exchange propagators has been parametrized in the preceeding subsection and the self-energy has been assumed to be momentum-independent. In contrast, the frequency dependence of both the self-energy and the exchange propagators is discretized on a grid of 40 points with includes zero frequency and logarithmically spaced points between 10^{-5} and $1.2\,\Lambda$. More precisely, $\Delta(k_0)$, $m_P(l_0)$ and $n_P(l_0)$ are put on that grid. If values between the grid points are needed, a monotonicity-preserving cubic Hermite spline interpolant implemented in routines of the NAG library is used.

The scale derivatives of $\Delta(k_0)$ and $P(l_0,0) = 1/m_P(l_0)$ are straightforwardly obtained from the flow equations at the grid points. The square inverse Lorentz width $n_P(l_0)$ could be obtained by calculating the second derivative of the right-hand sides of Eqs. (4.75)-(4.77) with respect to $\mathbf{l}$. This would however lead to harder loop integrands and hence a different strategy is pursued here. Namely, the second momentum-derivative of P at $\mathbf{l} = 0$ is calculated from a three-point stencil. Due to the spatial inversion symmetry, which implies $P(l_0,\mathbf{l}) = P(l_0,-\mathbf{l})$, only two values at zero momentum and at $\mathbf{l} = \mathbf{h}$ are needed. Note that the choice of $\mathbf{h}$ requires some care. Clearly, it should not be too large and if it is chosen too small the variation of $P(l_0,\mathbf{l})$ between $\mathbf{l} = 0$ and $\mathbf{h}$ may largely be affected by numerical errors. For stability reasons, it appears preferable to consider $P(l_0,\mathbf{h})$ as running couplings in the ODE solver and to calculate the Lorentz width at each scale according to

$$n_P(l_0) = \frac{1}{|\mathbf{h}|^2}\left[\frac{P(l_0,0)}{P(l_0,\mathbf{h})} - 1\right] .$$

For the results presented in the remainder of this chapter, $\mathbf{h}$ has been chosen as $0.8\,\sqrt{2\epsilon_0}$.

Let me now discuss the quadrature algorithms used for the loop integrals. In a serial code, it seems preferable to jointly calculate the frequency and momentum integrals using a multidimensional adaptive routine (see Ref. [110]). If a number of such integrals are calculated in parallel, memory access issues are likely. For a small number of cores these issues seem to play a minor role [134] – presumably due to efficient prefetching. In the Nambu-normal approximation, the numerical requirements can be met by using a few cores only and hence one may in principle also resort to such a multidimensional quadrature routine.

On the other hand, the reduced flow equations in Nambu-normal approximation can be regarded as a good testbed for numerical methods that are suited for relaxing these approximations. I have therefore decided to implement the loop integrals in a way that should allow for an efficient parallelization to a larger number of cores. This comes at the price of a larger number of calls of the loop integrand, which is not high for the reduced flow equations (4.75)-(4.78).

The key features of this approach are the following. In an inner loop, the momentum integrals are calculated, while the frequency integral corresponds to the outer loop. Consequently, the integrand is only needed at a given frequency within the momentum quadrature. This way, the thread communication overhead can be significantly reduced, since the momentum dependence of the integrand at that frequency is then determined by only a small number of parameters. In other words, the memory is now transversed less randomly, which can have a great impact on the performance if the overall number of parameters in the loop integrand is large.

The momentum integrals are performed using the one-dimensional adaptive routine `D01ALF` form the NAG library. For the self-energy and the exchange propagators at $\mathbf{l} = 0$, the angular integration can trivially be performed analytically. For the exchange propagators at $\mathbf{l} = \mathbf{h}$, two one-dimensional quadratures are nested, where the angular integration is performed in the inner loop. For the Chubukov model, this strategy is superior to a two-dimensional adaptive quadrature. This is presumably due to the continuous rotational symmetry of the model and a two-dimensional routine seems still preferable for a lattice model with a fourfold symmetry, such as the Hubbard model.

5.2.3. Calculation of the frequency integrals

For the additive frequency-cutoff scheme used here, the frequency integral can be implemented in the following simple way. Recall that the self-energy and the exchange propagators already live on a fixed frequency grid. In order to obtain an integration mesh for the frequency integral, it therefore seems appealing to refine this grid. At the additional points introduced this way, interpolated values are used for the self-energy and for the exchange propagators. The form of the regulator dictates where the grid needs to be refined. Generically, contributions to the frequency integrals at high frequencies are less important than those from low frequencies. Moreover, the variation of the integrand will be suppressed below the infrared cutoff λ.

Let us now look at this in greater detail. The sign function in the regulator induces jumps at $p_0 = q_0$, where $q_0 = 0$ in the flow equation (4.78) for the self-energy and at $q_0 = \pm l_0/2$ in the flow equations (4.75)-(4.77) for the exchange propagators. For $|p_0 - q_0| \ll \lambda$, the integrand will only show a negligible variation, as the frequency enters either in

the regulated from via $\sqrt{p_0^2 + \lambda^2}$ or or via the self-energy and the exchange propagators. Since the frequency dependence of the couplings is generated from the loops, these latter quantities will also only vary weakly for $|p_0 - q_0| \ll \lambda$. If $|p_0 - q_0|$ is of the order of the infrared cutoff λ, additional grid points are needed in order to capture the variation of the regulator function. If the initial grid is well chosen, the variation of the self-energy and the exchange propagators is then still captured by a monotonicity-preserving spline interpolant. For $|p_0 - q_0| \gg \lambda$, the integrand will already have decayed to a large part and hence a relatively coarse frequency grid will suffice in this regime. Therefore, the integration mesh can be determined prior to any function call of the integrand. The precise values of the grid points will then depend on the scale and on q_0.

More precisely, the integration mesh M is obtained in the following way. It is chosen symmetric with respect to $q_0 \to -q_0$ and the following prescription is for positive frequencies and $q_0 \geq 0$.

i.) All points of the frequency grid A for the exchange propagators and the self-energy except q_0 are part of this mesh.

ii.) Define the distances of q_0 to its neighbors in A as

$$d_+(q_0) = \min_{p \in A, p > q_0} |p - q_0| \quad \text{and} \quad d_-(q_0) = \begin{cases} 0 & q_0 = 0 \\ \min_{p \in A, 0 < p < q_0} |p - q_0| & \text{otherwise} \end{cases} .$$

Further introduce $\lambda_\pm = \min[\lambda, \kappa d_\pm(q_0)]$, with a positive constant $\kappa < 1$. Then the points $q_0 \pm \epsilon$, $q_0 + 0.02\lambda_+$ and $q_0 + 0.08\lambda_+$ are added, where ϵ is chosen finite, but small in order to account for the jumps at q_0. If $\lambda_- \neq 0$, also $q_0 - 0.02\lambda_-$ and $q_0 - 0.08\lambda_-$ are added.

iii.) Between $q_0 + 0.08\lambda_+$ and some upper bound $q_0 + q_+$ for the refinement, additional logarithmically spaced grid points are introduced. These points should be more densely spaced than the points in A. If $q_0 \neq 0$, the same is done between $q_0 - 0.08\lambda_-$ and $\max(0, q_0 - q_-)$. The bounds $q_\pm$ for these insertions are given by

$$q_\pm = \max[\alpha\Lambda, \beta\lambda, \gamma d_\pm(q_0)] ,$$

where α, β and γ are positive constants.

iv.) Outside the frequency grid A, logarithmically spaced points are added upto an upper frequency ω_∞. If this cutoff frequency is chosen large enough, contributions from frequencies above are negligibly small.

As the exchange propagators and the self-energy are interpolated by splines, the frequency integrals are also calculated as the integral of the spline through the values of

the integrand on M.[1] This way, the self-energy and the exchange propagators on one hand and the complete integrands on the other are approximated by consistent interpolants, which may reduce numerical errors. Due to the discontinuity at q_0, the domain of integration has to be split into subsets where the integrand is known to be continuous.

Altogether, I have presented a numerical approach that allows for an efficient parallelization. For the flow equations in Nambu-normal approximation, the corresponding program is run on 8 up to 12 cores using shared memory (OpenMP) parallelization. More precisely, scale derivatives of the self-energy and exchange propagators for different frequency and momentum values are calculated in parallel. This corresponds to parallelizing the outermost loop. In principle, this may also be done within a distributed memory approach, and the frequency integral allows for further (nested) parallelization.

5.3. Characteristics of the fRG flow

In this section, numerical results for the fRG flow into the SDW phase of the Chubukov model in the Nambu-normal approximation are presented. The system parameters have been chosen as $\epsilon_0 = 3.0 \cdot 10^{-2}$ and $\epsilon_\Lambda = 0.58$, if not indicated otherwise. All calculations will be performed for zero temperature.

Note that, also in an fRG approach, the Chubukov model is not ultraviolet save, i.e. the results are strongly sensitive to the ultraviolet cutoff ϵ_Λ. If the goal was to obtain realistic values for the AF gap observed in a certain pnictide compound, one clearly would have to resort to a more elaborate model. At the present stage, the main focus however lies on methodological developments and therefore the ultraviolet cutoff can be fixed to the above (rather arbitrary) value without spoiling the key results of this chapter.

5.3.1. Scale dependence of the exchange propagators and the gap

Let us first consider the flow of the gap and the exchange propagators at zero momentum and frequency. For a typical choice of the model parameters, the scale-dependence of these quantities is depicted in Figs. 5.2 and 5.3, respectively. In qualitative agreement with the mean-field picture (cf. Figs. 4.1(a)-4.1(c)), the gap opens at the critical scale, where the radial vertex $M_z(0)$ shows a pronounced peak. Below the critical scale, the

[1] This is done by using the routine `E01BHF` from the NAG library which complements the routines `E01BEF` and `E01BFF` for the calculation of the spline coefficients and the interpolated values.

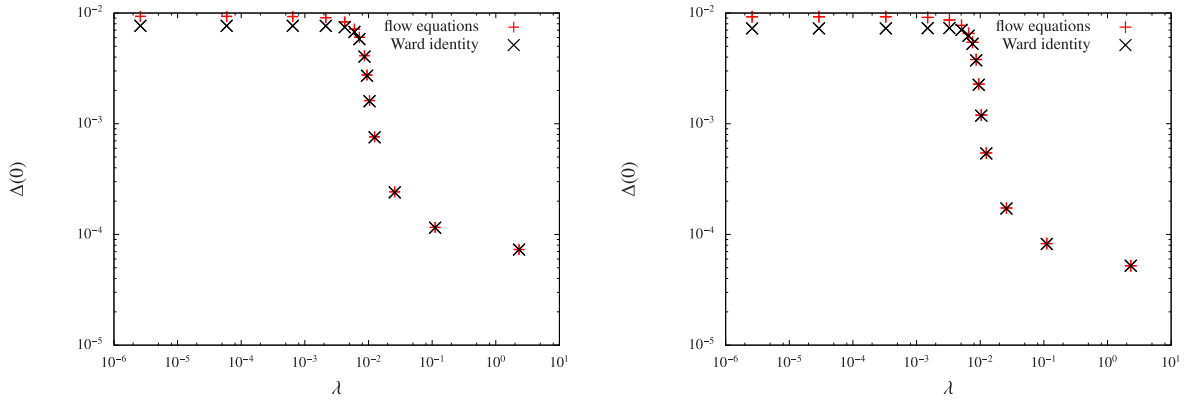

(a) $\Delta_0 = 7.0 \cdot 10^{-5}$ (b) $\Delta_0 = 5.0 \cdot 10^{-5}$

Figure 5.2.: Flow of the gap $\Delta(0)$ with the infrared cutoff λ at zero frequency for $U = 1.0$ and $\Delta_0 = 5.0 \cdot 10^{-5}$. The points labeled with 'flow equation' are obtained from the integration of Eqs. (4.75)-(4.78), while the points labeled with 'Ward identity' correspond to the value of the right-hand side of the WI (4.79) at the respective scale.

couplings saturate to their infrared values. In contrast to the radial vertex, which has moderate infrared values, the Goldstone vertex $M_{xy}(0)$ becomes large for $\lambda \to 0$.

By varying the seed field, i.e. by comparing Fig. 5.2(a) to Fig. 5.2(b) and Fig. 5.3(a) to Fig. 5.3(b), one finds that the increase of the gap is steeper for smaller Δ_0 and that the peak of the radial vertex then is more pronounced. Furthermore, the infrared value of the Goldstone vertex increases with decreasing Δ_0. Also this behavior is in qualitative agreement with the mean-field results of Chapter 4.1, while the mean-field picture becomes inadequate on a more quantitative level. One difference shall already be outlined here: While the CDW and singlet-pairing channels do not feed back on the other channels and the gap at the mean-field level, they will be found to have a significant impact on the flow in Section 5.3.3. At $l = 0$, the corresponding exchange propagators N and $D = -N$ grow in the flow until the critical scale is reached. Below, they decrease slightly, saturating to their infrared values. Their absolute values are equal, since the Nambu-normal spin-splitting ϵ_s is neglected in the flow equations (see Chapter 4.4.3) and they virtually behave independently of the value of Δ_0.

After having discussed the flow of the exchange propagators at $l = 0$, let us turn to their dependence on momentum and frequency. In Fig. 5.4, the flow of the squares n_P of the inverse Lorentz widths of their momentum profiles is depicted at $l_0 = 0$. (Large values of n_P correspond to narrow peaks.) Comparison with Fig. 5.3 suggests as a rule of thumb that the momentum profile of the exchange propagators around $l = 0$ is the more sharply peaked the larger their values at $l = 0$ are.

Let us now have a look at the frequency dependence of the exchange propagators P. For

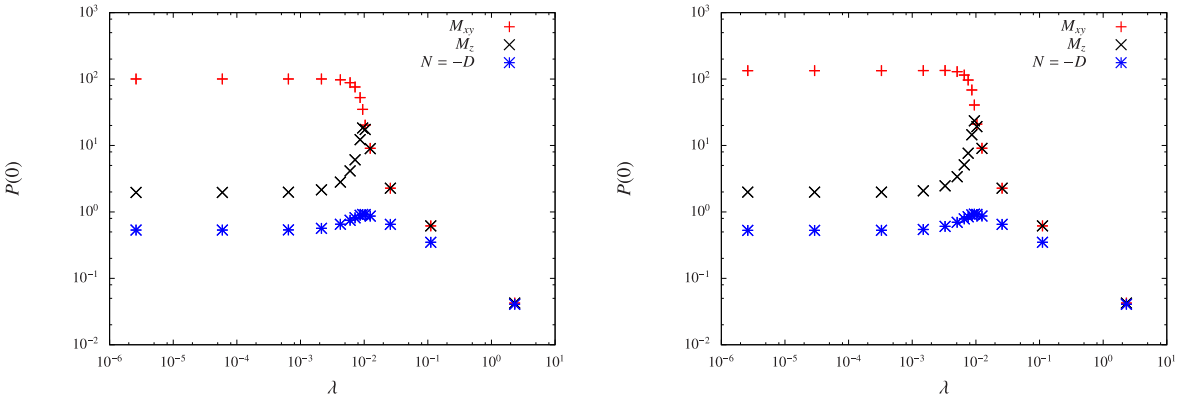

(a) $\Delta_0 = 7.0 \cdot 10^{-5}$ (b) $\Delta_0 = 5.0 \cdot 10^{-5}$

Figure 5.3.: Flow of the exchange propagators with the infrared cutoff λ at $l = 0$ for $U = 1.0$.

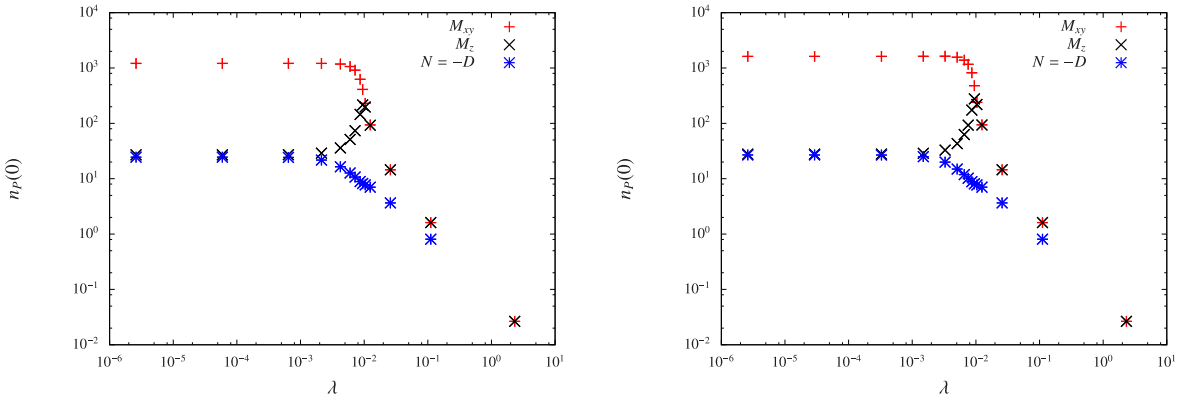

(a) $\Delta_0 = 7.0 \cdot 10^{-5}$ (b) $\Delta_0 = 5.0 \cdot 10^{-5}$

Figure 5.4.: Flow of the square n_P of the inverse Lorentz width of the exchange propagators P with the infrared cutoff λ at zero frequency for $U = 1.0$.

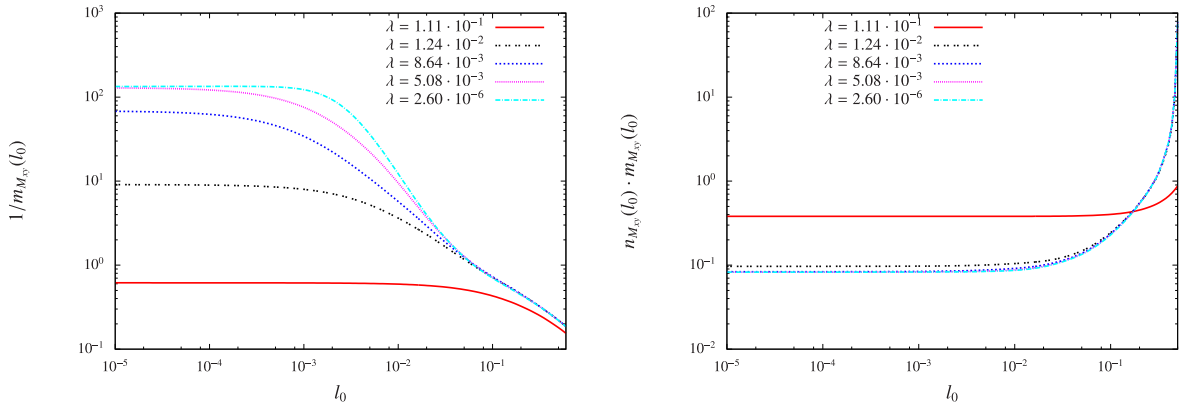

(a) $M_{xy}\,(l_0, 0)$ (b) Momentum decay of M_{xy}

Figure 5.5.: Frequency dependence (a) of the $\mathbf{l} = 0$ values of M_{xy} and (b) of its momentum decay for $U = 1.0$ and $\Delta_0 = 5.0 \cdot 10^{-5}$ at various stages of the flow, where l_0 denotes the transfer frequency. The curves shown here are the spline interpolants also used in the numerics.

zero momentum, they are given by $m_P(l_0)$. The value of $n_P(l_0)$, in contrast, describes the momentum decay at some frequency l_0. For $P = M_{xy}, M_z, N$, the parameters $1/m_P$ and n_P are depicted as a function of frequency at various stages of the flow in Figs. 5.5, 5.6 and 5.7, respectively. In the Goldstone and radial channels, $1/m_{M_{xy}}$ and $1/m_{M_z}$ decay monotonically in Figs. 5.5(a) and 5.6(a). The form of these curves neither resembles a Lorentzian or an exponential. One may wonder whether a sign change occurs in D and N in analogy to a singlet superfluid, where the magnetic exchange propagator changes sign at small frequencies. [49] In Fig. 5.7(a), one can however see that this is not the case and that $1/m_N$ decays with frequency in a way similar to the Goldstone and radial channels.

The parametrization of the exchange propagators introduced in Section 5.2.1 also allows for a frequency-dependent momentum decay length. In Figs. 5.5(b) and 5.6(b), however, the product $n_P(l_0)\, m_P(l_0)$ for the radial and Goldstone vertices remains constant up to relatively high frequencies. This is in agreement with the parametrization of the exchange propagators in Refs. [49,50]. In those works, real-valued exchange propagators P are described by a frequency dependent mass $m_P(l_0)$ and a momentum function $F_P(\mathbf{l})$ according to

$$P(l) = \frac{1}{m_P(l_0) + F_P(\mathbf{l})}\,. \tag{5.7}$$

In the present case, one may approximate $F_P(\mathbf{l}) \approx n_P(0)\, m_P(0)\, \mathbf{l}^2$, which only can safe half the computation time. For more refined momentum parametrizations, however, one may gain a much larger factor by neglecting the frequency dependence of the momentum decay in the spirit of Eq. (5.7). According to Fig. 5.7(b), this approximations seems less applicable for the CDW and singlet-pairing channels, where $n_N(l_0)\, m_N(l_0)$ varies at frequencies of the order of the critical scale. But employing Eq. (5.7) also for these

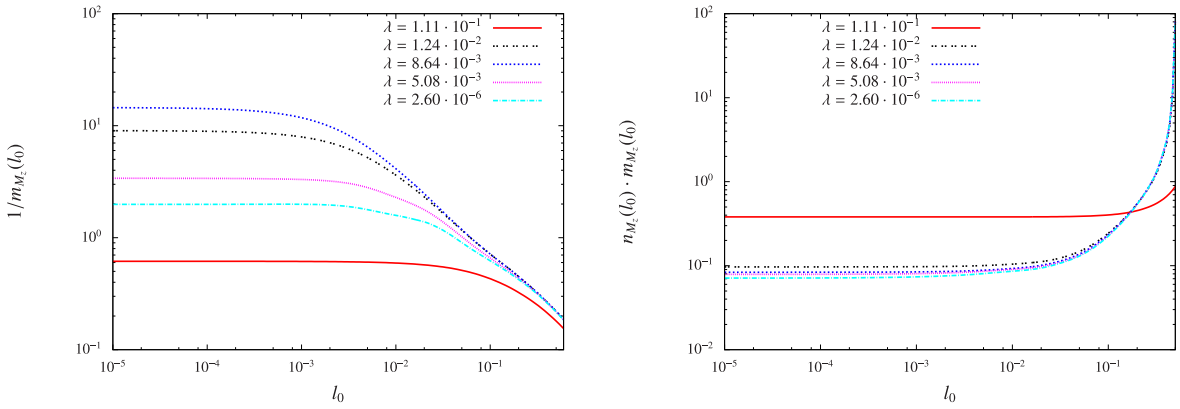

(a) $M_z\,(l_0, 0)$ (b) Momentum decay of M_z

Figure 5.6.: Frequency dependence (a) of the $\mathbf{l} = 0$ values of M_z and (b) of its momentum decay at various stages of the flow, where l_0 denotes the transfer frequency. The parameters have been chosen as in Fig. 5.5.

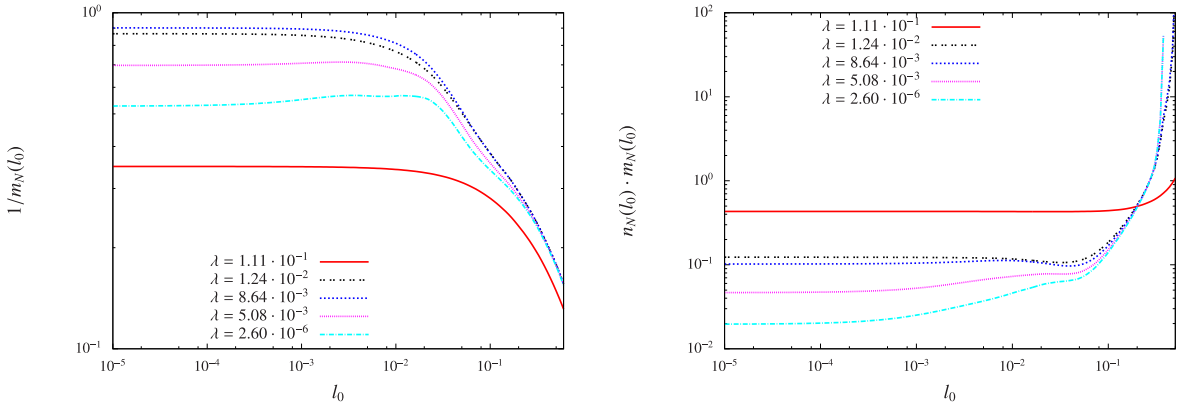

(a) $N\,(l_0, 0)$ (b) Momentum decay of N

Figure 5.7.: Frequency dependence (a) of the $\mathbf{l} = 0$ values of N and (b) of its momentum decay at various stages of the flow, where l_0 denotes the transfer frequency. The parameters have been chosen as in Fig. 5.5.

channels still should affect the results for the gap and the fulfillment of the WI only insignificantly.

Clearly, finding a parametrization of the frequency dependence of the *bosonic mass* may be a hard task. But a parametrization that differs from the above results at high frequencies may still provide a good effective description. This may be desirable if the Nambu-normal approximation underlying the flow equations (4.75)-(4.78) is relaxed at the price of an increased numerical cost. Probably the easiest such parametrization consists in completely neglecting the frequency dependence. I will comment on the validity of this approximation, when the fulfillment of the WI is discussed in the following subsection.

In contrast to the exchange propagators, the gap Δ shows only a negligible frequency dependence throughout the flow in agreement with the RPA result of Chapter 4.4.2.

5.3.2. Fulfillment of the Ward identity

The violation of the WI (4.79) provides a measure for the errors induced by the Katanin one-loop truncation and further approximations. For a singlet superfluid, the corresponding U(1) WI has been used as a measure of the quality of the approach pursued. [49] In the present case, having a look at the violation of the SU(2) WI seems indeed rewarding, since there are a number of approximations involved and since it is not yet clear how faithful they are on a more quantitative level.

In Fig. 5.8, the relative WI violation $(\Delta - \Delta_{\mathrm{WI}})/\Delta$ is plotted against the scale, where Δ is obtained from the fRG flow equations and Δ_{WI} denotes the corresponding value of the right-hand side of Eq. (4.79). It seems obvious that perturbation theory applies at high scales and that the WI is only weakly violated in that regime. Slightly above the critical scale, the curves in Fig. 5.8 start to increase and develop a dependence on the value of the seed field Δ_0. Generically, Δ is larger than Δ_{WI} and the WI violation gets worse for smaller seed fields. For the parameters of Fig. 5.8, the values of the WI violation ($\leq 25\%$) suggest that the results obtained have at least the right order of magnitude, while they are less faithful than in Ref. [49], where the relative WI violation is much smaller. Regarding the underlying approximations, this suggests that the flow equations (4.75)-(4.78) in Nambu-normal approximation are indeed applicable, while this approach should be extended in an attempt to proceed in a more qualitative direction.

By varying the interaction strength U, one finds the WI violation to increase with U and one might conjecture that the errors mainly stem from the one-loop truncation (and only to a small part from the other approximations involved). However, Fig. 5.8(b) leads to a

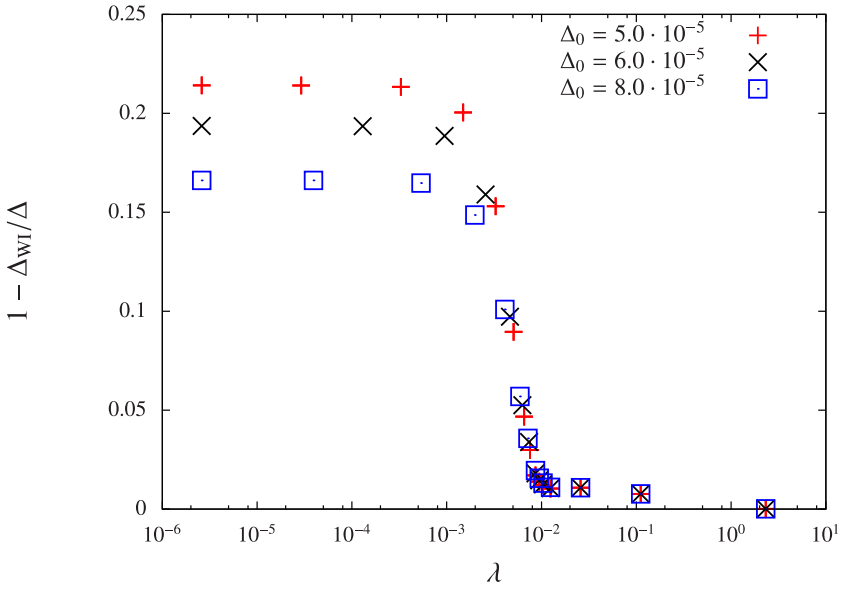

(a) $U = 1.0$

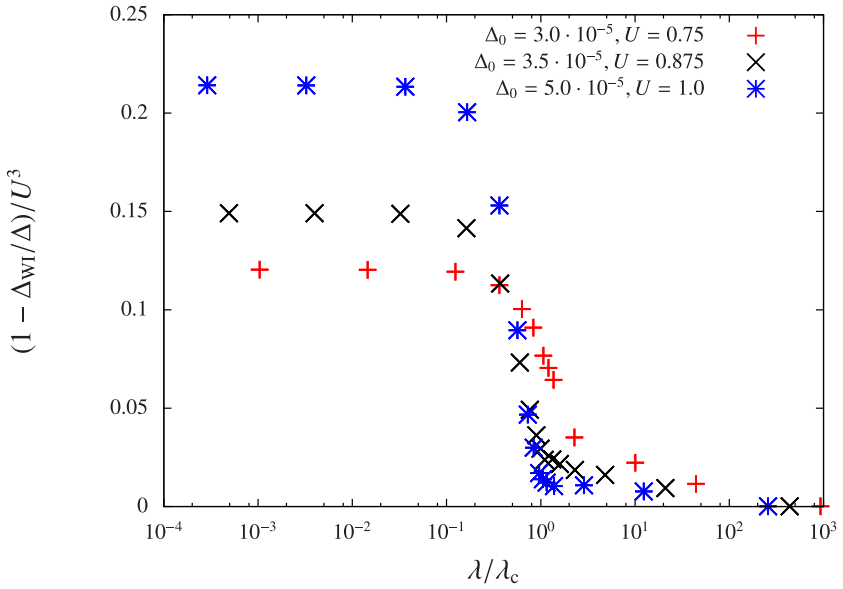

(b) Various values of U

Figure 5.8.: Relative violation of the WI (4.79) as a function of the scale λ for various values of U and Δ_0. The fRG results for the gap are denoted by Δ, while Δ_{WI} corresponds to the right-hand side of the WI (4.79). Results of different interaction strengths are divided by U^3 in order to be comparable in (b), where λ is also normalized by the critical scale λ_{c}.

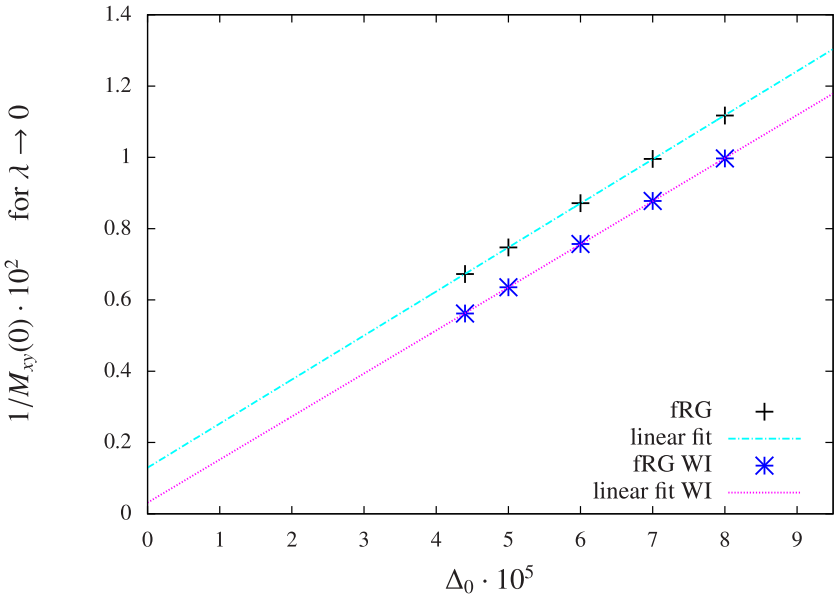

Figure 5.9.: Dependence of the infrared values of the Goldstone vertex $M_{xy}(0)$ on the seed field Δ_0 for gaps according to the flow equation (4.78) and the WI (4.79) for $U = 1.0$. See text for further explanation.

different conclusion. The error of the one-loop truncation can be expected to scale with U^3 (cf. Refs. [49,51]). In Fig. 5.8(b), the relative WI violation is therefore normalized by U^3 and the scale by its critical value λ_c. This allows for a comparison of the WI violation for different values of U. In contrast to the above conjecture, curves for different values of U do not coincide above the critical scale. Instead, their behavior suggests that there are considerable U^2 contributions to the WI violation. They can be regarded as a signature of the approximations made *within* the one-loop truncation, since second-order contributions in the bare interaction to the self-energy would be resummed completely in their absence. These errors may be caused by the approximations underlying the flow equations (4.75)-(4.78), i.e. the projection rule of Chapter 4.3.1 and the omission of some interaction terms, and by the parametrization of the momentum dependence. Taking higher-order terms in the gradient expansion of Section 5.2.1 into account or discretizing the momentum dependence of the exchange propagators seems to be an appropriate first step in looking for the origin of the U^2 WI violations. In addition, one may also consider different projection rules for the exchange parametrization.

So far, I have discussed the fulfillment of the WI by looking at the values of the gap. But there is another property associated with the WI. In the infrared, the interaction is dominated by the Goldstone vertex and therefore other contributions on the right-hand side of the WI (4.79) seem to be of minor importance. If the SU(2) and translational symmetries are *spontaneously* broken, i.e. if the gap does not vanish in the limit $\Delta_0 \to 0$, the Goldstone vertex must diverge as $M_{xy}(0) \propto \Delta_0^{-1}$ in this limit. Let us therefore check this property. In Fig. 5.9, the reciprocal value of the Goldstone vertex is depicted for

various values of the seed field. Simply integrating the flow equations (upper curve in Fig. 5.9) gives rise to points that agree well with their linear fit. However, if $1/M_{xy}(0)$ is extrapolated to $\Delta_0 \to 0$, one still obtains a finite Goldstone vertex as a consequence of WI violations.

The WI can now be enforced by determining Δ by iterating Eq. (4.79) until convergence is reached at each iteration step of the ODE solver. (Its scale-derivative needed in the loops, in contrast, is still obtained from the flow equation (4.78).) The resulting infrared values of $1/M_{xy}(0)$ constitute the lower curve in Fig. 5.9. Again, a linear dependence on the seed field is found. But now, the corresponding fit curve is much closer to the origin for vanishing seed field. This indicates that enforcing the WI not only somehow projects the fRG flow on the hypersurface in parameter space given by this identity, but also leads to physically meaningful results. An even more promising approach would constitute in applying an ODE solver with a constraint [135] as in Refs. [49, 50]. Since a number of steps in a more quantitative direction still need to be undertaken before, I refrain from this task here. (Except for Fig. 5.9, the WI is *not* enforced in all figures of this chapter, i.e. the gap is obtained from the flow equations.)

Let me note in passing that Δ_0 cannot be chosen arbitrarily small before the fermionic cutoff λ has been fully removed. This is due to the singular behavior of box diagrams with bosonic lines corresponding to the Goldstone vertex in the limit of a vanishing seed field. The discussion of these diagrams in Refs. [49, 51] also applies for the present case and the Δ_0 flow proposed in those works offers itself as a method for the removal of the seed field. But before such a flow is implemented, again a considerable amount of work remains to be done in order to first reduce the WI violation further.

5.3.3. Comparison to mean-field theory

The present analysis represents a first step beyond the mean-field picture in an fRG approach to antiferromagnetically ordered phases. The corresponding flow equations (4.75)-(4.78) reproduce the mean-field result in RPA (see Chapter 4.4.2). As can be seen from the preceeding section, the flow in Nambu-normal approximation behaves RPA-like in the sense that the coupling between different channels induces only finite renormalizations — in analogy to the fRG flow of the attractive Hubbard model into the superfluid phase. [49] Let us have a look at these renormalizations for the Chubukov model here. In Fig. 5.10, the ratio $\Delta/\Delta_{\mathrm{MF}}$ of the gaps obtained from fRG and mean-field theory is plotted against the interaction strength U. Note that the fRG values Δ are only upper estimates for the gap calculated for nonvanishing seed fields. For all data points depicted, a reduction of the gap through the coupling of different channels can be observed. The present data suggest that $\Delta/\Delta_{\mathrm{MF}}$ increases with the interaction strength U. A similar increase has also been found for the superconducting gap of the attractive

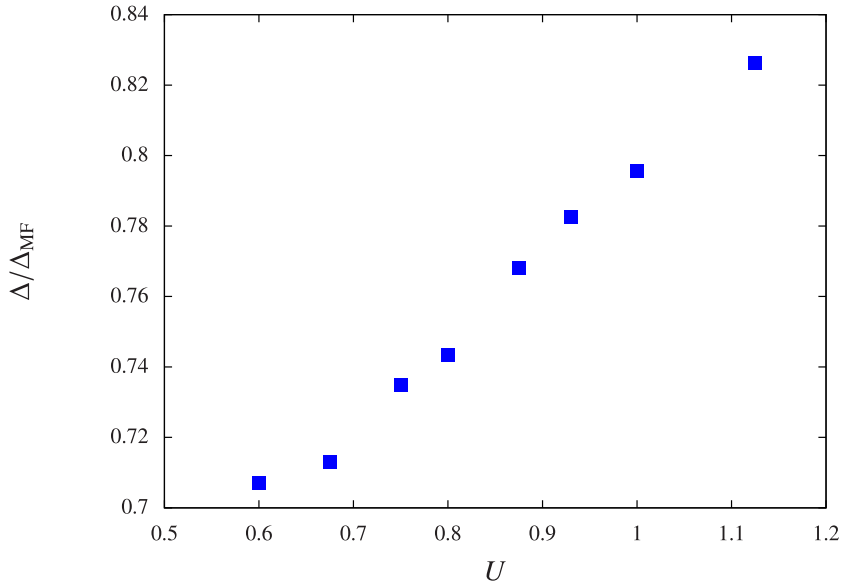

Figure 5.10.: Ratio of the fRG and mean-field gaps $\Delta = \Delta^{\lambda=0}(0)$ and Δ_{MF} as a function of U. See text for further explanation.

Hubbard model in Ref. [49].

Clearly, a reduction of the mean-field gap may also partly occur, if U^2 terms in the gap equation (5.1) were added. Such a self-consistency equation for the gap may be obtained in different ways. [131,136,137] While methods of this kind have been used for the two-dimensional Hubbard model in Refs. [136,137], such considerations have not yet been undertaken for the Chubukov model to the author's knowledge.

The renormalizations of the RPA result contained in the fRG values of Δ are caused by diagrams with bosonic lines *inside* closed loops on the right-hand sides of the flow equations (4.75)-(4.78). The importance of these vertex-correction and box diagrams may manifest itself in different ways.

i.) The frequency dependence of the vertices may affect the results. In static approximation, the WI then could hence be more strongly violated.

ii.) The feedback of the CDW and singlet-pairing channels on the other interaction channels and the gap, which is absent at the RPA level, may play a role. The WI should then be more strongly violated if the corresponding exchange propagators N and D are neglected.

Let us therefore first have a look at the impact of the frequency dependence, i.e. compare the flow with frequency-dependent vertices to the flow in static approximation. As already mentioned above, the fulfillment of the WI can be regarded as a hallmark of

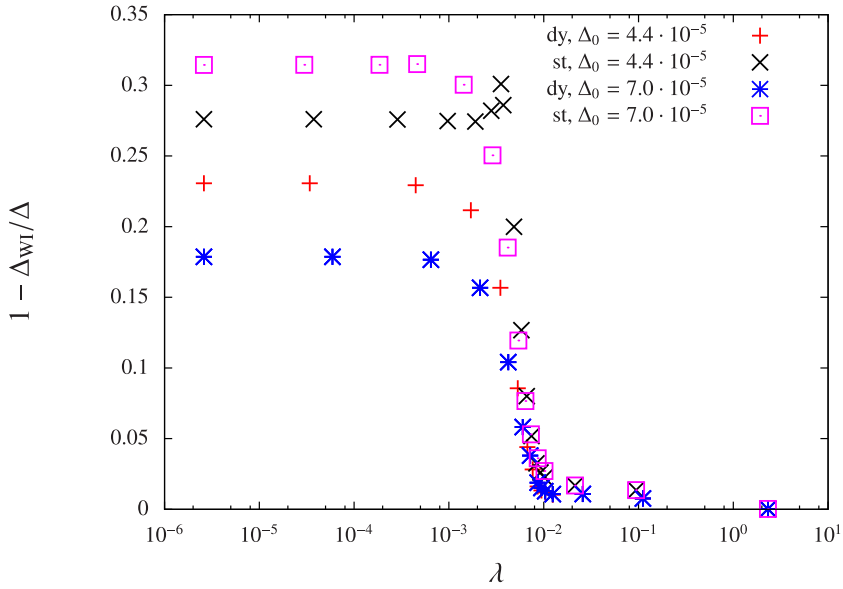

Figure 5.11.: Violation of the WI (4.79) as a function of the scale λ for frequency-dependent vertices (dy) and in static approximation (st). The fRG results for the gap are denoted by Δ, while Δ_{WI} corresponds to the right-hand side of the WI (4.79). The model parameters $\epsilon_0 = 3.0 \cdot 10^{-2}$ and $U = 1.0$ are kept fixed, while Δ_0 is varied.

the quality of the approximations employed. In Fig. 5.11, the relative WI violation $(\Delta - \Delta_{\mathrm{MF}})/\Delta$ is depicted for frequency-dependent vertices and in static approximation for $U = 1.0$. Apparently, relaxing the frequency dependence enhances the violation of the WI. As for the infrared values of the gap, the static approximation yields $\Delta_{\mathrm{st}} = 8.52 \cdot 10^{-3}$ for $\Delta_0 = 4.4 \cdot 10^{-5}$, while $\Delta = 9.23 \cdot 10^{-3}$ is obtained with frequency-dependent vertices. One may hence conclude that taking the frequency dependence of the vertices into account makes the present approach more powerful. Furthermore, the reduction of the mean-field gap is overestimated in static approximation. Also these findings are in agreement with those for the superfluid phase of the two-dimensional attractive Hubbard model.

Finally, let me discuss the importance of the feedback of the singlet-pairing and CDW channels on the fRG flow of the other quantities. The corresponding exchange propagators D and N are neglected for this purpose and the flow is then run for $U = 1.0$ and $\Delta_0 = 5.0 \cdot 10^{-5}$. In Fig. 5.12, the flows with and without the singlet-pairing and CDW channels are compared. One can observe that without these contributions the critical scale is slightly enhanced. In their absence, the Goldstone vertex grows more strongly slightly above the critical scale [see Fig. 5.12(a)]. This enhanced growth of the Goldstone vertex goes along with a strong violation of the WI [see Fig. 5.12(b)]. The value $1.60 \cdot 10^{-2}$ for the gap in the absence of D and N considerably exceeds the fRG result $\Delta = 9.25 \cdot 10^{-3}$ in their presence, wrongly predicting an enhancement of mean-field gap

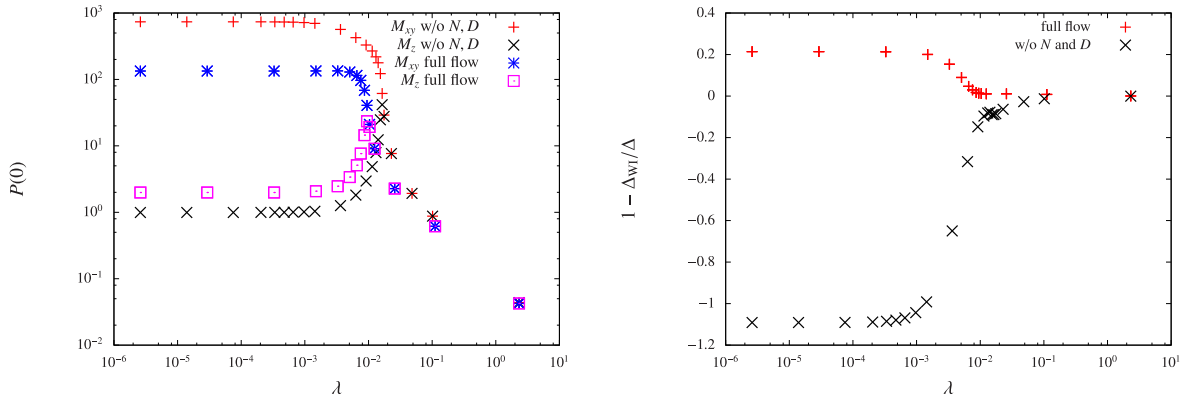

(a) Exchange propagators (b) WI violation

Figure 5.12.: Comparison of the flows with and without the CDW and singlet-pairing channels for $U = 1.0$ and $\Delta_0 = 5.0 \cdot 10^{-5}$. The exchange propagators $M_{xy}(0)$ and $M_z(0)$ (a) and the relative WI violation (b) are depicted as functions of the scale λ.

$\Delta_{\mathrm{MF}} = 1.16 \cdot 10^{-2}$. Moreover, a slightly larger value is obtained for the critical scale if these exchange propagators are neglected. Altogether, this invalidates the omission of the CDW and singlet-pairing channels as a sensible approximation. Regarding the violation of the WI, these channels seem to be more essential than the time-reversal breaking, $s^{\pm}$-wave and Nambu-anomalous terms omitted in the flow equations (4.75)-(4.78), which *a posteriori* justifies the underlying approximations.

One may wonder why the CDW and singlet-pairing channels seem to play such an essential role. At the RPA level, the flow of these two channels does not feed back on other scale-dependent quantities (see Chapter 4.4.2). If they are however neglected in a one-loop fRG approach, vertex-correction and box diagrams give rise to a strong enhancement of the mean-field result, which strongly violate the WI. The inclusion of the CDW and singlet-pairing channels with exchange propagators N and D, in contrast, only gives rise to a rather moderate reduction of the mean-field gap. This suggests that there are counteracting tendencies in the vertex-correction and box diagrams, which account for the effects beyond mean-field.

In the flow equation (4.76) for M_{xy}, the linear combination $P_2 = M_z/2 + 3D/2$ of exchange propagators appears inside the loops of these diagrams. Let me now recall that $D = -N$ takes on negative values, while M_z is positive. Consequently, a partial cancellation of these contributions in P_2 indeed reduces the impact of effects beyond the mean-field picture. At scales slightly above the critical scale, where $M_z(l) \simeq -3D(l)$ for small l, vertex-correction and box diagrams only give negligible contributions to the flow of the Goldstone vertex. If D is however neglected, the impact of these diagrams is exaggerated. This in turn gives rise to a strong growth of the Goldstone vertex, which results in a quite severe violation of the WI. Summarizing, the inclusion of the CDW and singlet-pairing channels appears to be essential for renormalizations of the mean-field

result, while they can be neglected at the RPA level.

5.4. Summary

In this chapter, the fRG flow into the SDW phase of the Chubukov model at perfect nesting has been studied. This has been done by numerically integrating the flow equations in Nambu-normal approximation (see Chapter 4.4.3). Although the numerical effort is limited in this approximation, the implementation of the fRG flow used here has been designed in a way that should allow for the parallel usage of a larger number of CPU cores. This way, it may serve as a prototypical code for future tasks. In particular, such tasks include relaxing the approximations of Chapter 4.4.3, i.e. taking Nambu-anomalous interactions, $s^{\pm}$-wave form factors and time-reversal breaking interaction terms into account. The parallelizability is accomplished by parametrizing the momentum dependence of the exchange propagators. In the present case, a Lorentz profile is assumed. This fairly simple parametrization may be extended in the spirit of a gradient expansion in future work.

Despite all the approximations involved, the results obtained in Nambu-normal approximation seem plausible. The flow yields results similar to the RPA in the sense that there are only finite renormalizations compared to RPA. However, the inclusion of the CDW and singlet-pairing channel is found to be crucial. The size of the gap is reduced by the contributions beyond RPA in a similar way as the superconducting gap of the attractive Hubbard model. [49] The frequency dependence of the gap clearly represents a feature beyond the mean-field picture. This dependence has been found to be negligibly weak in this chapter. The feedback of the frequency dependence of the exchange propagators on the zero frequency couplings, in contrast, considerably improves the fulfillment of the WI.

This gives rise to WI violations that are small enough not to spoil the results on a qualitative level. But clearly, in order obtain quantitative predictions for the AF gap, future work should be geared at improving the fulfillment of the WI. This can most clearly be seen from WI violations above the critical scale that are found to have U^2 contributions, which can be regarded as a clear sign of parametrization errors. These errors may be induced by the parametrization of the momentum dependence or by approximations underlying the flow equations in Nambu-normal approximation. In order to find this out, it seems advantageous to first improve the momentum profile of the exchange propagators, before different projection rules are considered and before interaction terms breaking discrete symmetries are included.

In the long run, the method used here should be carried over to the half-filled Hubbard model. Starting from the flow equations of Chapter 4.4.3, approximations in the

parametrization may be relaxed. Interaction terms that break the discrete translational and time-reversal (or equivalently spin-flip) symmetries have been neglected in this chapter and these terms seem to play a minor role, as the WI violation is then still quite weak. Pushing down the violation of the WI to the level of Refs. [49–51] by including such contributions can be expected to require much more computational effort than for singlet superfluids. In return, such an approach can shine light on the interplay between interaction terms that break discrete and continuous symmetries. In this chapter, I have presented a first step in extending fRG flows into an AF phase beyond mean-field and this first step seems promising as a starting point for proceeding towards more quantitative results.

Conclusion and Outlook

Together with other authors' work, I hope to have contributed to the larger goal of pushing fRG methods for fermions in a more quantitative direction. In this thesis, four different aspects of this goal have been discussed.

Form-Factor Expansions In a first channel-decomposed fRG approach to the Hubbard model, [24] the dependence on the weak momenta has been expressed by means of a form-factor expansion truncated behind a few terms. Subsequent work by Jutta Ortloff and others [67] has shown that the neglected remainder terms may play an important role in some regions of parameter space. I have therefore implemented a channel decomposition of the fRG flow equations which does *not* resort to a form-factor expansion (see Chapter 3.3.1). Effects that are potentially neglected by truncating such an expansion have been classified from a group-theoretic perspective in Chapter 1.2.3. The deformation of the $d_{x^2-y^2}$-wave pairing form factors observed in Chapter 3.3 constitutes an example for such an effect.

Point-Group Symmetries in Multiband Models In the form given in Chapter 1.2.3, the classification of instabilities on group-theoretical grounds requires the two-particle coupling function to transform trivially under all point-group operations. For a multiband model expressed in a basis set of non-hybridizing Bloch functions with arbitrarily chosen phases, this is not necessarily the case. In Chapter 2.2, I have shown that, for a large class of multiband models, these phases can however be fixed in such a way that the coupling functions of the interaction show the desired trivial point-group behavior. A Bloch basis with this property is called a *natural* one in this work. In all other bases, the point-group symmetries are represented in a more sophisticated way, which is also discussed in Chapter 2.2.

These findings may be useful not only within a fRG framework, but also in the context of other many-particle methods. Let me note in passing that exploiting the point-group symmetries is generically more straightforward if one chooses to work in the orbital picture and in direct (and not in reciprocal) space, as in the singular-mode fRG approach of Refs. [33, 43, 44].

Multiband Effects In the band language and in a natural basis, multiband Hubbard models show a number of features that are not present in a single-band model. For example, the interaction acquires some momentum dependence through the transformation from orbitals to bands. In the case of the Emery model at weak coupling, this so-called orbital makeup has been found to play a role on a quantitative level in Chapter 3.3.5, while it does not affect the qualitative picture.

Since the low-energy physics of correlated electronic systems can be expected to be governed by quasiparticle excitations close to the Fermi level, an effective action for those degrees of freedom has been used as a starting point for the fRG in the instability analyses of Chapter 3. Bands outside a low-energy window then only appear implicitly through a renormalization of the couplings of this effective action. Although this effective action has been truncated behind the two-particle term in previous studies, it contains three-particle and higher terms, which are induced by virtual excitations outside the low-energy window. In Chapter 2.4, an extension of the conventional one-loop truncation of the fRG flow equations has been given, which takes this three-particle term into account.

Estimating the impact of this term within a g-ology approach to a simple two-band model in Chapter 3.1 suggests that such three-particle interactions may have a strong impact on the phase diagram. This behavior may however be induced by the approximations underlying the g-ology. Namely, the limited number of running couplings leads to an artificial mutual exclusion of competing instabilities, which then can affect large parts of the phase diagram. In contrast, the results for the Emery model presented in Chapter 3.3 suggest a generically minor role of the three-particle term. In a way, this justifies its omission in previous work on multiband models.

fRG Flows into Antiferromagnetic Phases fRG flows into phases of broken symmetry allow for a complete removal of the cutoff for models with non-Fermi-liquid ground states. Complementary to recent work on singlet superconductors, [49,50] a prototypical approach for fRG flows into antiferromagnetically ordered phases has been developed in this thesis. In analogy to the cases of singlet pairing [48, 57] and charge-density wave ordering, [45,46] the exact solution of a reduced mean-field model for antiferromagnetism has been reproduced in Chapter 4.1 within an fRG framework.

For fRG studies of antiferromagnetism, a channel decomposition has been proposed in Chapter 1.4. In Chapter 4.2–4.4, a hierarchy of approximations of the corresponding flow equations has been devised. As a guiding principle, the signatures of the breaking of the continuous spin symmetry are kept at all levels of approximation, whereas *interaction* terms breaking the discrete translational and time-reversal symmetries are neglected. This principle ensures that the mean-field results can be recovered from the fRG flow equations in random-phase approximation. In particular, this still holds if only s-wave

contribution are retained among the remaining interaction terms.

The flow equations in this Nambu-normal approximation (see Chapter 4.4.3) are implemented for a simple two-pocket model originally proposed in Ref. [108]. The gap obtained in this way is found to be reduced compared to the mean-field picture in Chapter 5.3.3. The violation of the SU(2) Ward identity suggests that these results are qualitatively right. On a more quantitative level, however, the dependence of this violation on the interaction strength bears signatures of parametrization errors. This may be due to the momentum parametrization used in this implementation and/or due to the approximations underlying the flow equations, i.e. neglected interaction terms or the projection rule underlying the exchange parametrization of the interaction in Chapter 4.3.1. The origin of these errors may be revealed in future studies by taking an improved parametrization of the exchange propagators into account, by consider other projection rules and/or by going beyond the Nambu-normal approximation.

The resulting numerics may then be very demanding, especially in the latter case. In order to be able to successively relax approximations in the flow equations, the fRG code described in Chapter 5.2 has been designed in a way that should grant good scaling behavior with an increasing number of processor cores. In the current implementation, box diagrams consume a large part of the computational resources. This problem is not limited to fRG flows into phases of broken symmetry, but also occurs in instability analyses.

In a multiband approach, the resulting requirements for computation time can be an issue. The so-called singular mode fRG (SMFRG) saves computational resources by considering vertex-correction and box diagrams in a projection to short bond lengths. So far, this approach has been pursued for instability analyses of two-dimensional multiband models with frequency-independent vertices. [33, 43, 44] However, an adaption to frequency-dependent vertices and to phases of broken symmetries may turn out to be rewarding.

But also in the symmetric phase, the SMFRG may help to improve methods used in this thesis. For the three-band Emery model and the single-band Hubbard model, the estimated gap function for pairing gets deformed with an increasing incommensurability of the antiferromagnetic ordering vector, as laid out in Chapter 3.3. Within a form-factor expansion, such an admixture of higher harmonics can only be taken into account if a larger number of basis functions for the corresponding irreducible representation are included. In the SMFRG, the projection to short bond lengths allows for the inclusion of a relatively large number of form factors at low expense. Especially for the iron pnictides, where the gap functions obtained from fRG show a rich structure, [38, 40] this projection should pay off.

Before I conclude, let me come back again to fRG flows into phases of broken spin-

symmetry. In the case of antiferromagnetism, the integration of the flow equations in the presence of both momentum non-conserving and time-reversal breaking interactions seems to be a formidable task. In the implementation of Chapter 5, these terms have therefore been neglected. In order to gain some intuition for the time-reversal breaking contributions to the interaction, one might more easily consider fRG flows with spin splitting, but without a breaking of the translational symmetry. Due to the absence of a sign problem, quantum Monte Carlo results are available for the Kane-Mele-Hubbard model, [80–82] which therefore would offer itself for such a fRG study. It might also be interesting to study the impact of a spin-orbit term on the pairing on a honeycomb lattice in analogy to Ref. [32].

Also in other cases different fRG approaches could benefit from one another. For example, SMFRG methods might be carried over to models for iron-based superconductors and to flows into antiferromagnetically ordered phases, as already mentioned above. I would like to conclude by expressing the hope that future fRG studies of various kinds may promote a more quantitative understanding of the low-temperature behavior of correlated materials.

Appendix A.

Large parts of this Appendix have previously been published in Ref. [59].

A.1. Three group-theoretic corollaries on exchange parametrizations

In this appendix, I show that the statements made in Chapter 1.2.3 directly follow from the two lemmas named after Schur. (In the literature, as in Ref. [74], Chap. 3-2, the lemma I call Schur's first is often simply referred to as Schur's lemma. The lemma I refer to as Schur's second appears as a nameless lemma right below the first in Ref. [74].)

This Appendix will not be restricted to a specific point-group but an exchange parametrization for some general point group $\mathcal{G}$ is discussed. Therefore, the following statements are not limited to a particular lattice geometry or to the symmetric phase. More precisely, I consider a coupling function $\Phi(l, p, q)$ that depends strongly on l and weakly on p and q. This coupling function should be symmetric under the point group $\mathcal{G}$, i.e. I require $\Phi(R_{\hat{O}}l, R_{\hat{O}}p, R_{\hat{O}}q) = \Phi(l, p, q)\ \forall\, \hat{O} \in \mathcal{G}$, where the $R_{\hat{O}}$ are rotation operators acting on the respective momenta. If the dependence of Φ on the weak frequencies p_0 and q_0 is then dropped, it can then be expanded in form factors f_i that transform according to irreducible representations (IRs) of the point-group $\mathcal{G}$ of Φ. This expansion reads as

$$\Phi(l, p, q) = \sum_{ij} f_i(\mathbf{p} - \mathbf{l}/2)\, f_j(\mathbf{q} \pm \mathbf{l}/2)\, P_{ij}(l)\,,$$

where the sign in the argument of f_j is $-$ in the particle-particle channel(s) and $+$ in the particle-hole channels. Since the dependence on the weak frequencies p_0 and q_0 is suppressed, the form factors can be chosen real.

In a Hubbard-Stratonovich spirit, $P_{ij}(l)$ may be interpreted as the propagator of an exchange boson. The $1 + D$ momentum l then corresponds to the center-of-mass motion of this composite particle, while $p - l/2$ and $q \pm l/2$ are the momenta of the relative motion of its constituents — two electrons or two holes in the particle-particle channel(s)

and one electron and one hole in the particle-hole channels. In this picture, the form factors then play the role of fermion-boson vertices with the indices i and j labeling different bosonic flavors.

If the form-factors are chosen to be orthonormal, i.e. if

$$\int d\mathbf{q}\, f_i(\mathbf{q})\, f_j(\mathbf{q}) = \delta_{ij}\,,$$

the bosonic propagator can be straightforwardly obtained from a given Φ by applying the projection rule

$$P_{ij}(l) = \int d\mathbf{p}\, d\mathbf{q}\; f_i(\mathbf{p} - \frac{\mathbf{l}}{2})\, f_j(\mathbf{q} \pm \frac{\mathbf{l}}{2})\, \Phi\left(l, (l_0/2, \mathbf{p}), (\mp l_0/2, \mathbf{q})\right)\,. \tag{A.1}$$

Let me now continue with the proof of the non-mixing conjecture.

Corollary A.1.1 (No mixing) *Let $P(l)$ be a bosonic propagator that has been projected out of a $\mathcal{G}$-symmetric coupling function Φ according to Eq. (A.1). Suppose that, for fixed l, $P(R_{\hat{O}}l) = P(l)\ \forall\, \hat{O} \in \mathcal{K}$, where $\mathcal{K}$ is a subgroup of $\mathcal{G}$. If the basis set of form factors is then organized in blocks corresponding to IRs of $\mathcal{K}$, blocks that mix form factors of inequivalent IRs of $\mathcal{K}$ must vanish.*

Proof Consider the projection rule (A.1) for $P_{ij}(R_{\hat{O}}l)$ and matrices $M^{\alpha}_{\hat{O}}$ of the αth IR of $\mathcal{K}$ which transform the form factors according to

$$f_i(R_{\hat{O}}\mathbf{k}) = \sum_{i'} \left(M^{\alpha}_{\hat{O}}\right)_{ii'} f_{i'}(\mathbf{k})\,.$$

Furthermore, the IR of $\mathcal{K}$ that transforms f_i is labeled with α and the one transforming f_j with β. After substituting the integration variables $\mathbf{p}$ and $\mathbf{q}$ by $R_{\hat{O}}\mathbf{p}$ and $R_{\hat{O}}\mathbf{q}$, respectively, the point-group symmetry of Φ is exploited. For the block $P^{\alpha\beta}(l)$ relating the αth and βth IR, one then finds

$$P^{\alpha\beta}(R_{\hat{O}}l) = \left(M^{\alpha}_{\hat{O}}\right)^{\dagger} P^{\alpha\beta}(l)\, M^{\beta}_{\hat{O}}\,. \tag{A.2}$$

Since the left-hand side equals $P^{\alpha\beta}(l)$ according to the premise, Schur's second lemma applies. Therefore, if the αth and βth IR of $\mathcal{K}$ cannot be related by an equivalence transformation, the block $P^{\alpha\beta}$ must vanish. ∎

In Chapter 1.2.3, Corollary A.1.1 has been used for $\mathcal{K} = \mathcal{L}_{\mathbf{l}}$, where $\mathcal{L}_{\mathbf{l}}$ denotes the little group of the bosonic momentum $\mathbf{l}$. If the premise $P(R_{\hat{O}}l) = P(l)\ \forall\, \hat{O} \in \mathcal{K}$ were satisfied as a consequence of some approximation, this approximation would neglect the mixing of inequivalent IRs of $\mathcal{K}$.

For the next two corollaries, the following definition appears useful.

Definition I call a set of form factors *well behaved* under a point-group $\mathcal{K}$ if its elements transform according to either identical or inequivalent IRs of $\mathcal{K}$ consisting of unitary matrices.

The point-group behavior of the bosonic propagator is governed by the following law.

Corollary A.1.2 *Consider again a bosonic propagator $P(l)$ that has been projected out of a $\mathcal{G}$-symmetric coupling function Φ with form factors which are well behaved under $\mathcal{G}$. Blocks $P^{\alpha\beta}$ relating equivalent* one-dimensional *IRs α and β of $\mathcal{G}$ then are fully $\mathcal{G}$-symmetric, i.e. $P^{\alpha\beta}(R_{\hat{O}}l) = P^{\alpha\beta}(l)\ \forall\, \hat{O} \in \mathcal{G}$ for arbitrary l.*

Proof One can observe that, also in the present case, Eq. (A.2) holds, with α and β now labeling IRs of the *full* point group $\mathcal{G}$. This equation is trivially fulfilled if a block vanishes according to Corollary A.1.1. For non-vanishing blocks, well-behaved form factors give rise to $M^{\alpha}_{\hat{O}} = M^{\beta}_{\hat{O}}$. If α and β then label one-dimensional IRs of $\mathcal{G}$, these matrices are just complex numbers, which cancel. ∎

If the mixing of inequivalent IRs of $\mathcal{G}$ is neglected, the remaining one-dimensional irreducible blocks of $P(l)$ are hence $\mathcal{G}$-symmetric.

Finally, Schur's first lemma directly gives rise to the following corollary.

Corollary A.1.3 *Suppose that, for fixed l, $P(R_{\hat{O}}l) = P(l)\ \forall\, \hat{O} \in \mathcal{K}$, where $P(l)$ is a bosonic propagator obtained from a $\mathcal{G}$-symmetric coupling function and where $\mathcal{K}$ is a subgroup of $\mathcal{G}$. For a well-behaved set of form factors under $\mathcal{K}$, the non-vanishing irreducible blocks $P^{\alpha\beta}(l)$ of $P(l)$ then are a multiple of a unit matrix, with α and β labeling IRs of $\mathcal{K}$.*

Proof Again, Eq. (A.2) holds. For well-behaved form factors, the representation matrices $M^{\alpha}_{\hat{O}}$ and $M^{\beta}_{\hat{O}}$ with $\hat{O} \in \mathcal{K}$ are equal to one another, if $P^{\alpha\beta}$ does not vanish according to Corollary A.1.1. Since $P(R_{\hat{O}}l) = P(l)\ \forall \hat{O} \in \mathcal{K}$, Eq. (A.2) simply states that $M^{\alpha}_{\hat{O}}$ and $P^{\alpha\beta}$ commute $\forall \hat{O} \in \mathcal{K}$. According to Schur's first lemma, $P^{\alpha\beta}$ then must be a multiple of a unit matrix. ∎

Appendix B.

Point group symmetries and natural Bloch bases – Prototypical models

Large parts of this Appendix have previously been published in Ref. [83].

In this Appendix, the findings of Chapter 2.2 are illustrated for two models for which the transformation from the orbital to the band picture is analytically accessible. A particular focus will be on the discussion of discontinuities in this transformation. While the first example is a simplified version of the Emery model in Chapter 3.2.1, the second example, an extended Hubbard model on the honeycomb lattice, can be regarded as a generic $2D$ system with a sixfold symmetry.

B.1. Fourfold symmetry: Emery model without oxygen-oxygen hopping

B.1.1. Model Hamiltonian

As a first example, let us consider the Emery model devised for the description of the Copper-oxide planes of the high-T_c cuprates. [53] This model includes the Cu $3d$-orbitals at the center of the Wigner-Seitz cell as well as the oxygen $2p$-orbitals at the boundaries of the unit cell with fields d and p_x or p_y, respectively (cf. Fig. B.1). In order to keep the have an analytically accessible orbital-to-band transformation, the discussion here is restricted to the (probably unrealistic [5, 7, 8, 54]) case of vanishing oxygen-oxygen hopping.

For simplicity, let me first consider the quadratic part H_0 of the Emery Hamiltonian H_0+H_{int} and start from a real space formulation, i.e. form a basis of hybridizing Wannier

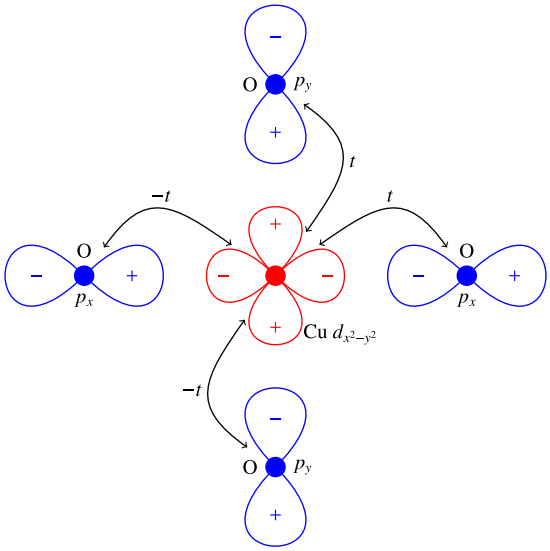

Figure B.1.: Orbitals of the Emery model depicted for one unit cell of the direct lattice. Note that the signs of the electronic orbitals violate the point-group (C_{4v}) symmetry of the underlying lattice. The $+$ and $-$ signs in this Figure correspond to the sign of the orbital wave functions at the respective positions. The black arrows correspond to the hopping terms in the Hamiltonian in Eq. (B.1).

states. For the labeling of the atoms, the following convention is chosen. While a particular Copper atom is located at the center $\mathbf{R}$ of some direct unit cell, the neighboring oxygen atoms in positive x and y direction also belong to the unit cell with center $\mathbf{R}$. The nearest oxygen atoms in negative x and y direction, in contrast, belong to neighboring cells. The one-particle Hamiltonian then reads as

$$\begin{aligned} H_0 = \epsilon \sum_{\mathbf{R},\sigma,\nu} p^\dagger_{\nu,\sigma}(\mathbf{R})\, p_{\nu,\sigma}(\mathbf{R}) + t \sum_{\mathbf{R},\sigma,\nu} \left[d^\dagger_\sigma(\mathbf{R})\, p_{\nu,\sigma}(\mathbf{R}) + p^\dagger_{\nu,\sigma}(\mathbf{R})\, d_\sigma(\mathbf{R}) \right] \\ - t \sum_{\mathbf{R},\sigma,\nu} \left[d^\dagger_\sigma(\mathbf{R})\, p_{\nu,\sigma}(\mathbf{R} - \hat{\boldsymbol{\nu}}) + p^\dagger_{\nu,\sigma}(\mathbf{R} - \hat{\boldsymbol{\nu}})\, d_\sigma(\mathbf{R}) \right] , \end{aligned} \tag{B.1}$$

where $\hat{\boldsymbol{\nu}}$ represents the primitive lattice vector pointing in positive ν-direction, i.e. either in x- or y-direction. In Eq. (B.1), ϵ denotes the energy separation of the copper d- and oxygen p-orbitals and t corresponds to the absolute value of the transfer integrals between neighboring copper and oxygen atoms. Note that the hopping t corresponds to $t_{pd}/2$ in Eq. (3.11), where also hopping between the oxygen atoms is taken into account. The length of these primitive lattice vectors is just the distance between neighboring Copper atoms, which I henceforth set to unity. If one now switches to a Bloch representation

with wavevectors $\mathbf{k}$ in the first Brillouin zone $\mathbb{T} = [-\pi, \pi) \times [-\pi, \pi)$ according to

$$d_\sigma(\mathbf{R}) = \int_{\mathbb{T}} d\mathbf{k}\, e^{i\mathbf{k}\cdot\mathbf{R}}\, \tilde{d}_\sigma(\mathbf{k})$$
$$p_{\nu,\sigma}(\mathbf{R}) = \int_{\mathbb{T}} d\mathbf{k}\, e^{i\mathbf{k}\cdot\mathbf{R}}\, \tilde{p}_{\nu,\sigma}(\mathbf{k})\,,$$

one obtains

$$H_0 = \epsilon \sum_{\sigma,\nu} \int_{\mathbb{T}} d\mathbf{k}\; \tilde{p}^\dagger_{\nu,\sigma}(\mathbf{k})\, \tilde{p}_{\nu,\sigma}(\mathbf{k}) + t \sum_{\sigma,\nu} \int_{\mathbb{T}} d\mathbf{k} \left[\tilde{d}^\dagger_\sigma(\mathbf{k})\, \tilde{p}_{\nu,\sigma}(\mathbf{k}) + \tilde{p}^\dagger_{\nu,\sigma}(\mathbf{k})\, \tilde{d}_\sigma(\mathbf{k}) \right]$$
$$- t \sum_{\sigma,\nu} \int_{\mathbb{T}} d\mathbf{k} \left[e^{-i\mathbf{k}\cdot\hat{\boldsymbol{\nu}}}\, \tilde{d}^\dagger_\sigma(\mathbf{k})\, \tilde{p}_{\nu,\sigma}(\mathbf{k}) + e^{+i\mathbf{k}\cdot\hat{\boldsymbol{\nu}}}\, \tilde{p}^\dagger_{\nu,\sigma}(\mathbf{k})\, \tilde{d}_\sigma(\mathbf{k}) \right] . \tag{B.2}$$

This expression is now cast into the form

$$H_0 = \sum_\sigma \int_{\mathbb{T}} d\mathbf{k}\, \tilde{\Psi}^\dagger_\sigma(\mathbf{k})\, \tilde{\mathcal{H}}_0(\mathbf{k})\, \tilde{\Psi}_\sigma(\mathbf{k})$$

with orbitors

$$\tilde{\Psi}_\sigma(\mathbf{k}) = \begin{pmatrix} \tilde{d}_\sigma(\mathbf{k}) \\ \tilde{p}_{x,\sigma}(\mathbf{k}) \\ \tilde{p}_{y,\sigma}(\mathbf{k}) \end{pmatrix} .$$

The one-particle coupling function $\tilde{\mathcal{H}}_0(\mathbf{k})$ then clearly is 2π periodic in both directions and hence no discontinuities occur at the boundary of the BZ. Moreover, $\tilde{\mathcal{H}}_0(\mathbf{k})$ has complex entries and hence is hermitian, but not symmetric.

For numerical calculations, it may, however, be convenient to have only real valued coupling functions. This can be accomplished by a regauging of the fields: If Eq. (B.2) is expressed in terms of new orbitors

$$\Psi_\sigma(\mathbf{k}) = \begin{pmatrix} \tilde{d}_\sigma(\mathbf{k}) \\ e^{-i(\mathbf{k}\cdot\hat{\mathbf{x}}-\pi)/2}\, \tilde{p}_{x,\sigma}(\mathbf{k}) \\ e^{-i(\mathbf{k}\cdot\hat{\mathbf{y}}-\pi)/2}\, \tilde{p}_{y,\sigma}(\mathbf{k}) \end{pmatrix} ,$$

one obtains the one-particle coupling function $\mathcal{H}_0(\mathbf{k})$, which is given by

$$\mathcal{H}_0(\mathbf{k}) = \begin{pmatrix} 0 & 2t\, \sin(k_x/2) & 2t\, \sin(k_y/2) \\ 2t\, \sin(k_x/2) & \epsilon & 0 \\ 2t\, \sin(k_y/2) & 0 & \epsilon \end{pmatrix} , \tag{B.3}$$

which is real valued. This comes at the price of loosing the continuity of the one-particle coupling function at the boundary of the BZ. A basis of hybridizing Bloch states with a continuous one-particle coupling function will henceforth be called a *proper* one. Note that the improper basis of Eq. (B.3) is related to the proper one by a unitary

transformation that is discontinuous in $\mathbf{k}$. Since the Hamiltonian is local in momentum space, this basis transformation corresponds to a unitary transformation of the one-particle coupling function $\mathcal{H}_0(\mathbf{k})$.

In real space, the interacting part of the Hamiltonian reads

$$\begin{aligned} H_{\text{int}} = U_d \sum_{\mathbf{R}} :\, n_{d,\uparrow}(\mathbf{R})\, n_{d,\downarrow}(\mathbf{R}) \,: + U_p \sum_{\mathbf{R},\nu} :\, n_{p,\nu,\uparrow}(\mathbf{R})\, n_{p,\nu,\downarrow}(\mathbf{R}) \,: \\ + U_{pd} \sum_{\mathbf{R},\nu} :\, n_d(\mathbf{R})\, n_{p,\nu}(\mathbf{R}) + n_d(\mathbf{R})\, n_{p,\nu}(\mathbf{R} - \hat{\boldsymbol{\nu}}) \,: \,. \end{aligned} \tag{B.4}$$

In this equation, $: O :$ denotes the normal ordering of an operator product O. Only density-density terms are considered here, but additional Hund's rule terms would not spoil the reasoning in the following. Eq. (B.4) is now transformed to reciprocal space. If one chooses to work in the same basis as in Eq. (B.3), one obtains

$$\begin{aligned} H_{\text{int}} = {} & \frac{U_d}{2} \sum_{\sigma,\tau} \int_{\mathbb{T}} d\mathbf{k}_1 \ldots d\mathbf{k}_4 \;\, \delta_{\{\mathbf{k}\}} \;\, d^\dagger_\sigma(\mathbf{k}_1)\, d^\dagger_\tau(\mathbf{k}_2)\, d_\tau(\mathbf{k}_3)\, d_\sigma(\mathbf{k}_4) \\ & + \frac{U_p}{2} \sum_{\sigma,\tau,\nu} \int_{\mathbb{T}} d\mathbf{k}_1 \ldots d\mathbf{k}_4 \;\, \delta_{\{\mathbf{k}\}} \, (-1)^{(\mathbf{k}_1+\mathbf{k}_2-\mathbf{k}_3-\mathbf{k}_4)\cdot\hat{\boldsymbol{\nu}}/(2\pi)} \;\, p^\dagger_{\nu,\sigma}(\mathbf{k}_1)\, p^\dagger_{\nu,\tau}(\mathbf{k}_2)\, p_{\nu,\tau}(\mathbf{k}_3)\, p_{\nu,\sigma}(\mathbf{k}_4) \\ & + 2U_{pd} \sum_{\sigma,\tau,\nu} \int_{\mathbb{T}} d\mathbf{k}_1 \ldots d\mathbf{k}_4 \;\, \delta_{\{\mathbf{k}\}} \;\, \cos\left[\frac{(\mathbf{k}_4 - \mathbf{k}_1)\cdot\hat{\boldsymbol{\nu}}}{2}\right] \;\, p^\dagger_{\nu,\sigma}(\mathbf{k}_1)\, d^\dagger_\tau(\mathbf{k}_2)\, d_\tau(\mathbf{k}_3)\, p_{\nu,\sigma}(\mathbf{k}_4) \end{aligned} \tag{B.5}$$

$$= \sum_{\alpha_1,\ldots,\alpha_4} \sum_{\sigma_1,\ldots,\sigma_4} \Psi^{\dagger\alpha_1}_{\sigma_1}(\mathbf{k}_1)\, \Psi^{\dagger\alpha_2}_{\sigma_2}(\mathbf{k}_2)\, \Psi^{\alpha_3}_{\sigma_3}(\mathbf{k}_3)\, \Psi^{\alpha_4}_{\sigma_4}(\mathbf{k}_4)\, \mathcal{V}^{\alpha_1,\ldots,\alpha_4}_{\sigma_1,\ldots\sigma_4}(\mathbf{k}_1,\mathbf{k}_2,\mathbf{k}_3,\mathbf{k}_4) \tag{B.6}$$

where

$$\delta_{\{\mathbf{k}\}} = \begin{cases} 1 & \text{for} \quad (\mathbf{k}_1 + \mathbf{k}_2 - \mathbf{k}_3 - \mathbf{k}_4) = 2\pi\mathbf{n}\,, \quad \mathbf{n} \in \mathbb{Z}^2 \\ 0 & \text{otherwise} \end{cases}$$

ensures momentum conservation. For an umklapp processes, i.e. for $\mathbf{n} \neq 0$, the sign structure of the U_p term is nontrivial due to the improper Bloch basis chosen. The integrals in Eq. (B.5) restrict all four momenta to the first BZ. If $\mathbf{k}_1 + \mathbf{k}_2 - \mathbf{k}_3$ is related to $\mathbf{k}_4$ by a non-vanishing reciprocal vector, this term may acquire a minus sign depending on whether n_ν is even or odd. Working in an improper Bloch basis requires therefore some care, since ignoring these phases could be pernicious.

Before switching to the band language, let us again look at the quadratic part of the Hamiltonian. From Eq. (B.3), one can observe that $\mathcal{H}_0(\mathbf{k})$ does not transform trivially under operations in the point-group of the underlying square lattice. More precisely, one has $\mathcal{H}_0(R_{\hat{O}}\mathbf{k}) \neq \mathcal{H}_0(\mathbf{k})$ for a general point-group operation $\hat{O} \in C_{4v}$ with a corresponding rotation matrix $R_{\hat{O}}$ for the momentum quantum number. Apparently, if the electronic orbitals transform nontrivially under point-group operations, this gives rise to a tight-binding model with vertex functions that also lack such a trivial behavior. In the present

case, the phase of the electronic one-particle wavefunctions transform nontrivially under the point group, as visible in Fig. B.1. This sign structure is inherited by the hopping integrals between these orbitals. For example, hopping from a Copper atom to the lower oxygen atom is inequivalent to hopping to the upper one. Note that one should avoid speaking of a spontaneously broken symmetry in this case. Physical symmetry breaking would be associated with the whole electronic groundstate and observables derived from it. In the present case, however, the occupation of the two p-orbitals is equal unless additional terms are included or their degeneracy is broken explicitly, hence the groundstate and responses do not break the point group symmetry. Therefore, as will be pointed out in the following, the C_{4v} symmetry is still manifest in the tight-binding Hamiltonian and therefore all observables respect this symmetry, while the phase of the electronic wave function is only an auxiliary quantity.

In this place, the following questions seem appropriate:

i) In what way is the point-group symmetry of the lattice manifest in the Emery model, and,

ii) is there an alternative, explicitly C_{4v}-symmetric formulation of the Emery model with vertex functions that behave trivially under the point-group operations?

These questions will be addressed in the following two subsections.

B.1.2. C_{4v} symmetry

In the (improper) Bloch basis of Eq. (B.3), in addition to a real-valued coupling function $\mathcal{H}_0(\mathbf{k})$, the Hamiltonian shows a nice behavior under point-group operations $\hat{O} \in C_{4v}$. These operations can always be written as a product of the mirror operations $\hat{I}$ and $\hat{I}'$ with respect to the y axis and a BZ diagonal, respectively. More precisely, I define $\hat{I}'$ as the permutation operation on the coordinates $R_{\hat{I}'}\mathbf{k} = (k_y, k_x)^{\mathrm{T}}$. In Fig. B.2(a), one can easily see that the other symmetry elements of C_{4v} can be generated by successive application of $\hat{I}$ and $\hat{I}'$. Under the reflection $\hat{I}$ of the x coordinate, the one-particle coupling function transforms as

$$\mathcal{H}_0(R_{\hat{I}}\mathbf{k}) = M_{\hat{I}}\,\mathcal{H}_0(\mathbf{k})\,M_{\hat{I}}^{\dagger}\,, \quad M_{\hat{I}} = \begin{pmatrix} 1 & 0 & 0 \\ 0 & -1 & 0 \\ 0 & 0 & 1 \end{pmatrix}\,, \tag{B.7}$$

i.e. the sign of the hybridization matrix element between the d- and p_x-orbitals gets flipped. This is due to the nontrivial C_{4v}-behavior of specific orbitals.

Under coordinate exchange $\hat{I}'$, $\mathcal{H}_0(\mathbf{k})$ also shows a simple behavior. The p_x- and p_y-

orbitals then change their roles and one has

$$\mathcal{H}_0(R_{\hat{I}'}\mathbf{k}) = M_{\hat{I}'}\,\mathcal{H}_0(\mathbf{k})\,M_{\hat{I}'}^{\dagger}\,, \quad M_{\hat{I}'} = \begin{pmatrix} 1 & 0 & 0 \\ 0 & 0 & 1 \\ 0 & 1 & 0 \end{pmatrix}. \tag{B.8}$$

Note that this property does not arise from a non-trivial point-group behavior of the electronic structure, but from the presence of two atoms of the same kind in different locations in the unit cell. Since, in the present example, $\hat{I}'$ maps these two atoms onto one another, one should not expect $\mathcal{H}_0(\mathbf{k})$ to transform trivially under $\hat{I}'$. So altogether, one finds that the point-group symmetry of the lattice manifests itself in Eqs. (B.7) and (B.8). In other words, the one-particle Hamiltonian H_0 is invariant under the transformations

$$\Psi_\sigma(\mathbf{k}) \to \Psi'_\sigma(R_{\hat{I}}\mathbf{k}) = M_{\hat{I}}\Psi_\sigma(\mathbf{k})\,, \quad \mathcal{H}_0(\mathbf{k}) \to \mathcal{H}_0(R_{\hat{I}}\mathbf{k}) \tag{B.9}$$

and

$$\Psi_\sigma(\mathbf{k}) \to \Psi'_\sigma(R_{\hat{I}'}\mathbf{k}) = M_{\hat{I}'}\Psi_\sigma(\mathbf{k})\,, \quad \mathcal{H}_0(\mathbf{k}) \to \mathcal{H}_0(R_{\hat{I}'}\mathbf{k}) \tag{B.10}$$

in the improper Bloch basis of Eq. (B.3).

As will become clear in Chapter 2.2.2, the matrices $M_{\hat{I}}$ and $M_{\hat{I}'}$ directly stem from the Bloch orbitals in the corresponding basis according to

$$\left(M_{\hat{O}}\right)_{\alpha,\beta} = \int d\mathbf{r}\ \langle R_{\hat{O}}\mathbf{r}\,|\phi^\alpha_\sigma(R_{\hat{O}}\mathbf{k})\rangle\,\big\langle\,\phi^\beta_\sigma(\mathbf{k})\big|\,\mathbf{r}\big\rangle$$

for arbitrary spin orientation σ and $\hat{O} \in C_{4v}$. The rotated position $R_{\hat{O}}\mathbf{r}$ in the first scalar product probes the symmetry of the electronic wavefunctions, giving rise to the precise form of $M_{\hat{I}}$. In addition, it accounts for the action of $\hat{O}$ on the nuclear positions, since some of the corresponding Wannier states $|\psi^\alpha_\sigma(\mathbf{R})\rangle$ may belong to atoms away form the center $\mathbf{R}$ of the respective unit cell according to the conventions introduced in Chapter 2.1.1. In the present example, this leads to the representation matrix $M_{\hat{I}'}$. Moreover, the wavevector $\mathbf{k}$ is rotated to $R_{\hat{O}}\mathbf{k}$ in the first scalar product, which corresponds to a rotation of the direct unit cells, $\mathbf{k}$ being the reciprocal space variable corresponding to their centers $\mathbf{R}$.

These representation matrices are hence not fully determined by the point-group behavior of the electronic orbitals, but also the point-group behavior of the nuclear positions matters. In this context, I would like to recall that the electronic orbitals correspond to basis functions of the irreducible representations of D_{4h}, since they are truly three-dimensional. As a lattice model of a CuO plane, the Emery model is however only two-dimensional and therefore the point group is reduced to C_{4v}. For the Emery model, the representation matrices $M_{\hat{I}}$ and $M_{\hat{I}'}$ (and consequently of all other operations $\hat{O} \in C_{4v}$) decay into irreducible blocks – for the Cu orbitals transforming with the irreducible representation A_1 and for the O p-orbitals transforming with E. The reader should be

aware that this is due to the lattice structure. For the example of graphene in the following section, reducible representation matrices will emerge from irreducible electronic orbitals centered around inequivalent lattice positions.

Let me now return to the transformation behavior of the Emery Hamiltonian. The one-particle Hamiltonian density

$$\Psi_\sigma^\dagger(\mathbf{k})\,\mathcal{H}_0(\mathbf{k})\,\Psi_\sigma(\mathbf{k}) \tag{B.11}$$

transforms to

$$\Psi'^\dagger_\sigma(R_{\hat{O}}\mathbf{k})\,\mathcal{H}_0(R_{\hat{O}}\mathbf{k})\,\Psi'_\sigma(R_{\hat{O}}\mathbf{k}) = \Psi_\sigma^\dagger(\mathbf{k})\,M_{\hat{O}}^\dagger\,\mathcal{H}_0(R_{\hat{O}}\mathbf{k})\,M_{\hat{O}}\,\Psi_\sigma(\mathbf{k})\,,\quad \hat{O}=\hat{I},\hat{I}'\,. \tag{B.12}$$

The invariance of the one-particle Hamiltonian density then follows from

$$\mathcal{H}_0(R_{\hat{O}}\mathbf{k}) = M_{\hat{O}}\,\mathcal{H}_0(\mathbf{k})\,M_{\hat{O}}^\dagger\,,\quad \hat{O}=\hat{I},\hat{I}'\,,$$

i.e., it looks the same in the original and in the transformed frame.

Let us check this invariance claim also for the interacting part H_{int} in Eq. (B.5) of the Hamiltonian. As one may easily verify, it is invariant under the transformations in Eqs. (B.9) and (B.10) and therefore the full, interacting Emery Hamiltonian has a manifest C_{4v} symmetry. More formally, this means

$$\begin{aligned}
&\mathcal{V}^{\alpha_1,\ldots,\alpha_{2n}}_{a_1,\ldots,a_{2n}}(\mathbf{k}_1,\ldots,\mathbf{k}_n;\mathbf{k}_{n+1},\ldots,\mathbf{k}_{2n})\;\Psi^{\alpha_1\,\dagger}_{a_1}(\mathbf{k}_1)\ldots\Psi^{\alpha_n\,\dagger}_{a_n}(\mathbf{k}_n)\;\Psi^{\alpha_{n+1}}_{a_{n+1}}(\mathbf{k}_{n+1})\ldots\Psi^{\alpha_{2n}}_{a_{2n}}(\mathbf{k}_{2n})\\
\to\quad &\mathcal{V}^{\alpha_1,\ldots,\alpha_{2n}}_{a_1,\ldots,a_{2n}}(R_{\hat{O}}\mathbf{k}_1,\ldots,R_{\hat{O}}\mathbf{k}_{2n})\;\Psi'^{\alpha_1\,\dagger}_{a_1}(R_{\hat{O}}\mathbf{k}_1)\ldots\Psi'^{\alpha_n\,\dagger}_{a_n}(R_{\hat{O}}\mathbf{k}_n)\\
&\quad\times\Psi'^{\alpha_{n+1}}_{a_{n+1}}(R_{\hat{O}}\mathbf{k}_{n+1})\ldots\Psi'^{\alpha_{2n}}_{a_{2n}}(R_{\hat{O}}\mathbf{k}_{2n})\,,
\end{aligned}$$

where

$$\mathcal{V}^{\alpha_1\ldots\alpha_4}_{\boldsymbol{\sigma}}(R_{\hat{O}}\mathbf{k}_1,\ldots,R_{\hat{O}}\mathbf{k}_4) = M_{\hat{O}\alpha_1,\beta_1}M_{\hat{O}\alpha_2,\beta_2}\mathcal{V}^{\beta_1\ldots\beta_4}_{\boldsymbol{\sigma}}(\mathbf{k}_1,\ldots,\mathbf{k}_4)\,M^\dagger_{\hat{O}\alpha_3,\beta_3}M^\dagger_{\hat{O}\alpha_4,\beta_4}$$

for $\hat{O}\in C_{4v}$, i.e. the interaction term in the Hamiltonian looks the same in the new reference frame. In the following subsection, it will be shown that this somewhat hidden symmetry translates to a more explicit one in the band language for a suitably chosen band gauge.

B.1.3. Band language and natural Bloch basis

Let us now switch to new fields $\boldsymbol{\chi}_\sigma(\mathbf{k}) = u(\mathbf{k})\,\Psi_\sigma(\mathbf{k})$ with wavevector-dependent, unitary $u(\mathbf{k})$ in which the one-particle Hamiltonian

$$H_0 = \sum_\sigma\int_{\mathbb{T}} d\mathbf{k}\,\Psi^\dagger_\sigma(\mathbf{k})\,\mathcal{H}_0(\mathbf{k})\,\Psi_\sigma(\mathbf{k}) = \sum_\sigma\int_{\mathbb{T}} d\mathbf{k}\,\boldsymbol{\chi}^\dagger_\sigma(\mathbf{k})\,\mathcal{B}_0(\mathbf{k})\,\boldsymbol{\chi}_\sigma(\mathbf{k})$$

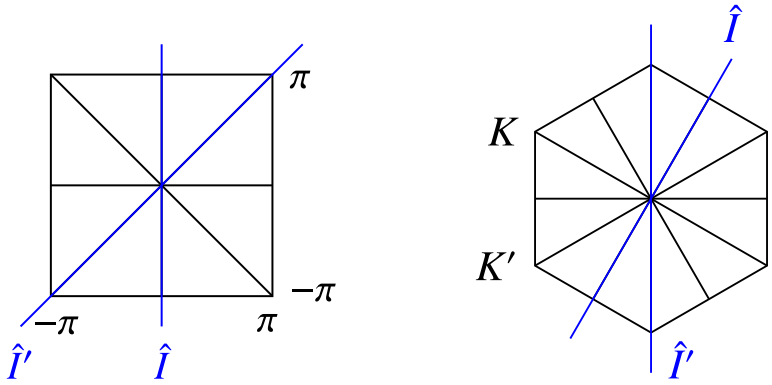

(a) C_{4v} (b) C_{6v}

Figure B.2.: (a) Symmetry elements of C_{4v} in the first BZ $\mathbb{T}$ of the Emery model. (b) First BZ $\mathbb{H}$ for the honeycomb lattice with lines corresponding to mirror axes. All C_{4v} and C_{6v} operations can be interpreted as products of two mirror operations $\hat{I}$ and $\hat{I}'$ with respect to the blue axes.

is diagonal. The diagonalized coupling function

$$\mathcal{B}(\mathbf{k}) = u(\mathbf{k})\,\mathcal{H}_0(\mathbf{k})\,u^\dagger(\mathbf{k}) = \begin{pmatrix} \frac{\epsilon}{2}[1-r(\mathbf{k})] & 0 & 0 \\ 0 & \epsilon & 0 \\ 0 & 0 & \frac{\epsilon}{2}[1+r(\mathbf{k})] \end{pmatrix}$$

then contains the band dispersion with the short-hand notation

$$r(\mathbf{k}) = \sqrt{1 + 16\left(\frac{t}{\epsilon}\right)^2 \left[\sin^2(k_x/2) + \sin^2(k_y/2)\right]}\,.$$

The bands have been labeled according to the energies in ascending order. In this order, they correspond to the antibonding, nonbonding and bonding solutions of the quadratic part of the Hamiltonian. One possible choice for the transformation matrices $u(\mathbf{k})$ then reads as

$$u(\mathbf{k}) = \begin{pmatrix} \frac{\epsilon}{4t}N_1(\mathbf{k})[1+r(\mathbf{k})] & -\sin(k_x/2)\,N_1(\mathbf{k}) & -\sin(k_y/2)\,N_1(\mathbf{k}) \\ 0 & -\sin(k_y/2)\,N_2(\mathbf{k}) & \sin(k_x/2)\,N_2(\mathbf{k}) \\ \frac{\epsilon}{4t}N_3(\mathbf{k})[1-r(\mathbf{k})] & -\sin(k_x/2)\,N_3(\mathbf{k}) & -\sin(k_y/2)\,N_3(\mathbf{k}) \end{pmatrix} \tag{B.13}$$

with normalization factors

$$\begin{aligned} N_1(\mathbf{k}) &= \left\{\frac{\epsilon}{4t}\left[1+r(\mathbf{k})\right]^2 + \sin^2(k_x/2) + \sin^2(k_y/2)\right\}^{-1/2} \\ N_2(\mathbf{k}) &= \left[\sin^2(k_x/2) + \sin^2(k_y/2)\right]^{-1/2} \\ N_3(\mathbf{k}) &= \left\{\frac{\epsilon}{4t}\left[1-r(\mathbf{k})\right]^2 + \sin^2(k_x/2) + \sin^2(k_y/2)\right\}^{-1/2}\,. \end{aligned}$$

Note that this transformation matrix inherits discontinuities at the boundary of the BZ, since we have started from an improper basis of the non-hybridizing Bloch states. Moreover, the bands with labels 2 and 3 are degenerate at $\mathbf{k} = 0$ and so there is some freedom in choosing $u(0)$. One possibility results from the limit

$$\lim_{k_y \to 0} u(0, k_y) = \begin{pmatrix} 1 & 0 & 0 \\ 0 & -1 & 0 \\ 0 & 0 & -1 \end{pmatrix}$$

while another one is obtained by approaching the origin on the y axis, i.e.

$$\lim_{k_x \to 0} u(k_x, 0) = \begin{pmatrix} 1 & 0 & 0 \\ 0 & 0 & 1 \\ 0 & 1 & 0 \end{pmatrix} .$$

Therefore, there must a discontinuity at the origin. In contrast to the discontinuities at the BZ boundary, it is not lifted in the proper Bloch basis. Moreover, one can observe that the lowest band only has d-wave character at the origin, while the other two ones are degenerate and consist purely of the p-orbitals.

In a next step, let us look at the interaction in the band language. It reads as

$$H_{\text{int}} = \sum_{\sigma_1 \ldots \sigma_4} \sum_{\alpha_1 \ldots \alpha_4} \int_{\mathbb{T}} d\mathbf{k}_1 \ldots d\mathbf{k}_4 \; \delta_{\{\mathbf{k}\}} \, \delta_{\sigma_1,\sigma_2} \, \delta_{\sigma_3,\sigma_4} \, f^{\boldsymbol{\alpha}}(\mathbf{k}_1, \mathbf{k}_2, \mathbf{k}_3, \mathbf{k}_4) \, \chi^\dagger(\xi_1) \, \chi^\dagger(\xi_2) \, \chi(\xi_3) \, \chi(\xi_4) \, ,$$

with the coupling function

$$\begin{aligned} f^{\boldsymbol{\alpha}}(\mathbf{k}_1, \mathbf{k}_2, \mathbf{k}_3, \mathbf{k}_4) = {} & \frac{U_d}{2} \, u_{\alpha_1,1}(\mathbf{k}_1) \, u_{\alpha_2,1}(\mathbf{k}_2) \, u^*_{\alpha_3,1}(\mathbf{k}_3) \, u^*_{\alpha_4,1}(\mathbf{k}_4) \\ & + \sum_\nu \frac{U_p}{2} \, (-1)^{(\mathbf{k}_1 + \mathbf{k}_2 - \mathbf{k}_3 - \mathbf{k}_4) \cdot \hat{\boldsymbol{\nu}}/(2\pi)} \; u_{\alpha_1,\nu}(\mathbf{k}_1) \, u_{\alpha_2,\nu}(\mathbf{k}_2) \, u^*_{\alpha_3,\nu}(\mathbf{k}_3) \, u^*_{\alpha_4,\nu}(\mathbf{k}_4) \\ & + \sum_\nu 2U_{pd} \, \cos\left[\frac{(\mathbf{k}_4 - \mathbf{k}_1) \cdot \hat{\boldsymbol{\nu}}}{2} \right] \; u_{\alpha_1,\nu}(\mathbf{k}_1) \, u_{\alpha_2,1}(\mathbf{k}_2) \, u^*_{\alpha_3,1}(\mathbf{k}_3) \, u^*_{\alpha_4,\nu}(\mathbf{k}_4) \, , \end{aligned} \tag{B.14}$$

where $\xi_i = (\alpha_i, \sigma_i, \mathbf{k}_i)$ includes the band index α_i as well as spin and momentum quantum numbers. Even the U_d term, which has a trivial momentum-dependence in the orbital language, now acquires some orbital makeup through the transformation $u(\mathbf{k})$.

Let us now discuss the point-group behavior in the band language. One can observe that the band dispersion behaves trivially under point-group operations, i.e., that $\mathcal{B}(R_{\hat{O}}\mathbf{k}) = \mathcal{B}(\mathbf{k})$. The question now is whether this also holds for the vertex function of the two-particle interaction. The transformation matrix elements $u(\mathbf{k})$ in Eq. (B.14) transform trivially for the d-orbital irrespective of the band index α, i.e.

$$u_{\alpha,1}(R_{\hat{O}}\mathbf{k}) = u_{\alpha,1}(\mathbf{k}) \quad \forall \hat{O} \in C_{4v} \, ,$$

while the matrix elements for the p-orbitals show a nontrivial behavior. If these other elements were to transform according to

$$u_{\alpha,2}(R_{\hat{J}}\mathbf{k}) = -u_{\alpha,2}(\mathbf{k}) \tag{B.15}$$

and

$$u_{\alpha,2}(R_{\hat{I}'}\mathbf{k}) = u_{\alpha,3}(\mathbf{k})\,, \quad u_{\alpha,3}(R_{\hat{I}'}\mathbf{k}) = u_{\alpha,2}(\mathbf{k})\,, \tag{B.16}$$

the coupling function f would be invariant under $\mathbf{k}_i \to R_{\hat{O}}\mathbf{k}_i\ \forall \hat{O} \in C_{4v}$. These conditions follow from the form of f in Eq. (B.14) up to the signs, which are fixed by the quadratic part given in Eq. (B.3). A fourth (redundant) condition

$$u_{\alpha,3}(R_{\hat{J}}\mathbf{k}) = -u_{\alpha,3}(\mathbf{k})\,, \quad \hat{J} = \hat{I}'\hat{I}\hat{I}'$$

follows from Eqs. (B.15) and (B.16).

For $\alpha = 2$, however, the transformation matrix given in Eq. (B.13) violates the conditions in Eqs. (B.15) and (B.16). But there is some freedom in the choice of $u(\mathbf{k})$, as eigenvectors of complex matrices are only determined up to a phase factor. In the present case, changing these phase factors corresponds to a basis transformation between Bloch states. Moreover, this phase can be fixed locally in momentum space or, in other words, individually for each $\mathbf{k}$. This way, one may introduce additional discontinuities in the transformation matrix. This is also the case for non-hybridizing Bloch states with $u(\mathbf{k})$ according to Eq. (B.13) for $k_y \geq k_x \geq 0$ or $k_y < k_x < 0$ and

$$u(\mathbf{k}) = \begin{pmatrix} \frac{\epsilon}{4t}N_1(\mathbf{k})[1+r(\mathbf{k})] & -\sin(k_x/2)\,N_1(\mathbf{k}) & -\sin(k_y/2)\,N_1(\mathbf{k}) \\ 0 & \sin(k_y/2)\,N_2(\mathbf{k}) & -\sin(k_x/2)\,N_2(\mathbf{k}) \\ \frac{\epsilon}{4t}N_3(\mathbf{k})[1-r(\mathbf{k})] & -\sin(k_x/2)\,N_3(\mathbf{k}) & -\sin(k_y/2)\,N_3(\mathbf{k}) \end{pmatrix}$$

otherwise. In other words, the the flat band with index $\alpha = 2$ is multiplied by a factor -1 for $k_x \to -k_x$ and for $k_x \leftrightarrow k_y$. One can observe that Eqs. (B.15) and (B.16) are fulfilled in this new basis and that f hence behaves trivially under all C_{4v} operations, i.e.

$$f^{\boldsymbol{\alpha}}(R_{\hat{O}}\mathbf{k}_1, R_{\hat{O}}\mathbf{k}_2, R_{\hat{O}}\mathbf{k}_3, R_{\hat{O}}\mathbf{k}_4) = f^{\boldsymbol{\alpha}}(\mathbf{k}_1, \mathbf{k}_2, \mathbf{k}_3, \mathbf{k}_4) \quad \forall\, \hat{O} \in C_{4v}\,.$$

Therefore, the new Bloch basis is a natural one. This implies, that the full Hamiltonian is symmetric under

$$\boldsymbol{\chi}_\sigma(\mathbf{k}) \to \boldsymbol{\chi}'_\sigma(R_{\hat{O}}\mathbf{k}) = \boldsymbol{\chi}_\sigma(\mathbf{k}) \quad \forall \hat{O} \in C_{4v}\,, \tag{B.17}$$

i.e. the electron band operators do not need to be transformed or reordered.

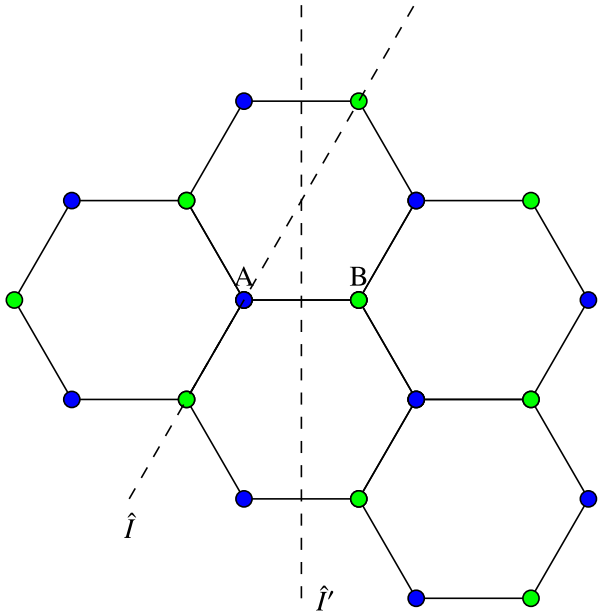

Figure B.3.: Honeycomb lattice with interpenetrating sublattices A and B. Also the mirror axes of the point-group operations $\hat{I}$ and $\hat{I}'$ are depicted here.

B.2. Sixfold symmetry: Graphene

B.2.1. Model Hamiltonian

Let us also look at an example of a six-fold symmetry. More precisely, consider a model for spinful fermions on the honeycomb lattice describing the p_z-orbitals in a graphene monolayer (for a review see Ref. [138]). Such a tight-binding description of graphene has a long history. [139] Also other materials with a honeycomb lattice, such as $In_3Cu_2VO_9$ are of interest. [140–142] As can be seen from Fig. B.3, we are dealing with two interpenetrating sublattices with creation operators $a^\dagger_\sigma(\mathbf{R})$ and $b^\dagger_\sigma(\mathbf{R})$, where $\mathbf{R}$ denotes the position of the unit cell. In the following, I assign the position quantum number $\mathbf{R}$ to an A site and the B site which is the nearest neighbor to its right. The two other nearest neighbors of the A site then are attributed to the unit cells with $\mathbf{R}+\delta_2$ and $\mathbf{R}+\delta_3$. If the distance between nearest neighbors is again set to unity, one has $\delta_1 = 0$, $\delta_2 = (-3/2, \sqrt{3}/2)$ and $\delta_3 = (-3/2, -\sqrt{3}/2)$ for the primitive translations. In

the following, I consider a Hamiltonian

$$\begin{aligned} H = &-t \sum_{\sigma,\mathbf{R},\delta} \left[a_\sigma^\dagger(\mathbf{R})\, b_\sigma(\mathbf{R}+\delta) + b_\sigma^\dagger(\mathbf{R}+\delta)\, a_\sigma(\mathbf{R}) \right] \\ &+ U \sum_{\mathbf{R}} : n_\uparrow^{(a)}(\mathbf{R})\, n_\downarrow^{(a)}(\mathbf{R}) + n_\uparrow^{(b)}(\mathbf{R})\, n_\downarrow^{(b)}(\mathbf{R}) : \\ &+ V \sum_{\mathbf{R},\delta,\sigma,\tau} : n_\sigma^{(a)}(\mathbf{R})\, n_\tau^{(b)}(\mathbf{R}+\delta) + n_\sigma^{(b)}(\mathbf{R}+\delta)\, n_\tau^{(a)}(\mathbf{R}) : \end{aligned} \tag{B.18}$$

with nearest-neighbor hopping t, on-site interaction U and nearest-neighbor interaction V. As before, let us first look at the quadratic part H_0 and switch to reciprocal space according to

$$\begin{aligned} a_\sigma(\mathbf{R}) &= \int_{\mathbb{H}} d\mathbf{k}\, e^{i\mathbf{k}\cdot\mathbf{R}}\, a_\sigma(\mathbf{k}) \\ b_\sigma(\mathbf{R}) &= \int_{\mathbb{H}} d\mathbf{k}\, e^{i\mathbf{k}\cdot\mathbf{R}}\, b_\sigma(\mathbf{k}) \end{aligned}$$

where the momentum integrals run over the first BZ $\mathbb{H}$ depicted in Fig. B.2(b). In terms of the orbitors

$$\Psi_\sigma(\mathbf{k}) = \begin{pmatrix} a_\sigma(\mathbf{k}) \\ b_\sigma(\mathbf{k}) \end{pmatrix}, \tag{B.19}$$

the one-particle Hamiltonian reads

$$H_0 = -t \sum_\sigma \int_{\mathbb{H}} d\mathbf{k}\, \Psi_\sigma^\dagger(\mathbf{k})\, \mathcal{H}_0(\mathbf{k})\, \Psi_\sigma(\mathbf{k}), \quad \mathcal{H}_0(\mathbf{k}) = \begin{pmatrix} 0 & h(\mathbf{k}) \\ h(\mathbf{k})^* & 0 \end{pmatrix}$$

with $h(\mathbf{k}) = \sum_\delta e^{i\delta\cdot\mathbf{k}}$. The one-particle coupling function $\mathcal{H}_0(\mathbf{k})$ vanishes at the valley points $K = 2\pi(-1/\sqrt{3}, 1/3)$ and $K' = 2\pi(-1/\sqrt{3}, -1/3)$. If $\mathcal{H}_0(\mathbf{k})$ is expanded around these points, one obtains a Dirac Hamiltonian. [143]

In reciprocal space, the interacting part H_{int} of the Hamiltonian reads as

$$\begin{aligned} H_{\text{int}} = U &\int_{\mathbb{H}} d\mathbf{k}_1 \ldots d\mathbf{k}_4\, \delta_{\{\mathbf{k}\}} \left[a_\uparrow^\dagger(\mathbf{k}_1)\, a_\downarrow^\dagger(\mathbf{k}_2)\, a_\downarrow(\mathbf{k}_3)\, a_\uparrow(\mathbf{k}_4) + b_\uparrow^\dagger(\mathbf{k}_1)\, b_\downarrow^\dagger(\mathbf{k}_2)\, b_\downarrow(\mathbf{k}_3)\, b_\uparrow(\mathbf{k}_4) \right] \\ + V \sum_{\sigma,\tau} &\int_{\mathbb{H}} d\mathbf{k}_1 \ldots d\mathbf{k}_4\, \delta_{\{\mathbf{k}\}} \left[h(\mathbf{k}_3 - \mathbf{k}_2)\; a_\sigma^\dagger(\mathbf{k}_1)\, b_\tau^\dagger(\mathbf{k}_2)\, b_\tau(\mathbf{k}_3)\, a_\sigma(\mathbf{k}_4) \right. \\ &\left. + h(\mathbf{k}_4 - \mathbf{k}_1)\; b_\sigma^\dagger(\mathbf{k}_1)\, a_\tau^\dagger(\mathbf{k}_2)\, a_\tau(\mathbf{k}_3)\, b_\sigma(\mathbf{k}_4) \right], \end{aligned}$$

where $\delta_{\{\mathbf{k}\}}$ again ensures momentum conservation up to reciprocal lattice vectors.

As the spacings δ are primitive vectors of the direct lattice, $h(\mathbf{k})$ is periodic in reciprocal space or, if all momenta are folded back to the first BZ, continuous at the zone boundary. We are hence already working in a proper basis. For the present example, the behavior

under point-group operations is already fairly simple in this basis: In the case of the honeycomb lattice, the point group is C_{6v}. All operations of this group can be written as products of two mirror operations $\hat{I}$ and $\hat{I}'$ with respect to axes going through the lattice sites and the middle of the bonds between neighboring sites, respectively. In Figs. B.3 and B.2(b), the y axis has been chosen to coincide with the mirror axis of $\hat{I}'$, while the mirror axis of $\hat{I}$ is rotated by $\pi/6$ with respect to y axis. Clearly, $\hat{I}$ maps the two sublattices onto themselves and $\hat{I}'$ maps them unto on another. One can observe that $h(R_{\hat{I}}\mathbf{k}) = h(\mathbf{k})$ and $h(R_{\hat{I}'}\mathbf{k}) = h(\mathbf{k})^*$. This leads to a simple behavior of the one-particle coupling function

$$\mathcal{H}_0(R_{\hat{I}}\mathbf{k}) = \mathcal{H}_0(\mathbf{k})\,, \quad \mathcal{H}_0(R_{\hat{I}'}\mathbf{k}) = M_{\hat{I}'}\,\mathcal{H}_0(\mathbf{k})\,M_{\hat{I}'}^\dagger\,, \quad M_{\hat{I}'} = \begin{pmatrix} 0 & 1 \\ 1 & 0 \end{pmatrix}.$$

As for the interacting part, one may substitute $\delta_{\{\mathbf{k}\}}h(\mathbf{k}_4 - \mathbf{k}_1) = \delta_{\{\mathbf{k}\}}h(\mathbf{k}_3 - \mathbf{k}_2)^*$. Therefore, H_{int} is left unchanged under $\mathbf{k}_i \to R_{\hat{I}}\mathbf{k}_i$ and the a and b operators are interchanged under $\mathbf{k}_i \to R_{\hat{I}'}\mathbf{k}_i$. So altogether, the full Hamiltonian is invariant under the two operations

$$\Psi_\sigma(\mathbf{k}) \to \Psi'_\sigma(R_{\hat{I}}\mathbf{k}) = \Psi_\sigma(\mathbf{k})\,, \quad \Psi_\sigma(\mathbf{k}) \to \Psi'_\sigma(R_{\hat{I}'}\mathbf{k}) = M_{\hat{I}'}\Psi_\sigma(\mathbf{k})\,.$$

This reflects the C_{6v} symmetry of the system, since all operations in these group can be written as products of the identity, $\hat{I}$ and $\hat{I}'$.

Note that the resulting representation matrices $M_{\hat{O}}$ are reducible. This may seem counterintuitive in first place, since the underlying (hybridizing) Bloch states have p_z character, which corresponds to the A_{2u} irreducible representation of D_{6h}. (In a way similar as in the case of the Emery model, the point group D_{6h} of the three-dimensional electronic structure gets reduced to C_{6v} in the two-dimensional lattice model.) Since one has two inequivalent sites per unit-cell, however, the resulting nontrivial point-group behavior of the nuclear positions gives rise to reducible representation matrices. In the Bloch basis with states

$$\left|c_\sigma^\pm\right\rangle = \frac{1}{\sqrt{2}}\left[a_\sigma^\dagger(\mathbf{k}) \pm b_\sigma^\dagger(\mathbf{k})\right]|0\rangle\,,$$

one would obtain representation matrices with blocks corresponding to the A_1 and B_2 irreducible representations of C_{6v}, i.e.

$$\tilde{M}_{\hat{I}} = \begin{pmatrix} 1 & 0 \\ 0 & 1 \end{pmatrix}, \qquad \tilde{M}_{\hat{I}'} = \begin{pmatrix} 1 & 0 \\ 0 & -1 \end{pmatrix}.$$

Note this is not yet the band basis and consequently the states $|c_\sigma^\pm\rangle$ hybridize almost everywhere on the BZ. For the considerations in this thesis, the reducibility or irreducibility of the representation matrices does not play a role and switching from reducible to irreducible orbitals may be of little practical use.

B.2.2. Band language and natural basis

Now let us again switch to the band language, where one has

$$H_0 = \sum_\sigma \int_{\mathbb{H}} d\mathbf{k}\, \boldsymbol{\chi}^\dagger_\sigma(\mathbf{k})\, \mathcal{B}(\mathbf{k})\, \boldsymbol{\chi}_\sigma(\mathbf{k})\,, \quad \mathcal{B}(\mathbf{k}) = t \begin{pmatrix} +|h(\mathbf{k})| & 0 \\ 0 & -|h(\mathbf{k})| \end{pmatrix}$$

for the one-particle Hamiltonian. Again the dispersion transforms trivially, i.e. $\mathcal{B}(R_{\hat{O}}\mathbf{k}) = \mathcal{B}(\mathbf{k})\ \forall \hat{O} \in C_{6v}$. The band operators $\boldsymbol{\chi}_\sigma(\mathbf{k}) = u(\mathbf{k})\, \Psi_\sigma(\mathbf{k})$ are obtained from the orbitors $\Psi_\sigma(\mathbf{k})$ by transformation matrices

$$u(\mathbf{k}) = \frac{1}{\sqrt{2}} \begin{pmatrix} e^{i\phi(\mathbf{k})} & -1 \\ 1 & e^{-i\phi(\mathbf{k})} \end{pmatrix}. \tag{B.20}$$

The phase $\phi(\mathbf{k}) = \arg h(\mathbf{k})$ changes sign under $\mathbf{k} \to R_{\hat{I}'}\mathbf{k}$ while it is left invariant under $\mathbf{k} \to R_{\hat{I}}\mathbf{k}$.

If the interacting part

$$H_{\text{int}} = \sum_{\sigma_1 \ldots \sigma_4} \sum_{\alpha_1 \ldots \alpha_4} \int_{\mathbb{T}} d\mathbf{k}_1 \ldots d\mathbf{k}_4\ \delta_{\{\mathbf{k}\}}\, f^{\boldsymbol{\alpha}}(\mathbf{k}_1, \mathbf{k}_2, \mathbf{k}_3, \mathbf{k}_4)\, \delta_{\sigma_1,\sigma_4}\, \delta_{\sigma_2,\sigma_3} \chi^\dagger(\xi_1)\, \chi^\dagger(\xi_2)\, \chi(\xi_3)\, \chi(\xi_4)$$

of the Hamiltonian is expressed in terms of the band pseudo-spinors $\boldsymbol{\chi}$, the coupling function $f^{\boldsymbol{\alpha}}(\mathbf{k}_1, \mathbf{k}_2, \mathbf{k}_3, \mathbf{k}_4)$ is given by

$$\begin{aligned} f^{\boldsymbol{\alpha}}(\mathbf{k}_1, \mathbf{k}_2, \mathbf{k}_3, \mathbf{k}_4) = \frac{U}{2} \big[& u_{\alpha_1,1}(\mathbf{k}_1)\, u_{\alpha_2,1}(\mathbf{k}_2)\, u^*_{\alpha_3,1}(\mathbf{k}_3)\, u^*_{\alpha_4,1}(\mathbf{k}_4) \\ & + u_{\alpha_1,2}(\mathbf{k}_1)\, u_{\alpha_2,2}(\mathbf{k}_2)\, u^*_{\alpha_3,2}(\mathbf{k}_3)\, u^*_{\alpha_4,2}(\mathbf{k}_4) \big] \\ & + V\, h(\mathbf{k}_3 - \mathbf{k}_2)\, u_{\alpha_1,1}(\mathbf{k}_1)\, u_{\alpha_2,1}(\mathbf{k}_2)\, u^*_{\alpha_3,2}(\mathbf{k}_3)\, u^*_{\alpha_4,2}(\mathbf{k}_4) \\ & + V\, h(\mathbf{k}_3 - \mathbf{k}_2)^*\, u_{\alpha_1,2}(\mathbf{k}_1)\, u_{\alpha_2,2}(\mathbf{k}_2)\, u^*_{\alpha_3,1}(\mathbf{k}_3)\, u^*_{\alpha_4,1}(\mathbf{k}_4)\,. \end{aligned}$$

Obviously, the two-particle coupling function behaves trivially under $\mathbf{k}_i \to R_{\hat{I}}\mathbf{k}_i$, since the transformation matrix $u(\mathbf{k})$ does so. The behavior under $\mathbf{k}_i \to R_{\hat{I}'}\mathbf{k}_i$ would also be trivial, if the transformation matrix obeyed $u(R_{\hat{I}'}\mathbf{k}) = u(\mathbf{k})\, M_{\hat{I}'}$. Unfortunately, this is not the case in Eq. (B.20). However, a trivial behavior of the two-particle coupling function can be enforced by a basis transformation which yields

$$u(\mathbf{k}) = \frac{1}{\sqrt{2}} \begin{pmatrix} -1 & e^{-i\phi(\mathbf{k})} \\ e^{i\phi(\mathbf{k})} & 1 \end{pmatrix}$$

for $k_x < 0$ and

$$u(\mathbf{k}) = \frac{1}{\sqrt{2}} \begin{pmatrix} e^{i\phi(\mathbf{k})} & -1 \\ 1 & e^{-i\phi(\mathbf{k})} \end{pmatrix}$$

elsewhere. Note that, for the present model, $u(\mathbf{k})$ is continuous everywhere on the BZ in this *natural* band gauge.

B.3. Alternative proof of the existence of a natural basis

B.3.1. Non-degenerate bands

In this Appendix, a short, alternative proof the existence of a natural basis is presented. I will first only allow for band degeneracies at high-symmetry points, where the little group equals the full point group. After considering this more special case, let me generalize this proof to band structures with degeneracies at arbitrary points.

It is textbook knowledge (see, for example, Chapter 8-4 of Ref. [74]) that non-degenerate bands transform with one-dimensional irreducible representations of the point group. On a more formal level, this means that band pseudo-spinors $\boldsymbol{\eta}$ behave according to

$$\boldsymbol{\eta}_a(\mathbf{k}) \to \boldsymbol{\eta}'_a(R_{\hat{O}}\mathbf{k}) = N_{\hat{O}}(\mathbf{k})\,\boldsymbol{\eta}_a(\mathbf{k})\,, \qquad (N_{\hat{O}}(\mathbf{k}))_{\alpha\beta} = \delta_{\alpha\beta}\, e^{i\theta^{\alpha}_{\hat{O}}(\mathbf{k})}\,. \tag{B.21}$$

The phase shifts $\theta^{\alpha}_{\hat{O}}(\mathbf{k})$ obey the group law

$$\theta^{\alpha}_{\hat{C}}(\mathbf{k}) = \theta^{\alpha}_{\hat{B}}(R_{\hat{A}}\mathbf{k}) + \theta^{\alpha}_{\hat{A}}(\mathbf{k}) \quad \text{for} \quad \hat{C} = \hat{B}\hat{A}\,. \tag{B.22}$$

The transformation rule (B.21) is also fulfilled in the presence of band degeneracies at high-symmetry points $\mathbf{q}$, where $\mathbf{q} = R_{\hat{O}}\mathbf{q}\ \forall \hat{O} \in \mathcal{G}$. At these points, the phase shifts $\theta^{\alpha}_{\hat{O}}(\mathbf{k})$ must vanish for all bands α and all point-group operations $\hat{O} \in \mathcal{G}$. If Eq. (B.21) holds everywhere on the BZ, one may always introduce phases $\varphi_\alpha(\mathbf{k})$ such that $\theta^{\alpha}_{\hat{O}}(\mathbf{k}) = \varphi_\alpha(R_{\hat{O}}\mathbf{k}) - \varphi_\alpha(\mathbf{k})$. After $\varphi_\alpha(\mathbf{k})$ is fixed at some arbitrary point $\mathbf{k}$, it is uniquely defined on the star of $\mathbf{k}$ by virtue of the group law (B.22).

The consequences of this are twofold. For one thing, the vertex functions now transform with phase factors attached to their external legs, i.e. one has $\mathcal{B}(R_{\hat{O}}\mathbf{k}) = \mathcal{B}(\mathbf{k})$ and Eq. (2.17) holds for the interaction. Moreover, one may now perform a phase transformation

$$\boldsymbol{\eta}^{\alpha}_a(\mathbf{k}) \to \boldsymbol{\chi}^{\alpha}_a(\mathbf{k}) = e^{-i\varphi_\alpha(\mathbf{k})}\,\boldsymbol{\eta}^{\alpha}_a(\mathbf{k})\,,$$

which renders all these phases equal to unity. The corresponding Bloch basis is then a natural one, since it transforms according to Eq. (2.14) under point-group operations.

B.3.2. General case

Let us now allow for the bands to touch in arbitrary locations of the BZ, provided that the point-group symmetry of the band structure is still respected. This means, that if there is a degeneracy at $\mathbf{k}$, this degeneracy can also be found on the star of $\mathbf{k}$. Eq. (B.21) now generalizes to

$$\boldsymbol{\eta}_a(\mathbf{k}) \to \boldsymbol{\eta}'_a(R_{\hat{O}}\mathbf{k}) = \tilde{N}_{\hat{O}}(\mathbf{k})\,\boldsymbol{\eta}_a(\mathbf{k})\,,$$

with unitary representation matrices $\tilde{N}_{\hat{O}}(\mathbf{k})$ which are equal to unity at high-symmetry points and which decay into irreducible blocks. If the bands do not touch at $\mathbf{k}$, these blocks are one-dimensional, just as before. At band degeneracies, however, they may contain higher-dimensional irreducible blocks mixing the degenerate bands under point-group operations. The group law for the new representation matrices

$$\tilde{N}_{\hat{C}}(\mathbf{k}) = \tilde{N}_{\hat{B}}(R_{\hat{A}}\mathbf{k})\,\tilde{N}_{\hat{A}}(\mathbf{k}) \quad \text{for} \quad \hat{C} = \hat{B}\hat{A}\,,$$

allows for a decomposition

$$\tilde{N}_{\hat{O}}(\mathbf{k}) = w^{\dagger}(R_{\hat{O}}\mathbf{k})\,w(\mathbf{k}) \tag{B.23}$$

with unitary matrices w. This decomposition is not unique and Eq. (B.23) rather imposes a constraint on possible choices of $w(\mathbf{k})$. If one assumes some arbitrary unitary w at $\mathbf{k}$, w is uniquely defined on the star of $\mathbf{k}$ according to this constraint. Moreover, if w has the block structure of the $\tilde{N}_{\hat{O}}$ at $\mathbf{k}$, this also holds on the star of $\mathbf{k}$. One may now perform a basis transformation

$$\boldsymbol{\eta}_a^{\alpha}(\mathbf{k}) \to \boldsymbol{\chi}_a^{\alpha}(\mathbf{k}) = w(\mathbf{k})\,\boldsymbol{\eta}_a^{\alpha}(\mathbf{k})$$

with w decomposing the representation matrices $\tilde{N}_{\hat{O}}$. Such a basis transformation then renders the $\tilde{N}$ all equal to a unit matrix and Eq. (2.14) holds. If one now further requires that the $\tilde{N}_{\hat{O}}(\mathbf{k})$ and $w(\mathbf{k})$ have the same irreducible block structure everywhere on the BZ, only degenerate bands get mixed. Hence, the one-particle Hamiltonian is still diagonal after the transformation and the new basis is a natural one.

Appendix C.

Supplementary material for fRG flows into antiferromagnetic phases

Large parts of Section C.1 have previously been published in Ref. [60].

C.1. Generalized, anisotropic mean-field model

In this appendix section, the mean-field model of Eq. (4.1) is generalized to an action

$$\mathcal{A} = \int dk\, \bar{\psi}_\sigma(k)\, (ik_0 - \epsilon_{\mathbf{k}})\, \psi_\sigma(k) + \frac{J}{\Omega}\, \mathbf{S}_Q \cdot \mathbf{S}_{-Q} + \frac{\alpha J}{\Omega}\, S^z_Q S^z_{-Q} \tag{C.1}$$

with xxz-type interaction, which breaks the SU(2)-symmetry for a non-vanishing anisotropy α. Equation (C.1) interpolates between the isotropic case and an Ising-type interaction at $\alpha \to \infty$ for positive α or an interaction of xy-type for $-1 < \alpha < 0$. In the following, the former will be referred to as the Ising regime and the latter as the xy-regime. The RG flow equations can be parametrized in exactly the same way as for the mean-field model in Eq. (4.1). Again, this leads to the flow equations (4.12)–(4.14), but now with the initial conditions $J_z^\infty = 4J(1+\alpha)$, $J_{xy}^\infty = 4J$, and $\Delta = \Delta_0$ in the ultraviolet. The formal solution of the flow equations now reads as

$$J_z = \frac{4J\,(1+\alpha)}{1 + 4J\,(1+\alpha)\, B_{\uparrow\uparrow}}\,, \tag{C.2}$$

$$J_{xy} = \frac{4J}{1 + 4J\, B_{\uparrow\downarrow}}\,, \tag{C.3}$$

$$\Delta - \Delta_0 = -4J\,(1+\alpha)\; B_{\uparrow\downarrow}\, \Delta\,. \tag{C.4}$$

The gap equation (C.4) can be derived analogously to Eq. (4.17). Note that the Ward identity Eq. (1.12) has been derived for a spin-symmetric interaction and thus no longer

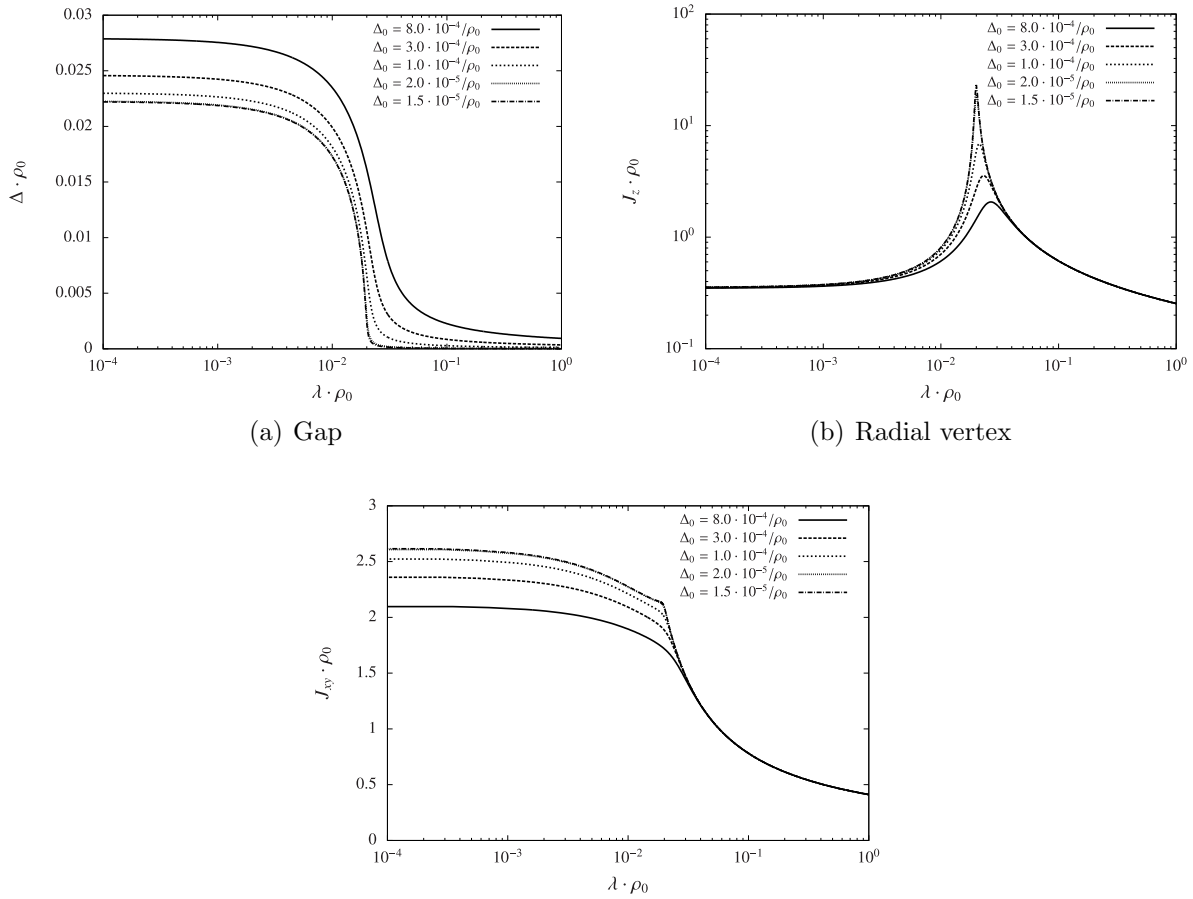

(a) Gap

(b) Radial vertex

(c) Goldstone vertex

Figure C.1.: Flow of the gap Δ (a) and of the radial and Goldstone vertices J_z and J_{xy} (b),(c) for $\alpha = 0.2$, zero temperature, perfect nesting, and a constant density of states ρ_0 ($W = 2/\rho_0$, $J = 0.09/\rho_0$). In (c), the curves for different values of the bare gap Δ_0 become discernible below the critical scale.

holds. So, a constraint that forces J_{xy} to diverge in the limit $\Delta_0 \to 0$ is now absent: for non-zero positive α, the Goldstone modes are gapped. As a consequence, the denominator of Eq. (C.3) no more needs to be zero for $\Delta_0, \lambda \to 0$, but may now take on finite values.

I now discuss the case of relatively weak anisotropies ($\alpha = \pm 0.2$) for $J > 0$ both in the Ising and in the xy-regimes. In Fig. C.1, the flow of the three couplings is depicted for $\alpha = +0.2$. The flow of J_z in Fig. C.1(b) again is peaked at some critical scale λ_{crit}, which is now enhanced as can be seen from Eq. (C.2). At this scale, the gap in Fig. C.1(a) starts to grow significantly and reaches a saturation value in the infrared.

So far the results only quantitatively differ from the case of isotropic interaction. The

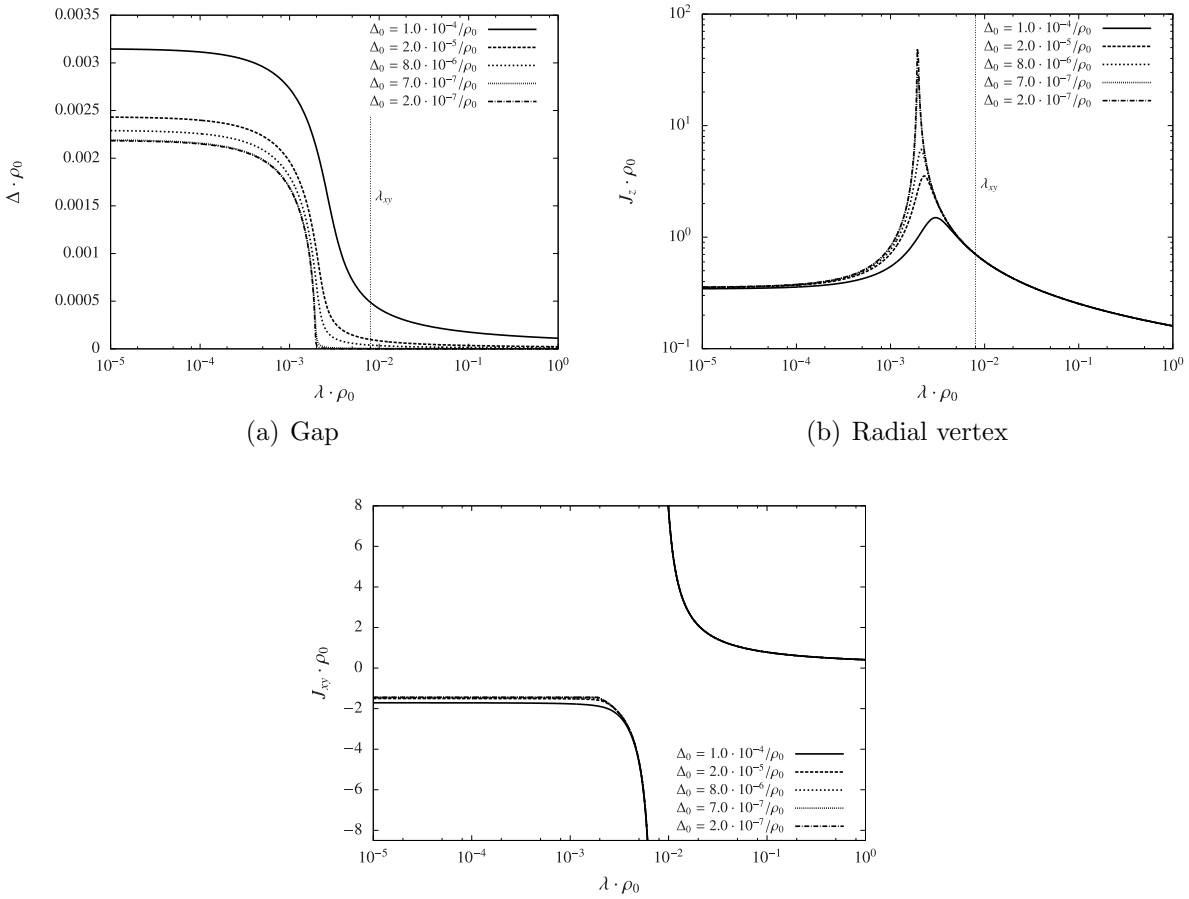

(a) Gap

(b) Radial vertex

(c) Goldstone vertex

Figure C.2.: Flow of Δ and J_z according to Eqs. (4.12) and (4.14) (a),(b) and of J_{xy} according to Eq. (C.5) (c) for $\alpha = -0.2$, zero temperature, perfect nesting and a constant density of states ρ_0 (all other parameters as in Fig. C.1). Below $\lambda_{xy} \approx 8 \cdot 10^{-3}/\rho_0$, the results are unphysical.

crucial difference occurs in the flow of J_{xy}. Inserting the modified gap equation (C.4) into Eq. (C.3) yields

$$J_{xy} = \frac{4J\,(1+\alpha)\,\Delta}{\Delta_0 + \alpha\Delta}\,, \tag{C.5}$$

which gives finite values in the limit $\lambda, \Delta_0 \to 0$.

Let us now consider the flow in the xy-regime with an anisotropy factor $\alpha = -0.2$ (see Fig. C.2). Therefore the spins should be aligned in the xy-plane rather than in the z-direction in the ground state. Since our formalism does not allow for a staggered in-plane magnetization, we should encounter an instability corresponding to spins ordered along a direction in the xy-plane. The flow of the gap and J_z does not seem to differ much from the previous case. From Eq. (C.5), we however find that for $-1 < \alpha < 0$,

J_{xy} undergoes a sign change at some scale λ_{xy} as shown in Fig. C.2(c). Of course, this divergence forbids direct integration of the flow equation (4.13) down to the infrared. Instead, a flow to strong coupling is observed. According to Fig. C.2(c), this instability occurs at about $\lambda_{xy} = 8 \cdot 10^{-3}/\rho_0$. At this scale, both Δ and J_z remain finite. Formally, the flow of J_z and Δ (Eqs. (4.12) and (4.14)) can be continued below λ_{xy}. The result obtained is similar to the previous cases (see Figs. C.2(a) and C.2(b)). Again J_z has a peak at a scale $\lambda_{13} < \lambda_{xy}$, where Δ starts to grow significantly. Note however that the formal solution of the flow equations (4.12) for J_z and (4.14) for Δ becomes unphysical at scales $\lambda < \lambda_{xy}$, as the instability corresponds to a staggered magnetization in the xy-plane. The corresponding seed field, however, was set to zero in the x and y directions *before* the thermodynamic limit was taken, which is not the physical order of the limits for spontaneous symmetry breaking. Of course, with some additional effort, one could now allow for a xy-symmetry-breaking component of the self-energy in straight analogy to what was has been done for the z direction. That way, one could follow the flow further through the xy-instability. At the level presented here, we can infer that the formalism with symmetry breaking only in the z direction is faithful enough to allow for additional instabilities. This is important in order to preserve the unbiased character of the RG approach.

C.2. Regularity of time-reversal breaking interactions

In Chapter 4.2.3, time-reversal breaking contributions to the interaction are neglected. After resorting to further approximations, the mean-field result can be reproduced in Chapter 4.4.2. However, the role of the time-reversal breaking contributions remains still unclear in that discussion. Obviously, such terms may already take on nonvanishing values at the RPA level, if they are not artificially excluded. For a nS_z term, for example, the diagram in Fig. C.3(c) seems to comply with the symmetries. These terms may therefore have an impact on the RPA result and might even diverge in the limit of a vanishing seed field Δ_0. In the following, I will show that, in the Hubbard model, these terms vanish for zero transfer frequencies and momenta, i.e. at $l = 0$. Since exchange propagators decouple at different values of l in RPA, this rules out divergencies of the time-reversal breaking part of the interactions for $\Delta_0 \to 0$.

Let me recall that fermion-boson vertices are frequency- and momentum-independent in RPA. The loop integrals in the diagrams of Fig. C.3 therefore reduce to

$$B^{\{s\}}_{\sigma\sigma'}(l) = \int d'p \; G^{s_1 s_2}_{\sigma}(p + l/2) \, G^{s_3 s_4}_{\sigma'}(p - l/2)$$

as all other factors can be pulled out. These fermionic bubbles obey the RPN constraint

$$B^{\{s\}}_{\sigma\sigma'}(l) = B^{\{-s\}}_{-\sigma-\sigma'}(l)^* = B^{\{-s\}}_{-\sigma-\sigma'}(-l) \, .$$

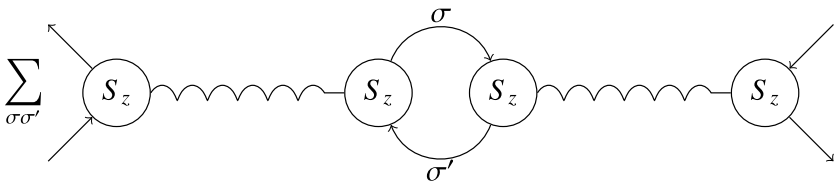

(a) S_z^2 term

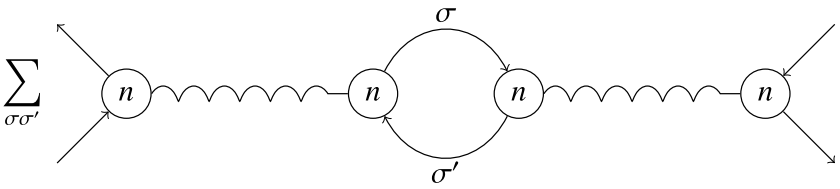

(b) CDW term

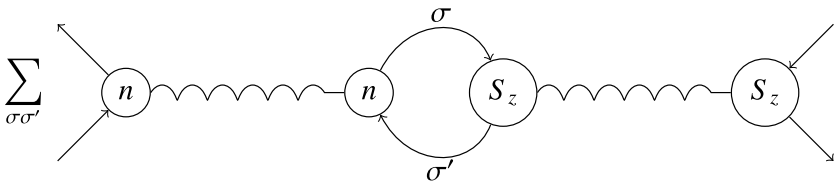

(c) nS_z term

Figure C.3.: Time-reversal invariant and time-reversal breaking diagrams RPA diagrams. σ and σ' denote the spin-projection quantum numbers of the internal fermionic lines. Nodes label with n and S_z represent fermion-boson vertices with a spin dependence of the form $\delta_{\sigma\sigma'}$ and $\tau^z_{\sigma\sigma'}$, respectively. For simplicity, Nambu indices are suppressed here.

Let us now first have a look at the scale derivatives of the S_z^2 and CDW terms at RPA level, which are depicted in the diagrams of Fig. C.3(a),(b). Since in the fermion-boson vertices inside the loops diagrams are either both symmetric or both antisymmetric under a spin flip in those diagrams, only the spin-symmetric part

$$B_{\mathrm{eq}+}^{\{s\}}(l) \equiv B_{\uparrow\uparrow}^{\{s\}}(l) + B_{\downarrow\downarrow}^{\{-s\}}(-l)$$

of the loop integrals contributes. In Fig. C.3(c), however, one of the internal fermion-boson vertices is symmetric and the other one is antisymmetric under a spin flip. Consequently, a nS_z interaction is generated from the spin-antisymmetric part

$$B_{\mathrm{eq}-}^{\{s\}}(l) \equiv B_{\uparrow\uparrow}^{\{s\}}(l) - B_{\downarrow\downarrow}^{\{-s\}}(-l)$$

of the loop integral.

The S_x^2, S_y^2 and S_xS_y contributions to the interaction behave analogously, where S_x plays the role of n, where S_y replaces S_z and where $B_{\uparrow\uparrow}^{\{s\}}(l)$ and $B_{\downarrow\downarrow}^{\{-s\}}(-l)$ are to be substituted by $B_{\uparrow\downarrow}^{\{s\}}(l)$ and $B_{\downarrow\uparrow}^{\{-s\}}(-l)$, respectively. The S_xS_y term is then generated by a fermionic bubble of the form

$$B_{\mathrm{op}-}^{\{s\}}(l) \equiv B_{\uparrow\downarrow}^{\{s\}}(l) - B_{\downarrow\uparrow}^{\{-s\}}(-l)\,.$$

Since the U(1) symmetry is preserved, the particle-particle channels are not coupled to the particle-hole channels at the RPA level, an hence the pairing channels are not considered here. (In particular, pair-exchange contributions are irrelevant in RPA for a repulsive bare interaction.)

In Chapter 4.4.2, only values of the exchange propagators at zero momentum and frequency are needed in order to recover the mean-field results. Let us therefore look at the loop integrals at $l = 0$ now. One can observe that

$$B_{\mathrm{eq}-}^{\{s\}}(0) = -B_{\mathrm{eq}-}^{\{-s\}}(0)\,,$$
$$B_{\mathrm{op}-}^{\{s\}}(0) = -B_{\mathrm{op}-}^{\{-s\}}(0)\,,$$

or that, in other words, the time-reversal breaking interactions with $l = 0$ are generated by Nambu-antisymmetric contributions to particle-hole bubbles. If the bare interactions are symmetric under a flip of all four Nambu indices as for example a Hubbard interaction, time-reversal breaking interactions are also Nambu-antisymmetric at $l = 0$.

In the classification of Chapter 4.3.1, Nambu-antisymmetric interactions can be interpreted as mixing terms between trivial and sign-changing form factors. If these two form factors belong to different irreducible representations of the model, these terms are prohibited by the point-group symmetries according to Corollary A.1.1. This is the case for the Hubbard model, where the trivial form factor has a plain s-wave form and the sign-changing one corresponds to a $d_{x^2-y^2}$-wave. Consequently, time-reversal breaking terms vanish for $l = 0$ at the RPA level for the Hubbard model. For the Chubukov

model, such terms are still allowed, but it seems unlikely that such form-factor mixing terms play a major role or even diverge in the limit of a vanishing seed field.

At least for the Hubbard model, this justifies the *a priori* omission of time-reversal breaking terms in the RPA analysis of Chapter 4.4.2. Also beyond RPA and for the Chubukov model, one may expect the time-reversal breaking contributions to stay regular.

References

[1] E. Zeidler, *Quantum field theory I — Basics in Mathematics and Physics.* Springer, Berlin, Heidelberg, 2006.

[2] K.-Y. Yang, T. Rice, and F.-C. Zhang, "Phenomenological theory of the pseudogap state," *Phys. Rev. B* **73** (2006) 174501.

[3] G. Kotliar, S. Savrasov, K. Haule, V. Oudovenko, O. Parcollet, and C. Marianetti, "Electronic structure calculations with dynamical mean-field theory," *Rev. Mod. Phys.* **78** (2006) 865–951.

[4] D. Vollhardt, K. Byczuk, and M. Kollar, "Dynamical mean-field theory," in *Strongly Correlated Systems*, A. Avella and F. Mancini, eds., vol. 171 of *Springer Series in Solid-State Sciences*, pp. 203–236. Springer Berlin Heidelberg, 2012.

[5] C. Weber, K. Haule, and G. Kotliar, "Optical weights and waterfalls in doped charge-transfer insulators: A local density approximation and dynamical mean-field theory study of $La_{2-x}Sr_xCuO_4$," *Phys. Rev. B* **78** (2008) 134519.

[6] L. de' Medici, X. Wang, M. Capone, and A. Millis, "Correlation strength, gaps, and particle-hole asymmetry in high-T_c cuprates: A dynamical mean field study of the three-band copper-oxide model," *Phys. Rev. B* **80** (2009) 054501.

[7] C. Weber, K. Haule, and G. Kotliar, "Strength of correlations in electron- and hole-doped cuprates," *Nat Phys* **6** no. 8, (2010) 574–578.

[8] C. Weber, K. Haule, and G. Kotliar, "Apical oxygens and correlation strength in electron- and hole-doped copper oxides," *Phys. Rev. B* **82** (2010) 125107.

[9] X. Wang, L. de' Medici, and A. Millis, "Role of oxygen-oxygen hopping in the three-band copper-oxide model: Quasiparticle weight, metal insulator and magnetic phase boundaries, gap values, and optical conductivity," *Phys. Rev. B* **83** (2011) 094501.

[10] C. Weber, C. Yee, K. Haule, and G. Kotliar, "Scaling of the transition temperature of hole-doped cuprate superconductors with the charge-transfer energy," *EPL (Europhysics Letters)* **100** no. 3, (2012) 37001.

[11] M. Hettler, A. Tahvildar-Zadeh, M. Jarrell, T. Pruschke, and H. Krishnamurthy, "Nonlocal dynamical correlations of strongly interacting electron systems," *Phys. Rev. B* **58** (1998) R7475–R7479.

[12] P. R. Kent, T. Saha-Dasgupta, O. Jepsen, O. Andersen, A. Macridin, T. Maier, M. Jarrell, and T. Schulthess, "Combined density functional and dynamical cluster quantum Monte Carlo calculations of the three-band Hubbard model for hole-doped cuprate superconductors," *Phys. Rev. B* **78** (2008) 035132.

[13] M. Potthoff, "Self-energy-functional approach to systems of correlated electrons," *The European Physical Journal B* **32** (2003) 429–436.

[14] C. Dahnken, M. Aichhorn, W. Hanke, E. Arrigoni, and M. Potthoff, "Variational cluster approach to spontaneous symmetry breaking: The itinerant antiferromagnet in two dimensions," *Phys. Rev. B* **70** (2004) 245110.

[15] M. Aichhorn, E. Arrigoni, Z. Huang, and W. Hanke, "Superconducting gap in the Hubbard model and the two-gap energy scales of high-T_c cuprate superconductors," *Phys. Rev. Lett.* **99** (2007) 257002.

[16] W. Hanke, M. Kiesel, M. Aichhorn, S. Brehm, and E. Arrigoni, "The 3-band Hubbard-model versus the 1-band model for the high-T_c cuprates: Pairing dynamics, superconductivity and the ground-state phase diagram," *The European Physical Journal Special Topics* **188** (2010) 15–32.

[17] K. Wilson, "Renormalization group and critical phenomena. II. Phase-space cell analysis of critical behavior," *Phys. Rev. B* **4** (1971) 3184–3205.

[18] J. Berges, N. Tetradis, and C. Wetterich, "Non-perturbative renormalization flow in quantum field theory and statistical physics," *Physics Reports* **363** no. 46, (2002) 223 – 386.

[19] W. Metzner, M. Salmhofer, C. Honerkamp, V. Meden, and K. Schönhammer, "Functional renormalization group approach to correlated fermion systems," *Rev. Mod. Phys.* **84** (2012) 299–352.

[20] T. Enss, *Renormalization, conservation laws and transport in correlated electron systems.* PhD thesis, Universität Stuttgart, 2005.

[21] C. Halboth and W. Metzner, "d-wave superconductivity and Pomeranchuk instability in the two-dimensional Hubbard model," *Phys. Rev. Lett.* **85** (2000) 5162–5165.

[22] J. Reiss, D. Rohe, and W. Metzner, "Renormalized mean-field analysis of antiferromagnetism and d-wave superconductivity in the two-dimensional Hubbard model," *Phys. Rev. B* **75** (2007) 075110.

[23] C. Honerkamp, M. Salmhofer, N. Furukawa, and T. Rice, "Breakdown of the Landau-Fermi liquid in two dimensions due to umklapp scattering," *Phys. Rev. B* **63** (2001) 035109.

[24] C. Husemann and M. Salmhofer, "Efficient parametrization of the vertex function, Ω scheme, and the t, t' Hubbard model at van Hove filling," *Phys. Rev. B* **79** (2009) 195125.

[25] C. Husemann, K.-U. Giering, and M. Salmhofer, "Frequency-dependent vertex functions of the (t, t') Hubbard model at weak coupling," *Phys. Rev. B* **85** (2012) 075121.

[26] K.-U. Giering and M. Salmhofer, "Self-energy flows in the two-dimensional repulsive Hubbard model," *Phys. Rev. B* **86** (2012) 245122.

[27] S. Uebelacker and C. Honerkamp, "Self-energy feedback and frequency-dependent interactions in the functional renormalization group flow for the two-dimensional Hubbard model," *Phys. Rev. B* **86** no. 23, (2012) 235140.

[28] C. Honerkamp, "Density waves and cooper pairing on the honeycomb lattice," *Phys. Rev. Lett.* **100** (2008) 146404.

[29] M. Scherer, S. Uebelacker, and C. Honerkamp, "Instabilities of interacting electrons on the honeycomb bilayer," *Phys. Rev. B* **85** (2012) 235408.

[30] T. Lang, Z. Meng, M. Scherer, S. Uebelacker, F. Assaad, A. Muramatsu, C. Honerkamp, and S. Wessel, "Antiferromagnetism in the Hubbard model on the Bernal-stacked honeycomb bilayer," *Phys. Rev. Lett.* **109** (2012) 126402.

[31] M. Scherer, S. Uebelacker, D. Scherer, and C. Honerkamp, "Interacting electrons on trilayer honeycomb lattices," *Phys. Rev. B* **86** (2012) 155415.

[32] W. Wu, M. Scherer, C. Honerkamp, and K. Le Hur, "Correlated Dirac particles and superconductivity on the honeycomb lattice," *Phys. Rev. B* **87** (2013) 094521.

[33] W.-S. Wang, Y.-Y. Xiang, Q.-H. Wang, F. Wang, F. Yang, and D.-H. Lee, "Functional renormalization group and variational Monte Carlo studies of the electronic instabilities in graphene near $\frac{1}{4}$ doping," *Phys. Rev. B* **85** (2012) 035414.

[34] F. Wang, H. Zhai, and D.-H. Lee, "Antiferromagnetic correlation and the pairing mechanism of the cuprates and iron pnictides: A view from the functional renormalization group studies," *EPL (Europhysics Letters)* **85** no. 3, (2009) 37005.

[35] F. Wang, H. Zhai, and D.-H. Lee, "Nodes in the gap function of LaFePo, the gap function of the Fe(Se,Te) systems, and the STM signature of the $s_{\pm}$ pairing," *Phys. Rev. B* **81** (2010) 184512.

[36] R. Thomale, C. Platt, J. Hu, C. Honerkamp, and B. Bernevig, "Functional renormalization-group study of the doping dependence of pairing symmetry in the iron pnictide superconductors," *Phys. Rev. B* **80** (2009) 180505.

[37] C. Platt, C. Honerkamp, and W. Hanke, "Pairing in the iron arsenides: A functional RG treatment," *New Journal of Physics* **11** no. 5, (2009) 055058.

[38] R. Thomale, C. Platt, W. Hanke, and B. Bernevig, "Mechanism for explaining differences in the order parameters of FeAs-based and FeP-based pnictide superconductors," *Phys. Rev. Lett.* **106** (2011) 187003.

[39] C. Platt, R. Thomale, C. Honerkamp, S.-C. Zhang, and W. Hanke, "Mechanism for a pairing state with time-reversal symmetry breaking in iron-based superconductors," *Phys. Rev. B* **85** (2012) 180502.

[40] C. Platt, W. Hanke, and R. Thomale to appear in *Advances of Physics*.

[41] S. Uebelacker and C. Honerkamp, "Multiband effects on superconducting instabilities driven by electron-electron interactions," *Phys. Rev. B* **85** (2012) 155122.

[42] M. Kiesel and R. Thomale, "Sublattice interference in the kagome Hubbard model," *Phys. Rev. B* **86** (2012) 121105.

[43] W.-S. Wang, Z.-Z. Li, Y.-Y. Xiang, and Q.-H. Wang, "Competing electronic orders on kagome lattices at van Hove filling," *Phys. Rev. B* **87** (2013) 115135.

[44] Q.-H. Wang, C. Platt, Y. Yang, C. Honerkamp, F. Zhang, W. Hanke, T. Rice, and R. Thomale, "Theory of superconductivity in a three-orbital model of

Sr_2RuO_4," *EPL (Europhysics Letters)* **104** no. 1, (2013) 17013.

[45] R. Gersch, C. Honerkamp, D. Rohe, and W. Metzner, "Fermionic renormalization group flow into phases with broken discrete symmetry: Charge-density wave mean-field model," *The European Physical Journal B* **48** (2005) 349–358.

[46] R. Gersch, J. Reiss, and C. Honerkamp, "Fermionic functional renormalization-group for first-order phase transitions: A mean-field model," *New Journal of Physics* **8** no. 12, (2006) 320.

[47] R. Gersch, C. Honerkamp, and W. Metzner, "Superconductivity in the attractive Hubbard model: functional renormalization group analysis," *New Journal of Physics* **10** no. 4, (2008) 045003.

[48] A. Eberlein and W. Metzner, "Parametrization of nambu vertex in a singlet superconductor," *Progress of Theoretical Physics* **124** no. 3, (2010) 471–491.

[49] A. Eberlein and W. Metzner, "Effective interactions and fluctuation effects in spin-singlet superfluids," *Phys. Rev. B* **87** (2013) 174523.

[50] A. Eberlein and W. Metzner, "Superconductivity in the two-dimensional t-t'-Hubbard model," *Phys. Rev. B* **89** (2014) 035126.

[51] A. Eberlein, *Functional renormalization group study of fluctuation effects in fermionic superfluids*. PhD thesis, Universität Stuttgart, 2013.

[52] T. Maier, S. Graser, D. Scalapino, and P. Hirschfeld, "Origin of gap anisotropy in spin fluctuation models of the iron pnictides," *Phys. Rev. B* **79** (2009) 224510.

[53] V. Emery, "Theory of high-T_c," *Phys. Rev. Lett.* **58** (1987) 2794–2797.

[54] O. Andersen, A. Liechtenstein, O. Jepsen, and F. Paulsen, "LDA energy bands, low-energy Hamiltonians, t', t'', $t_\perp(k)$, and $J_\perp$," *Journal of Physics and Chemistry of Solids* **56** no. 12, (1995) 1573 – 1591.

[55] M. Hybertsen, M. Schlüter, and N. Christensen, "Calculation of coulomb-interaction parameters for La_2CuO_4 using a constrained-density-functional approach," *Phys. Rev. B* **39** (1989) 9028–9041.

[56] C. Karrasch, R. Hedden, R. Peters, T. Pruschke, K. Schönhammer, and V. Meden, "A finite-frequency functional renormalization group approach to the single impurity Anderson model," *Journal of Physics: Condensed Matter* **20** no. 34, (2008) 345205.

[57] M. Salmhofer, C. Honerkamp, W. Metzner, and O. Lauscher, "Renormalization group flows into phases with broken symmetry,"
Progress of Theoretical Physics **112** no. 6, (2004) 943–970.

[58] M. Salmhofer and C. Honerkamp, "Fermionic renormalization group flows,"
Progress of Theoretical Physics **105** no. 1, (2001) 1–35.

[59] S. Maier, J. Ortloff, and C. Honerkamp, "Multi-orbital effects in functional renormalization group: A weak-coupling study of the Emery model,"
Phys. Rev. B **88** (2013) 235112.

[60] S. Maier and C. Honerkamp, "Renormalization group flow for fermions into antiferromagnetically ordered phases: Method and mean-field models,"
Phys. Rev. B **86** (2012) 134404.

[61] H. Krahl, J. Müller, and C. Wetterich, "Generation of d-wave coupling in the two-dimensional Hubbard model from functional renormalization,"
Phys. Rev. B **79** (2009) 094526.

[62] H. Krahl, S. Friederich, and C. Wetterich, "Incommensurate antiferromagnetic fluctuations in the two-dimensional Hubbard model,"
Phys. Rev. B **80** (2009) 014436.

[63] S. Friederich, H. Krahl, and C. Wetterich, "Four-point vertex in the Hubbard model and partial bosonization," *Phys. Rev. B* **81** (2010) 235108.

[64] S. Friederich, H. Krahl, and C. Wetterich, "Functional renormalization for spontaneous symmetry breaking in the Hubbard model,"
Phys. Rev. B **83** (2011) 155125.

[65] W. Metzner, J. Reiss, and D. Rohe, "Magnetic and superconducting correlations in the two-dimensional Hubbard model,"
physica status solidi (b) **243** no. 1, (2006) 46–56.

[66] C. Honerkamp and M. Salmhofer, "Magnetic and superconducting instabilities of the Hubbard model at the van Hove filling," *Phys. Rev. Lett.* **87** (2001) 187004.

[67] J. Ortloff *et al.* in preparation.

[68] M. Kiesel, C. Platt, W. Hanke, D. Abanin, and R. Thomale, "Competing many-body instabilities and unconventional superconductivity in graphene,"
Phys. Rev. B **86** (2012) 020507.

[69] M. Kiesel, C. Platt, W. Hanke, and R. Thomale, "Model evidence of an anisotropic chiral $d+id$-wave pairing state for the water-intercalated $Na_xCoO_2 \cdot y\ H_2O$ superconductor," *Phys. Rev. Lett.* **111** (2013) 097001.

[70] J. Negele and H. Orland, *Quantum Many-Particle Systems*. Addison-Wesley, 1988.

[71] A. Katanin, "Fulfillment of ward identities in the functional renormalization group approach," *Phys. Rev. B* **70** (2004) 115109.

[72] M. Vojta, Y. Zhang, and S. Sachdev, "Quantum phase transitions in d-wave superconductors," *Phys. Rev. Lett.* **85** (2000) 4940–4943.

[73] Q.-H. Wang private communication, 2013.

[74] M. Tinkham, *Group theory and quantum mechanics*. McGraw-Hill Book Company, New York, San Francisco, Toronto, London, 1964.

[75] J. Otsuki, "Two-particle self-consistent approach to unconventional superconductivity," *Phys. Rev. B* **85** (2012) 104513.

[76] K.-U. Giering private communication, 2013.

[77] A. Katanin and A. Kampf, "Order-parameter symmetries for magnetic and superconducting instabilities: Bethe-Salpeter analysis of functional renormalization-group solutions," *Phys. Rev. B* **72** (2005) 205128.

[78] D. Scherer, M. Scherer, *et al.* in preparation, 2013.

[79] S. Göttel, S. Andergassen, C. Honerkamp, D. Schuricht, and S. Wessel, "Critical scales in anisotropic spin systems from functional renormalization," *Phys. Rev. B* **85** (2012) 214406.

[80] M. Hohenadler, T. Lang, and F. Assaad, "Correlation effects in quantum spin-Hall insulators: A quantum Monte Carlo study," *Phys. Rev. Lett.* **106** (2011) 100403.

[81] D. Zheng, G.-M. Zhang, and C. Wu, "Particle-hole symmetry and interaction effects in the Kane-Mele-Hubbard model," *Phys. Rev. B* **84** (2011) 205121.

[82] M. Hohenadler, Z. Meng, T. Lang, S. Wessel, A. Muramatsu, and F. Assaad, "Quantum phase transitions in the Kane-Mele-Hubbard model," *Phys. Rev. B* **85** (2012) 115132.

[83] S. Maier, C. Honerkamp, and Q.-H. Wang, "Interplay between point-group symmetries and the choice of the Bloch basis in multiband models," *Symmetry* **5** no. 4, (2013) 313–343.

[84] S. Maier and C. Honerkamp, "Effective three-particle interactions in low-energy models for multiband systems," *Phys. Rev. B* **85** (2012) 064520.

[85] A. Fetter and J. Walecka, *Quantum Theory of Many-Particle Systems*. McGraw Hill, 1971.

[86] O. Vafek and K. Yang, "Many-body instability of coulomb interacting bilayer graphene: Renormalization group approach," *Phys. Rev. B* **81** (2010) 041401.

[87] N. Marzari, A. Mostofi, J. Yates, I. Souza, and D. Vanderbilt, "Maximally localized Wannier functions: Theory and applications," *Rev. Mod. Phys.* **84** (2012) 1419–1475.

[88] K. Sun and E. Fradkin, "Time-reversal symmetry breaking and spontaneous anomalous Hall effect in Fermi fluids," *Phys. Rev. B* **78** (2008) 245122.

[89] J. Polchinski, "Renormalization and effective Lagrangians," *Nuclear Physics B* **231** no. 2, (1984) 269 – 295.

[90] M. Salmhofer, *Renormalization: An Introduction*. Springer, Berlin Heidelberg, 1999.

[91] P. Kopietz, L. Bartosch, and F. Schütz, *Introduction into the Functional Renormalization Group*. Springer, Berlin Heidelberg, 2010.

[92] M. Kinza, J. Ortloff, and C. Honerkamp, "Effective low-energy Hamiltonians for interacting nanostructures," *Phys. Rev. B* **82** (2010) 155430.

[93] F. Aryasetiawan, M. Imada, A. Georges, G. Kotliar, S. Biermann, and A. Lichtenstein, "Frequency-dependent local interactions and low-energy effective models from electronic structure calculations," *Phys. Rev. B* **70** no. 19, (2004) 195104.

[94] M. Imada and T. Miyake, "Electronic structure calculation by first principles for strongly correlated electron systems," *Journal of the Physical Society of Japan* **79** no. 11, (2010) 112001.

[95] C. Honerkamp, "Effective interactions in multiband systems from constrained summations," *Phys. Rev. B* **85** (2012) 195129.

[96] A. Katanin, "Two-loop functional renormalization group approach to the one- and two-dimensional Hubbard model," *Phys. Rev. B* **79** no. 23, (2009) 235119.

[97] P. Anderson, *The Theory of Superconductivity in the High-T_c Cuprates*. Princeton University Press, Princeton, 1997.

[98] D. Scalapino, "A common thread: The pairing interaction for unconventional superconductors," *Rev. Mod. Phys.* **84** (2012) 1383–1417.

[99] J. Hu and N. Hao, "S_4 symmetric microscopic model for iron-based superconductors," *Phys. Rev. X* **2** (2012) 021009.

[100] E. Pavarini, I. Dasgupta, T. Saha-Dasgupta, O. Jepsen, and O. Andersen, "Band-structure trend in hole-doped cuprates and correlation with $T_{c\max}$," *Phys. Rev. Lett.* **87** (2001) 047003.

[101] O. Andersen and L. Boeri, "On the multi-orbital band structure and itinerant magnetism of iron-based superconductors," *Annalen der Physik* **523** no. 1-2, (2011) 8–50.

[102] T. Miyake, K. Nakamura, R. Arita, and M. Imada, "Comparison of *Ab initio* low-energy models for LaFePO, LaFeAsO, $BaFe_2As_2$, LiFeAs, FeSe, and FeTe: Electron correlation and covalency," *Journal of the Physical Society of Japan* **79** no. 4, (2010) 044705.

[103] J. Lichtenstein, S. Maier, C. Honerkamp, C. Platt, R. Thomale, O. Andersen, and L. Boeri, "Functional renormalization group study of an eight-band model for the iron arsenides," `arXiv:1403.5487 [cond-mat.supr-con]`.

[104] C. Varma, "Theory of the pseudogap state of the cuprates," *Phys. Rev. B* **73** (2006) 155113.

[105] M. Fischer and E.-A. Kim, "Mean-field analysis of intra-unit-cell order in the Emery model of the CuO_2 plane," *Phys. Rev. B* **84** (2011) 144502.

[106] N. Furukawa, T. Rice, and M. Salmhofer, "Truncation of a two-dimensional Fermi surface due to quasiparticle gap formation at the saddle points," *Phys. Rev. Lett.* **81** no. 15, (1998) 3195–3198.

[107] H. Schulz, "Superconductivity and antiferromagnetism in the two-dimensional Hubbard model: Scaling theory," *EPL (Europhysics Letters)* **4** no. 5, (1987) 609.

[108] A. Chubukov, D. Efremov, and I. Eremin, "Magnetism, superconductivity, and pairing symmetry in iron-based superconductors," *Phys. Rev. B* **78** (2008) 134512.

[109] A. Katanin and A. Kampf, "Renormalization group analysis of magnetic and superconducting instabilities near van Hove band fillings," *Phys. Rev. B* **68** (2003) 195101.

[110] J. Berntsen, T. Espelid, and A. Genz, "Algorithm 698: Dcuhre: An adaptive multidemensional integration routine for a vector of integrals," *ACM Trans. Math. Softw.* **17** (1991) 452–456.

[111] F. Zhang and T. Rice, "Effective Hamiltonian for the superconducting Cu oxides," *Phys. Rev. B* **37** (1988) 3759–3761.

[112] C. Husemann, *Competing Orders in the Hubbard Model*. PhD thesis, Universität Leipzig, 2009.

[113] V. Hankevych, I. Grote, and F. Wegner, "Pomeranchuk and other instabilities in the $t - t'$ Hubbard model at the van Hove filling," *Phys. Rev. B* **66** (2002) 094516.

[114] A. Neumayr and W. Metzner, "Renormalized perturbation theory for Fermi systems: Fermi surface deformation and superconductivity in the two-dimensional Hubbard model," *Phys. Rev. B* **67** (2003) 035112.

[115] S. Bulut, W. Atkinson, and A. Kampf, "Spatially modulated electronic nematicity in the three-band model of cuprate superconductors," *Phys. Rev. B* **88** (2013) 155132.

[116] C. Husemann and W. Metzner, "Incommensurate nematic fluctuations in the two-dimensional Hubbard model," *Phys. Rev. B* **86** (Aug, 2012) 085113.

[117] M. Greiter and R. Thomale, "No evidence for spontaneous orbital currents in numerical studies of three-band models for the CuO planes of high temperature superconductors," *Phys. Rev. Lett.* **99** (2007) 027005.

[118] Y. Ando, K. Segawa, S. Komiya, and A. Lavrov, "Electrical resistivity anisotropy from self-organized one dimensionality in high-temperature superconductors," *Phys. Rev. Lett.* **88** (2002) 137005.

[119] R. Daou, J. Chang, D. LeBoeuf, O. Cyr-Choiniere, F. Laliberte, N. Doiron-Leyraud, B. Ramshaw, R. Liang, D. Bonn, W. Hardy, and L. Taillefer,

"Broken rotational symmetry in the pseudogap phase of a high-T_c superconductor," *Nature* **463** no. 7280, (2010) 519–522.

[120] V. Hinkov, S. Pailhes, P. Bourges, Y. Sidis, A. Ivanov, A. Kulakov, C. Lin, D. Chen, C. Bernhard, and B. Keimer, "Two-dimensional geometry of spin excitations in the high-transition-temperature superconductor $YBa_2Cu_3O_{6+x}$," *Nature* **430** no. 7000, (2004) 650–654.

[121] V. Hinkov, D. Haug, B. Fauqu, P. Bourges, Y. Sidis, A. Ivanov, C. Bernhard, C. Lin, and B. Keimer, "Electronic liquid crystal state in the high-temperature superconductor $YBa_2Cu_3O_{6.45}$," *Science* **319** no. 5863, (2008) 597–600.

[122] R. Fernandes and J. Schmalian, "Competing order and nature of the pairing state in the iron pnictides," *Phys. Rev. B* **82** (2010) 014521.

[123] M. Le Tacon, A. Sacuto, A. Georges, G. Kotliar, Y. Gallais, D. Colson, and A. Forget, "Two energy scales and two distinct quasiparticle dynamics in the superconducting state of underdoped cuprates," *Nat Phys* **2** no. 8, (2006) 537–543.

[124] K. Tanaka, W. Lee, D. Lu, A. Fujimori, T. Fujii, Risdiana, I. Terasaki, D. Scalapino, T. Devereaux, Z. Hussain, and Z.-X. Shen, "Distinct Fermi-momentum-dependent energy gaps in deeply underdoped Bi2212," *Science* **314** no. 5807, (2006) 1910–1913.

[125] P. Strack, R. Gersch, and W. Metzner, "Renormalization group flow for fermionic superfluids at zero temperature," *Phys. Rev. B* **78** (2008) 014522.

[126] B. Obert, C. Husemann, and W. Metzner, "Low-energy singularities in the ground state of fermionic superfluids," *Phys. Rev. B* **88** (2013) 144508.

[127] T. Morris, "The exact renormalization group and approximate solutions," *International Journal of Modern Physics A* **9** no. 14, (1994) 2411–2449.

[128] C. Yang and S. Zhang, "SO_4 symmetry in a Hubbard model," *Mod. Phys. Lett. B* **04** no. 11, (1990) 759.

[129] S. Östlund, "Symmetries and canonical transformations of the Hubbard model on bipartite lattices," *Phys. Rev. Lett.* **69** (1992) 1695–1698.

[130] L. Banyai and K. Elsayed, "Time reversal and many-body non-equilibrium Green functions," *Annals of Physics* **233** no. 2, (1994) 165 – 181.

[131] A. Georges and J. Yedidia, "Onsager reaction terms for quantum many-body systems: Application to antiferromagnetic and superconducting order in the Hubbard model," *Phys. Rev. B* **43** (1991) 3475–3482.

[132] R. Brankin, I. Gladwell, and L. Shampine, *RKSUITE Release 1.0*, 1991. `http://www.netlib.org/ode/rksuite/`.

[133] The Numerical Algorithms Group Ltd, *NAG Library Manual, Mark 23 Contents*. Oxford, UK, 2011. `http://www.nag.co.uk/numeric/FL/nagdoc_fl23`.

[134] A. Eberlein private communication, 2013.

[135] U. Ascher, H. Chin, and S. Reich, "Stabilization of DAEs and invariant manifolds," *Numerische Mathematik* **67** no. 2, (1994) 131–149.

[136] P. Kopietz, "Onsager-reaction-field correction in the half-filled Hubbard model," *Phys. Rev. B* **48** (1993) 13789–13797.

[137] T. Schauerte and P. van Dongen, "Symmetry breaking in the Hubbard model at weak coupling," *Phys. Rev. B* **65** (2002) 081105.

[138] A. Castro Neto, F. Guinea, N. M. Peres, K. Novoselov, and A. Geim, "The electronic properties of graphene," *Rev. Mod. Phys.* **81** (2009) 109–162.

[139] P. Wallace, "The band theory of graphite," *Phys. Rev.* **71** (1947) 622–634.

[140] V. Kataev, A. Möller, U. Löw, W. Jung, N. Schittner, M. Kriener, and A. Freimuth, "Structural and magnetic properties of the new low-dimensional spin magnet,"
Journal of Magnetism and Magnetic Materials **290** no. 0, (2005) 310 – 313.

[141] A. Möller, U. Löw, T. Taetz, M. Kriener, G. André, F. Damay, O. Heyer, M. Braden, and J. Mydosh, "Structural domain and finite-size effects of the antiferromagnetic S = 1/2 honeycomb lattice in $InCu_{2/3}V_{1/3}O_3$,"
Phys. Rev. B **78** (2008) 024420.

[142] Y. Yan, Z. Li, T. Zhang, X. Luo, G. Ye, Z. Xiang, P. Cheng, L. Zou, and X. Chen, "Magnetic properties of the doped spin-$\frac{1}{2}$ honeycomb-lattice compound $In_3Cu_2VO_9$," *Phys. Rev. B* **85** (2012) 085102.

[143] J. Slonczewski and P. Weiss, "Band structure of graphite,"
Phys. Rev. **109** (1958) 272–279.

[144] S. Maier and J. Ankerhold, "Quantum Smoluchowski equation: A systematic study," *Phys. Rev. E* **81** (2010) 021107.

[145] S. Maier and J. Ankerhold, "Low-temperature quantum fluctuations in overdamped ratchets," *Phys. Rev. E* **82** (2010) 021104.

Publications

The compilation of this thesis is solely to the author. A large part of the work presented here has however been published in previous articles and has been done in collaboration with the authors listed below, which I cordially appreciate. Parts of these publications are contained in particular, but not exclusively, in Chapters 1–4 and the Appendices. The respective publications are indicated in the abstracts at the beginning of each of these chapters and appendices.

List of publications:

- S. Maier and C. Honerkamp, "Effective three-particle interactions in low-energy models for multiband systems,"
  Phys. Rev. B **85** (2012) 064520. [84]

- S. Maier and C. Honerkamp, "Renormalization group flow for fermions into antiferromagnetically ordered phases: Method and mean-field models,"
  Phys. Rev. B **86** (2012) 134404. [60]

- S. Maier, C. Honerkamp, and Q.-H. Wang, "Interplay between point-group symmetries and the choice of the Bloch basis in multiband models,"
  Symmetry **5** no. 4, (2013) 313–343. [83]

- S. Maier, J. Ortloff, and C. Honerkamp, "Multi-orbital effects in functional renormalization group: A weak-coupling study of the Emery model,"
  Phys. Rev. B **88** (2013) 235112. [59]

- A publication that will contain parts of Chapter 4 and 5 and Appendix C.2 is being prepared.

Neither another publication [103], to which I have contributed to a small part, is included in this thesis nor are Refs. [144, 145], which outgrew my diploma thesis.

Acknowledgments

At the end of my doctoral studies, I would like to say thanks for the support I experienced in different ways during the last, formative years.

First of all, I feel indebted to my supervisor Prof. C. Honerkamp for taking me as a graduate student, for always helpful advice regarding my research and for giving me the opportunity to attend stimulating conferences and summer schools. In this place, I also would like to thank Prof. M. Salmhofer for co-refereeing this thesis.

Acknowledgments are also directed to my collaborators: I am happy to have been able to build on work by J. Ortloff in performing the instability analysis of the Emery model. I am also thankful to Q.-H. Wang of Nanjing, China for sharing his experience on symmetries in multiband models from numerical calculations with my supervisor and me. In this place, I would also like to mention my collaborators for a piece of work on the iron pnictides to which I contributed to a small part and which is therefore not included in this thesis. Namely, I would like to thank J. Lichtenstein, L. Boeri and O. K. Andersen from MPI Stuttgart and R. Thomale and C. Platt from the University of Würzburg.

Furthermore, I would like to express my gratitude for fruitful discussions to a number of people. Among these are my fellow graduate students M. Kinza, G. Klingschat, J. Lichtenstein, D. Sanchez de la Peña, M. Scheb and S. Uebelacker and T. C. Lang and M. M. Scherer, who were postdocs at the Institute for Theoretical Solid State Physics and the head of the computational physics group, Prof. S. Wessel. I am glad to be able to look back on conversations with A. Eberlein, K.-U. Giering, C. Husemann, A. Katanin, W. Metzner, B. Obert, M. Salmhofer, D. Rohe and R. Thomale — in particular during workshops of the DFG programs FOR 723 and SPP 1458. In particular, discussions with Andreas and Kay have paved the road to entering phases of antiferromagnetic order in this thesis. I am happy to have been given advice on numerical questions by T. C. Lang and S. Wessel as well as to have experienced the friendly support provided by members of the high-performance computing team at the RWTH Center for Computation and by the admins at our institute, G. Klingschat and U. Kahlert. I am thankful to Julian, who has cross-read essential parts of this thesis.

Summarizing, I have enjoyed working in an open atmosphere, where I was given the

freedom I desired and where the head of the group always kept his office door open for his graduate students. I would therefore like to thank all members and guests of the Institute of Theoretical Solid State Physics and the secretaries, who have contributed to this atmosphere.

Finally, I would like to thank the Deutsche Forschungsgemeinschaft for financial support via FOR 723 and SPP 1458.

Curriculum Vitae

Stefan Maier
born on December 17, 1983 in Günzburg a. d. Donau, Germany

2003	**Abitur** Dossenberger-Gymnasium, Günzburg
Oct. 2003 – Nov. 2009	**Studies of Physics** (Diploma) University of Ulm, Ulm, Germany
Aug. 2007 – May 2008	**Studies of Physics** (M.Sc.) University of New Mexico, Albuquerque, New Mexico, USA
Dec. 2008 – Nov. 2009	**Diploma thesis** *"Quantum corrections in the presence of strong damping"* University of Ulm Advisor: Prof. J. Ankerhold
since Jan. 2010	**Ph.D. studies** RWTH Aachen University, Aachen, Germany Advisor: Prof. C. Honerkamp